COLLISION ACTIVE A TAIWAN : APPORTS GEOPHYSIQUE ET TECTONIQUE

****

THESE

présentée à

l'Université de Bretagne Occidentale

par

Shu-Kun HSU

en vue de l'obtention du diplôme de

DOCTORAT

Spécialité : Géophysique - Géodynamique

****

Soutenue publiquement le 14 Septembre 1995 devant la commission d'examen :

Jean-Pierre Réhault	Président
Jacques Angelier	Rapporteur
Serge Lallemand	Rapporteur
Joachim Déramond	Examinateur
Thierry Juteau	Examinateur
Chuen-Tien Shyu	Examinateur
Jean-Claude Sibuet	Directeur de thèse

COLLISION ACTIVE A TAIWAN : APPORTS GEOPHYSIQUE ET TECTONIQUE

****

THESE

présentée à

l'Université de Bretagne Occidentale

par

Shu-Kun HSU

en vue de l'obtention du diplôme de

DOCTORAT

Spécialité : Géophysique - Géodynamique

****

Soutenue publiquement le 14 Septembre 1995 devant la commission d'examen :

Jean-Pierre Réhault	Professeur à l'Université de Bretagne Occidentale Président
Jacques Angelier	Professeur à l'Université de Pierre et Marie Curie Rapporteur
Serge Lallemand	CNRS, Laboratoire de Géophysique et Tectonique, Université de Montpellier II Rapporteur
Joachim Déramond	Professeur à l'Université de Toulouse Examinateur
Thierry Juteau	Professeur à l'Université de Bretagne Occidentale Examinateur
Chuen-Tien Shyu	Professeur à l'Université de Taiwan, Taiwan Examinateur
Jean-Claude Sibuet	Ifremer, DRO/GM, Centre de Brest Directeur de thèse

Scientific hypothesis can not be proven to be absolute true,
yet we should subject it to constant falsification attempts.

K. R. Popper (1968)

No. 52

許樹坤
于 IFREMER

Avant-propos

Ce travail a debuté lorsque je travaillais dans le bureau du centre de sismologie du *Central Weather Bureau* à Taiwan. Les professeurs Chuen-Tien Shyu et Char-Shine Liu m'ont encouragé à venir en France et à travailler dans le cadre de la coopération franco-taiwanaise en océanographie. Pendant la conférence de *TAICRUST* à Taiwan en Juin 1991, j'ai rencontré Jean-Claude Sibuet et Serge Lallemand. Grâce à eux, j'ai pu éviter les déboires administratifs pour commencer ma thèse. J'aurais dû travailler dès le début de ma thèse sur les données de la campagne *ATAI,* qui malheureusement n'a pas été programmée.

L'étude géodynamique de la région autour de Taiwan utilisant les données d'origine marine étant peu avancée, le but de mon travail a été, dans un premier temps, de compiler une base des données bathymétriques, gravimétriques et magnétiques. Ne disposant pas de nouvelles données, j'ai poursuivi le travail par analyse de la base de données existantes du NGDC (*National Geophysical Data Center*). A celles-ci sont venues s'ajouter les données bathymétriques et magnétiques, qui m'ont été gracieusement fournies par les professeurs Chuen-Tien Shyu et Char-Shine Liu.

Je tiens à remercier Jean-Claude Sibuet pour m'avoir initié au domaine tectonique. Ce mémoire a commencé par l'étude du bassin d'Okinawa. Ensuite, mon étude s'est étendue jusqu'au bassin de Tainan à travers Taiwan. Jean-Claude a également été très gentil de m'accorder une grande liberté de pensée et de me corriger au moment approprié. Il a largement contribué à ce mémoire.

Je suis très reconnaissant envers le professeur Chuen-Tien Shyu, Directeur de l'Institut d'Océanographie de l'Université de Taiwan. Il m'a toujours fait confiance depuis mes études à l'Institut d'Océanographie de l'Université de Taiwan. D'ailleurs, il a bien voulu accepter de participer à mon jury, bien qu'il soit débordé par des affaires administratives. De même, j'adresse mes remerciements au professeur Char-Shine Liu. Grâce à lui, le programme de coopération franco-taiwanais en océanographie avance à vive allure.

J'ai été bien assisté par Pascal Pelleau qui est très sympathique et qui m'a beaucoup aidé à résoudre mes problèmes informatiques. D'ailleurs, Pascal a beaucoup de chance d'avoir un super patron, Michel Voisset. C'était un très grand plaisir de pouvoir travailler avec Louis Géli dont j'apprécie le dynamisme. Jean-Louis Olivet m'a fait partager son point de vue de géodynamique globale. Il m'a fait penser à un proverbe chinois : "il n'est pas possible de manger un grand gâteau sans laisser tomber de petits sésames". Les discussions que j'ai eues avec Paul Beuzart étaient très agréables de part sa connaissance générale. L'optimisme de Serge Monti m'a fait souvent oublier des soucis. D'ailleurs, il m'a appris ce que sont les "qualités" des cartes bathymétriques.

Table des matières

Résumé

— Ce travail de recherche présente d'une part le développement de méthodes de traitement de données géophysiques et d'autre part une nouvelle hypothèse pour expliquer la surrection de Taiwan.

Trois techniques ont été développées, deux concernant la correction des erreurs aux points de croisement et la troisième permettant de localiser les frontières géologiques. (1) Une technique d'ajustement linéaire a été développée pour corriger automatiquement les erreurs aux points de croisement. Les artefacts dus aux erreurs aux points de croisement peuvent être ainsi minimisés, lors du contourage. (2) Une technique de modélisation de la variation temporelle a aussi été développée pour réduire les erreurs de mesures dues, soit aux variations diurnes magnétiques, soit aux variations de marées, soit aux erreurs d'orbite satellitaire, par exemple. (3) Une technique basée sur le signal analytique de haute résolution, composé du gradient de la n-ième dérivée verticale du potentiel selon les deux directions horizontales et la direction verticale, a été également mise au point pour interpréter les données magnétiques et gravimétriques. Cette méthode permet de détecter les frontières géologiques sans posséder d'informations *à priori* sur les sources ou sans connaître les paramètres de l'orientation magnétique régionale ou de la direction de l'aimantation.

Un nouveau modèle de collision arc-arc est proposé pour expliquer l'orogène de Taiwan. La surrection de Taiwan serait causée par la collision entre l'arc de Luzon et l'ancien arc des Ryukyus. Elle peut être décrite en cinq étapes : (1) il y a 20 Ma, à l'emplacement de Taiwan se situait l'ancienne zone de subduction des Ryukyus qui s'étendait probablement du sud-ouest de Taiwan au sud du Japon. (2) Entre 20 et 13 Ma, la subduction de la partie sud-ouest de la fosse des Ryukyus aurait cessé, créant les conditions cinématiques nécessaires à la formation de l'arc de Luzon. De plus, une portion de la plaque de la Mer des Philippines aurait été piégée dans la partie nord-est de la Mer de Chine du Sud, par transfert vers le nord-est de la grande faille de décrochement limitant initialement la Mer de Chine du Sud et la Mer des Philippines. (3) Entre 13 et 8 Ma, avant la surrection de Taiwan, l'initiation de la collision entre les deux arcs aurait eu lieu à proximité de 123,5°E. A l'ouest de 123,5°E, l'ancien arc des Ryukyus aurait subi une indentation due à la collision de l'arc de Luzon dans la direction de la convergence de la plaque de la Mer des Philippines par rapport à la plaque eurasiatique (environ N310°). Le début de la surrection de Taiwan daterait de 8 Ma avec début de la fermeture de l'ancien bassin arrière-arc. (4) Il y a 3 Ma, la collision active se poursuivait accompagnée par une compression plus active au niveau des arcs de Luzon et des Ryukyus et la reprise du fonctionnement des failles inverses dans le bassin arrière-arc soulevé. Le mélange de Lichi se serait mis en place dans la Vallée Longitudinale, à la frontière des deux arcs. (5) Actuellement, la collision arc-arc est toujours active mais se situe préférentiellement dans la partie centrale de Taiwan (23°N ; 121,2°E). Au Nord de cette région en compression, la partie sud-ouest du bassin d'Okinawa se trouve de nouveau en régime extensif.

9

Abstract

—This thesis mainly consists of two aspects: the development of three techniques of processing geophysical data, and a hypothesis to account for the uplift of Taiwan.

Three techniques have been developed: (1) A linear adjustment technique was developed to adjust track data in order to eliminate the errors at the intersections (cross-over errors, XOEs) of track data.—The XOEs should be eliminated because they could produce linear pseudo-structures in contoured maps, which induce a bias in the geologic interpretation. (2) Another cross-over technique was developed to particularly reduce the XOEs due to the temporal variation in data, such as the magnetic diurnal variation, the tidal variation or the satellite orbit error. In this method, a variation function could be adopted to model the temporal variation, used to correct the variation errors. (3) An enhanced analytic signal, composed of the nth-order vertical derivative values of two horizontal gradients and one vertical gradient of the potential field data, was developed to automatically detect geologic boundaries, such as faults or contacts. The major advantage of this method is that no *a priori* information is needed before the application and the result is independent of ambient parameters, such as the direction of magnetization.

A new model of arc-arc collision is proposed to explain the process of Taiwan orogeny. Namely, the uplift of Taiwan could be explained by the collision between the Luzon arc and the former Ryukyu arc and could be described in five stages: **(1)** About 20 Ma ago, the paleo-location of Taiwan was occupied by the former Ryukyu subduction zone which extended from southwest of Taiwan to the south of Japan. **(2)** Between 20 and 13 Ma ago, the subduction of the Philippine Sea plate beneath the southwest portion of the former Ryukyu arc stopped and the formation of the Luzon arc started. In addition, a portion of the Philippine Sea plate was trapped in the region between Taiwan and the Luzon islands. **(3)** Between 13 and 8 Ma, before the uplift of Taiwan the southern part of the Ryukyu arc was indented by the passage of the northern tip of the Luzon arc. The initial contact between the two arcs would be near 123.5°E. West of 123.5°E, the former Ryukyu arc was indented in the direction of convergence of the Philippine Sea plate relative to Eurasia (about N310°). About 8 Ma ago, the active collision in Taiwan began. The ancient backarc basin was first compressed and the existing normal faults in the ancient backarc basin were reactivated as reversed faults. **(4)** About 3 Ma ago, the active collision continued and the two arc were compressed. The Lichi melange appeared in the Longitudinal Valley considered as the convergent boundary. **(5)** Presently, the collision between the two arcs has migrated from northern to the central Taiwan (near 23°N; 121.2°E) and the southwesternmost Okinawa trough has resumed its extension.

10

INTRODUCTION

Introduction

Ce mémoire est essentiellement consacré à la compréhension du processus de la collision active au niveau de Taiwan, par interprétation des données de géophysique marine. Il est composé de deux parties :

- La première partie présente six articles qui ont été publiés ou sous presse au cours de ce travail. Les trois premiers concernent le traitement des données et les trois autres portent sur l'interprétation géodynamique de la région de Taiwan.

Deux méthodes ont été développées pour corriger les erreurs aux points de croisement entre les profils de données géophysiques, de façon à minimiser les artefacts lors du contourage (Hsu, 1995 ; Hsu et al., 1995a). Ces erreurs aux points de croisement ont plusieurs origines (les erreurs de navigation, les variations temporelles, la nature des systèmes d'acquisition, etc). Afin de les corriger, nous avons mis au point une technique d'ajustement linéaire et une technique permettant de modéliser la variation temporelle.

Une technique basée sur le signal analytique de haute-résolution a également été développée, pour localiser les frontières géologiques à partir des données magnétiques ou gravimétriques (Hsu et al., 1995b). Le principal avantage de cette méthode est qu'elle est indépendante de la direction d'aimantation. Ainsi, il n'y a pas besoin d'information *à priori* avant de l'appliquer. Elle peut, éventuellement, être utilisée pour localiser les isochrones magnétiques.

Dans les trois derniers articles, nous proposons une nouvelle interprétation de la surrection de Taiwan.

L'analyse des données bathymétriques multi-faisceaux a permis d'identifier de nombreuses orientations de failles normales le long du bassin d'Okinawa permettant de mieux appréhender les différentes phases cinématiques décrivant l'évolution du bassin d'Okinawa (Sibuet et al., 1995).

La synthèse des données bathymétriques, gravimétriques et séismologiques a permis de proposer un nouveau modèle de collision pour expliquer la surrection de Taiwan : une collison arc-arc (Hsu et Sibuet, 1995). Dans ce contexte, nous proposons l'hypothèse de l'existence d'une zone de subduction, avec un système de l'arc et bassin arrière-arc, qui se serait devenue fossile avant la surrection de Taiwan. La collision active à Taiwan aurait été précédée par une collision entre l'arc de Luzon et la partie sud de l'arc des Ryukyus, à proximité de 123,5°E (Hsu et al., 1995c). L'arc des Ryukyus aurait, par conséquent, subit une indentation dans la direction de la convergence de la plaque de la Mer des Philippines (~N310°) par rapport à la plaque eurasiatique

avant la collision active à Taiwan.

- La deuxième partie présente une synthèse générale de la collision active à Taiwan et complète les articles de Hsu et Sibuet (1995) et de Hsu et al. (1995c). Dans cette partie, nous discutons aussi les frontières majeures entre les plaques de la Mer des Philippines et eurasiatique, au niveau de Taiwan. Finalement, nous comparons le modèle de collision arc-arc avec les données géodésiques et la distribution des intensités des séismes dans la région de Taiwan. Enfin, une cinématique plausible et plus détaillée de la collision arc-arc à Taiwan est proposée.

PARTIE I : PUBLICATIONS

XCORR: a cross-over technique to adjust track data

Une technique d'ajustement linéaire est développée pour corriger les erreurs aux points de croisement. Grâce à cette méthode, les artefacts apparaissant le long des routes d'acquisition peuvent être réduits. A l'aide de cette méthode, nous avons produit des cartes contourées à partir des données bathymétriques, gravimétriques et magnétiques (Hsu et al., 1995b).

17

XCORR: A CROSS-OVER TECHNIQUE TO ADJUST TRACK DATA

SHU-KUN HSU

IFREMER, Département des Géosciences, Centre de Brest, B.P. 70, 29280 Plouzane, France
e-mail: hsu@ifremer.fr

Abstract—Cross-over errors (XOEs) from track data may give rise to pseudostructures in a contoured map. Such pitfalls can be reduced by adjusting all the measured values. FORTRAN programs are presented to determine automatically cross-over points (XOPs) and XOEs, to adjust XOEs to zero and to correct the data proportionally between every two XOPs.

Key Words: Cross-over error, Adjustment, Correction, Geophysics, FORTRAN

INTRODUCTION

Gravity, geomagnetic, and bathymetric surveys always show different values at the intersections of track lines. These discrepancies (termed XOEs, Fig. 1) can be revealed by cross-over analysis. The origin of these XOEs may come from navigation errors, systematic errors, diurnal variation, instrumental drift, inaccurate Eötvös correction, etc. Thus, pseudostructures can be produced in contoured maps which induce a bias in geologic interpretation. Several attempts had been made to remove instrumental drift of gravity measurement, diurnal variation in geomagnetic survey, or orbit error of satellite altimetry by using regression techniques (Wessel and Watts, 1988; Yarger, Robertson, and Wentland, 1978; Sander and Mrazek, 1982; Tai, 1988). However, after correction, residual XOEs remain. For this reason, Mittal (1984) has proposed a linear interpolation algorithm to smooth the residual XOEs in a survey network.

This study is inspired by Mittal and the adjustment performed for a simple survey network will be extended to arbitrary track surveys. Each track line is considered as a time series. Basically, the adjustment of track data is done with two steps: one program automatically locates all the XOPs and the corresponding XOEs in order to give every track an appropriate weight (usually one cruise can be regarded as one track, or it can be separated and considered as several tracks owing to a large time gap of two successive data points); another program eliminates all the XOEs at XOPs and adjusts all the measured values by taking into account the corrections at XOPs. However it is noted that pseudostructures do remain because of sparseness of XOPs.

METHODS

Instead of the overlapping block technique (Wessel, 1989), a new and simple algorithm which allows us to locate all the XOPs and to calculate their XOEs is based on the following steps (program XOVERH, Appendix 1):

Step 1: Consider every two consecutive measured points of a same track as a reference segment; for example, points A and B in track 1 (Fig. 2A). Then, from the reference segment, we can define a block-area as

$$x_a \leqslant x \leqslant x_b$$

$$y_a \leqslant y \leqslant y_b.$$

Step 2: Compare all the other segments, composed by every two measured points of the same
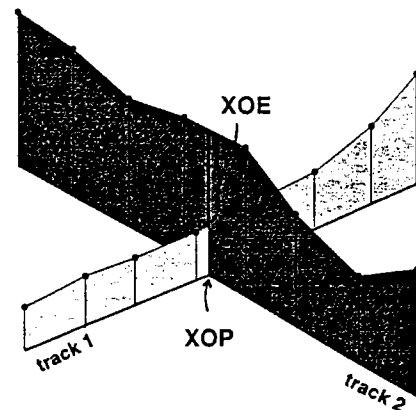
Figure 1. Schematic diagram showing cross-over error (XOE) at one cross-over point (XOP) from two tracks. Solid circles represent measured values. Between two measured values linear interpolation is used.
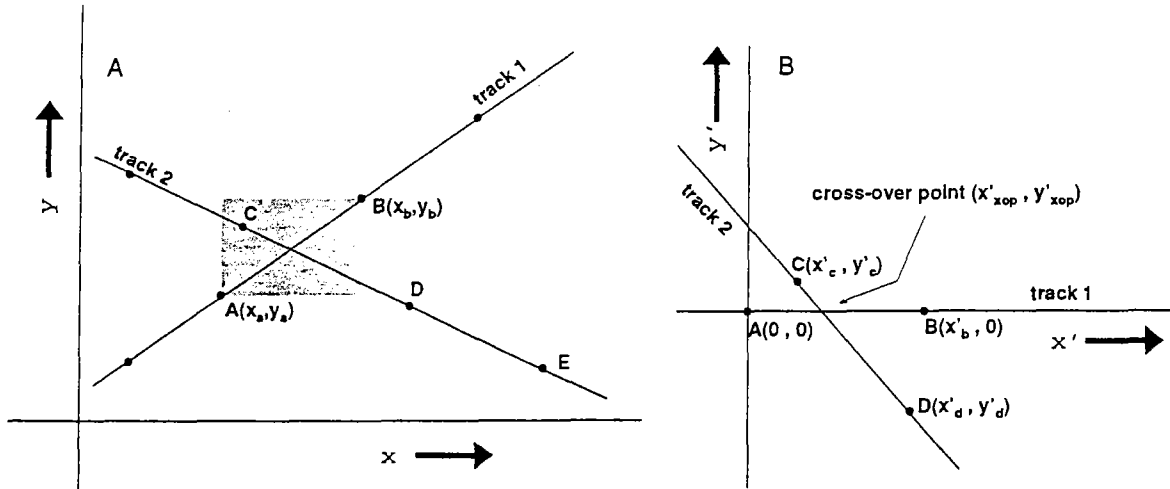
Figure 2. Diagrams showing methods for locating XOP. A—A reference segment AB defines block-area indicated by shaded area. Segments CD is not completely outside this area, whereas segment DE is completely outside this area. It suggests possibility of intersection between segment AB and segment CD. B—Transformation of coordinates for points A, B, C, and D. If XOP exists, points C and D should be located in upper and lower quadrants respectively, and solution is inside segment AB.

track, with the block-area and kick off those segments (e.g. segment DE in Fig. 2A) which are completely outside it. This can be done fast with four GOTO instructions of FORTRAN.

Step 3: If one segment (e.g. segment CD in Fig. 2A) has the possibility of intersecting with the reference segment, we can verify it by transforming these two segments into a new coordinate system (Fig. 2B), whose x' axis is the direction of line AB and point A is the new origin.

Step 4: Verify if points C and D are located in the upper quadrant and lower quadrant, respectively. If yes, then the solution of segment AB and segment CD can be determined easily by

$$x'_{xop} = x'_c - y'_c \times (x'_c - x'_d)/(y'_c - y'_d) \qquad (1)$$

$$y'_{xop} = 0. \qquad (2)$$

If the solution is inside segment AB (i.e. $0 \leqslant x'_{xop} \leqslant x'_b$), it is an XOP. We then transform it to the original coordinate system.

Step 5: Linear interpolation is made for segment AB and segment CD, and XOE is the difference between two interpolated values. Here the simple linear interpolation is used, because other schemes of interpolation pro-

duced similar results (Wessel and Watts, 1988).

It is noted that the computation speed of the present algorithm depends upon $(M + 1) \times M/2$, where M represents total number of measured points. Therefore, if necessary, one might separate one's dataset into several small area datasets in order to process them separately. The result will not change; however, one can save computation time.

Once the information of XOEs is obtained, an appropriate weight can be assigned to every track. For example,

$$W_i = N \bigg/ \sum_{j=1}^{N} (D_{ij})^2,$$

where W_i denotes the weight for the ith track and D_{ij} denotes the jth XOE for the ith track, whereas N represents the total number of XOPs in the ith track. This simple computation can be done by the readers.

Finally, the adjustment of all the track data is done with the program XCORR (Appendix 2). Basically, the reasonable value at each XOP is

$$V_{xop} = (V_i W_i + V_j W_j)/(W_i + W_j) \qquad (3)$$

where

V_i is the interpolated value for one XOP belonging to the ith track,

(Figure 3 opposite)

Figure 3. A—Upper diagram shows example data of four imaged tracks. Numbers denote measured values at corresponding measured points (solid circles). B—Lower diagram shows result of adjusted values by program XCORR with relative weight data shown in Table 2. Note that adjusted data of beginning and end of each track are kept.
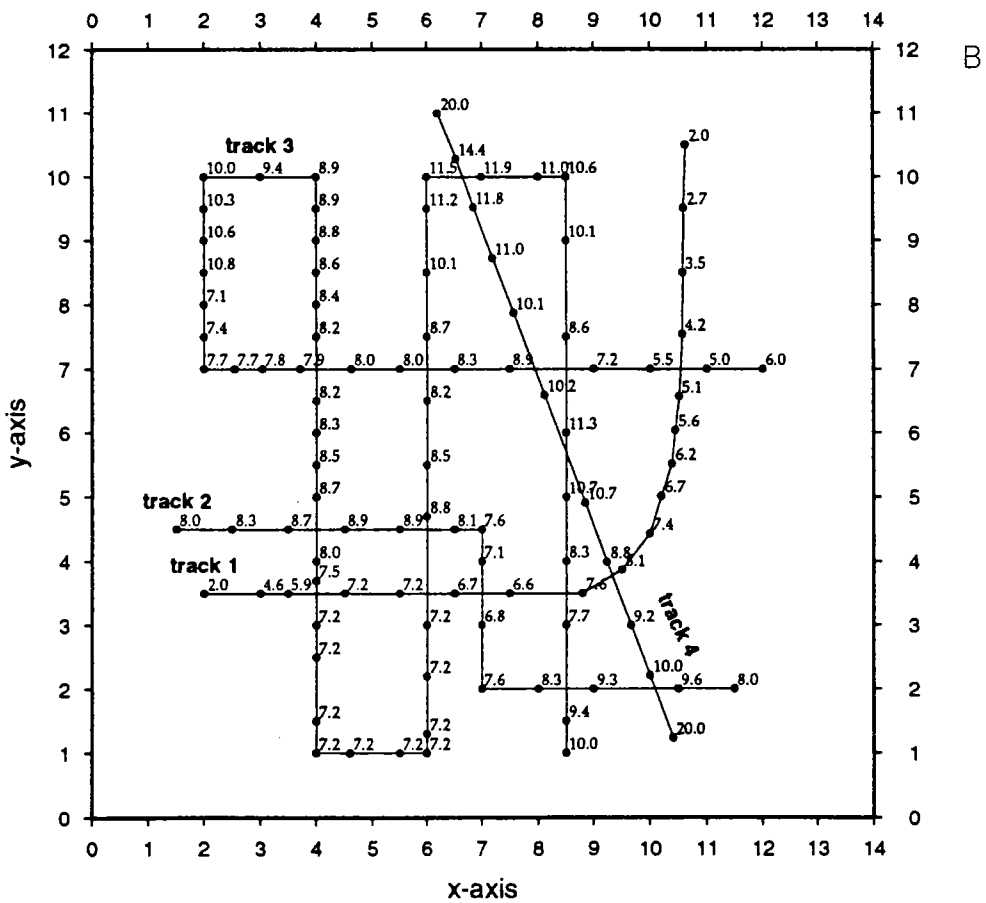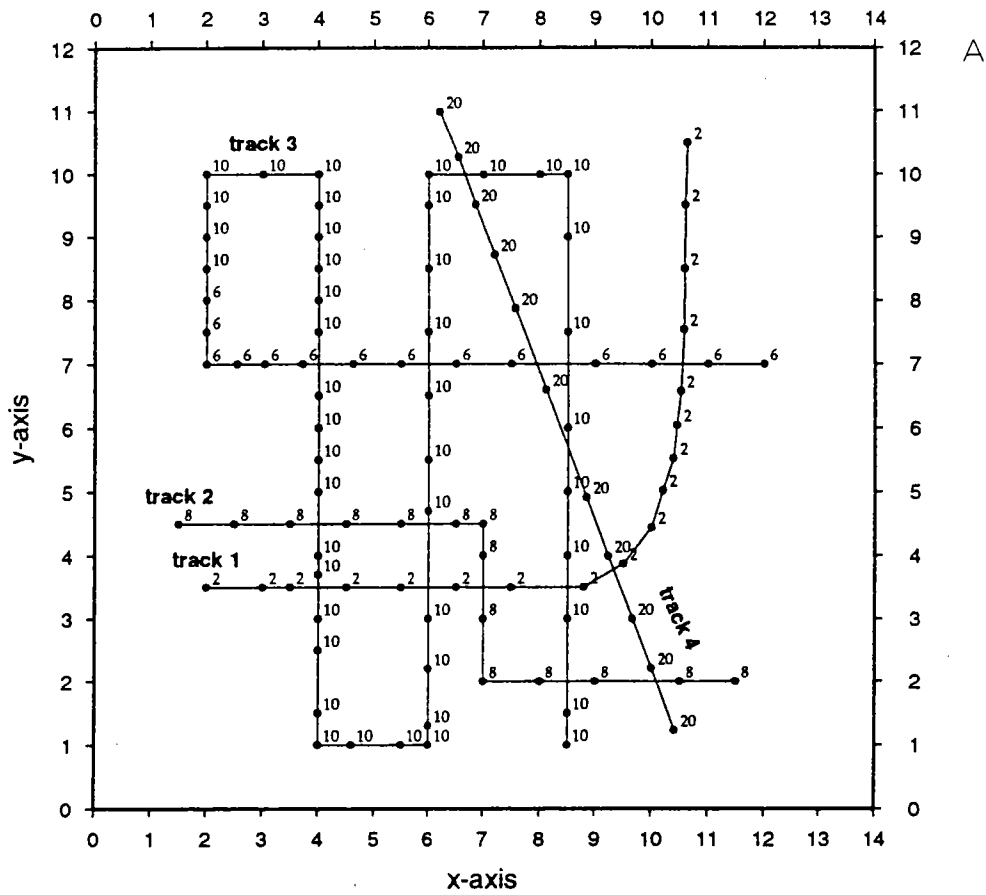
Figure 3—*Caption opposite.*
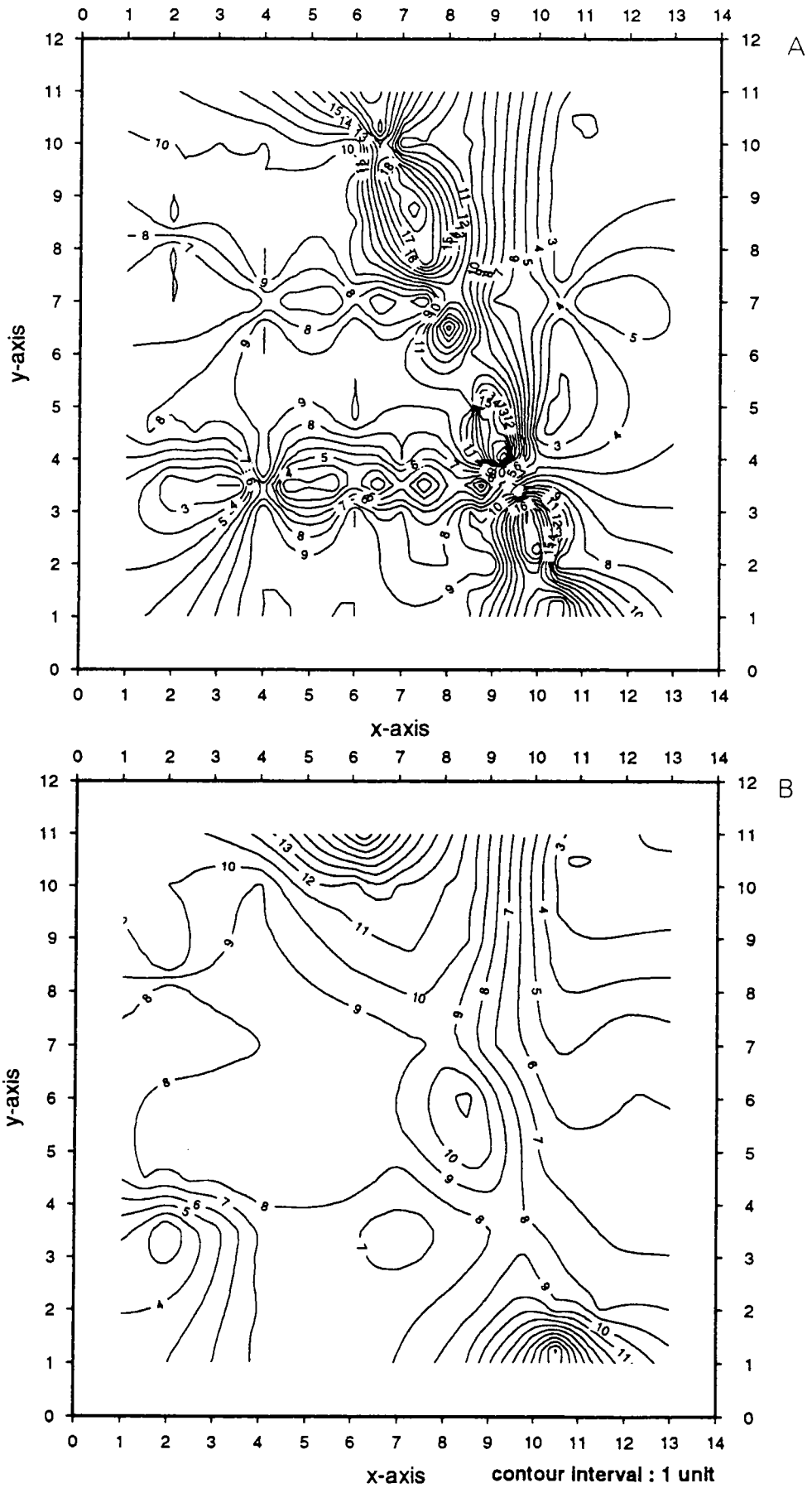
Figure 4—*Caption opposite.*

contour interval : 1 unit

Table 1. Result of XOVERH from model data shown in Figure 3A

x -axis	y -axis	XOE	mean	track	track
4.00000	3.50000	-8.0	6.0	1	3
6.00000	3.50000	-8.0	6.0	1	3
7.00000	3.50000	-6.0	5.0	1	2
8.50000	3.50000	-8.0	6.0	1	3
9.32294	3.77641	-18.0	11.0	1	4
10.53436	7.00000	-4.0	4.0	1	3
4.00000	4.50000	-2.0	9.0	2	3
6.00000	4.50000	-2.0	9.0	2	3
8.50000	2.00000	-2.0	9.0	2	3
10.08911	2.00000	-12.0	14.0	2	4
8.50000	7.00000	-4.0	8.0	3	3
7.94030	7.00000	-14.0	13.0	3	4
6.00000	7.00000	-4.0	8.0	3	3
4.00000	7.00000	-4.0	8.0	3	3
6.64505	10.00000	-10.0	15.0	3	4
8.50000	5.70467	-10.0	15.0	3	4

Table 2. Relative weight data for tracks in Figure 3A

| track	relative weight
1	0.0106
2	0.0260
3	0.0196
4	0.0058

V_j is the interpolated value for the same XOP belonging to the jth track,

V_{xop} is the adjusted value at the same XOP computed from V_i and V_j,

W_i is the relative weight of the ith track, and W_j is the relative weight of the jth track.

Hence, the corrections for V_i and V_j are, respectively, $V_i - V_{xop}$ and $V_j - V_{xop}$. Following expression (3), reasonable values are obtained for all the XOPs and associated XOEs become zero. From the corrections of every two consecutive XOPs on the same track, the measured values are adjusted by subtracting a proportional correction according to the distances to the two XOPs.

When a track crosses itself and generates only one XOP (loop case), a zero correction is assigned to the farthest measured point. Moreover, because there is only one XOP at the beginning or the end part of each cruise, only one correction could be taken into

consideration to adjust these measured data; however, we may discard these data for avoiding local extreme values.

NUMERICAL EXAMPLE

To illustrate the importance of this adjustment, a numerical model with unusual values shown in Figure 3A is employed. The result from program XOVERH is displayed in Table 1. The mathematical sign of each XOE is determined from the interpolated value of the former track minus the one of the latter track and each mean is determined by two interpolated values at the corresponding XOP. From this table, a relative weight is assigned to each track (Table 2). The adjusted values from program XCORR are indicated in Figure 3B. Pseudolineation structures have been reduced (Figs. 4A and 4B) and the contoured map becomes more reliable. Nevertheless, as the data of the beginning and the end of every track are kept, local extreme values can be noticed (Fig. 4B).

REFERENCES

Mittal, P. K., 1984, Algorithm for error adjustment of potential field data along a survey network: Geophysics, v. 49, no. 4, p. 467–469.

Sander, E. L., and Mrazek, C. P., 1982, Regression technique to remove temporal variation from geomagnetic survey data: Geophysics, v. 47, no. 10, p. 1437–1443.

Tai, C. K., 1988, Geosat crossover analysis in tropical pacific 1. Constrained sinusoidal crossover adjustment: Jour. Geophys. Res., v. 93, no. C9, p. 10621–10629.

Wessel, P., 1989, XOVER: a cross-over error detector for track data: Computers & Geosciences, v. 15, no. 3, p. 333–346.

Wessel, P., and Watts, A. B., 1988, On the accuracy of marine gravity measurements: Jour. Geophys. Res., v. 93, no. B1, p. 393–413.

Yarger, H. L., Robertson, R. R., and Wentland, R. L., 1978, Diurnal drift removal from aeromagnetic data using least squares: Geophysics, v. 46, no. 6, p. 1148–1156.

(Figure 4 opposite)

Figure 4. A—(Top) contoured map of Figure 3A where several pseudostructures occur. B—(Bottom) contoured map of Figure 3B. Pseudostructures have been reduced. Local extreme values near borders are the result of unadjusted data at beginning and end of each track (see text).

23

APPENDIX 1

Program XOVERH

```
c
c*******************************************************************
c description :                                                   *
c                                                                 *
c **1 This program allows us to find the XOPs among several different *
c      tracks as well as themselves, and compute their discrepancies  *
c      (XOEs). 'Continuous' data of each track will be considered.  *
c      Namely, the distance between two consecutive measured points *
c      less than 0.07degree(about ship speed 15 knots times 15 minutes)*
c      is considered as a 'continuous' data. If not, XOP will not be  *
c      found. It's a rough definition, but it's quite satisfactory *
c      for geophysical data analysis. However, one can modify this  *
c      condition by changing data 'vdist' to one's need.          *
c                                                                 *
c **2 Algorithm is constructed by three principal steps :         *
c                                                                 *
c         step 1 - give a block-area as a reference segment defined by *
c                  two consecutive points of a same track.        *
c         step 2 - compare and sort other data with this block_area *
c                  and kick off all the other segments which have no *
c                  possibility of intersection with the reference  *
c                  segment.                                        *
c         step 3 - transform sorted data to the new coordinate system *
c                  of reference segment for verifing possibilities of *
c                  crossover, then compute the coordinates of XOP  by *
c                  linear interpolation.                          *
c                                                                 *
c input parameters (unformatted):                                 *
c                                                                 *
c  rlon : longitude of measured data (east: positive, west: negative) *
c  rlat : latitude of measured data (north: positive, south: negative)*
c  val  : measured value                                          *
c  track : identifier of track ( an integer to represent a track ) *
c                                                                 *
c output parameters :                                             *
c                                                                 *
c    xlon : longitude of calaulated crossover point               *
c    xlat : latitude of calculated crossover point                *
c    vx : difference value(XOE) at one XOP                        *
c    vmean : mean value at the same XOP                           *
c    track : identifiers of two intersecting segments             *
c                                                                 *
c NOTE 1 : this program has been successfully tested by using SUN *
c          workstation (UNIX system) and Micro-VAX II (VAX system) *
c NOTE 2 : total measured points is limited in 200000 points. one can *
c          modify the parameter "numb" according to one's computer *
c          capacity and one's need                                *
c NOTE 3 : data area near the longitude of E180 and W180 should use *
c          the definition of 0 - 360 degree as longitude coordinate *
c          for avoiding discontinuity                             *
c                                                                 *
c*******************************************************************
c
          character*40 file1,file2
          parameter ( numb = 200000)
          real*8 rlat(numb),rlon(numb),val(numb)
          real*8 suplat,inflat,suplon,inflon
          integer track(numb)
          real*8 xlon,xlat,f(4),vx1,vx2,vx,vmean,vdist
          data vdist/0.07/
c
c *** open files as input and output
c
          write(*,*)' input filename : '
          read(*,'(a)') file1
          write(*,*)' output filename : '
          read(*,'(a)') file2
          open(10,file=file1,status='old')
          open(20,file=file2,status='new')
```

```
c
c *** input data to be processed from file1
c
        do np=1,numb
          read(10,*,end=100) rlon(np),rlat(np),val(np),track(np)
        end do
100     vdist=vdist*vdist
        do k=1,np-4
          if(track(k).ne.track(k+1)) goto 220
          if(((rlon(k+1)-rlon(k))**2.+(rlat(k+1)-rlat(k))**2.).gt.
     &     vdist) goto 220
c
c *** define one block-area from any two consecutive points (as A
c     and B), considered as a reference segment, in a same track.
c
          suplat=dmax1(rlat(k),rlat(k+1))
          inflat=dmin1(rlat(k),rlat(k+1))
          suplon=dmax1(rlon(k),rlon(k+1))
          inflon=dmin1(rlon(k),rlon(k+1))
          do m=k+2,np-2
            if(track(m).ne.track(m+1)) goto 200
            if(((rlon(m+1)-rlon(m))**2.+(rlat(m+1)-rlat(m))**2.).gt.
     &        vdist) goto 200
c
c *** kick off any other segment (as C and D) which is completely
c     outside the block-area.
C
            if(rlat(m).gt.suplat.and.rlat(m+1).gt.suplat) goto 200
            if(rlat(m).lt.inflat.and.rlat(m+1).lt.inflat) goto 200
            if(rlon(m).gt.suplon.and.rlon(m+1).gt.suplon) goto 200
            if(rlon(m).lt.inflon.and.rlon(m+1).lt.inflon) goto 200
c
c *** find XOP by trans subroutine
c
        call trans(rlon(k),rlat(k),rlon(k+1),rlat(k+1),rlon(m),rlat(m),
     &      rlon(m+1),rlat(m+1),xlon,xlat,f,ic)
c
c *** calculate the XOE of the segments AB and CD
c     by linear interpolation.
c
            if(ic.eq.1) then
              vx1=f(1)*val(k+1)+f(2)*val(k)
              vx2=f(3)*val(m+1)+f(4)*(val(m))
              vx=(vx1-vx2)
              vmean=(vx1+vx2)/2
c
c *** write output data to a device (logical unit 20)
c
              write(20,198)xlon,xlat,vx,vmean,track(k),track(m)
198           format(1x,f9.5,2x,f8.5,1x,f9.1,1x,f9.1,3x,i5,1x,i5)
            end if
200       end do
220     end do
        close(10)
        close(20)
        stop
        end
```

APPENDIX 2

Program XCORR

```
c
c****************************************************************************
c                                                                          *
c description:                                                             *
c                                                                          *
c   XCORR will compute the corrections for every XOP and proportionally*
c   adjust the original data by considering the corrections.              *
c                                                                          *
c input parameters (unformatted):                                         *
c                                                                          *
c   A - data file                                                         *
c                                                                          *
c     rlon   (first column)  : longitude of measured data                *
c     rlat   (second column) : latitude of measured data                 *
c     val    (third column)  : measured value                            *
c     track  (fourth column) : identifier of track                       *
c                                ( a positive integer to represent a track ) *
c   B - weight file (weight.dat)                                         *
c                                                                          *
c     noct (first column)  : identifier of track                         *
c     wt   (second column) : relative weight for track noct              *
c                                                                          *
c output parameters :                                                     *
c                                                                          *
c     xlon : longitude                                                    *
c     xlat : latitude                                                     *
c     val : corrected data                                                *
c     track : identifiers of track                                        *
c                                                                          *
c other parameters :                                                      *
c                                                                          *
c     ns : serial number of XOP                                           *
c     dist : distance to XOP                                              *
c     cc : correction at XOP                                              *
c     ves : adjusted value at XOP                                         *
c     x, y : coordinates of XOP                                           *
c                                                                          *
c NOTE : (see XOVERH)                                                     *
c                                                                          *
c****************************************************************************
        character*40 file1,file2,keep*1
        parameter ( numb = 200000)
        real*8 rlat(numb),rlon(numb),val(numb)
        real*8 suplat,inflat,suplon,inflon,dist1,dist2,dist
        integer track(numb),ns(0:numb),noc(0:numb)
        real*8 xlon,xlat,f(4),vx1,vx2,ves,w(500),wt,cv,vdist
        real*8 dl(0:numb),x(0:numb),y(0:numb),cc(0:numb),rx,ry
        data vdist/0.07/
c
c *** open files as input and output
c
        write(*,*)' input filename : '
        read(*,'(a)') file1
        write(*,*)' output filename : '
        read(*,'(a)') file2
        print *,'keep adjusted end values of each track or not ? (y/n)'
        read(*,'(a)') keep
        open(10,file=file1,status='old')
        open(20,file=file2,status='new')
        open(22,file='weight.dat',status='old')
c
c *** input file data to be processed
c
        do np=1,numb
          read(10,*,end=100) rlon(np),rlat(np),val(np),track(np)
        end do
        write(*,8)numb
8       format(1x,' points of data are more than ',i17,'!!attention!!')
100     close(10)
c
c *** input weight data of every track
c
```

```
            do i=1,numb
               read(22,*,end=101) noct,wt
                  w(noct)=wt
            end do
101         close(22)
            vdist=vdist*vdist
            ni=0
            do k=1,np-4
               if(track(k).ne.track(k+1)) goto 220
               if(((rlon(k+1)-rlon(k))**2.+(rlat(k+1)-rlat(k))**2.).gt.
     &         vdist) goto 220
c
c *** define a block-area from any two consecutive points (as A
c      and B), which is considered as a reference segment.
c
            suplat=dmax1(rlat(k),rlat(k+1))
            inflat=dmin1(rlat(k),rlat(k+1))
            suplon=dmax1(rlon(k),rlon(k+1))
            inflon=dmin1(rlon(k),rlon(k+1))
            do m=k+2,np-2
               if(track(m).ne.track(m+1)) goto 200
               if(((rlon(m+1)-rlon(m))**2.+(rlat(m+1)-rlat(m))**2.).gt.
     &         vdist) goto 200
c
c *** kick off any other segment (as D and E) which is completely
c      outside the block-area.
c
               if(rlat(m).gt.suplat.and.rlat(m+1).gt.suplat) goto 200
               if(rlat(m).lt.inflat.and.rlat(m+1).lt.inflat) goto 200
               if(rlon(m).gt.suplon.and.rlon(m+1).gt.suplon) goto 200
               if(rlon(m).lt.inflon.and.rlon(m+1).lt.inflon) goto 200
c
c *** find the XOP by subroutine trans
c
            call trans(rlon(k),rlat(k),rlon(k+1),rlat(k+1),rlon(m),rlat(m),
     &         rlon(m+1),rlat(m+1),xlon,xlat,f,ic)
c
c *** calculate the XOE of the segments AB and CD by linear
c      interpolation and save the correction data in array cc
c
               if(ic.eq.1) then
                  vx1=f(1)*val(k+1)+f(2)*val(k)
                  vx2=f(3)*val(m+1)+f(4)*(val(m))
                  wt=w(track(k))+w(track(m))
                  ves=(w(track(k))*vx1+w(track(m))*vx2)/wt
                  ns(ni+1)=k
                  ns(ni+2)=m
                  dl(ni+1)=dist(rlon(k),rlat(k),xlon,xlat)
                  dl(ni+2)=dist(rlon(m),rlat(m),xlon,xlat)
                  x(ni+1)=xlon
                  x(ni+2)=xlon
                  y(ni+1)=xlat
                  y(ni+2)=xlat
                  noc(ni+1)=track(k)
                  noc(ni+2)=track(m)
                  cc(ni+1)=vx1-ves
                  cc(ni+2)=vx2-ves
                  ni=ni+2
               end if
200         end do
220      end do
         if(ni.eq.0) goto 999
c
c *** bubble effect : sort XOPs according to their serial number
c
            do 300 i=1,ni-1
            do 400 j=i+1,ni
                  if (ns(i).lt.ns(j)) goto 400
                  if (ns(i).eq.ns(j).and.dl(i).le.dl(j)) goto 400
                  it1=ns(i)
                  t2=x(i)
                  t3=y(i)
                  t4=cc(i)
```

```
                  it5=noc(i)
                  t6=dl(i)
                  ns(i)=ns(j)
                  x(i)=x(j)
                  y(i)=y(j)
                  cc(i)=cc(j)
                  noc(i)=noc(j)
                  dl(i)=dl(j)
                  ns(j)=it1
                  x(j)=t2
                  y(j)=t3
                  cc(j)=t4
                  noc(j)=it5
                  dl(j)=t6
400       continue
300       continue
c
c **** adjust the original data by considering the corrections
c
          x(0)=rlon(1)
          y(0)=rlat(1)
          x(ni+1)=rlon(np-1)
          y(ni+1)=rlat(np-1)
          ns(0)=1
          ns(ni+1)=np-1
          cc(0)=0.
          cc(ni+1)=0.
          do m=ns(0),ns(1)
          dist1=dist(rlon(m),rlat(m),x(0),y(0))
          dist2=dist(rlon(m),rlat(m),x(1),y(1))
          cv=(dist1*cc(1)+dist2*cc(0))/(dist1+dist2)
          if (keep.eq.'y') then
c------ keep values from one correction ------
          val(m)=val(m)-cv
          else
c------ or delete them ----------------------
          val(m)=9999999.
          endif
c-------------------------------------------------
          end do
          do m=ns(ni)+1,ns(ni+1)
          dist1=dist(rlon(m),rlat(m),x(ni),y(ni))
          dist2=dist(rlon(m),rlat(m),x(ni+1),y(ni+1))
          cv=(dist1*cc(ni+1)+dist2*cc(ni))/(dist1+dist2)
          if (keep.eq.'y') then
c------ keep values from one correction ------
          val(m)=val(m)-cv
          else
c------ or delete them ----------------------
          val(m)=9999999.
          endif
c-------------------------------------------------
          end do
          do 700 k=1,ni-1
                  if (ns(k).eq.ns(k+1).and.dl(k).eq.dl(k+1)) goto 700
                  if (ns(k).eq.ns(k+1)) goto 688
                  if (noc(k).eq.noc(k+1)) then
c
c *** loop case : only one XOP at a same track
c
                  if (x(k).eq.x(k+1).and.y(k).eq.y(k+1)) then
                     if((ns(k+1)-ns(k)).le.3) goto 688
                     dist2=0.
                     max=0
                     do j=ns(k)+1,ns(k+1)
                     dist1=dist(rlon(j),rlat(j),x(k),y(k))
                     if(dist1.gt.dist2) then
                             dist2=dist1
                             rx=rlon(j)
                             ry=rlat(j)
                             max=j
                     endif
                     end do
                     do m=ns(k)+1,max-1
```

28

```
                        dist1=dist(rlon(m),rlat(m),rx,ry)
                        cv=cc(k)*dist1/dist2
c                       ----------------
                        val(m)=val(m)-cv
c                       ----------------
                  end do
                  do m=max+1,ns(k+1)
                        dist1=dist(rlon(m),rlat(m),rx,ry)
                        cv=cc(k+1)*dist1/dist2
c                       ----------------
                        val(m)=val(m)-cv
c                       ----------------
                  end do
                  goto 688
            endif
c
c *** normal case : adjust measured values with two corrections
c
                  do m = ns(k)+1,ns(k+1)
                  dist1=dist(rlon(m),rlat(m),x(k),y(k))
                  dist2=dist(rlon(m),rlat(m),x(k+1),y(k+1))
                  cv=(dist1*cc(k+1)+dist2*cc(k))/(dist1+dist2)
c                 ----------------
                  val(m)=val(m)-cv
c                 ----------------
                  end do
            else
c
c *** case of separation of tracks : adjust measured values in beginning
c                                    and end of tracks (one correction)
c
                  n3=0
                  do j=ns(k),numb
                        if (track(j).ne.track(j+1)) goto 750
                        n3=n3+1
                  end do
750               if (n3.le.1) goto 760
                  dist1=dist(rlon(ns(k)+n3),rlat(ns(k)+n3),x(k),y(k))
                  do m = ns(k)+1,ns(k)+n3
                        dist2=dist(rlon(m),rlat(m),x(k),y(k))
                        cv=cc(k)*(dist1-dist2)/dist1
                        if (keep.eq.'y') then
c----------------------------- keep values from one correction ------
                        val(m)=val(m)-cv
                        else
c----------------------------- or delete them -----------------------
                        val(m)=9999999.
                        endif
c-------------------------------------------------------------------
                  end do
760               n4=ns(k+1)-ns(k)-n3
                  if ( n4.le.1) goto 688
                  dist1=dist(rlon(ns(k+1)-n4+1),rlat(ns(k+1)-n4+1),
     &            x(k+1),y(k+1))
                  do m = ns(k+1)-n4+1,ns(k+1)
                        dist2=dist(rlon(m),rlat(m),x(k+1),y(k+1))
                        cv=cc(k+1)*(dist1-dist2)/dist1
                        if (keep.eq.'y') then
c----------------------------- keep values from one correction ------
                        val(m)=val(m)-cv
                        else
c----------------------------- or delete them -----------------------
                        val(m)=9999999.
                        endif
c-------------------------------------------------------------------
                  end do
            endif
688         if(dl(k).eq.0.) then
c           -------------------------
            val(ns(k))=val(ns(k))-cc(k)
c           -------------------------
            endif
700   continue
c
c *** save the adjusted data in a file (unit20)
```

```
c
            do i = 1,np-1
                   if(val(i).eq.9999999.) goto 890
                   write(20,880) rlon(i),rlat(i),val(i),track(i)
  880              format(1x,f9.5,1x,f8.5,1x,f10.1,2x,i5)
  890       end do
  999       close(20)
            stop
            end


            real*8 function dist(x1,y1,x2,y2)
            real*8 x1,y1,x2,y2
            dist=dsqrt((x1-x2)**2+(y1-y2)**2)
            return
            end


            subroutine trans(x1,y1,x2,y2,x3,y3,x4,y4,xlon,xlat,f,ic)
c
c****************************************************************
c                                                              *
c ** subroutine is to transform the coordinates in order to verify *
c    the existence of XOP and compute its coordinates          *
c ** input parameters :                                        *
c          x1,y1,x2,y2 : coordinates of reference segment AB   *
c          x3,y3,x4,y4 : coordinates of the other segment CD   *
c    return parameters :                                       *
c          xlon : longitude of XOP                             *
c          xlat : latitude of XOP                              *
c          f    : distance fraction to each segment            *
c          ic   : report of intersection ( if ic=1, there is a XOP; *
c                 if ic = 0, then no )                         *
c                                                              *
c****************************************************************
            real*8 x1,y1,x2,y2,x3,y3,x4,y4,xlon,xlat,dist,cosv,sinv,f(4)
            real*8 x2tr,y2tr,x3tr,y3tr,x4tr,y4tr,ox
            if((x1.eq.x2.and.y1.eq.y2).or.(x3.eq.x4.and.y3.eq.y4))goto 15
            dist=dsqrt( (x2-x1)*(x2-x1) + (y2-y1)*(y2-y1) )
            cosv=(x2-x1)/dist
            sinv=(y2-y1)/dist
            x2tr=(x2-x1)*cosv+(y2-y1)*sinv
            y2tr=-1.*(x2-x1)*sinv+(y2-y1)*cosv
            x3tr=(x3-x1)*cosv+(y3-y1)*sinv
            y3tr=-1.*(x3-x1)*sinv+(y3-y1)*cosv
            x4tr=(x4-x1)*cosv+(y4-y1)*sinv
            y4tr=-1.*(x4-x1)*sinv+(y4-y1)*cosv
c
c *** after transformation, verify the position of point C and D,
c     if they locate in upper and lower quadrant respectively. there
c     could be a XOP. check it again later.
c
            if(y3tr.ge.0..and.y4tr.le.0.)goto 20
            if(y3tr.le.0..and.y4tr.ge.0.)goto 20
  15        ic=0
            return
c
c *** general case of crossover : find the intersection point 'ox'
c     of two segments AB and CD, while 'oy'=0.
c
  20        if ((y4tr-y3tr).ne.0.) then
               ox=x3tr-y3tr*(x4tr-x3tr)/(y4tr-y3tr)
               f(3)=dabs(y3tr)/(dabs(y3tr) + dabs(y4tr))
c
c *** special case : two parallel segments in one line
c
            else
               ox=(x2tr+x3tr+x4tr)/4.
               if(ox.lt.dmin1(x3tr,x4tr).or.ox.gt.dmax1(x3tr,x4tr))then
                      ic=0
                      return
               endif
               f(3)=dsqrt((x3tr-ox)**2.)/(dsqrt((x4tr-ox)**2.)+dsqrt((x3tr-ox)
      &        **2.))
            endif
c
```

```
c *** return the coordinates of XOP in original reference and
c      distance fractions to the point A, B, C, and D.
c      (if XOP is in the interior of segment AB)
c

       if(ox.lt.0..or.ox.gt.x2tr) then
          ic=0
          return
       endif
       ic=1
       f(1)=ox/x2tr
       f(2)=1.-f(1)
       f(4)=1.-f(3)
       xlon=ox*cosv+x1
       xlat=ox*sinv+y1
       return
       end
```

31

The effect of introducing continuity conditions in the constrained sinusoidal crossover adjustement method to reduce satellite orbit errors

Certaines données mesurées comportent une partie due aux variations temporelles (par exemple, les variations de marées, magnétiques ou encore les orbites satellitaires). Ces variations peuvent être modélisées en donnant à chaque cycle périodique une formulation mathématique. Cette méthode permet, donc, d'éliminer les variations temporelles. Afin de compiler les données magnétiques au large de Taiwan, la variation diurne des données de certaines campagnes a donc été corrigée avant d'appliquer le programme XCORR.

The effect of introducing continuity conditions in the constrained sinusoidal crossover adjustment method to reduce satellite orbit errors

Shu-Kun Hsu and Louis Géli

Ifremer, Departement des Géosciences, Centre de Brest, France

Guénal Davalan

Laboratoire d'Informatique, Université de Bretagne Occidentale, France

Abstract. The constrained sinusoidal crossover adjustment method [*Tai*, 1988] is one of the most efficient and frequently used method to remove the orbit error in satellite altimetry. In this method, the orbit error for each different satellite revolution is represented by a different sine wave, with wavelength equal to the circumference of the earth. One drawback of this method is that the orbit error function is theoretically not forced to be continuous between every two successive revolutions. In this short note, we study the effect of introducing rigorous continuity conditions between every two successive revolutions, and constraints to avoid an offset from a probable variation datum level. To achieve the continuity, the orbit error for each revolution is modelled as a temporal function composed of a sinusoidal function and a second-order polynomial. Examples using ERS-1 data show that for local studies, when one demands the geoid height in the neighbourhood of the junction between every two successive cycles, it is recommended to fulfill the continuity conditions. Otherwise, the simple constrained sinusoidal crossover adjustment method must be preferred.

Introduction

If we except the case of Topex/Poseidon, the primary error on altimetric measurements of sea surface topography is the orbit error, caused by uncertainty of the geoid and imperfect knowledge of the spacecraft position due to modelling errors in the estimation of satellite altitude from ground-based tracking data [*Balmino*, 1993]. Commonly used techniques for reducing orbit error consist in minimizing the crossover differences of altimetric profiles [e.g., *Rapp*, 1983] or the repeat differences of collinear tracks [*Cheney et al.*, 1983]. In the least square scheme, the orbit error over one given segment (part of revolution) is described by linear, quadratic or cubic polynomials or sinusoidal functions, depending on the length of the segments being processed (regional or global crossover adjustments). *Marsh et al.* [1982], for instance, assigned a bias and tilt to each undisrupted satellite track (e.g., two segments separated by an island are given different bias and tilt coefficients). *Tai* [1988] developed the constrained sinusoidal crossover adjustment method, writing the orbit error in a simple sinusoidal form over

each revolution. Because this method is found to have many excellent qualities, it is frequently used. However, this method presents a theoretical disadvantage that the orbit error function is not continuous at the junction between every two successive revolutions. This note is a brief study on the effect of theoretically forcing the continuity of the orbit error function.

Method

As we will see hereafter, the simple constrained sinusoidal crossover adjustment method does not allow the continuity of the orbit error function between every two successive revolutions, unless the sine function is the same for all the different revolutions. To achieve the continuity, we adopt a combination of three existing techniques which have been applied to a great variety of geophysical cases: the constrained sinusoidal crossover adjustment method [*Tai*, 1988], the polynomial adjustment method [e.g., *Marsh et al.*, 1982] and the trigonometric adjustment method of *Sander and Mrazek* [1982]. The temporal function which represents the orbit error on the mth satellite revolution can be expressed as :

$$f_m(t) = \sum_{n=1}^{N} A_{m,n} \sin(\frac{2\pi nt}{T_0}) + \sum_{n=1}^{N} B_{m,n} \cos(\frac{2\pi nt}{T_0})$$
$$+ a_m t^2 + b_m t + c_m \qquad (1)$$

with the continuity condition $f_m(T_0) = f_{m+1}(0)$ and the continuity condition of the first derivative at the junction of every two revolutions. Where $0 \le t \le T_0$; $A_{m,n}$, $B_{m,n}$, a_m, b_m, c_m are unknown coefficients of mth revolution; T_0 is the fundamental period of a revolution; N is an integer representing the maximum harmonic order for each revolution.

The complete set of the unknowns, Ncoef, required to determine the temporal variation function is Ncoef = M (2 N +3), where M is the number of revolutions.

For N=1, the above equation is basically reduced to the one proposed by *Tai* [1988], except that, in addition to the sinusoidal function, we have introduced a two degree polynomial function. In the absence of the polynomial terms, discontinuities in the temporal variation function and in its first derivative appear at the junction of two consecutive revolutions m and m+1 (occurring in the *Tai*'s method), unless the conditions $B_{m,1} = B_{m+1,1}$ and $A_{m,1} = A_{m+1,1}$ are satisfied. Unfortunately in this case, the temporal function turns into a pure monofrequency trigonometric function. Important advantages of taking into account the continuity conditions thus appear more clearly in the case of high inclination

of the satellite orbit. The higher the inclination, the greater the importance of the continuity conditions. Were, for instance, the orbit perfectly polar (e.g., close to 90° inclination), the model function obtained with Tai's method would - in absence of sea ice - be practically continuous due to the existence of crossovers near to the pole. Again, this would yield a pure monofrequency sinusoidal function, with the same coefficients for all the different cycles.

The addition of a flexible polynomial expansion allows us to avoid a fixed value at the junction of every two consecutive revolutions, and the continuity conditions become significant. The continuity conditions between two consecutive revolutions m and m+1, for $N \geq 1$ can therefore be written in the following way :

$$\sum_{n=1}^{N} B_{m,n} + a_m T_0^2 + b_m T_0 + c_m = \sum_{n=1}^{N} B_{m+1,n} + c_{m+1} \quad (2)$$

$$\sum_{n=1}^{N} \frac{2\pi n}{T_0} A_{m,n} + 2a_m T_0 + b_m = \sum_{n=1}^{N} \frac{2\pi n}{T_0} A_{m+1,n} + b_{m+1} \quad (3)$$

If there is one crossover occurring between the kth revolution (time t_i) and the mth revolution (time t_j), the crossover error can be written as:

$$d_{k,m}(t_i, t_j) = f_k(t_i) - f_m(t_j)$$

$$= \sum_{n=1}^{N} A_{k,n} \sin(\frac{2\pi n t_i}{T_0}) + \sum_{n=1}^{N} B_{k,n} \cos(\frac{2\pi n t_i}{T_0}) + a_k t_i^2 + b_k t_i + c_k$$

$$- \sum_{n=1}^{N} A_{m,n} \sin(\frac{2\pi n t_j}{T_0}) - \sum_{n=1}^{N} B_{m,n} \cos(\frac{2\pi n t_j}{T_0}) - a_m t_j^2 - b_m t_j - c_m$$

$$(4)$$

To avoid the variation curve far from a probable variation datum level (unique solution), we need to constrain the integral of the polynomial term for each revolution near zero. This constraint for the mth revolution is

$$2a_m T_0^3 + 3b_m T_0^2 + 6c_m T_0 = 0 \quad (5)$$

To summarize, one can say that equation (5) is simply a non-bias constraint. The sinusoidal terms of the orbit error function are necessarily unbiased, since they never depart from a zero average. However, this is not the case for the polynomial components of the function. That is why equation (5) only involve the latter coefficients.

Now, the set of equations to determine the unknown coefficients is made up from all the crossover errors, the continuity conditions between every two successive revolutions and the non-bias constraints; i.e., the total number of equations Neq is equal to Nxop + 3 M -2, where Nxop is the number of crossovers and M the number of revolutions. For convenience, it can be expressed in a matrix form

$$Gx = d \quad (6)$$

where boldfaces denote matrix; G is a Neq x Ncoef matrix which consists of coefficients of sine, cosine, polynomial terms, continuity conditions as well as constraints; x is a vector, consisting of the Ncoef unknown coefficients (or parameters) to be determined and d the errors. Hence, the least square error E can be simply described as

$$E = [d - Gx]^T W [d - Gx] \quad (7)$$

where T denotes the transpose of a matrix and the matrix W defines the relative contribution (weight) of each individual equation. From a numerical point of view, the continuity conditions (2) and (3) are given a very large but finite weight and the constraint (5) a slight weight.

One computes the derivatives of error E with respect to each parameter, then the unknown coefficients can be estimated in the sense of least squares [Menke, 1984, chapter 4] and the normal equations are :

$$x^{est} = [G^T W G]^{-1} G^T W d \quad (8)$$

where -1 denotes the inverse matrix.

Clearly, equation (8) is not always suitable for any type of geophysical measurements, in particular, when there is not enough information to estimate the model parameters (underdetermination). In general, a priori information is necessary to be added in the simultaneous equations. A popular way is to minimize the model parameters. In that case, equation (6) becomes

$$x^{est} = [G^T W G + \varepsilon^2 I]^{-1} G^T W d \quad (9)$$

where I denotes identity matrix, and ε^2 is a balance factor of underdetermined and overdetermined parts. It is noted that a large balance factor ε^2 means that the underdetermined part overwhelms the result, and one way to find ε^2 is to use the try and error method [Menke, 1984]. Also to be noted is that $G^T G$ and ε^2 are dimensionless, provided a_m is expressed in s^{-2}, b_m in s^{-1}, and c_m is dimensionless.

Concerning the choice of N in equation (1), it is difficult to give an analytic answer because it depends on the number of crossovers and an a priori understanding about the probable temporal variation. Generally speaking, one must note that: 1) to optimally eliminate the temporal variation is not the same question than to minimize the crossover error to zero; 2) using a lower value of N than expected corresponds to a waste of information. On the contrary, a too high value of N might give rise to high-frequency errors. For instance, for correcting marine magnetic data from geomagnetic diurnal variation effects, comparisons with corrections made with data from geomagnetic observatories indicate that diurnal variations can be well corrected using N =2 to 5, and ε^2 = 1 to 2 (the performance of the method, however, depends on the number of crossover points). For satellite altimetry, since the orbit error of satellite altimetry has a well known predominant spectral peak corresponding to the revolution period, its basic feature can be modelled as a slowly varying sinusoidal wave around the Earth. N=1 is essentially sufficient and ε^2 is estimated about 0.01 [Tai, 1988; Menke, 1984]. These are the values used hereafter.

Application to ERS-1 Data

In the present example, we use the ERS-1 data collected during the ninth 35-day cycle, from January 20 to February 24, 1993. This cycle includes 501 revolutions, involving a total number of 45935 crossovers. Corrections for tropospheric and ionospheric errors were made using the corrections available in the Ocean Products (OPR) provided by the European Space Agency. The data we used has been edited in a way detailed in Blanc and Géli [1994]. The inclination of the satellite orbit is 98.531. For the sake of the demonstration, the latitude of the junction between every two successive revolutions was arbitrarily
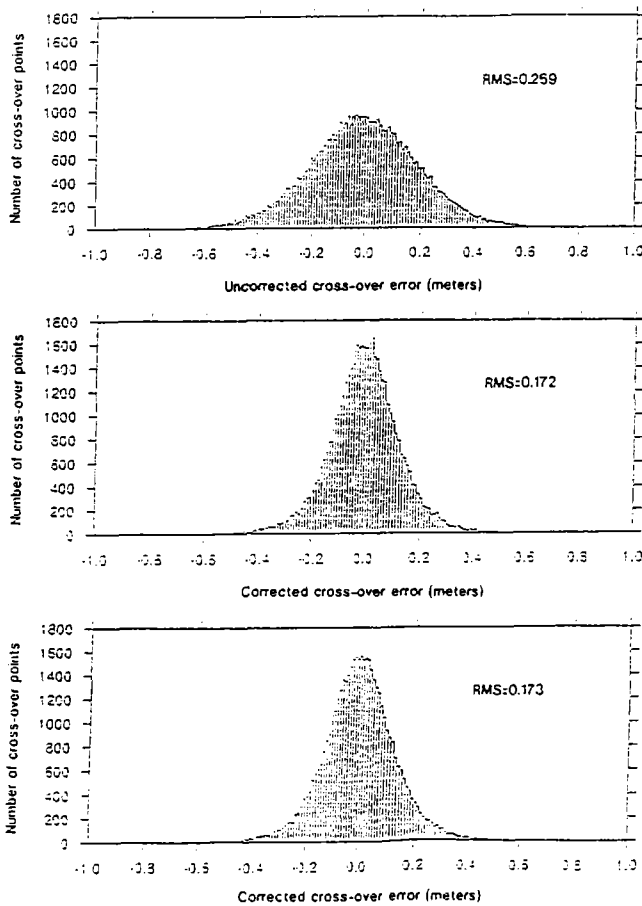
Figure 1. Histograms of RMS cross-over errors before (up) and after correction of the orbit error, applied with *Tai*'s method (middle) and with our method (down). The data we use (from the 9th ERS-1 35-day cycle, from January 20 to February 24 1993) have been provided by CLS/Argos in april 1994 by CLS/Argos. A finer orbit was derived since then using Topex/Poseidon, and the orbit error calculations have been updated.

Figure 2. Orbit error model obtained with *Tai*'s method (up) and with our method (down), between hours 200 and 250 hours Note discontinuities at the junction of every two cycles when the continuity conditions are not explicitely taken into account. Also note the difference of amplitude level between the two functions.

chosen as the highest latitude reached by the satellite, that is: 81.469°N. The search for crossovers and the adjustment were both performed at the Ifremer computing center on a Convex 3840 having 4 parallel processors and 2 Gigabytes of central memory. Observed computing times using the VECLIB library implemented on the Convex machine are of about five minutes for the adjustment using *Tai*'s method, and of about twelve minutes when the continuity conditions are considered.

The original RMS (Figure 1) on all the crossover errors over the complete set of crossover points is 0.269 m before crossover adjustment (it is important to note that the dataset we use here were provided by CLS/Argos in april 1994; since then, results have been considerably improved, as new and more precise orbits were calculated; in the special ERS-1/Topex session of the AGU 1994 fall meeting, results have been presented with orbit errors of less than 10 cm before adjustment!). The RMS obtained on this dataset after a global adjustment using *Tai*'s method is 0.172 m (Figure 1). As expected, the corresponding orbit error temporal function exhibits large discontinuities at the end of each revolution (Figure 2). The RMS obtained after a global adjustment using our method (0.173 m) is not significantly different from the one obtained with *Tai*' s method, although new constraints have been added to the system of equations (6). This
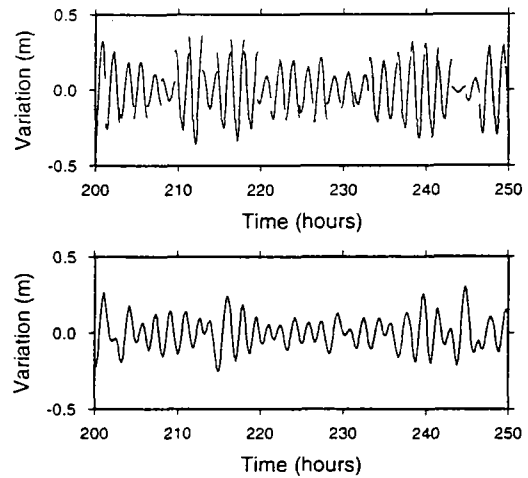
can be simply explained by the fact that the number of crossovers is by two orders of magnitude greater than the number of revolutions. Consequently, adding continuity conditions does not change significantly the proportions between the rows and the columns of the system. The amplitude level of the function computed with our method is smaller than the one computed with *Tai*'s method (Figure 2). The amount of correction to apply to the altimetric measurements is smaller when the orbit error model function is constrained with continuity conditions. In addition, it is worthy remarking that the continuity conditions allow us to estimate the Fourier spectrum of the orbit error function (Figure 3), which is impossible when only the *Tai*'s method is used. The power spectrum clearly indicate that other components than the fundamental period are present in the signal.

The geoid data was gridded in two antipodic regions : one in the northern Norwegian-Greenland Sea, close to the latitude of junction between two successive revolutions (Figure 4), and one in Pacific-antarctic Ridge area of the southern Pacific (Figure 5). In the first case, our method yield better results than the *Tai*'s method, with less apparent spurious effects between two adjacent traces, but the differences are not very significant. In the second case, far away from the latitude of junction between two successive revolutions, the *Tai*'s method provide better results. This can be easily explained because of the fact that when one
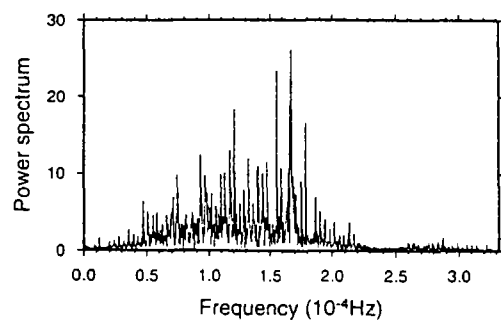

Figure 3. Power spectrum of the temporal orbit error function obtained with our method for the complete ERS-1 35-day cycle from January 20 to February 24 1993.
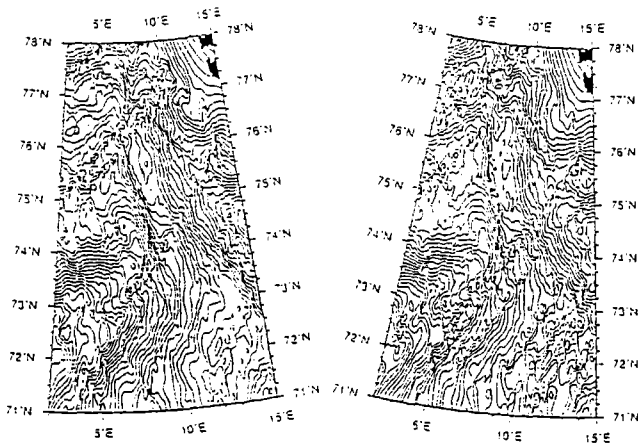
Figure 4. Gridded mean sea surface (meters) in the northern Norwegian-Greenland Sea. Isocontours are every 0.25 m. Gridding was performed using the curvature splines in tension method [*Smith and Wessel*, 1990] with a mesh size of 5' x 5'. (Left) Data adjustment performed with our method, with continuity conditions. (Right) Data adjustment performed with *Tai*'s method.
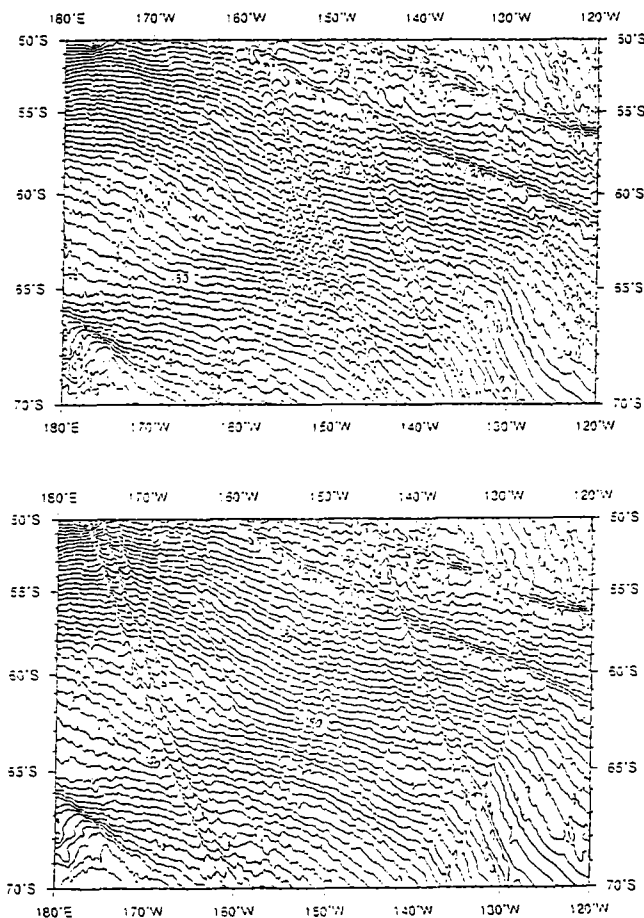

Figure 5. Gridded mean sea surface (meters) in the Pacific-Antarctic Ridge area of the southern Pacific. Isocontours are every 1 m. Gridding was performed using the curvature splines in tension method [*Smith and Wessel*, 1990] with a mesh size of 5' x 5'. (Up) Data adjustment performed with our method, with continuity conditions. (Down) Data adjustment performed with *Tai*'s method. The fact that the tracks oriented NW-SE appear to be less corrected is not systematic at all. In some other geographical areas (not shown here), this may be different.

takes into account additional equations (like the continuity conditions), the crossover adjustment is necessarily achieved with less accuracy. If, in addition, one takes into account the gain of computing time and the simplicity of the programming process, the *Tai*'s method must be preferred.

Conclusion

With the launching of the European Space Agency ERS-1 and the US/French Topex/Poseidon missions in, respectively, july 1991 and august 1992, global observations of the oceans with satellite altimetry entered a new era. Using Topex/Poseidon data to enhance ERS-1 data can yield RMS errors of 10 cm on ERS-1/ERS-1 crossovers [*Le Traon et al*, 1994]. This type of improvement is, however, feasible only when ERS-1 and Topex/Poseidon are flying simultaneously. One may thus expect that synthetic methods based on the minimization the crossover differences of altimetric profiles will still be necessary. The conclusion of this study is that special attention must be paid to the results when the considered area is very close to the latitude of junction of every two successive satellite revolutions. In that case, it is theoretically more reasonable to write the continuity conditions, but in practice, the difference is not very significant. Elsewhere, and more generally, for global studies, the simple *Tai*'s method must be preferred. However, it is recommended to start each satellite revolution over land (over Antarctica, for instance).

References

Balmino G., Orbit choice and the theory of radial orbit error for altimetry, in : Rummel and Sanso, Editors, Satellite altimetry in geodesy and altimetry, Lecture notes in Earth Sciences. Springer Verlag, 1993.

Blanc F., and Géli L., Mean sea surface height, geoid and free-air gravity anomalies in the Siberian Epicontinental seas derived from ERS-1 radar altimetry : preliminary results. PEGASE Project Progress Report 2. Internal Report, CLS, july 1994, 1994.

Cheney, R. E., Marsh, J. G., and Beckly, B. D. Global mesoscale variability from collinear tracks of Seasat altimeter data, *J. Geophys. Res.*, 88, 4343-4354., 1983.

Le Traon, P.-Y., Gaspar P., Bouyssel F., Makhmara H., Using Topex/Poseidon data to enhance ERS-1 data, *J. Atm. and Ocean. Tech.*, 1995 (in press)

Marsh, J. G., Cheney, R.E., Martin, J. V., and McCarthy J. J., Computation of a precise mean sea surface in the eastern North Pacific using satellite altimetry, *EOS, Trans, AGU*, 63, 178-179, 1982.

Menke, W.,Geophysical data analysis: discrete inverse theory, Academic Press, Inc., 260pp. 1984.

Rapp, R. H., The determination of geoid undulation and gravity anomalies from seasat altimeter data, *J. Geophys. Res.*, 88, 1552-1562, 1983.

Sander, E. L., and Mrazek, C. P., Regression technique to remove temporal variation from geomagnetic survey data, *Geophysics*, 47, 1437-1443, 1982.

Smith W. H. F., and Wessel P., Gridding with continuous curvature splines in tension, *Geophysics*, 55, 293-305, 1990.

Tai, C. K., Geosat crossover analysis in tropical pacific: 1, constrained sinusoidal crossover adjustment, *J. Geophys. Res.*, 93, 10621-10629, 1988.

S. K. Hsu and L. Géli, Ifremer, DRO/GM, Centre de Brest, B.P. 70, 29280 Plouzané, France.

G. Davalan, Laboratoire d'Informatique, Université de Bretagne Occidentale, 29200, Brest, France

High-resolution detection of geologic boundaries from potential field
anomalies: an enhanced analytic signal technique

La méthode du signal analytique est basée sur les gradients des données potentielles, qui peuvent être déduits des données potentielles. Cette méthode nous permet d'identifier les frontières géologiques, soit des failles, soit des contacts de domaines différents. Grâce à cette méthode, nous avons identifié des discontinuités dans la partie sud du bassin d'Okinawa (Hsu et al., 1995b) ainsi que sur l'île de Taiwan (p. 212).

High-resolution detection of geologic boundaries from potential field anomalies: an enhanced analytic signal technique

Shu-kun Hsu[1,2], Jean-Claude Sibuet[1], and Chuen-Tien Shyu[3]

[1] Ifremer, Centre de Brest, BP 70, 29280 Plouzané, France

[2] Département des Sciences de la Terre, Université de Bretagne Occidentale,
BP 809, 29285 Brest, France

[3] Institute of Oceanography, National Taiwan University,
PO Box 23-13, Taipei, Taiwan, ROC

ABSTRACT

A high-resolution technique is developed to image geologic boundaries such as contacts and faults. The outlines of the geologic boundaries can be determined by tracing the maximum amplitudes of an enhanced analytic signal composed of the nth-order vertical derivative values of two horizontal gradients and one vertical gradient. The locations of the maximum amplitudes are independent of the ambient potential field. This technique is particularly suitable when interference effects are considerable and/or when both induced and remanent magnetizations are not negligible. The corresponding depth to each geologic boundary can be estimated from the amplitude ratio of the enhanced and the simple analytic signals, which provides a simple estimation technique.

Such a method has been applied to magnetic data acquired in the Ilan plain of Taiwan located at the southwestern end of the Okinawa trough. The quantitative analysis shows that the underlying geologic boundaries deepen southward and slightly eastward. The enlargement of the Ilan plain in the direction of the Okinawa trough and the existence of NNW and WNW trending faults near the city of Ilan reveal a discontinuity between the Okinawa trough backarc extension and the compressional process in Taiwan.

INTRODUCTION

Since the early 1970s, a variety of automatic or semiautomatic methods, based on the use of the horizontal and/or the vertical gradients (derivatives) of potential field anomalies, have been developed as efficient tools for the determination of geometric parameters, such as locations of boundaries and depths of the causative sources (e.g.,

O'Brien, 1971; Nabighian, 1972, 1974; Cordell, 1979; Rao et al., 1981; Thompson, 1982; Murthy, 1985; Barongo, 1985; Blakely and Simpson, 1986; Hansen et al., 1987; Hansen and Simmonds, 1993; Reid et al., 1990; Keating and Pilkington, 1990; Ofoegbu and Mohan, 1990; Roest et al., 1992; Marcotte et al., 1992; Marson and Klingele, 1993). The success of these methods is because of the fact that quantitative or semiquantitative solutions are found with no or a few assumptions. For instance, the main advantage of using the maximum amplitudes of the analytic signal to determine the location of the structural boundaries is that the result is independent of the earth's magnetic field parameters and of the direction of source magnetization (Nabighian, 1972, 1974; Roest et al., 1992). Such an invariable characteristic is advantageous in magnetic interpretation, especially when the contribution from remanent and induced magnetizations cannot be distinguished.

Thompson (1982) adopted Euler deconvolution to find locations and depths of 2-D geologic boundaries. Later on, his approach was successfully applied to 3-D gridded data by Reid et al. (1990). A drawback of using Euler deconvolution is that the user must define the structural index prior to its application. Unfortunately, the choice of structural index is crucial for the determination of the solutions. Cordell (1979) and Cordell and Grauch (1985) used only the maximum amplitudes of the horizontal gradients (without the vertical gradient) to locate near-vertical geologic boundaries from gravity or pseudogravity anomalies. In essence, the horizontal-gradient method is a special case of the use of the analytic signal where the gravity anomaly is equivalent to the vertical magnetization anomaly from the same causative body through Poisson's relationship (Baranov, 1957). In this case, even if we do not add the vertical gradient in computing the amplitude of the analytic signal, in the absence of interference, the resulting amplitude (a bell-shaped function) also has its maximum value directly over the abrupt boundaries [cf. equation (2) of Nabighian, 1972].

Since potential field data correspond to the superposition of effects from all causative sources, the determination of geologic boundaries usually suffers from nearby source interference which yields mislocations (Grauch and Cordell, 1986). To reduce interference effects, one may downward continue the data. Although this technique may provide increased resolution, it is not very stable with respect to taking high-order derivatives (Nabighian, 1974). Following the suggestion of Nabighian (1974) for the 2-D case, in the present paper, we propose an enhanced analytic signal technique for the interpretation of 3-D potential field anomalies.

THEORY

For 2-D and 3-D potential field anomalies, Nabighian (1972, 1984) has demonstrated that the horizontal and the vertical gradients form a pair of Hilbert transforms or analytic signals. One important characteristic is that the amplitude of the analytic signal, composed of these orthogonal gradients, exhibits a bell-shaped symmetric function located directly above the boundary of the structure (e.g., contact or fault). This idea had been extensively explained by Nabighian (1972, 1974) in the 2-D case and used in 3-D magnetic interpretation by Roest et al. (1992). Due to interference effects, the use of the simple analytic signal in the 3-D case seems insufficient to detect geologic boundaries (see discussion in Mohan, 1993). Since the existing interference is usually inevitable, improving resolution becomes a requirement.

In the 2-D case, Nabighian (1974) suggested using the following bell-shaped function to enhance the analytic signal from shallow sources:

$$(\frac{\partial^n G_h}{\partial h^n})^2 + (\frac{\partial^n G_z}{\partial h^n})^2 = \frac{(1^2 \times 2^2 \times 3^2 \times \cdots \times n^2)\alpha^2}{(d^2 + h^2)^{n+1}} , \tag{1}$$

where G_h and G_z are the horizontal and vertical gradients of the potential

      field anomaly, respectively ;

      h is the distance along the horizontal axis which is perpendicular to the strike

        of the 2-D structure;

      n is a positive integer;

      d is the depth to the top surface of the source; while the lower surface is at

        infinity;

      α = 2kFcsinq for the step model of magnetic anomaly is the ambient parameter;

      k is the susceptibility contrast of the step;

      F is the earth's magnetic field magnitude;

      q is the dip angle of the step model;

      $c = 1 - \cos^2 i \sin^2 B$ for total magnetic field anomalies;

      i is the inclination of the earth's magnetic field; and

      B is the angle between magnetic north and positive h-axis.

In the 3-D case, the simple analytic signal is defined by Nabighian (1984) as

$$A_0(x,y) = \frac{\partial G}{\partial x}\hat{x} + \frac{\partial G}{\partial y}\hat{y} + i\frac{\partial G}{\partial z}\hat{z} , \tag{2}$$

and its amplitude as

$$|A_0(x,y)| = \sqrt{(G_x)^2 + (G_y)^2 + (G_z)^2} ,$$ (3)

where G is the potential field anomaly;

$$G_x = \frac{\partial G}{\partial x}; \quad G_y = \frac{\partial G}{\partial y}; \text{ and } G_z = \frac{\partial G}{\partial z}.$$

To extend equation (1) into the 3-D case, we define the n-order enhanced analytic signal as

$$A_n(x,y) = \frac{\partial}{\partial x}(\frac{\partial^n G}{\partial z^n})\hat{x} + \frac{\partial}{\partial y}(\frac{\partial^n G}{\partial z^n})\hat{y} + i\frac{\partial}{\partial z}(\frac{\partial^n G}{\partial z^n})\hat{z} ,$$ (4)

and its amplitude as

$$|A_n(x,y)| = \sqrt{(\nabla^n G_x)^2 + (\nabla^n G_y)^2 + (\nabla^n G_z)^2} ,$$ (5)

where $\nabla^n = -\dfrac{\partial^n}{\partial z^n}.$

For n=2, equation (4) corresponds to the enhanced analytic signal derived from second vertical derivative, and the amplitude of equation (5) becomes

$$|A_2(x,y)| = \sqrt{(\nabla^2 G_x)^2 + (\nabla^2 G_y)^2 + (\nabla^2 G_z)^2} .$$ (6)

Equation (6) is used hereafter as an example to demonstrate the improvement of the detection of geologic boundaries. First of all, it is noted that the amplitude of enhanced and simple analytic signals are invariant with respect to the coordinate system (see Appendix A). Considering that the observed surface is outside the sources, Laplace's equation is satisfied for the potential field anomalies (Grant and West, 1976, p. 213), then

$$\frac{\partial^2}{\partial x^2} + \frac{\partial^2}{\partial y^2} + \frac{\partial^2}{\partial z^2} = 0.$$ (7)

Considering equations (1) and (7) in the absence of interference effects from nearby boundaries (ideal situation), for one geologic boundary of an arbitrary strike equation (1) can be written in the 3-D case (see the derivation in detail in Appendix A) as

$$(\frac{\partial^n G_x}{\partial z^n})^2 + (\frac{\partial^n G_y}{\partial z^n})^2 + (\frac{\partial^n G_z}{\partial z^n})^2 = \frac{(1^2 \times 2^2 \times 3^2 \times \cdots \times n^2)\alpha^2}{(d^2 + h^2)^{n+1}} .$$ (8)

Hence, each maximum amplitudes of the second-order enhanced analytic signal (at h=0), being a peak of a bell-shaped function, is written as

$$\left| A_2(x,y) \right|_{max} = \frac{|2\alpha|}{d^3} ,$$ (9)

while the corresponding maximum amplitude of the simple analytic signal in the 3-D case is (cf. the 2-D case of Nabighian, 1974):

$$\left| A_0(x,y) \right|_{max} = \frac{|\alpha|}{d}.$$ (10)

Equations (8), (9) and (10) suggest at least two possible ways of estimating the depth to the top of the boundary. One is to estimate the offset from the position of the maximum amplitude to a specific position where the amplitude is, for example, $\left| A_2(x,y) \right|_{max} / 2\sqrt{2}$ (i.e., when h = d); however, this is not easily done in practice. The other is to compute the depth from the amplitude ratio of equations (9) and (10); i.e.,

$$d = \sqrt{2} \times \sqrt{\frac{\left| A_0(x,y) \right|_{max}}{\left| A_2(x,y) \right|_{max}}} .$$ (11)

For real data, in addition to interfering anomalies, several factors may induce bias in the locations of the geologic boundaries and the estimation of the corresponding depths. For instance, the assumption of the infinite bottom surface is unrealistic. Thus, we should assume either that the geologic boundaries are near-vertical (abrupt) or that step-like sources are thick enough to give sufficient resolution for discriminating the locations of the top and the bottom boundaries. The larger the distance between the top and the bottom surfaces, the better the resolution is obtained to detect individual boundaries or edges. Due

to the enhancement of the analytic signal, the detection resolution for location (or outline) of geologic boundaries is increased and the result is less affected by interference. Equation (11) is used as an approach for estimating the depths to boundaries, even though it is not very valid in the fact that the locations of maxima for the enhanced and the simple analytic signals may be different on account of interference effects. Practically, we use the locations of the maximum amplitudes of the second-order enhanced analytic signal to ensure the locations of boundaries and the corresponding amplitudes of the simple analytic signal for the same locations are adopted, in this study, to give depth estimation. This may lead to some depth discrepancies depending on the extent of interference effects. However, peak values of amplitudes are less influenced from interference effects than their nearby values and such a depth estimation approach will be shown efficiently simple. Alternatively, the depth estimation from the amplitude ratio concept could be achieved by introducing another maximum amplitude such as the maximum amplitude of the first-order enhanced analytic signal (see Appendix A). Once the depth for each location of the maximum amplitude of the enhanced analytic signal has been obtained, the ambient parameter α can be estimated, for example, from equation (9).

Since numerical approximation for the gradient and the curvature values (by finite-difference method and/or Fourier transform) is required, we should pay close attention to the occurrence of high-frequency error and ensure that the observed data are smooth enough to avoid unwanted effects.

The maximum amplitudes of both the enhanced and the simple analytic signals are not independent of α, the ambient parameter of equations (9) and (10). They are related to the intensity of the magnetization (kF), the inclination (i) of the earth's field and the strike (B) of the geologic boundary. For a given geologic boundary, the amplitude of the enhanced analytic signal becomes small when the geologic boundary is close to the magnetic equator or when its strike is near parallel to the magnetic north (i.e., c in equation (1) becomes close to zero). For this reason, caution is needed for the boundary identification directly over the amplitude image of analytic signals derived from magnetic anomalies. By contrast, for gravity anomalies, the amplitudes of analytic signals are independent of latitudes and boundary orientations and are only related to density contrasts and depths of boundaries.

The locations of the maximum amplitudes of the enhanced analytic signal can be either automatically determined by the method of Blakely and Simpson (1986) or inspected from shaded or color maps of the amplitudes.

TEST CASES

46

Isolated source (model 1)

For simplicity, the magnetic anomaly shown in Figure 1a, was produced by using a 5×5 km^2 infinite rectangular vertical prism (Bhattacharyya, 1964) located at a depth of 3 km (Figure 1f, parameters in Table 1). Results of the simple analytic signal method used by Roest et al. (1992) (Figure 1) and of the method we propose (Figure 2) are compared. Horizontal gradients of Figure 1a along the x and y directions (Figures 1b, 1c) are calculated on a 0.2 km grid spacing with a 5-point finite-difference method derived from the method of undetermined coefficients (Gerald and Wheatley, 1984, p. A5). The vertical gradient deduced from Figure 1a (Figure 1d) is calculated by the generalized Hilbert transform (Nabighian, 1984). Figure 1e shows the amplitude of the analytic signal (Roest et al., 1992) deduced from the three components of Figures 1b, 1c and 1d. Due to the interference effects, none of the boundaries is detected. By using the method of Blakely and Simpson (1986) with indices 2 and 3, only three maxima are found (Figure 1f).

To obtain the enhanced amplitude of the second-order enhanced analytic signal (equation (7)), we use the same grid spacing and the 5-point finite-difference method as above. The curvature values of Figures 1b, 1c and 1d are approximated to produce the three required components (Figures 2b, 2c and 2d). Because the numerical computation is an approximation, high frequency noise appears in the background. However, when the amplitudes of the enhanced analytic signal are computed, the background noise significantly decreases (Figure 2e) and generally a threshold control of enhanced amplitudes can be assigned to improve the degree of confidence. As shown in Figures 2e and 2f, the maximum amplitudes of the enhanced analytic signal delineate the boundaries of the prism quite well. The locations of maxima, determined by the method of Blakely and Simpson (1986) using indices 2 and 3 and amplitudes greater than 5 nT/km^3 (threshold control) to avoid numerical approximation errors, show that this method achieves a higher resolution than the simple analytic signal method (cf. Figures 1f and 2f). Depths to the top surface are estimated between 2.03 to 2.25 km from equation (11) instead of 3 km in the given model. This provides about 70% accuracy in depth estimation; however, we shall mention again that the performance of depth estimation depends on the extent of the interference effects if the amplitude ratio method is applied.

Multiple sources (model 2)

In order to demonstrate that the ambient magnetic parameters do not influence detection of geologic boundaries, a more sophisticated model is adopted (Figure 3). The

characteristics of each prism are shown in Table 1. The same procedure used for model 1 was repeated to get the amplitudes of the enhanced and simple analytic signals. Figure 4a displays the amplitudes of the simple analytic signal used by Roest et al. (1992). Clearly, the maximum amplitudes used to determine the boundaries exhibit much interference, especially for the boundaries of prism 2C which is shallower than prism 2B and has a smaller intensity of magnetization than prism 2A. This interference phenomenon is also revealed in Figure 5a, where none of maxima for the prism 2C is detected except for the contiguous boundary between prisms 2C and 2B. By contrast, the enhanced analytic signal (Figure 4b) clearly identifies the boundaries of prisms. Note that the large amplitudes are associated with the shallow prism (2B) and that the effect of the boundary orientations with respect to the magnetic north (e.g., east-west trending boundaries of prism 2A) is clearly identified in Figure 4b. Similarly, the amplitudes are very weak for the right and left boundaries of prism 2C which are almost parallel to magnetic north. The same method of Blakely and Simpson (1986) has been used to determine the locations of the maxima using indices 2 and 3 and amplitudes greater than 5 nT/km^3 (Figure 5b). Obviously, our method exhibits a higher resolution for the detection of boundaries with the identification of 209 maxima. As expected from interference effects, depth estimation for the inner boundaries between prisms 2A, 2B and 2C are the poorest (Figure 5b). An average accuracy of about 80% in depth estimation is given in this case with the east-west trending boundaries yielding better depth estimates.

APPLICATION TO REAL DATA

Ilan plain

The Okinawa trough backarc basin extends from Japan to Taiwan and terminates in the Ilan plain (northeastern Taiwan, Figure 6). The width of the southern Okinawa trough progressively decreases to almost zero west of the Ilan plain, which explains the triangular form of the Ilan Plain. The plain is fringed by mountainous regions composed mainly of slightly metamorphosed Eocene to Miocene rocks (Figure 7). Quaternary fluvial deposits have filled the plain. The Lanyanghsi stream (about 4 km south of the Ilan city), flowing eastward, is the largest stream in the plain. The stream and its tributaries roughly follow the extended structural lineations, which can be inferred from the surrounding fold-thrust belts (Figure 7). The geologic setting of the Ilan plain is important in the sense that the extremity of the backarc basin was narrowed associated with the arc-arc collision in Taiwan (Hsu et al., 1995). Extensional processes in the Okinawa trough have been discussed (e.g., Lee and Lu, 1976; Bowin et al., 1978; Eguchi and Uyeda, 1983; Letouzey

48

and Kimura, 1985; Sibuet et al., 1987 and in press). Based on quantitative analysis of the magnetic anomalies together with known adjacent geology, the geologic structures beneath the Ilan plain are interpreted.

Data processing

In 1978, a total field magnetic survey was conducted in the Ilan plain (Yu and Tsai, 1979). The diurnal variation was corrected using a base magnetometer. The DGRF 1975 and DGRF 1980 were adopted for removal of the secular variation (Hsu, 1987). The sharp elongated negative magnetic anomaly located southwest of Ilan city (Figure 8a) was interpreted as a linear fracture zone and the positive linear anomaly as intrusive igneous rocks (Yu and Tsai, 1979). If the latter is assumed to be produced by a two-dimensional thick dike, the depth to the top surface of the intrusive body was estimated at 1.5 - 2.0 km and the width of the dike 4.7-5.7 km on the eastern side of the plain (Yu and Tsai, 1979; Hsu, 1987).

Following the same procedure used for the test cases, the distribution of amplitudes of the second-order enhanced analytic signal was obtained on a regular 0.2 km grid spacing (Figure 8b). The detected locations of maxima as well as the estimated depths are shown in Figure 8c. The unknown geology beneath the Ilan plain is inferred (Figure 9) by using Figures 7 and 8c. The sedimentological facies beneath the plain are inferred from the surrounding geology (e.g., Ho, 1986) and are subject to further modification. The linear structure located in the lower-part of the surveyed area (Figure 8c) is suspected to be an artefact caused by bad data reduction in a mountainous region.

New geologic insight

On the basis of Figures 8c and 9, new geologic insight is proposed for the Ilan plain. Several geologic boundaries located southwest of the Ilan city are east-west trending and tend to deepen southward and slightly eastward (Figure 8c). This reflects the existence of the southern flank of the underlying anticline whose axis is along facies 8 (Figure 9). The two well defined northern boundaries are interpreted as the eastern prolongations of the two contacts between the Eocene and Oligocene sedimentary units (facies 7 and 8 in Figure 9). They are buried less than one kilometer beneath the fluvial deposits and abruptly terminate at the west side of the Ilan city. The east-west trending boundary (1.5-2.5 km beneath the plain), located 6 km south of the Ilan city, is probably the prolongation of the Lishan fault, a major tectonic feature which has been interpreted as the boundary fault between the Hsüehshan Range (the belt between faults I and II in Figures 7 and 9) on

49

the west and the Miocene Lushan formation (facies 3 in Figures 7 and 9). The Lishan fault is considered to be a major thrust which dips steeply to the east (Biq, 1971; Wu, 1978); however, its northern part is not clear (Wu, 1978; Ho, 1986). This fault is still active and its seismicity suggests that its northeastern extension has a normal motion consistent with the extension system of the Okinawa trough backarc basin (Tsai et al., 1975). Since the prolongation of the Lishan fault into the Ilan plain is not well imaged (Figure 8c), the continuation of the Lishan fault into the Ilan plain may be complex or it may not be a simple fault. However, a recent study suggests that the Lishan fault corresponds to a suture zone along the axis of an ancient backarc basin uplifted because of the arc-arc collision in Taiwan (Hsu et al., 1995). All the roughly east-west features, including the Lishan fault, stop abruptly or change orientations near Ilan city. This suggests the existence of a major NNE left lateral strike-slip fault located just beneath the Ilan city. East of this fault, the geologic boundaries, about 1.5-2 km deep, present an eastward fan-shaped geometry which could be associated with the backarc extension of the Okinawa trough.

In summary, our proposed geologic picture below the Quaternary deposits of the Ilan plain (Figure 9) indicates a discontinuity between the tensional (to the east) and compressional (to the west) features in terms of strike-slip faults near the Ilan city. The river system in the Ilan plain is more or less controlled by the geologic boundaries as revealed by the similarity of the river system and the geologic boundaries (cf. Figures 7 and 9).

CONCLUSIONS

Based on vertical derivatives, the concept of using the 3-D enhanced analytic signal has been developed to reduce the effect of interference between closely spaced anomalies. This technique has the advantage of avoiding dependence on the ambient magnetic field and of aiding quantitative interpretation of potential field anomalies. The improved resolution allows us to better detect geologic boundaries of causative sources. The determination of depths to the top surfaces of causative boundaries from amplitude ratios of analytic signals [e.g., equation (11)] is feasible under several assumptions: the different resolution of the two analytic signals used to compute the depths must be accepted; each individual source must be considered as homogeneous; and the signal from the bottom surface of the source must be negligible. Care is needed for interpretation of amplitudes of the analytic signals derived from magnetic anomalies. Even though the locations of the maxima are directly over the geologic boundaries, the amplitudes vary as a function of α, the ambient magntic field parameter.

The improvement in resolution from the proposed technique provides a better visualization of outlines of geologic features. Such information could be used as a constraint when applying inversion or forward techniques. In addition, the quantitative analysis of the locations of geologic boundaries and associated depths is well suited to the method of Blakely and Simpson (1986).

This method has been applied to magnetic data acquired in the Ilan plain (northeastern Taiwan). The deduced tectonic and sedimentological map below the Quaternary deposits of the Ilan plain shows that the collisional process in Taiwan and the extensional backarc formation of the Okinawa trough are disconnected by the occurrence of strike-slip faults near the Ilan city.

ACKNOWLEDGMENTS

REFERENCES

Baranov, V., 1957, A new method for interpretation of aeromagnetic maps: Pseudo-gravimetric anomalies: Geophysics, 22, 359-383.

Barongo, J. O., 1985, Method for depth estimation on aeromagnetic vertical gradient anomalies: Geophysics, 50, 963-968.

Bhattacharyya, B. K., 1964, Magnetic anomalies due to prism-shaped bodies with arbitrary polarization: Geophysics, 29, 517-531.

Biq, C.-C., 1971, Some aspects of post-orogenic block tectonics in Taiwan. Recent crustal movements: R. Soc. N. Z. Bull., 9, 19-24.

Bowin, C., Lu, R. S., Lee, C. S., and Schouten, H., 1978, Plate convergence and accretion in Taiwan-Luzon region: Bull. Amer. Assoc. Geol., 62, 1645-1672.

Blakely, R. J., and Simpson, R. W., 1986, Approximating edges of source bodies from magnetic or gravity anomalies: Geophysics, 51, 1494-1498.

Cordell, L., 1979, Gravimetric expression of graben faulting in Santa Fe country and the Espanola basin, New Mexico: New Mexico Geol. Soc. Guidebook, 30th Field Conf., 59-64.

Cordell, L., and Grauch, V. J. S., 1985, Mapping basement magnetization zones from aeromagnetic data in the San Juan Basin, New Mexico, *in* Hinze, W. J., Ed., The utility of regional gravity and magnetic anomaly maps: Soc. Explor. Geophys., 181-197.

Eguchi, T., and Uyeda, S., 1983, Seismotectonics of the Okinawa trough and Ryukyu arc: Mem. Geol. Soc. China, **5**, 189-210.

Gerald, C. F., and Wheatley, P. O., 1984, Applied numerical analysis, 3rd ed.: Addison-Wesley Pub. Co. Inc., 579 p.

Grant, F. S., and West, G. F., 1976, Interpretation theory in applied geophysics: McGraw-Hill Inc., 584 p.

Grauch, V. J. S., and Cordell, L., 1987, Limitations of determining density or magnetic boundaries from the horizontal gradient of gravity or pseudogravity data: Geophysics, **52**, 118-124.

Hansen, R. O., and Simmonds, M., 1993, Multiple-source Wenner deconvolution: Geophysics, **58**, 1792-1800.

Hansen, R. O., Pawlowski, R. S., and Wang, X., 1987, Joint use of analytic signal and amplitude of horizontal gradient maxima for three-dimensional gravity data interpretation: 57th Ann. Internat. Mtg., Soc. Expl. Geophys., Expanded Abstracts, 100-102.

Ho, C.-S., 1986, An introduction to the geology of Taiwan: Explantory text of the geologic map of Taiwan: The ministry of economic affairs, ROC, 2nd ed., 164 p.

Hsu, S.-K., 1987, Using DGRF models and approximated derivatives to reduce datum-level error and to interpret magnetic anomalies: MS. thesis, National Taiwan University, 57 p. (in Chinese).

Hsu, S.-K., Sibuet, J.-C. and Monti, S., 1995, Arc-arc collision vs. backarc extension : Taiwan mountain building: Proceeding of the international symposium on the active collision in Taiwan, Taipei, Taiwan, R.O.C., 121-130.

Keating, P. B., and Pilkington, M., 1990, An automated method for the interpretation of magnetic vertical-gradient anomalies: Geophysics, **55**, 336-343.

Lee, C.-S., and Lu, R. S., 1976, Significance of the southwestern section of Ryukyu Inner Ridge in the exploration of geothermal resources in Ilan area: Mining Technical Digest, **14**, 114-120. (in Chinese).

Letouzey, J., and Kimura, M., 1985, Okinawa trough genesis: Structures and evolution of a backarc basin developed in a continent: Marine and Petroleum Geology, **2**, 111-130.

Marcotte, D. L., Hardwick, C. D., and Nelson, J. B., 1992, Automated interpretation of horizontal magnetic gradient profile data, Geophysics, **57**, 288-295.

Marson, I., and Klingele, E. E., 1993, Advantages of using the vertical gradient of gravity for 3-D interpretation: Geophysics, **58**. 1588-1595.

Mohan, N. L., 1993, Discussion on "Magnetic interpretation using the 3-D analytic signal by Roest, W. R., Verhoef, J., and Pilkington, M., 1992: Geophysics, **57**, 116-125", Geophysics, **58**, 1214.

Murthy, I. V. R., 1985, Magnetic interpretation of dike anomalies using derivatives: PAGEOPH, **123**, 232-238.

Nabighian, M. N., 1972, The analytic signal of two-dimensional magnetic bodies with polygonal cross-section: Its properties and use for automated anomaly interpretation: Geophysics, **37**, 507-517.

------------------ 1974, Additional comments on the analytic signal of two-dimensional magnetic bodies with polygonal cross-section: Geophysics, **39**, 85-92.

------------------ 1984, Toward a three-dimensional automatic interpretation of potential field data via generalized Hilbert transforms: Fundamental relation: Geophysics, **49**, 957-966.

O'Brien, D. P., 1971, CompuDepth: a new method for depth to basement computation: Presented at the 42th Ann. intrernat. Mtg., Soc. Expl. Geophys.

Ofoegbu, C. O., and Mohan, N. L., 1990, Interpretation of aeromagnetic anomalies over part of southeastern Nigeria using three-dimensional Hilbert transformation: PAGEOPH., **134**, 13-29.

Rao, D. A., Babu, H. V., and Narayan, P. V., 1981, Interpretation of magnetic anomalies due to dikes: The complex gradient method: Geophysics, **46**, 1572-1578.

Reid, A. B., Allsop, J. M., Granser, H., Millett, A. J., and Somerton, I. W., 1990, Magnetic interpretation in three dimensions using Euler deconvolution: Geophysics, **55**, 80-91.

Roest, W. R., Verhoef, J., and Pilkington, M., 1992, Magnetic interpretation using the 3-D analytic signal: Geophysics, **57**, 116-125.

Sibuet, J.-C., Letouzey, J., Barbier, F., Charvet, J., Foucher, J.-P., Hilde, T. W. C., Kimura, M., Chiao, L.-Y., Marsset, B., Muller, C., and Stéphan, J.-F., 1987, Backarc extension in the Okinawa trough: J. Geophys. Res., **92**,.14041-14063.

Sibuet, J.-C., Hsu, S.-K., Shyu, C.-T., and Liu, C.-S., in press, Structural and kinematic evolutions of the Okinawa trough backarc basin, *in* Taylor, B., Ed., Backarc basins: tectonics and magmatism, Plenum, New-York.

Thompson, D. T., 1982, EULDPH: A new technique for making computer-assisted depth estimates from magnetic data: Geophysics, **47**, 31-37.

Tsai, Y.-B., 1986, Seismotectonics of Taiwan: Tectonophysics, **125**, 17-38.

Tsai, Y.-B., Feng, C. C., Chiu, J. M., and Liaw, H. B., 1975, Correlation between microearthquakes and geologic faults in the Hsintien-Ilan area: Petrol. Geol. Taiwan, **12**, 149-167.

Wu, F. T., 1978, Recent tectonics of Taiwan: J. Phys. Earth, **26**, suppl., 265-299.

Yu, S.-B., and Tsai, Y.-B., 1979, Geomagnetic anomalies of Ilan plain, Taiwan: Petrol. Geol. Taiwan, **16**, 19-27.

Wessel, P., and Smith, W. H. F., 1991, Free software helps map and display data: EOS, trans. AGU, **72**, 441-446.

APPENDIX A

RELATIONSHIPS BETWEEN ENHANCED AMPLITUDES AND BOUNDARY DEPTHS

Any pair of orthogonally horizontal gradients in Cartesian coordinate system, for example G_x and G_y, can be rotated to a new coordinate system. If a system is rotated an arbitrary angle Φ counter-clockwise, then the new horizontal gradients can be expressed as

$$G_{x'} = G_x \cos(\Phi) - G_y \sin(\Phi), \tag{A-1}$$

$$G_{y'} = G_x \sin(\Phi) + G_y \cos(\Phi). \tag{A-2}$$

Taking the gradient operator $\nabla^n = -\dfrac{\partial^n}{\partial z^n} (= -\dfrac{\partial^n}{\partial z'^n})$ and defining $\nabla^0 = 1$, equations (A-1) and (A-2) become

$$
\begin{aligned}
\nabla^n G_{x'} &= \nabla^n (G_x \cos(\Phi) - G_y \sin(\Phi)) \\
&= \cos(\Phi)\nabla^n G_x - \sin(\Phi)\nabla^n G_y,
\end{aligned} \tag{A-3}
$$

and

$$
\begin{aligned}
\nabla^n G_{y'} &= \nabla^n (G_x \sin(\Phi) + G_y \cos(\Phi)) \\
&= \sin(\Phi)\nabla^n G_x + \cos(\Phi)\nabla^n G_y.
\end{aligned} \tag{A-4}
$$

54

By combining the square values of each side of equations (A-3) and (A-4), we obtain

$$(\nabla^n G_{x'})^2 + (\nabla^n G_{y'})^2 = (\nabla^n G_x)^2 + (\nabla^n G_y)^2. \qquad (A-5)$$

Since the vertical component $G_{z'} = G_z$ everywhere, then $\nabla^n G_{z'} = \nabla^n G_z$ and

$$(\nabla^n G_{x'})^2 + (\nabla^n G_{y'})^2 + (\nabla^n G_{z'})^2 = (\nabla^n G_x)^2 + (\nabla^n G_y)^2 + (\nabla^n G_z)^2. \qquad (A-6)$$

Equation (A-6) demonstrates that the amplitudes of both the enhanced ($n \geq 1$) and the simple ($n=0$) analytic signals are invariant with respect to the coordinate system. Furthermore, if the y'-direction is chosen to be parallel to the strike of a given geologic boundary (i.e., $G_{y'} = 0$ and $\dfrac{\partial^n}{\partial y'^n} = 0$) and Laplace's equation is valid (i.e., $\dfrac{\partial^2}{\partial z'^2} = -\dfrac{\partial^2}{\partial x'^2}$ because $\dfrac{\partial^2}{\partial y'^2} = 0$), the square value of the amplitude of the n-order enhanced analytic signal (i.e., equation (A-6)) becomes

$$(\nabla^n G_x)^2 + (\nabla^n G_y)^2 + (\nabla^n G_z)^2 = (\nabla^n G_{x'})^2 + (\nabla^n G_{z'})^2$$

$$= (\frac{\partial^n}{\partial z'^n}\frac{\partial G}{\partial x'})^2 + (\frac{\partial^n}{\partial z'^n}\frac{\partial G}{\partial z'})^2,$$

$$= (\frac{\partial^n}{\partial x'^n}G_{x'})^2 + (\frac{\partial^n}{\partial x'^n}G_{z'})^2, \quad \text{if } n = 2m;$$

$$\text{or} = (\frac{\partial^n}{\partial z'^{(2m-1)}}G_{x'})^2 + (\frac{\partial^n}{\partial z'^{(2m-1)}}G_{z'})^2$$

$$= (\frac{\partial^{2(m-1)}}{\partial z'^{2(m-1)}}\frac{\partial}{\partial z'}\frac{\partial}{\partial x'}G)^2 + (\frac{\partial^{2(m-1)}}{\partial z'^{2(m-1)}}\frac{\partial}{\partial z'}\frac{\partial}{\partial z'}G)^2$$

$$= (\frac{\partial^{2(m-1)}}{\partial x'^{2(m-1)}}\frac{\partial}{\partial z'}\frac{\partial}{\partial x'}G)^2 + (\frac{\partial^{2(m-1)}}{\partial x'^{2(m-1)}}\frac{\partial}{\partial x'^2}G)^2$$

$$= (\frac{\partial^n}{\partial x'^n}G_{z'})^2 + (\frac{\partial^n}{\partial x'^n}G_{x'})^2, \quad \text{if } n = 2m-1, \qquad (A-7)$$

where m is a positive integer.

In the absence of interference effects, equation (A-7) of the 3-D case is essentially equivalent to equation (1) of the 2-D case. Accordingly, a general form of equation (1), for one geologic boundary, can be written in the 3-D case as

$$\left(\frac{\partial^n G_x}{\partial z^n}\right)^2 + \left(\frac{\partial^n G_y}{\partial z^n}\right)^2 + \left(\frac{\partial^n G_z}{\partial z^n}\right)^2 = \frac{(1^2 \times 2^2 \times 3^2 \times \cdots \times n^2)\alpha^2}{(d^2 + h^2)^{n+1}}. \tag{A-8}$$

Each maximum amplitude of the n-order enhanced analytic signal (at h=0) is therefore related to a depth d of an arbitrary trending boundary by writing

$$\left|A_n(x,y)\right|_{max} = \sqrt{(\nabla^n G_x)^2 + (\nabla^n G_y)^2 + (\nabla^n G_z)^2}\Big|_{max}$$
$$= \frac{|1 \times 2 \times 3 \times \cdots \times n \times \alpha|}{d^{n+1}}. \tag{A-9}$$

For example, each maximum amplitude of the first-order enhanced analytic signal (n=1), used by Marson and Klingele (1993), corresponds to

$$\left|A_1(x,y)\right|_{max} = \sqrt{(\nabla^1 G_x)^2 + (\nabla^1 G_y)^2 + (\nabla^1 G_z)^2}\Big|_{max}$$
$$= \frac{|\alpha|}{d^2}. \tag{A-10}$$

For n=2, relationship of equation (9) is used in this study. High-order enhanced analytic signal can substantially reduce interference effects, whereas in real data the noise is also relatively amplified, which may render interpretation questionable except that potential data are quite smooth. In addition, 3-D enhanced amplitudes of more than second-order are, practically, not easily achievable.

FIGURE CAPTIONS

FIG. 1. (a) Total magnetic field anomaly of model 1 (table 1). (b) Horizontal-x gradient of (a). (c) Horizontal-y gradient of (a). (d) Vertical gradient of (a). (e) Amplitudes of the analytic signal from (b), (c) and (d). (f) Locations of maxima of (e) (open circles), determined by the method of Blakely and Simpson (1986). Solid lines represent the boundary of model 1. Solid arrows indicate the declination of the magnetization. M.N.: magnetic north.

FIG. 2. Enhanced analytic signal of model 1. (a) Total magnetic field anomaly of model 1 (table 1). (b) Curvature values of the horizontal-x gradient. (c) Curvature values of the horizontal-y gradient. (d) Curvature values of the vertical gradient. (e) Amplitudes calculated from (a), (b) and (c). (f) Locations of maxima of (e) (open circles), determined by the method of Blakely and Simpson (1986). The corresponding depths are estimated from equation (11). Solid arrows indicate the declination of the magnetization. M.N.: magnetic north. Solid line is the boundary of the model 1. Dotted line is the outline of the maximum amplitudes traced by hand.

FIG. 3. Schematic outlines of model 2 and corresponding total field magnetic anomaly. Magnetic parameters for each vertical rectangular prism are indicated in Table 1. Contour interval is 25 nT.

FIG. 4. (a) Amplitudes of the analytic signal of model 2 obtained by the method of Roest et al. (1992). (b) Amplitudes of the second-order enhanced analytic signal (this study). Solid arrows indicate the declination of the magnetization. M.N.: magnetic north. Note that the boundaries whose strikes are more perpendicular to the declination of the magnetization present large amplitudes and that the amplitude decreases when the top surface is deeper.

FIG. 5. (a) Locations of maxima of Figure 4a, determined by the method of Blakely and Simpson (1986). (b) Locations of maxima of Figure 4b, determined by the same method as above. Corresponding depths are estimated from equation (11). Solid arrows indicate the declination of the earth's field and the declination of the magnetization of each prism. M.N.: magnetic north. Solid lines are the boundaries of model 2 shown in Figure 3.

FIG. 6. The Ilan plain (black area in northern Taiwan) is located at the southwestern tip of the Okinawa trough.

FIG. 7. Geologic map around the Ilan plain (after Ho, 1986) with the major faults detected from satellite data (after Tsai, 1986). 1 = Recent clay, sand and gravel. 2 =

Pleistocene andesite and andesitic pyroclastics. 3 = Miocene argillite, slate, phyllite and sandstone interbeds. 4 = Early and Middle Miocene sandstone and shale. 5 = Oligocene to Miocene sandstone, shale and coaly shale. 6 = Oligocene argillite, slate and indurated sandstone. 7 = Oligocene quartzitic sandstone, slate and graphitic shale. 8 = Eocene to Oligocene slate, phyllite with sandstone interbeds. 9 = Eocene slate, phyllite with quartztic sandstone interbeds. 10 = Late Paleozoic and Mesozoic shist and gneiss. I = Chuchih fault. II = Lishan fault. The very thin lines represent streams in the Ilan plain. The dashed line is the limit of the magnetic survey.

FIG. 8. (a) Total field magnetic anomaly of the Ilan plain (survey area shown in Figure 7). Contour interval is 20 nT. (b) Amplitudes of the second-order enhanced analytic signal of (a). (c) Proposed geologic boundaries (lines) with corresponding depths (circles) estimated from equation (11) for amplitudes greater than 10 nT/km^3. The bottom boundary is suspected to be an artefact due to reduction of data. In this area, boundaries tend to deepen southward and slightly eastward.

FIG. 9. Interpreted geologic map of the Ilan plain area. Geologic context beneath the Ilan plain is completed by adding the information of Figure 8c and by inferring the sedimentological facies from the surrounding geology of Figure 7. The dashed line is the limit of the magnetic survey. Same legend as for Figure 7.

Table 1. Magnetic parameters for the rectangular vertical prisms of the test models. D.E.: declination of the earth's field. I.E.: inclination of the earth's field. D.M.: declination of the magnetization. I.M: inclination of the magnetization. h1: depth to the top surface. h2: depth to the bottom surface. I.O.M.: intensity of the magnetization (nT).

		D.E.	I.E.	D.M.	I.M.	length	width	h1	h2	I.O.M.
model 1		-5°	35°	-5°	35°	5 km	5 km	3 km	infinite	100
model 2	2A	-10°	40°	0°	35°	10 km	5 km	2 km	10 km	100
	2B	-10°	40°	-10°	40°	10 km	5 km	1 km	10 km	60
	2C	-10°	40°	170°	20°	10 km	5 km	2 km	10 km	80

figure 1

a) unit: nT

b) unit: nT/km³

c) unit: nT/km³

d) unit: nT/km³

e) unit: nT/km³

f) M.N.

○ 2.2 - 2.3 km
◦ 2.1 - 2.2 km
· 2.0 - 2.1 km

0   5 km
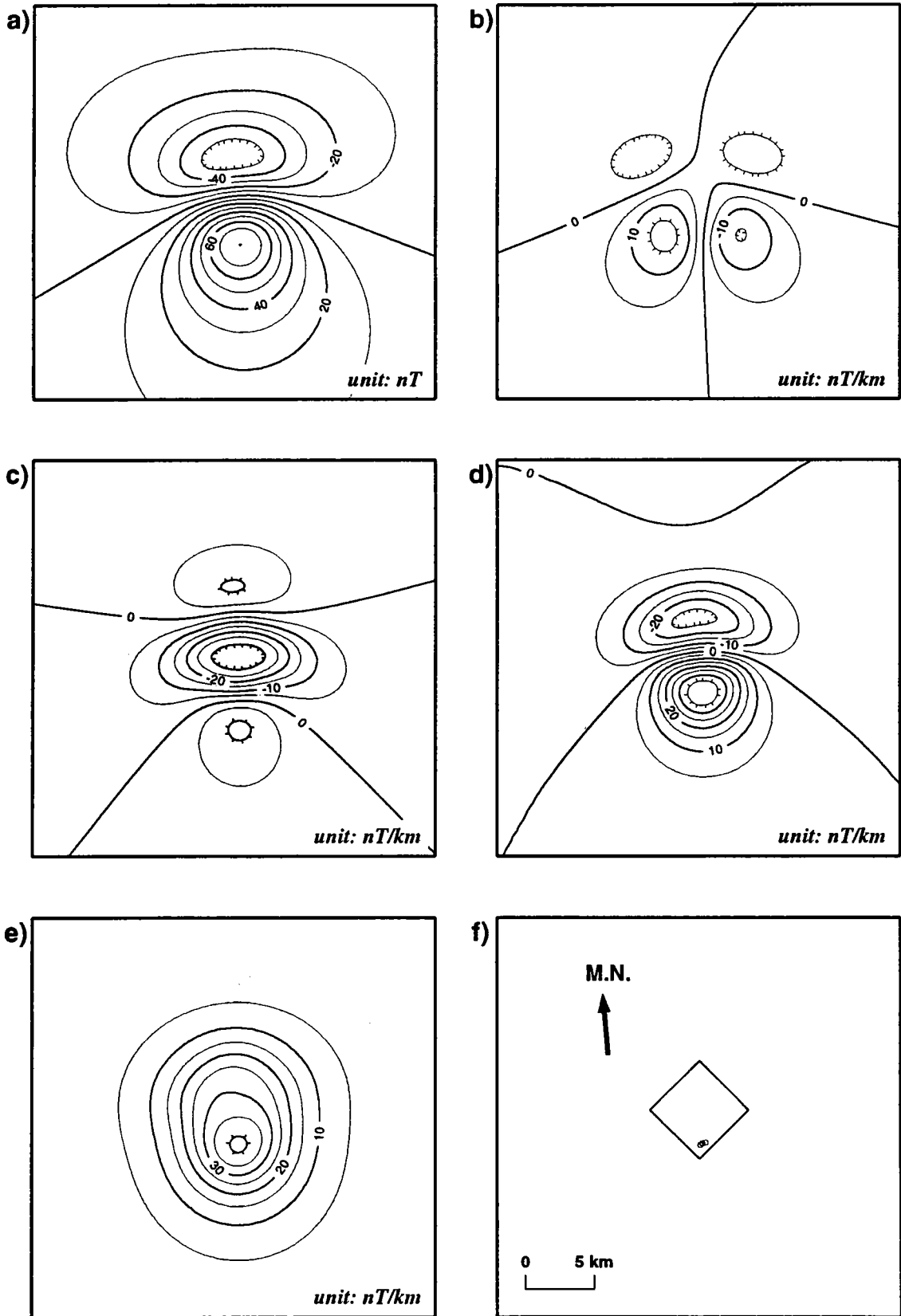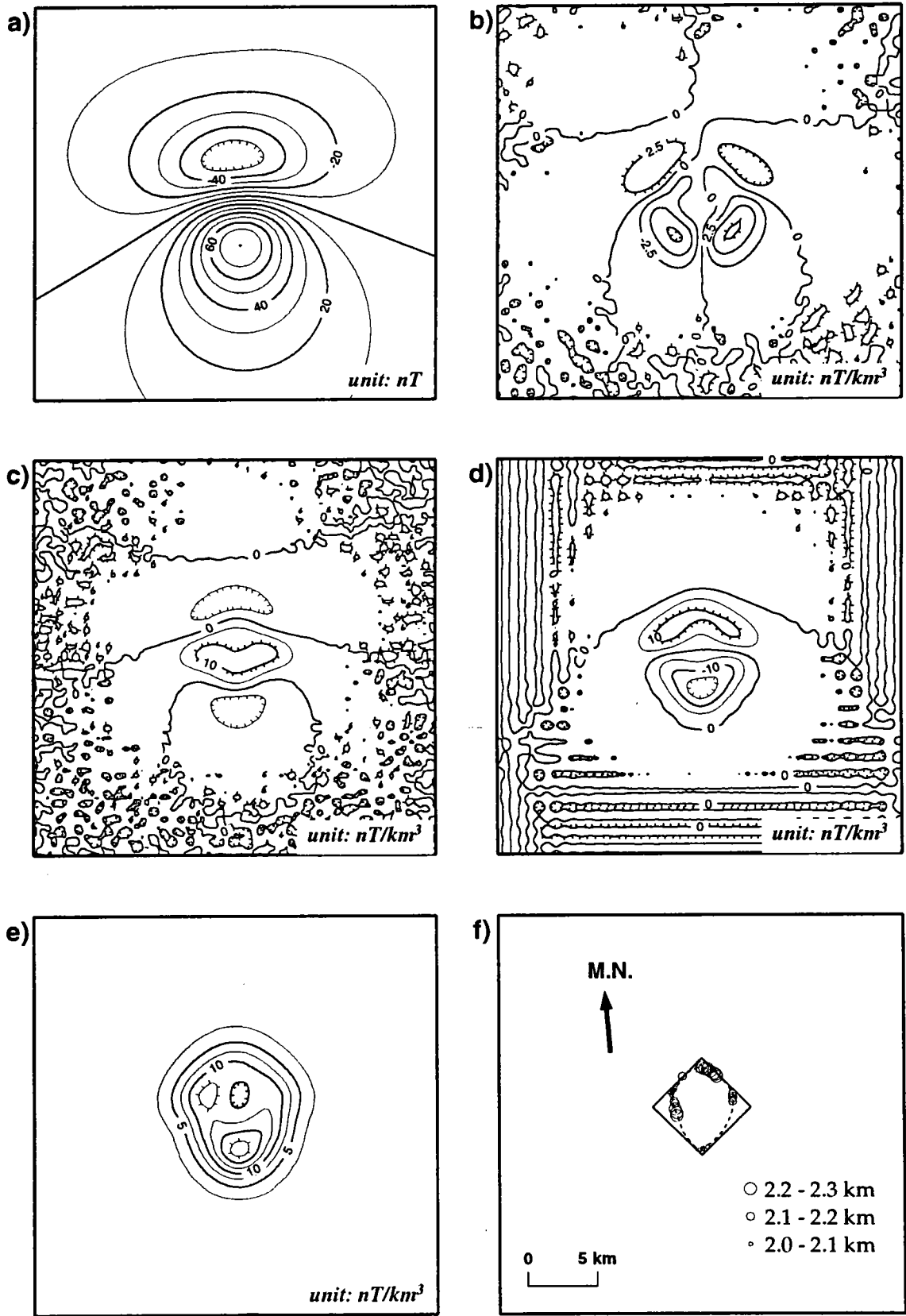
figure 2

figure 3

figure 4

a)

N

M.N.

2B

2A

2C

0   5km

b)

N

M.N.

2B

2A

2C

0   5km

○ 2.5 - 3.0 km
○ 2.0 - 2.5 km
○ 1.5 - 2.0 km
○ 1.0 - 1.5 km
∘ 0.5 - 1.0 km
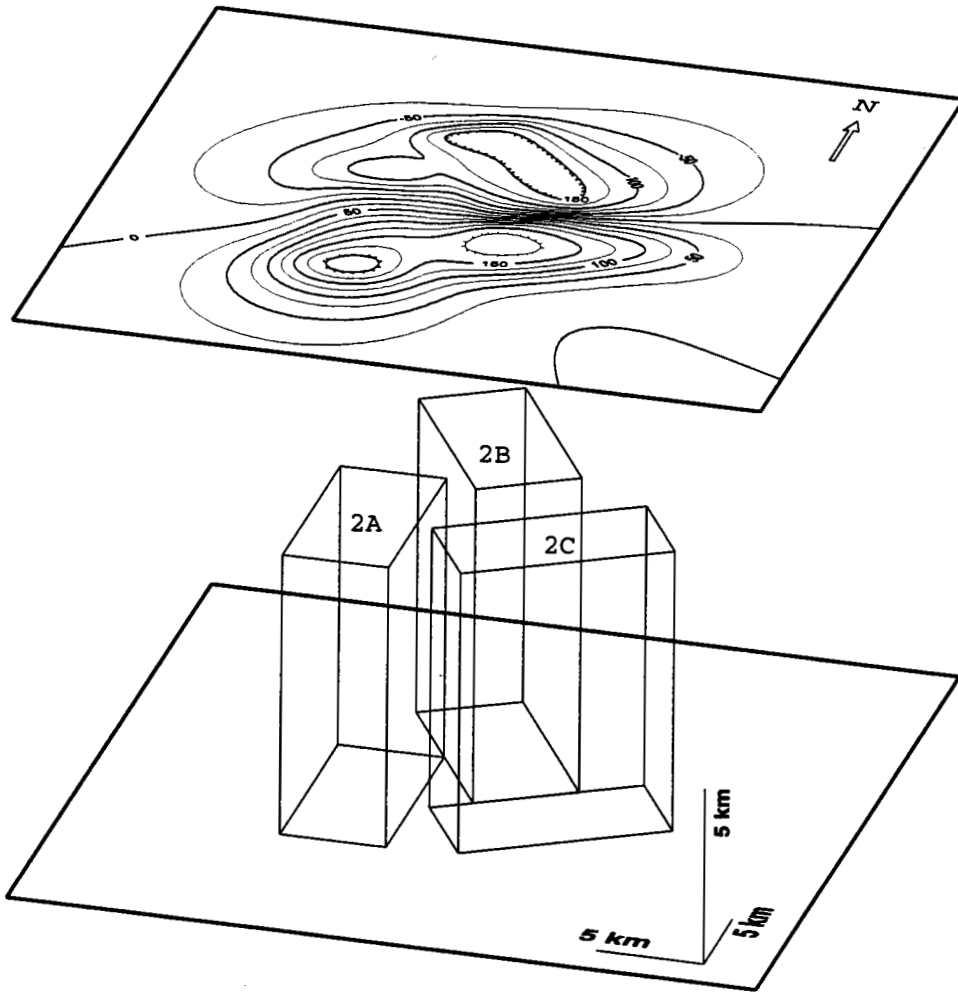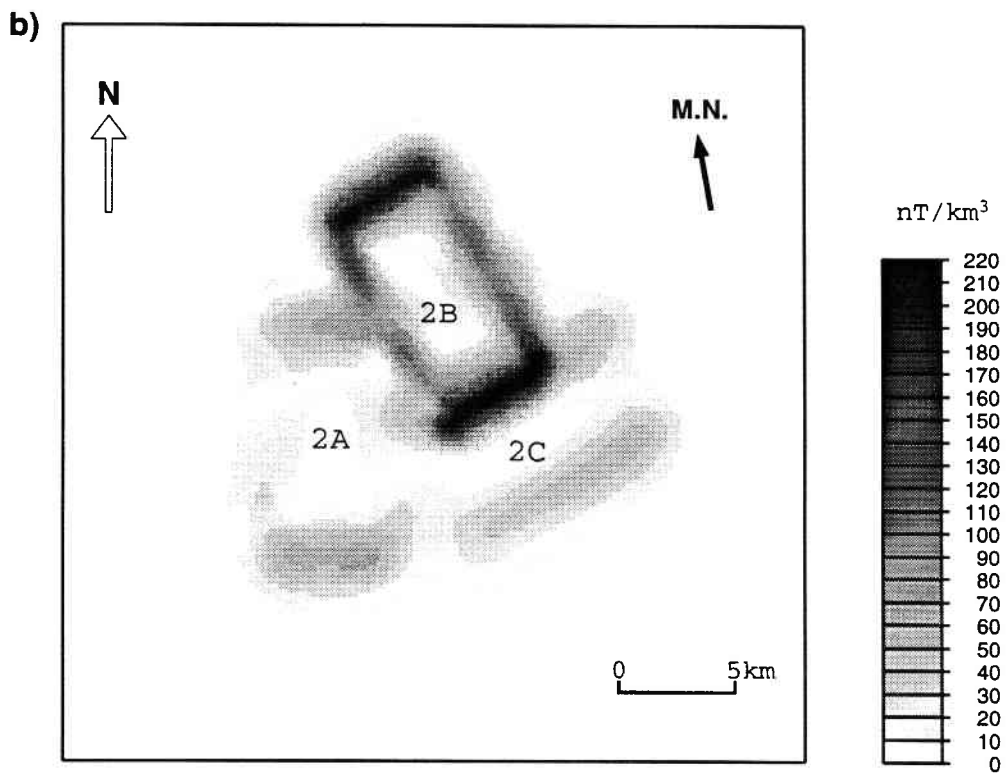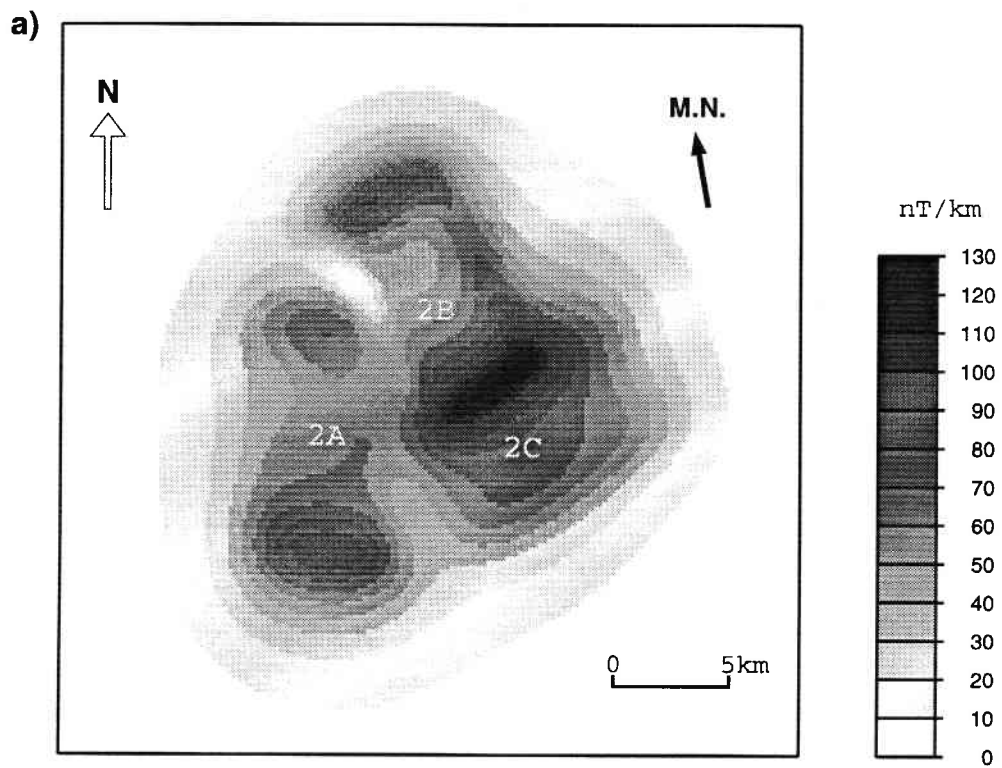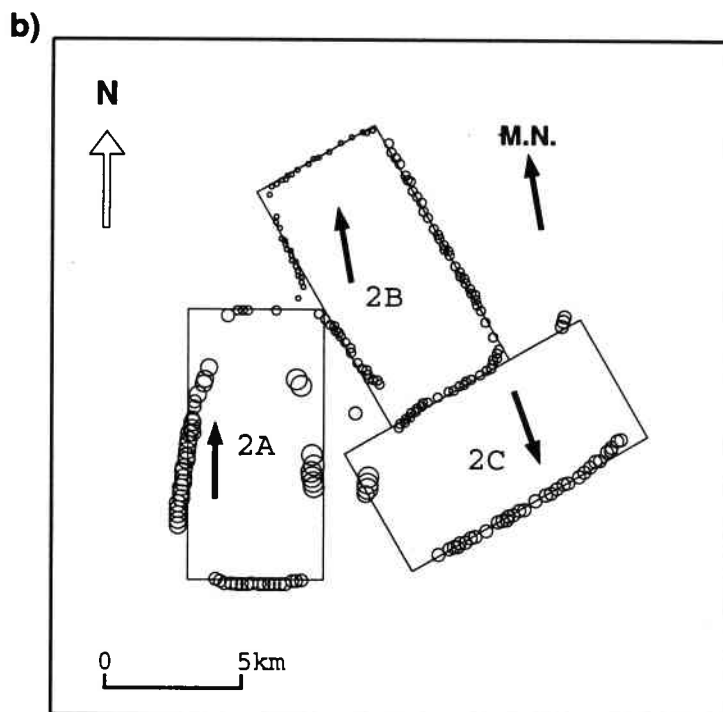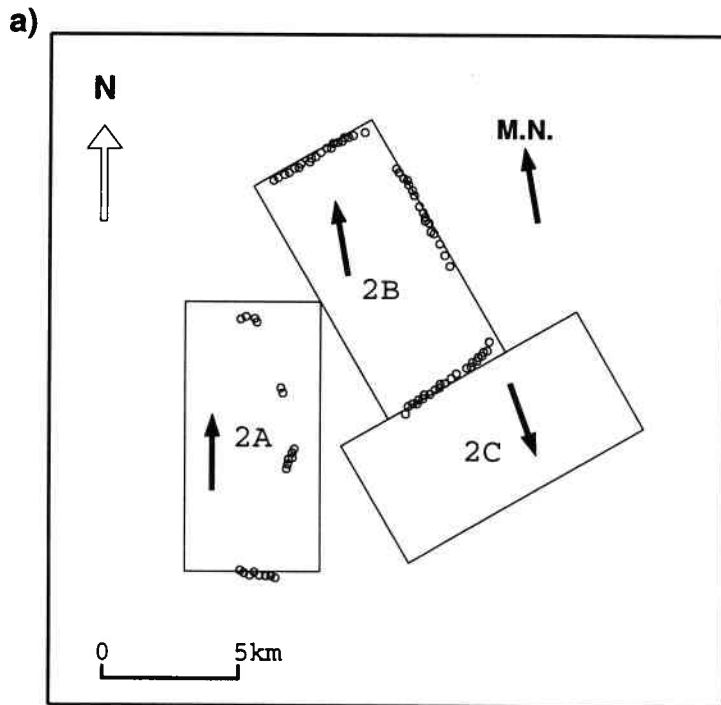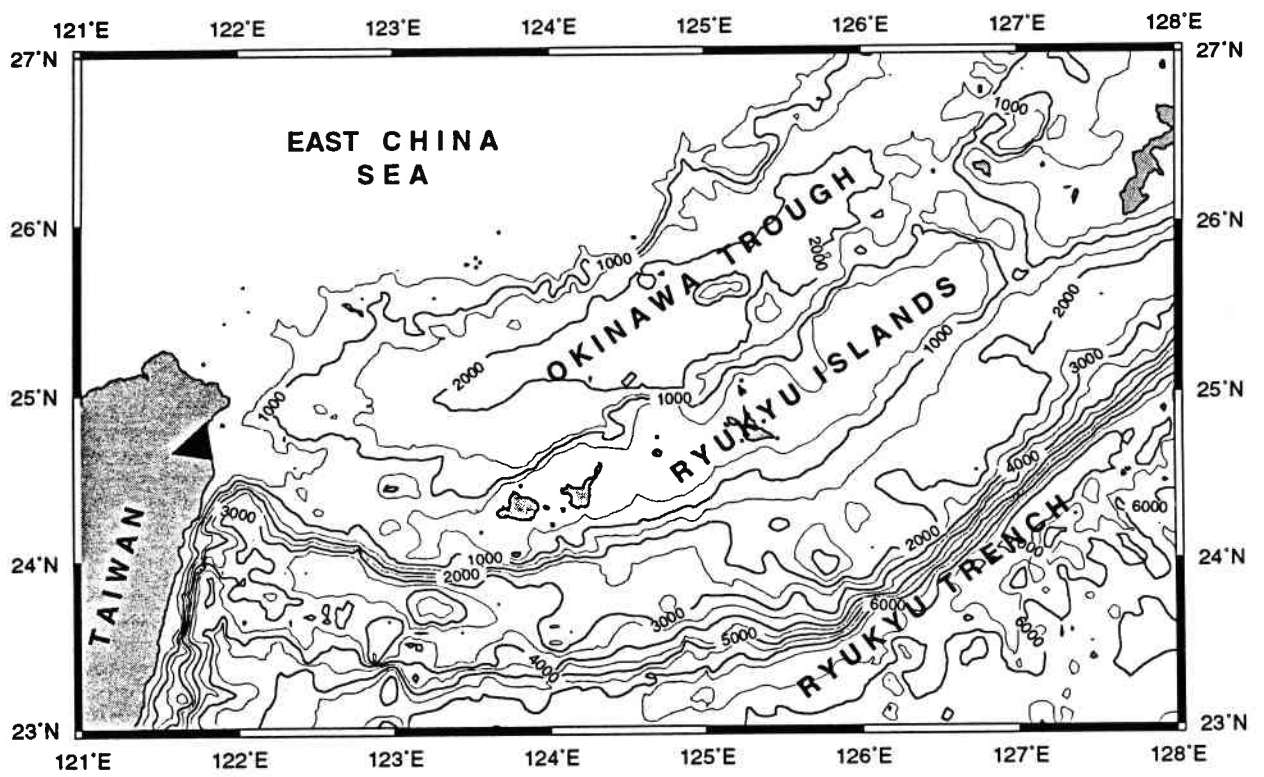
figure 5

figure 6

figure 7

figure 8a

b)

N 24°50'

N 24°35'

E 121°30'

E 121°55'

N

Ilan

nT/km³
660
630
600
570
540
510
480
450
420
390
360
330
300
270
240
210
180
150
120
90
60
30
0

0   5 km

figure 8b

c)

N 24°50'

N 24°35'

E 121°30'   E 121°55'

Ilan

2.0 - 2.5 km

1.5 - 2.0 km

1.0 - 1.5 km

0.5 - 1.0 km

0   5 km

figure 8c

Taipei

N 24°50'

N 24°35'

E 121°30'

E 121°55'

Kueishan Tao

Ilan

N

1
2
3
4
5
6
7
8
9
10

Thrust Faults

Faults

0   10km

Syncline Axis
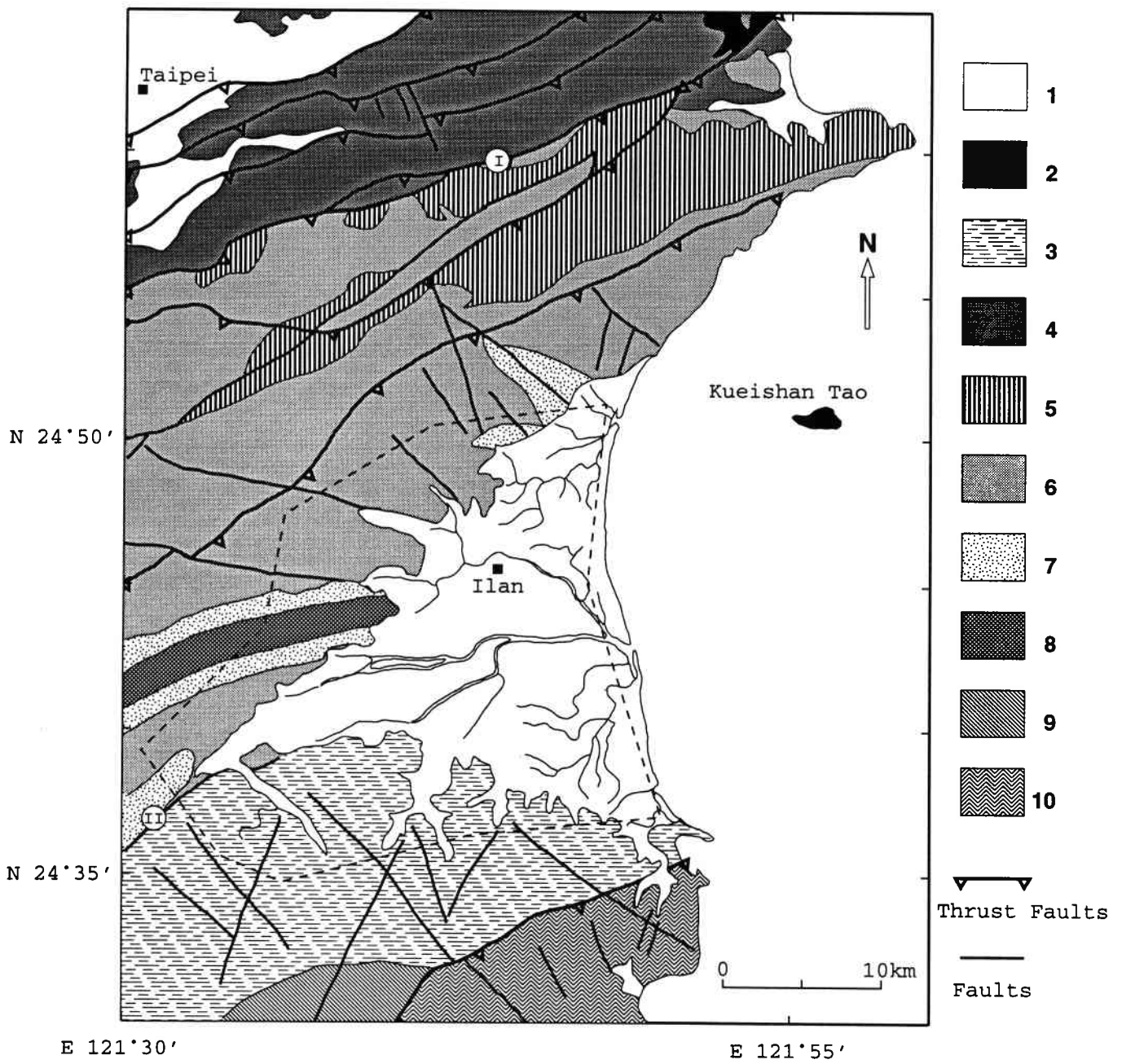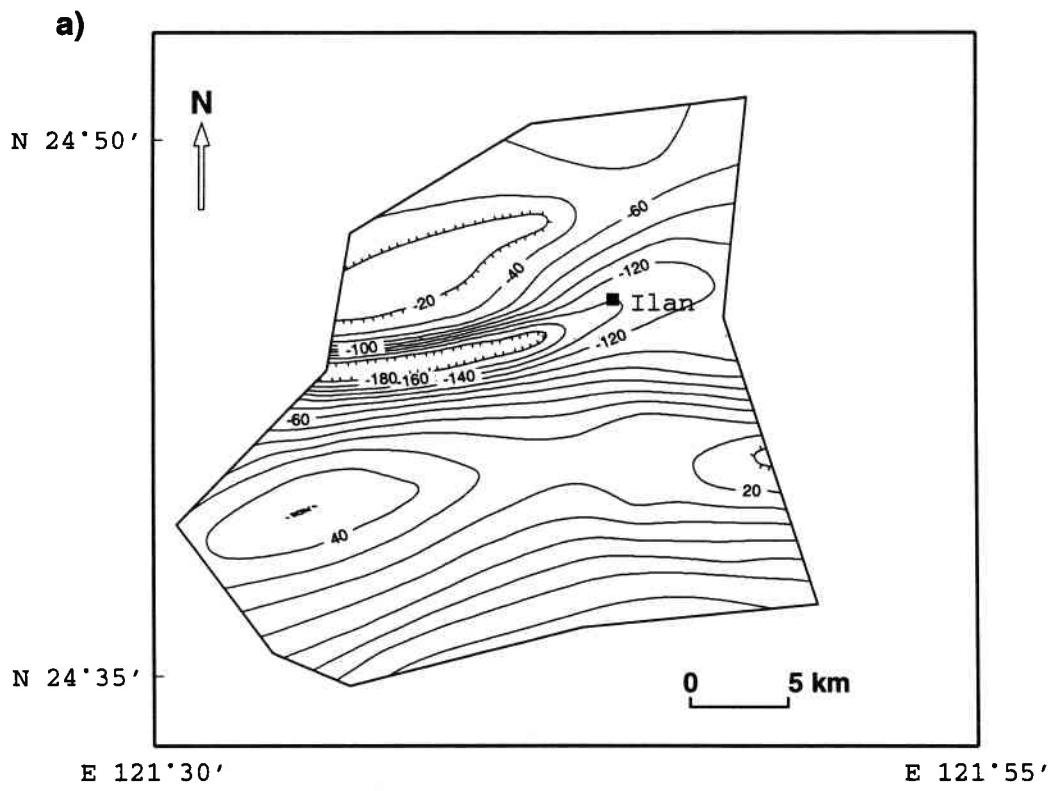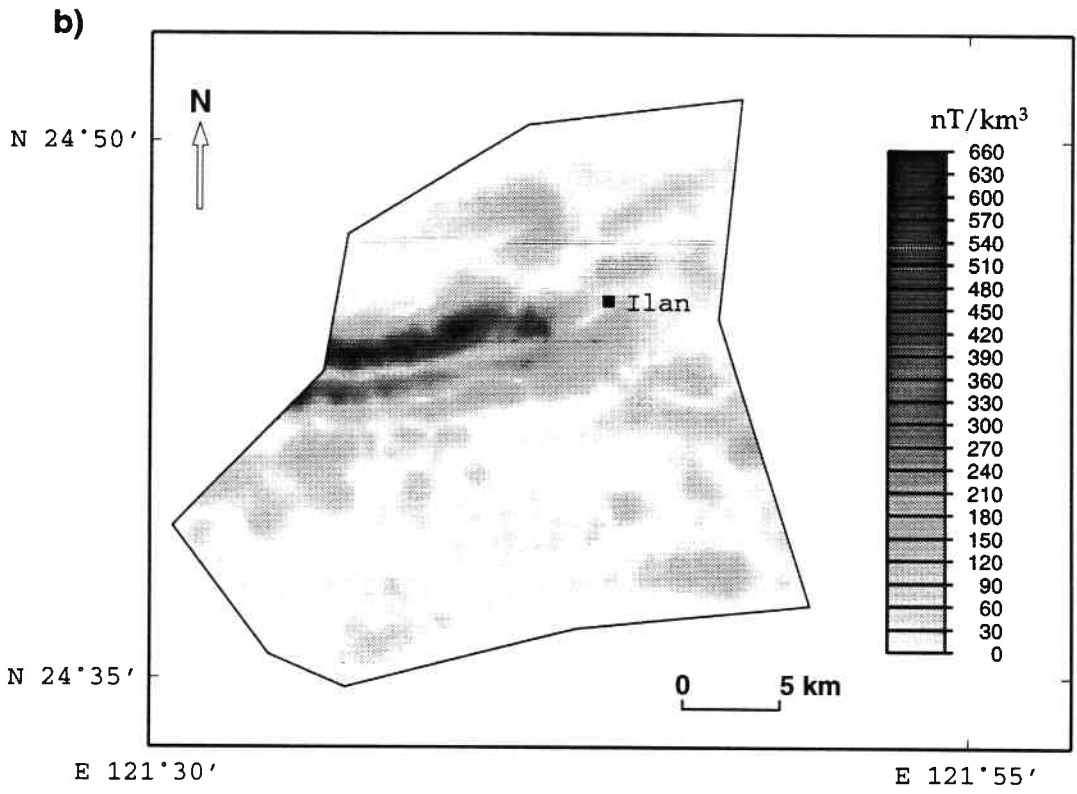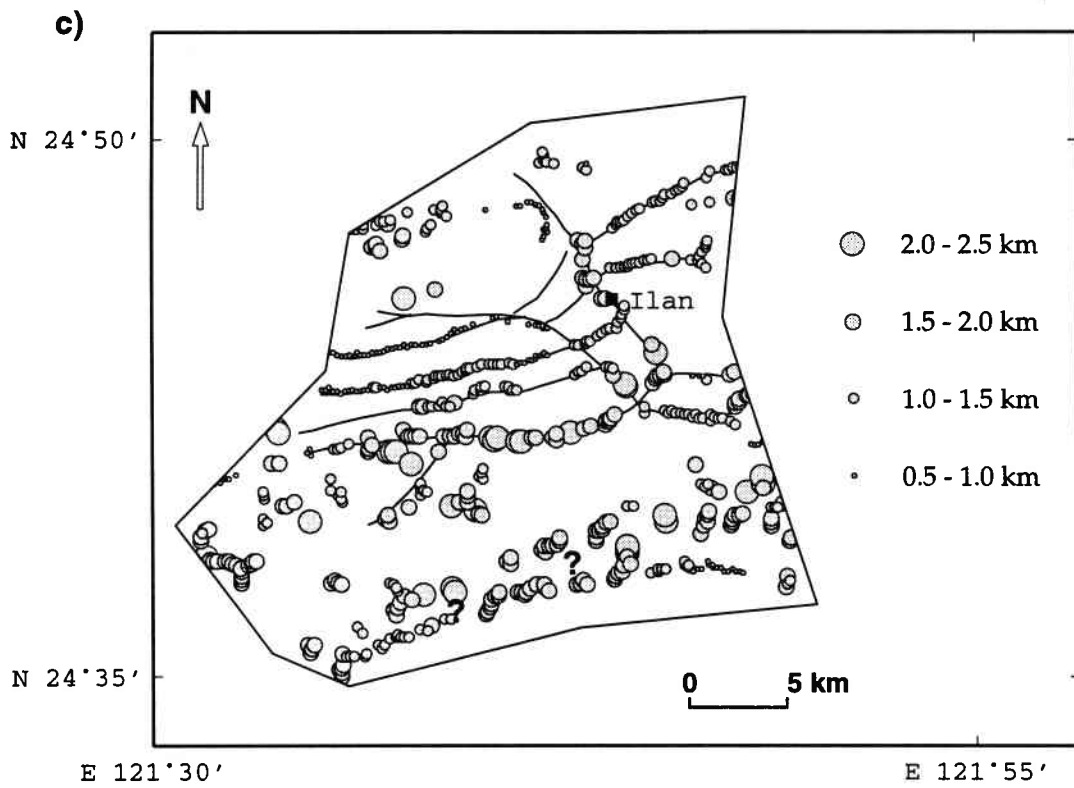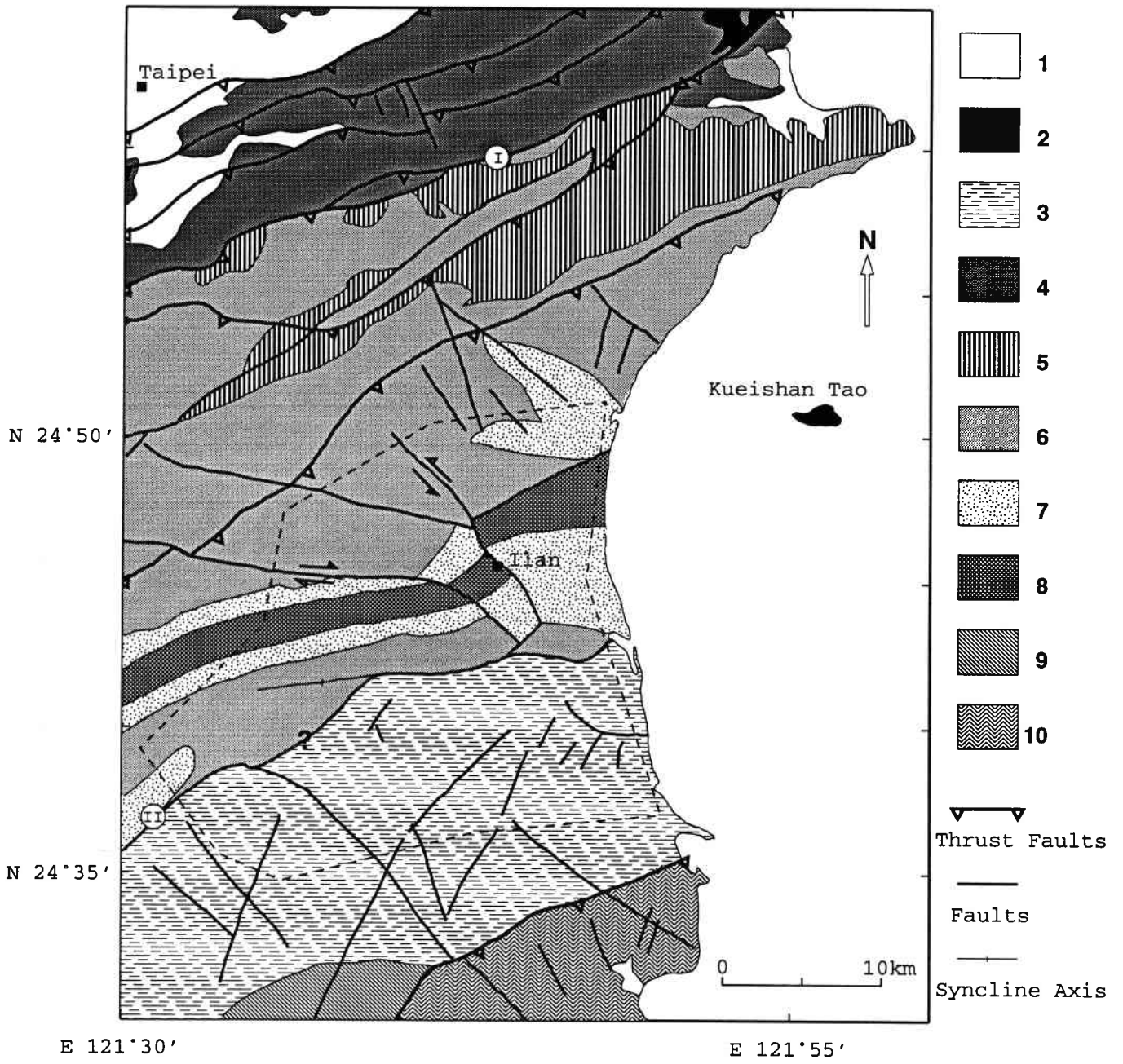
figure 9

Structural and kinematic evolution of the Okinawa trough backarc basin

A partir des données bathymétriques multi-faicseaux, l'identification des orientations de nombreuses failles normales dans le bassin d'Okinawa est effectuée. Basées sur la théorie du cisaillement pur, trois phases sont proposées pour expliquer l'évolution du bassin d'Okinawa. Les analyses des données gravimétriques et des profils sismiques effectuées dans le nord et le sud du bassin d'Okinawa montrent que l'extension au sud est légèrement plus élevée qu'au nord.

Structural and Kinematic Evolutions of the Okinawa Trough Backarc Basin

Jean-Claude Sibuet, Shu-Kun Hsu, Chuen-Tien Shyu, and Char-Shine Liu

ABSTRACT

Refraction data acquired in the Okinawa Trough show that the crust is of continental origin and that its thickness increases from 10 km in the southern Okinawa Trough to 30 km in the northern Okinawa Trough. The Okinawa Trough is still in a rifting stage. In the southern Okinawa Trough, magnetic anomalies are linked either to limited arc volcanic intrusions located on the northern side of the Ryukyu arc, to the axis of the main depressions where basaltic intrusions with volcanic arc affinities are present, or to volcanic products lying at different depths within the thinned continental crust. A link among partial melting occurring just above the Benioff zone, ascent of volcanic products through extended continental crust, and the amount of crustal extension are proposed. We also suggest that both arc and backarc basin volcanism are derived from the same source located above the Benioff zone. Melt preferentially rises through the fissures and faults created by extension in the continental crust. The total amount of extension across the Okinawa Trough has been estimated from refraction and gravity data. It decreases slightly from 80 km in the southern Okinawa Trough to 74 km in the northern Okinawa Trough. Parameters of rotation have been established for the entire opening of the Okinawa Trough and for the three phases of extension already identified: (1) The late Pleistocene to Recent phase of extension is characterized by normal faults with vertical offsets of a few meters changing progressively in direction along the Okinawa Trough. The amount of extension is about 5 km in the middle Okinawa Trough. (2) The early Pleistocene phase of extension is characterized by large tilted blocks which affect late Pliocene–early Pleistocene sediments. Directions of these normal faults change progressively along the Okinawa Trough. Extension in the northern Okinawa Trough is estimated as 25 km. The difference in azimuth of the normal faults for these two tectonic phases increases toward the northern Okinawa Trough. (3) The early Miocene phase of extension is poorly characterized from geological data but has been

Jean-Claude Sibuet and *Shu-Kun Hsu* • IFREMER, Centre de Brest, 29280 Plouzané, France. *Chuen-Tien Shyu* and *Char-Shine Liu* • Institute of Oceanography, National Taiwan University, Taipei, Taiwan, Republic of China.

343

calculated from parameters of other rotations. The corresponding pole of rotation is located 1500 km northeast of Kyushu; 50 km of extension in the northern Okinawa Trough and 75 km in the southern Okinawa Trough are expected. The proposed kinematic evolution of the Okinawa Trough differs considerably from the previous reconstructions and raises numerous questions, as for example, the interpretation of paleomagnetic measurements obtained in the southeastern Ryukyu Islands. The bending of the Okinawa Trough developed since the onset of the backarc basin extension, except for the southwestern portion of the Okinawa platelet whose pronounced bending is due to the collision in Taiwan.

1. INTRODUCTION

The island of Taiwan is located at the junction between the East China Sea continental margin and the Luzon arc (Fig. 9.1). East of Taiwan, the Okinawa Trough (OT) is linked to the subduction of the Philippine Sea plate beneath the Eurasian plate. South of Taiwan, the South China Sea on the Eurasia plate is subducted beneath the Luzon arc, which belongs to
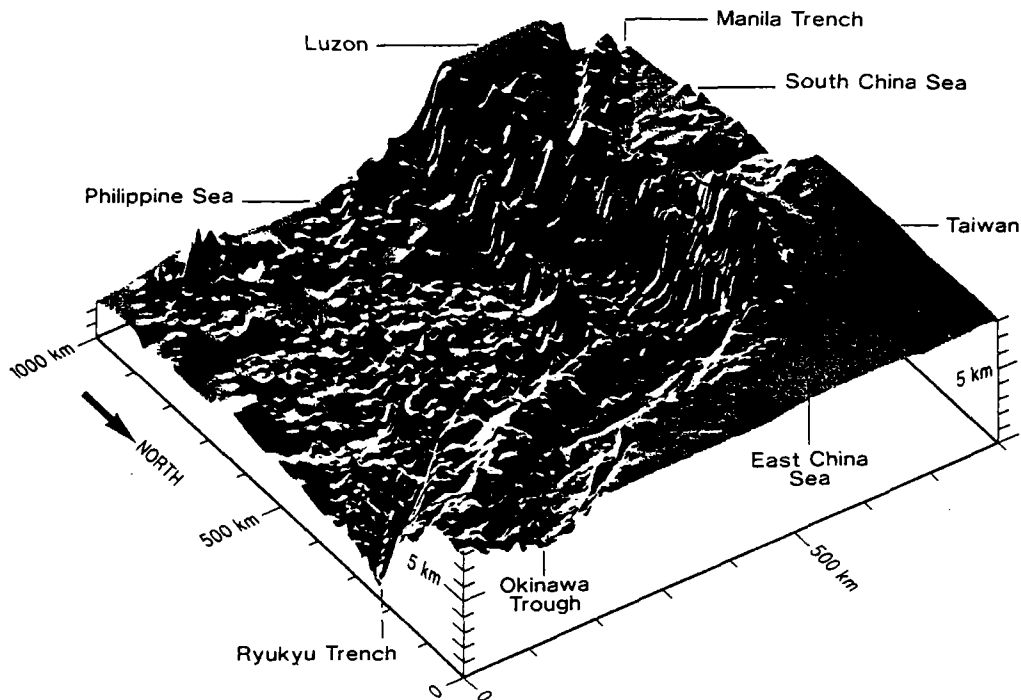
FIGURE 9.1. Block diagram of the deep ocean around Taiwan. Bathymetric data have been collected by numerous institutions and are available through the National Geographic Data Center (NGDC). Complementary data acquired east and south of Taiwan have been made available by the Institute of Oceanography of National Taiwan University. After cleaning and crossover adjustments (Hsu, in press), data have been gridded and represented with the GMT software package (Wessel and Smith, 1991). The viewing angle is chosen in order to image the southern Okinawa Trough and its relationship with the Ryukyu subduction zone but also the transfer of the convergent motion from the Manila Trench to the collision in Taiwan. South of Taiwan, the Philippine Sea plate overrides the Eurasian plate, whereas northeast of Taiwan, the Eurasian plate overrides the Philippine Sea plate. Shading from the south (azimuth 190°).

the Philippine Sea plate. The main convergent motion is thus transferred from the Manila Trench to the collision in Taiwan. In other words, south of Taiwan, the Philippine Sea plate overrides the Eurasian plate, whereas northeast of Taiwan the Eurasian plate overrides the Philippine Sea plate.

The Okinawa Trough is a curved backarc basin convex to the southeast and located behind the Ryukyu Trench and Ryukyu Islands (Fig. 9.2). It extends from the Ilan Plain in northern Taiwan to Kyushu Island in southern Japan. Its width increases from 100 km in the south to more than 200 km in the north, and its curvature is mainly restricted to the south. It abuts the narrow parallel curved belts of Taiwan, which are convex to the northwest over approximately the same distance. Several authors have suggested that the bending of the OT was due to the collision and the following indentation of the Philippine Sea plate within the Eurasian plate (Jarrard and Sasajima, 1980; Letouzey and Kimura, 1986), the indenter being the undeformed Luzon volcanic arc, located on the northwestern border of the Philippine Sea plate, against the continental part of the Eurasian plate.
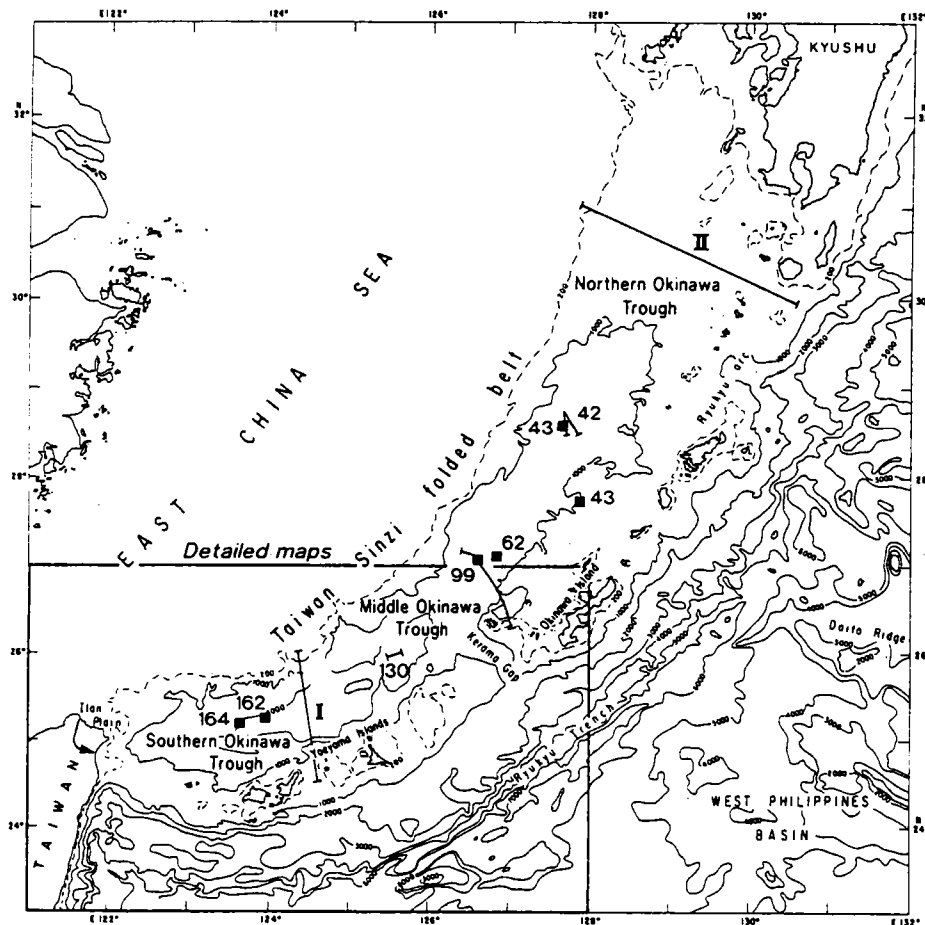
FIGURE 9.2. Map of the Okinawa Trough, Ryukyu arc, and surrounding areas with location of seismic, 3.5-kHz, and Sea Beam profiles shown in this study. Black squares represent Sea Beam detailed maps shown in this study with the corresponding profile numbers.

The purpose of this chapter is to determine the direction of normal faults that accommodate the different phases of extension along the OT, to determine if tensional features are inherited from previous tensional phases, to evaluate the amount of extension associated with each tensional phase, and to propose a coherent kinematic evolution of the OT. We will try to establish if the pronounced bending of the southern OT occurs during the formation of the backarc basin or if it is an inherited curvature since the initiation of the OT. Basic data used in this chapter are detailed swath bathymetyric data, single-channel seismic and 3.5-kHz data, and new compilations of all available bathymetric and magnetic data acquired east of Taiwan.

2. TECTONIC SETTING OF THE OKINAWA TROUGH

The OT formed by extension within the continental lithosphere, as first suggested by Uyeda (1977). The first rifting phase is dated middle to late Miocene and is associated with a broad uplift of the continental Ryukyu nonvolcanic arc and Taiwan–Sinzi folded belt, followed by normal faulting and subsidence (Sun, 1981; Letouzey and Kimura, 1986). This continental rifting phase (Table I) occurred after a major change in the direction of the Philippine Sea plate moving relative to the Eurasia plate in early Miocene (Le Pichon *et al.*, 1985). After 5 m.y. cessation of tectonic activity (Kimura, 1985), the second rifting phase (Table I), which is thought to be much more important than the previous one and resulted in the main formation of the OT, started about 2 m.y. ago at the Plio–Pleistocene boundary. The initiation of this phase is associated with the recent uplift of the Ryukyu arc at the Plio–Pleistocene boundary (Ujiie, 1980). Based on seismic correlations with drilling stratigraphy (Tsuburaya and Sato, 1985), an upper Pleistocene phase of extension, called the third phase of extension but much less developed than the lower Pleistocene phase, has been identified (Furukawa *et al.*, 1991b). This third phase of extension very probably extends to Recent times, as it is clearly expressed within the sediments deposited since late Pleistocene as normal faults characterized by small vertical offsets (Sibuet *et al.*, 1987). Consequently, the Okinawa backarc basin was formed through at least three tectonic phases (Table I) that occurred within a relatively short period of time. To explain the occurrence of closely consecutive tectonic phases in backarc basins, Sibuet *et al.* (1987) suggested that very slight changes in the subduction parameters (such as convergence rate, angle of convergence, angle of the Benioff zone) would induce major tectonic change in the backarc basin evolution.

2.1. Northern Okinawa Trough

The northern OT is considered to be in a rifting stage as revealed by refraction experiments of Ludwig *et al.* (1973), Kasahara *et al.* (1985), and Iwasaki *et al.* (1990). From a 190-km-long profile shot from Kyushu Island along the axis of the trough, Iwasaki *et al.* (1990) demonstrated that the velocity structure is characteristic of continental crust and that the Moho shallows toward the southwest from 27 to 30 km below the continental Kyushu Island to about 23–24 km at the SW end of the profile, where the trough is 1,000 m deep. Independently, Sibuet *et al.* (1987) showed that the thick sedimentary cover of the northern OT results from a massive supply of sediments from the Yangtze and Yellow rivers and was affected by tensional processes. Normal faults 120 to 150 km long and trending N040° to N060° limit tilted fault blocks to about 10 to 30 km wide. These faults related to the second tectonic phase and were active in late Pliocene–early Pleistocene

TABLE I

Main Phases of Extension in the Okinawa Trough

Age (m.y.)	Period	OT main tensional phases	Normal faults in the OT			
			Southern OT (25°N; 124.5°E)		Northern OT (29.5°N; 128.5°E)	
			Mean direction[a]	Amount of extension[b]	Mean direction[a]	Amount of extension[b]
0.01	Holocene (Recent)	3rd phase	90° ± 10°	5 km	74° ± 15°	6 km
0.7	Upper Pleistocene	2nd phase	80° ± 10°	8 km	55° ± 15°	25 km
1.7	Lower Pleistocene					
5	Pliocene	Cessation of tectonic activity				
12	Upper Miocene	1st phase	54° (calculated)	75 km (calculated)	58° (calculated)	57 km (calculated)
17	Middle Miocene					
	Lower Miocene					

[a]The mean directions of normal faults are extracted from Figs. 9.18a and b.
[b]The amounts of extension is computed from parameters of rotation (Table II).

(Fig. 9.3). Onlapping Pleistocene sediments partially filled half-grabens but are, in turn, normally faulted by the present-day third phase of extension. This phase of extension is characterized by faults of a different strike, which is about 25° clockwise from the previous trends. However, most of the deformation occurs during the early Pleistocene. All the early Pleistocene tilted fault blocks and half-grabens are arranged in a right-lateral en echelon pattern without evidence of transform motion between blocks, which suggests that the amount of extension varies along the blocks. However, the amount of total extension is approximately the same when local extensions are summed up perpendicularly to the OT over several en echelon tilted blocks (Sibuet et al., 1987).

2.2. Southern Okinawa Trough

The southern OT located SW of Okinawa Island, consists of a broad flat basin with over 2 km of sediments which were deposited mostly at a very high deposition rate in the
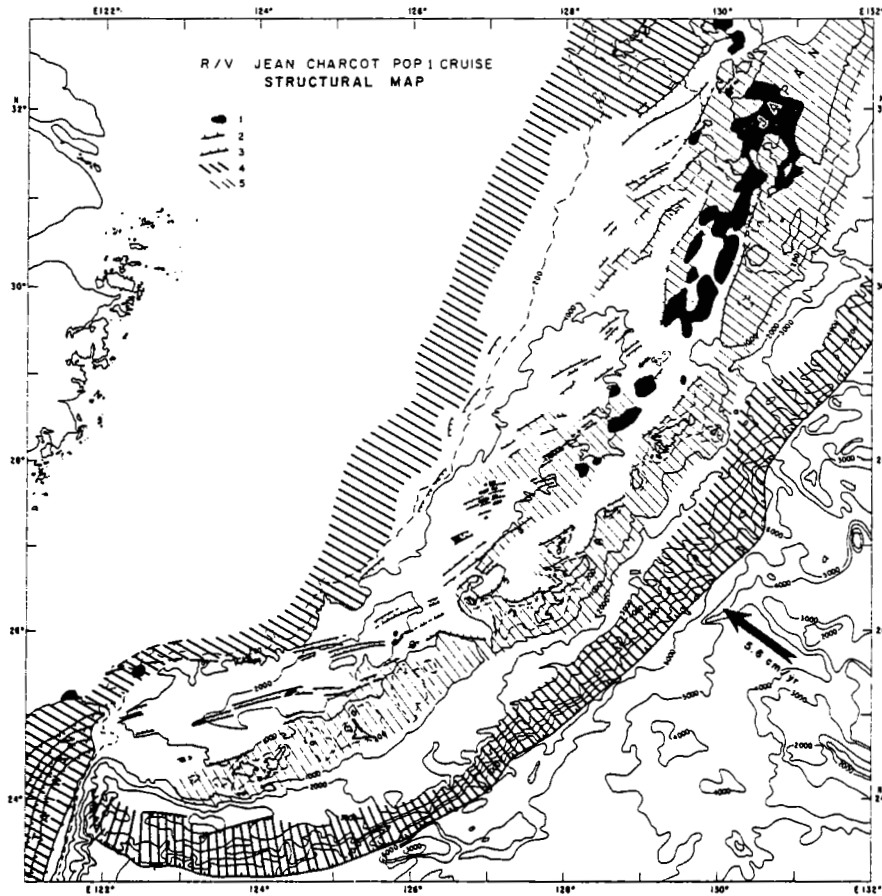
FIGURE 9.3. Geological and structural map of the Okinawa Trough from Sibuet *et al.* (1987): 1, present-day arc volcanism; 2, trench axis; 3, normal faults; 4, trench slopes and accretionary complex; 5, structural highs.

last 0.5 m.y. (Hilde *et al.*, 1984; Kimura, 1985). The trough ends at the eastern termination of the Ilan Plain right above the abrupt end of the Ryukyu Benioff zone defined by the associated cloud of deep earthquakes (Tsai, 1986). Based on the interpretation of multi-channel seismic (MCS) lines, Kimura (1985) suggested that most of the Okinawa depression (at least a band 80 km wide) was of oceanic origin. This was first questioned by Sibuet *et al.* (1987), who demonstrated that the backarc spreading phase only started very recently, as shown by the presence of en echelon and, in some cases, overlapping depressions oriented N070°–N080° with the presence of a few intruded volcanics (Fig. 9.3). During this period, extension and subsidence were recorded both within the whole sedimentary column by the downward curvature of seismic reflectors toward the center of elongated bathymetric depressions and within the depressions by normal faulting and intrusion of volcanics (Sibuet *et al.*, 1987). Magnetic anomalies up to 300 nT (Furukawa *et al.*, 1991a) are associated with these volcanic ridges, where vesicular basalts have been photographed and dredged. Sibuet *et al.* (1987) restricted the width of the oceanic part to a maximum of 20 km on each side of the axial depressions, and even suggest that the oceanic domain could have

been limited only to the volcanic ridges themselves. In 1988, a refraction seismic experiment with a deployment of 18 ocean bottom seismometers was conducted across the southern OT from the East China shelf to the Ryukyu nonvolcanic arc at about 124.5°E longitude (Hirata et al., 1991; profile I, Fig. 9.2). In the central part of the trough, the Moho is at least 18 km below the sea surface. Even if the Moho cannot be followed outside the trough axis, this is the first complete and comprehensive refraction data set available across the OT. As underlined by Hirata et al. (1991), the major contribution of this refraction profile is that the southern OT is still in a continental rifting stage and that the oceanic domain, if any, is limited to the volcanic ridges in the axial portion of the trough. This interpretation is confirmed by trace element analyses and isotopic ratios of basaltic samples collected during the R/V Jean Charcot POP1 cruise (October 1984) on the southern OT volcanic ridges, which show that these lavas are characteristic of arc volcanism (Sibuet et al., 1986; Boespflug, 1990). Analyses results are similar to those performed on samples of the Ryukyu arc (e.g., the Iizuma arc volcano in Japan; Ishizaka et al., 1977) which show either that the magmatic output comes from the Benioff zone at an optimal depth for arc magmatism generation or that the arc magmatism ascends through the crustal tensional features of the backarc basin. Since the major part of the southern OT is underlain by at least 10 km of continental crust, the southern OT is still in the stage of incipient rifting of a backarc basin with an incomplete thinning of the continental crust.

2.3. Middle Okinawa Trough

This system of backarc volcanic ridges of the southern OT ends in the middle OT, close to Okinawa Island where a series of parallel basaltic ridges oriented N075° (Fig. 9.3) associated with linear magnetic anomalies have been identified (Sibuet et al., 1987). These magnetic anomalies could be interpreted either in terms of dike intrusions or emplacement of early oceanic crust (Davagnier et al., 1987). This specific area represents the transition between the thinned continental crust and the first signs of possible backarc basin oceanic crust but also the transition from present-day arc volcanism, which decreases in intensity from Japan to north of Okinawa Island, to volcanism occurring within the backarc basin itself. It has been named the volcanic arc rift migration phenomenon (VAMP) area (Sibuet et al., 1987). Refraction data collected by Nagumo et al. (1986) show that a 10-km-thick upper crust of continental origin overlies a lower crust (6.8 km/s) of unknown thickness. Consequently, the crust is still of continental origin and more than 10 km thick. Lavas and pumices were sampled during the POP1 (R/V Jean Charcot cruise, 1984), DELP-84 (Wakashio cruise, 1984), and Shinkai 2000 dives (Uyeda et al., 1985a). Dredged olivine basalts are of island-arc type (Uyeda et al., 1985a,b; Kimura et al., 1986; Sibuet et al., 1986; Boespflug, 1990) and are younger than 1 m.y. (K-Ar and fission track ages; Kimura et al., 1986). Some dredged rhyolite, dacite, and dacitic andesite indicate a bimodal volcanism. Thus, as for the basalts dredged in the southern OT, petrologic and geochemical evidences do not support the existence of a typical oceanic crust in the VAMP area and the middle OT.

In summary, the whole OT is still in a rifting stage. The minimal crustal thickness is 10 km in the deepest southern OT but increases in the northeast direction, along the axis of the trough, to attain about 30 km in southern Japan as beneath the continental shelves of the East China Sea and Ryukyu arc. On tensional continental margins, the thickness of thinned crusts could reach a few kilometers, and synrift volcanism has been currently observed (e.g., northeast Atlantic continental margins; Sibuet, 1992). Complementary continental rifting, in order to reduce the thickness of the thinned continental crust within the OT, is still

anticipated before true oceanic crust would be emplaced. Consequently, the present-day observed backarc volcanism is considered there as products of arc magmatism emplaced through the system of normal faults where thinning is maximum rather than true backarc volcanism emplaced through a fully thinned continental crust. However, in the middle OT, as basalts have been emplaced over a width of 30 km (Sibuet *et al.*, 1987), a possibility exists there that no more continental thinning would occur. In the two schematic lithospheric cross sections proposed in Fig. 9.4, we postulate that the magmatic supply has the same origin for the arc and backarc basin volcanism and is issued from approximately the same area above the Benioff zone.

3. EXTENSIONAL TECTONICS IN THE OKINAWA TROUGH

Sibuet *et al.* (1987) demonstrated that normal faults that bound the tilted fault blocks (second phase) vary in direction from N040° to N060° in the northern OT and from N075° to N090° in the southern OT, following the direction of the northward concavity of the trough, but with a systematic offset with respect to the mean direction of the OT (Fig. 9.3). This is obvious on the OT structural map of Sibuet *et al.* (1987). These authors also noticed that small normal faults affecting the Upper Pleistocene and Quaternary sediments (third phase) were oriented slightly different from the trend of main normal faults related to the previous Lower Pleistocene tectonic phase (second phase). We performed detailed analyses of all Sea Beam data acquired during the POP1 cruise in order to discriminate the two families of normal faults.
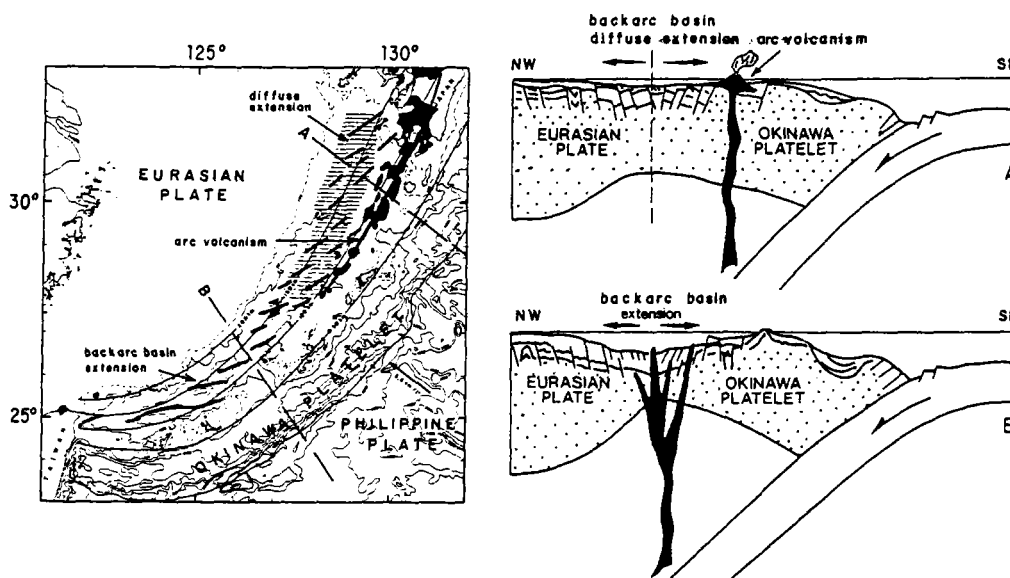
FIGURE 9.4. Map of the Okinawa Trough region showing the position of the trench, the present-day active volcanic arc, and the axes of depressions and elongated ridges of the Okinawa Trough. Depths of the Benioff zone are from Eguchi and Uyeda (1983). Cross sections of the backarc basin and forearc across the northern and southern OT are adapted from Sibuet *et al.* (1987). The magma supply has the same origin for the arc and backarc basin volcanisms and is generated from approximately the same area above the Benioff zone.

3.1. Identification of Two Families of Faults

Figures 9.5 and 9.6 show seismic profiles shot in the northern and middle OT. These profiles complement those already published (Lee et al., 1980; Kato et al., 1982; Sibuet et al., 1987) in illustrating the shallow crustal structures. Large tilted fault blocks generally 10 to 30 km wide are clearly evident on all the seismic sections.

On profiles 42 and 43 located in the northern OT (Figs. 9.5a, 9.5b), the major tilted block, which is the same on both sections, is about 10 km wide and presents a vertical offset of at least 1 km. The formation of this block is late Pliocene–early Pleistocene in age and is related to the second phase of extension. Depressions created during the second tectonic phase are almost completely filled with post–early Pleistocene sediments. A slight tectonic phase of early late Pleistocene could exist just after the deposition of the oldest infilled sediments as shown by the onlapping reflectors located over the slightly deformed deep sedimentary layer (located at 2.5 s.d.t.t. between 00H15 and 01H00 on profile 42). The late Pliocene to Recent third phase of extension is evidenced by normal faults that affect the upper part of the sedimentary section and by the small changes in the topography of the seabed (thin arrows in Fig. 9.5a). Thus, seismic data tell us that the second and third phases of extension are two different successive tectonic phases. However, no clear sign of remobilization of the large offset normal faults belonging to the second phase exists during the third phase.

In the middle OT, tilted blocks are especially well imaged from the arc platform to a distance of a few kilometers to the axis of the backarc basin (Fig. 9.6, 07H45 to 12H15 on profile 99). The 20-km large tilted block located on this profile between 08H10 and 09H30 is a textbook example. It displays all the expected conventional features for such a block formed in a tensional environment: tilting of the block over two thirds of its length without internal deformations, fast rotation of the block attested by the presence of a poorly developed V-shaped body of synrift sediments, and internal deformation of the deeper portion of the block between 08H10 and 08H40 by drag along the normal fault of the adjacent eastern block. Another large tilted block (between 10H30 and 11H30 on profile 99) displays a significant brittle deformation by drag during its tilting and subsidence. Three normal faults are observed within the southeastern half portion of the block, which allows us to reconstruct the initial shape of the block before extension. From dredged samples collected during the POP1 cruise (30°04'N; 128°31'E) and the Toka 1 oil well results (Nash, 1979), tilting occurred in late Pliocene–early Pleistocene (second phase) and has affected the whole sedimentary cover. Onlapping Upper Pleistocene to Recent sediments partly fill the depressions of the OT axial portion where subsidence is maximum (Fig. 9.6). These sediments are in turn normally faulted during the more recent phase of extension. Vertical offsets of the present-day third generation of faults are considerably smaller than those of the second generation. The recent normal faults observed on the seismic sections correspond to minor deformations of the sedimentary column between 12H20 and 14H30 and to a hummocky sea bottom between 12H00 and 12H40 on profile 99. A basaltic intrusion appears in the deepest portion of the OT where the amount of extension is maximum. Large normal faults developed during the second tectonic phase could have been reactivated, but, once again, there is no evidence for that from the available seismic data.

The 3.5-kHz records corresponding to the same portions of seismic profiles 42 and 43 shown in Fig. 9.5 much more clearly reveal normal faults that developed during the last two tectonic phases (Fig. 9.7). The vertical exaggeration of the 3.5-kHz profiles is 40. The large normal faults at 00H10 and 02H15 limit the two tilted blocks of the second generation
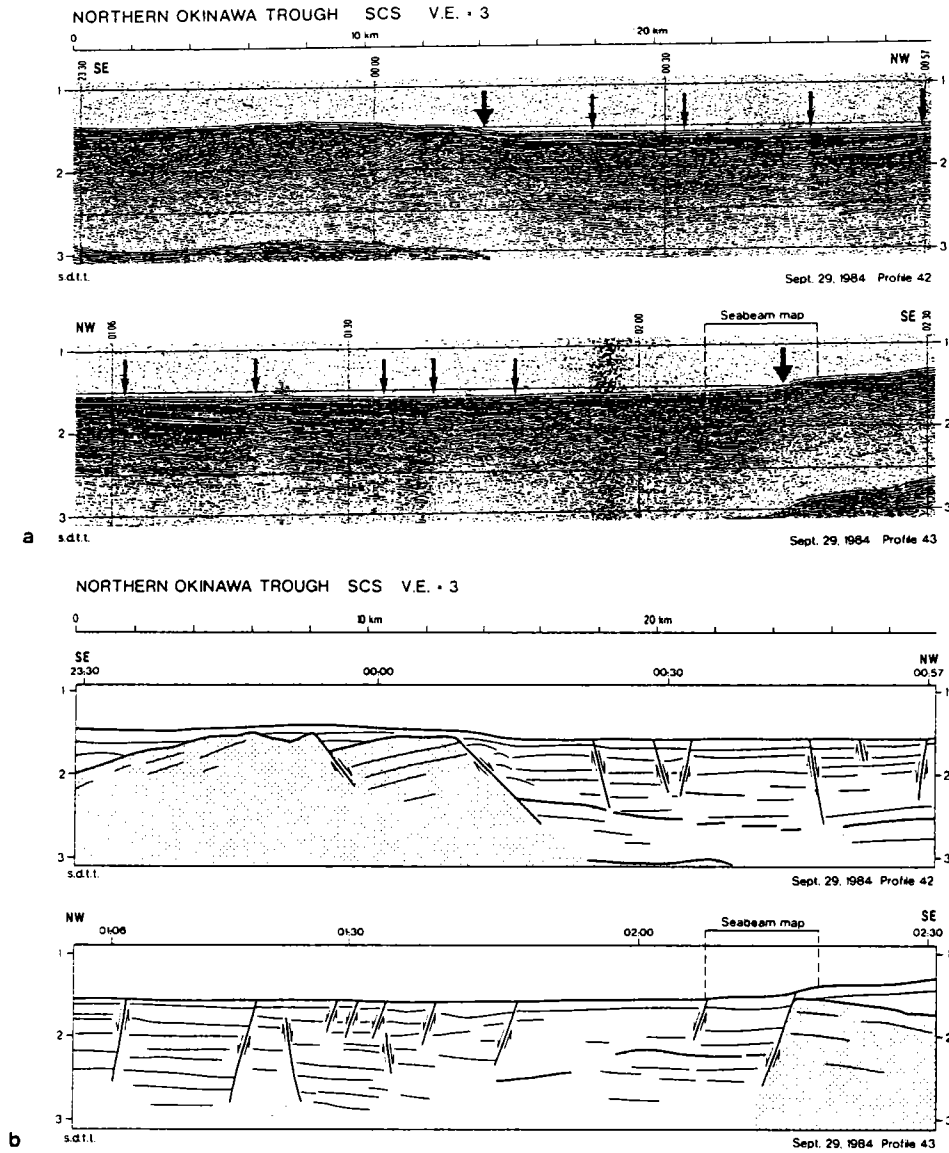
FIGURE 9.5. (a) Examples of the Plio–Pleistocene tilted fault block geometry (large arrows) and Recent normal faulting (small arrows) in the northern Okinawa Trough: IFREMER high-speed (10 knots), single-channel seismic profiles 42 and 43. Locations of profiles are shown in Fig. 9.2. (b) Structural interpretation of seismic profiles shown in (a). Tilted blocks formed during the second tensional phase (Table I) appear in gray. In light gray, deep sediments slightly deformed during early Pleistocene or early late Pleistocene by tensional movements assigned to the second phase of extension.
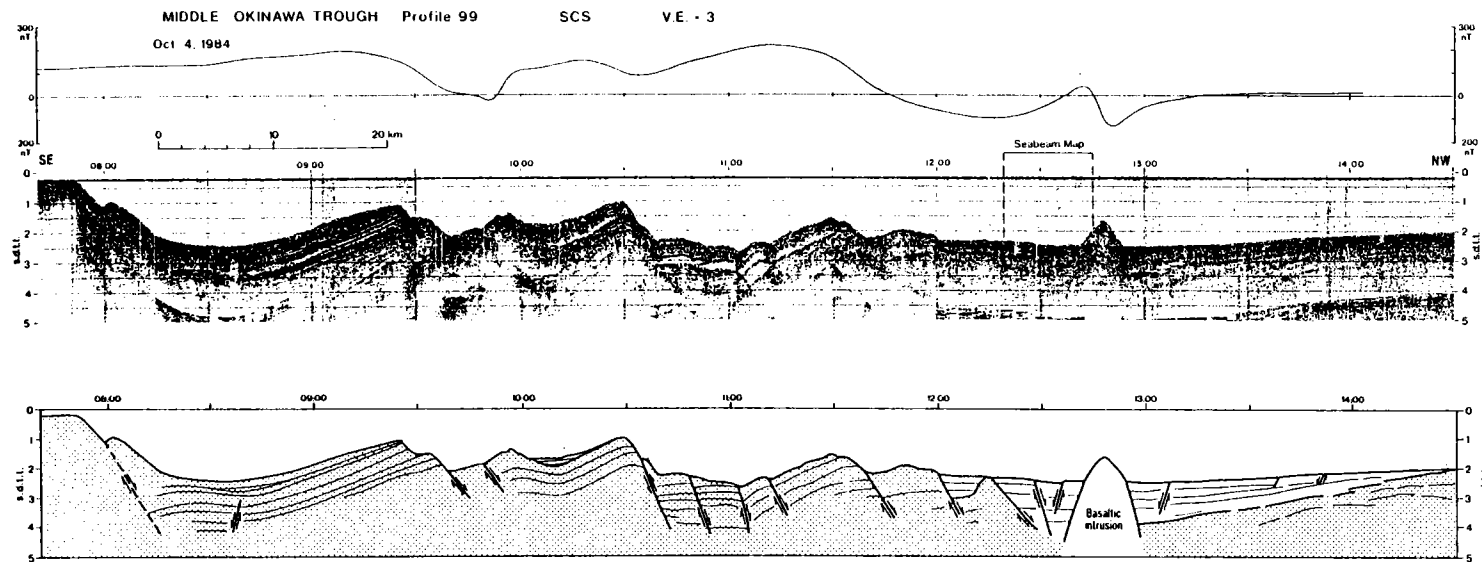
FIGURE 9.6. IFREMER high-speed (10 knots), single-channel seismic profile 99 shot in the middle Okinawa Trough from the arc platform to the axis of the trough. Location shown in Fig. 9.2. Plio-Pleistocene tilted fault blocks are especially well imaged, except in the axial part of the trough where present-day normal faults are only marked by minor deformations of sediments and seabed. A volcanic ridge associated with a 200-nT magnetic anomaly is emplaced in the axis of the depression, where subsidence is maximum. Tilted blocks formed during the second tensional phase (Table I) appear in gray in the structural interpretation of the seismic profile.

already identified in Fig. 9.5. However, between 12H20 and 14H30, numerous normal faults of the third generation, which are not imaged on the seismic sections because their topographic expression does not exceed a few meters, appear on the 3.5-kHz records as nearly vertical features. Profiles 42 and 43 differ only about 20° in azimuth with a course change at 01H03. The same normal faults appear between 01H11 and 01H20 on profile 43 and between 00H45 to 01H00 on profile 42. As profiles 42 and 43 are 2 to 3 km apart, this suggests that normal faults of the third generation present a lateral continuity of at least a few kilometers.

A section of the 3.5-kHz profile recorded in the axial part of the southern OT (Fig. 9.8, profile 130) completes the information given above. Two sedimentary units are identified: The lower folded unit corresponds to the upper part of the Pliocene sedimentary section slightly deformed by the Lower Pleistocene extension; the upper unit corresponds to onlapping Upper Pleistocene to Recent sediments and is still not much affected there by the last tectonic phase. The only evidence of recent deformation is the small bulge of Upper Pleistocene to Recent sediments which appears between 00H55 and 01H10. The recent
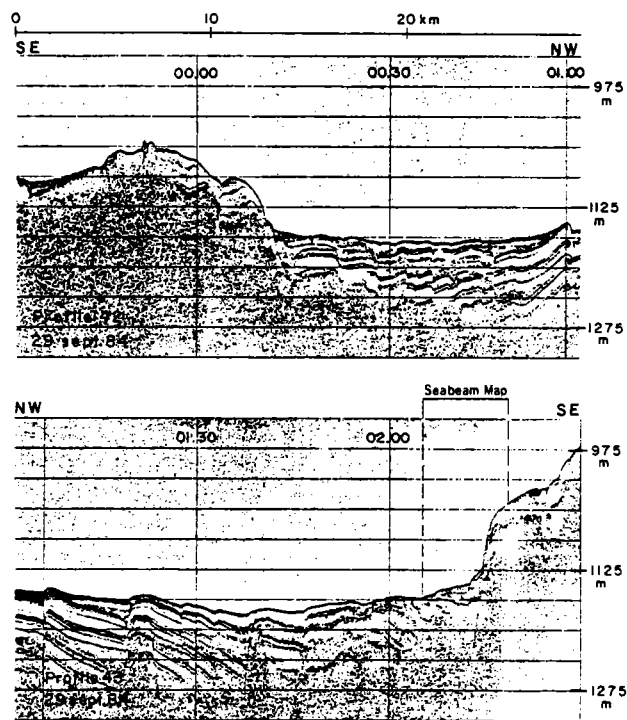
FIGURE 9.7. Portions of the 3.5-kHz profiles 42 and 43 (in northern Okinawa Trough) corresponding to the seismic sections shown in Fig. 9.5a. Location shown in Fig. 9.2. Vertical exaggeration is about 40. The Plio–Pleistocene tilted fault block is bounded by a 30-m-offset normal fault (00H10 on profile 42 and 02H15 on profile 43). Recent normal faults with a few-meter offsets affect Quaternary sediments.

FIGURE 9.8. Portion of the 3.5-kHz profile 130 (in southern Okinawa Trough) located in Fig. 9.2. Vertical exaggeration is about 40. The gently folded Plio–Pleistocene sedimentary unit is overlain by onlapping Upper Pleistocene Quaternary sediments slightly deformed between 00H55 and 01H10. The dotted line separates the two sedimentary units.
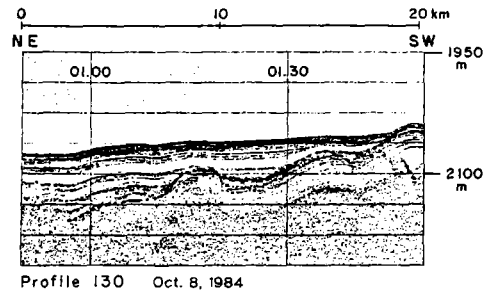
deformation seems to occur independently from the previous generation of faults and does not seem to systematically mobilize preexisting normal faults or zones of weakness.

The interpretation of seismic profiles shows that the second and third phases of extension are distinct and that normal faults belonging to each of these tensional phases could be easily differentiated.

3.2. Spatial Distribution of the Two Families of Faults

Normal faults which belong to the two fault families described previously have been identified from the POP1 3.5-kHz records, where they display a topographic offset larger than 4 m, and from the seismic profiles, where the offset is greater than 20 m. Most of the Sea Beam data acquired during this cruise have been reprocessed with a contour spacing of 2 m and displayed with an appropriate scale in order to examine the lateral extension and direction of the normal faults. The working scale is generally between 1/10,000 and 1/50,000, depending on the slope of the normal faults and on the water depth, as the width of the recorded band is about two thirds of the water depth. Examples are given in Figs. 9.9 to 9.14.

In the northern OT, swath bathymetric contours every 2 m are shown for a small section of the profile 43 (Fig. 9.9) along both the seismic and 3.5-kHz sections of Figs. 9.5 and 9.7. The lateral extension of the normal faults is at least as wide as the width of the Sea Beam band, which is 650 m. A normal fault of the second generation is oriented N052° and presents a vertical offset of 38 m. Two normal faults of the third generation are oriented N075° and present vertical offsets of 10 and 4 m. The difference in the orientation of these two different families of faults is 20° to 25° in the northern OT. The detailed Sea Beam map shown in Fig. 9.10 reveals seafloor topography along a small portion of the seismic profile 99 as shown in Fig. 9.6, located in the axial portion of the middle OT where present-day sediments are deformed by the third generation of faults. The basaltic intrusion appears in the northwest corner of the map (Fig. 9.10). Though the hummmocky character of the sea bottom is confirmed by the irregularity of bathymetric contours, the linearity of the normal faults is still expressed over a minimum of 1 km across the profile. The three normal faults and the southeastern limit of the basaltic intrusion belong to the last generation of faults. Two faults with offsets of 20 and 22 m are oriented N065°, the other two, with larger offsets, are oriented N045° (Fig. 9.10). The difference of 20° in the orientation of faults could be explained by the reactivation of faults oriented N045° which belong to the previous
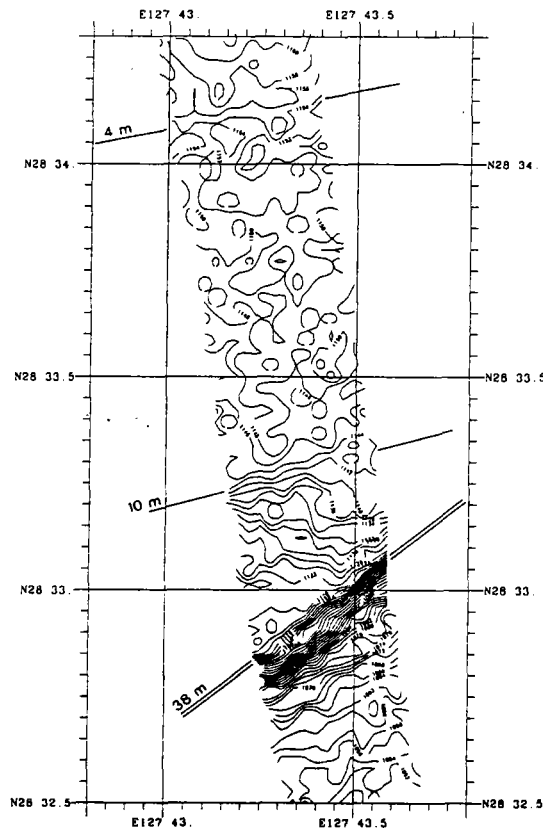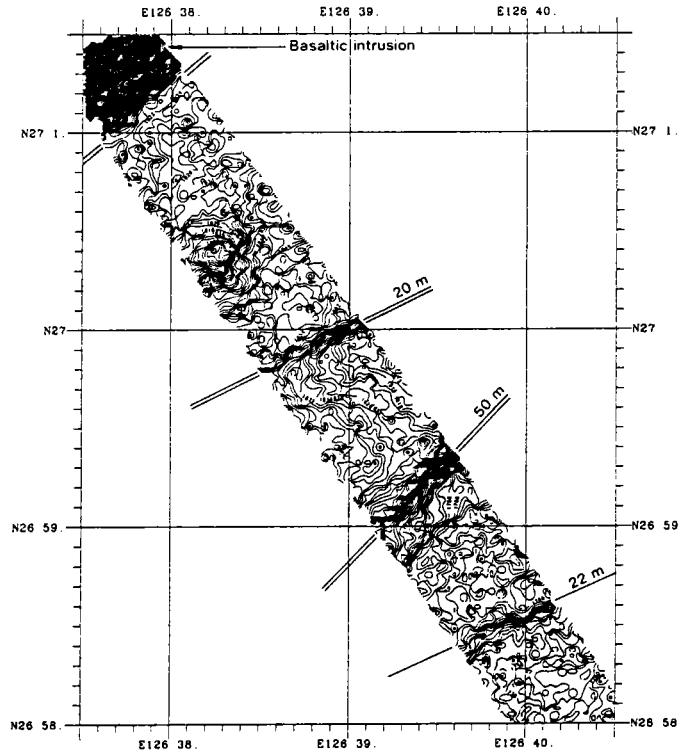
FIGURE 9.9. Sea Beam bathymetric map of a portion of profile 43 located in Figs. 9.2, 9.5, and 9.7, plotted in Mercator projection and contoured every 2 m. Directions and vertical offset values of the normal faults are also shown. The azimuths of early Pleistocene and Recent normal faults differ by 20° to 25° in the northern Okinawa Trough.

generation. Due to the massive sediment supply from the China continental shelf, deposition rates up to 4 km/m.y. have been noticed for the last 0.5 m.y. (Hilde et al., 1984; Kimura, 1985). Consequently, the subsidence at the axial portion of OT imaged on seismic profile 99 (Fig. 9.6) as well as on the swath bathymetric section (Fig. 9.10) is the expression of a significant amount of extension. A large part of the present-day extension seems to be absorbed by older faults.

Thus, the two families of faults may differ about 20° in azimuth locally. Small-offset normal faults are generally associated with the present-day phase of extension, and large-offset normal faults with the previous tectonic phase. Figures 9.11 and 9.12 (profiles 43 and 62 located in the middle OT) show that exceptions exist concerning the magnitude of offsets. On profile 62 (Fig. 9.12), a fault with 8-m offset belongs to the second generation of faults, while on profile 43 (Fig. 9.11), a fault with 30-m offset belongs to the third generation of faults.

However, in the southern OT, the two families of faults may not be differentiated (as shown in profiles 162 and 164, Figs. 9.13 and 9.14 respectively). All the hfaults, whatever is the magnitude of their vertical offsets, present strike directions which differ only by 10° to 15°. Consequently, the difference in strike azimuth between the two families of faults decreases from about 25° in the northern OT to about 20° in the middle OT and is not discernible in the southern OT.
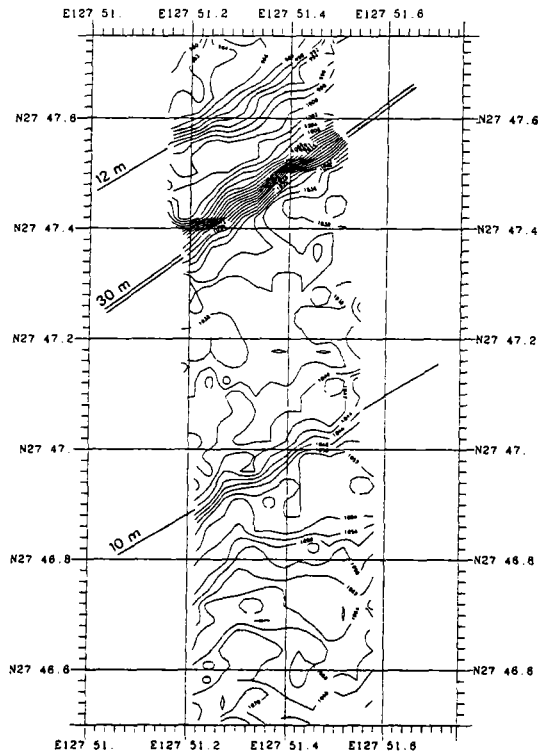
86

FIGURE 9.10. Sea Beam bathymetric map of a portion of profile 99 located in Figs. 9.2 and 9.6, plotted in Mercator projection and contoured every 2 m. Directions and vertical offset values of the normal faults are also shown. The azimuths of late Pleistocene and Recent normal faults differ by 20° in the middle Okinawa Trough. The subsidence of the axial part of the trough is due to the present-day normal faulting.

These observations have several implications. As extensional faults are well expressed in the sedimentary sections as a result of the high detritic input from mainland China, the present-day tectonic phase of extension activates again the directions of the previous phase of extension, as already known, but a new generation of faults also appears.

The new generation of faults progressively changes in azimuth along the OT, which means that these faults probably record the changes in stress regime.

In the Izu–Bonin arc, extension occurs in an intraoceanic island arc. Two families of normal faults, oriented 337° and 355°, are simultaneously active and have been identified in the 50-km-wide Sumisu rift (Taylor et al., 1991). This rift exhibits a zigzag pattern in plan view, and directions of faults are the same than those of the rift borders. Taylor et al. (1991) have shown that faults with both trends form a geometry with an orthorhombic symmetry which is consistent with theoretical models of fault formation in three-dimensional strain fields (Reches, 1983). This model predicts that the maximum strain direction is perpendicular to the bisector of the acute angle between the two fault trends. For the Sumisu rift, the extension direction is N076°. Though the difference in the directions of the two families of faults for the OT and Sumisu rift are similar (about 20°), the tectonic contexts are different: the two families are active simultaneously in an oceanic environment for the Sumisu rift
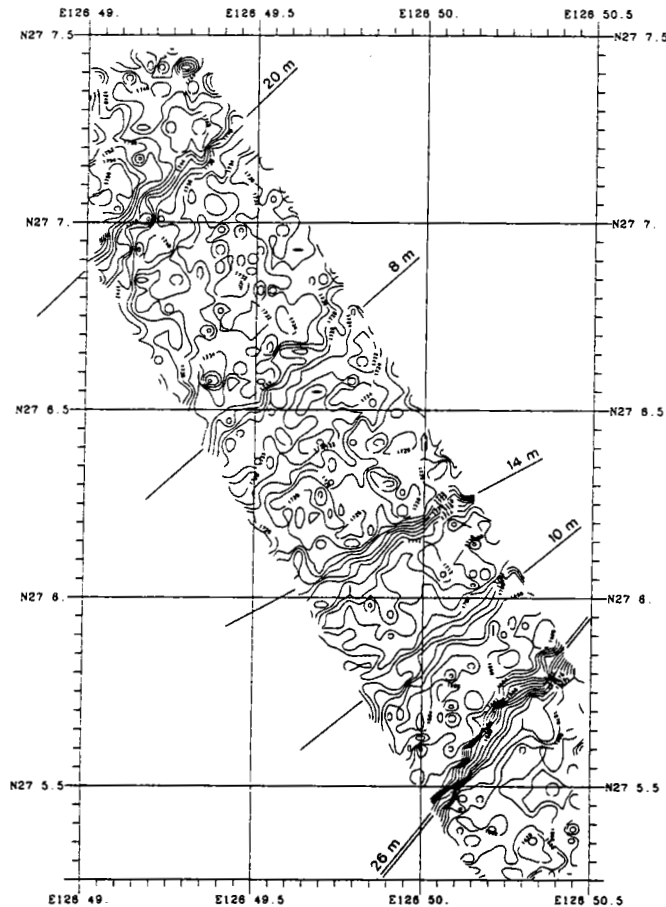
FIGURE 9.11. Sea Beam bathymetric map of a portion of profile 43 (middle Okinawa Trough) located in Fig. 9.2, plotted in Mercator projection and contoured every 2 m. Directions and vertical offset values of the normal faults are given. Small-offset normal faults are generally associated with the present-day phase of extension, but exceptions exist, as the 30-m-offset normal faults shows.

and belong to two consecutive tectonic phases in a thinned continental crust environment for the OT. Following the observations of Sibuet *et al.* (1991) in the Bay of Biscay, another explanation concerning the simultaneous presence of two families of faults in the Sumisu rift would be also possible. There, the plate boundary, which was active during the Pyrenean phase, follows previous lines of weakness as the former Bay of Biscay oceanic rift system. When the motion along the plate boundary is tensional, rift directions of the new oceanic crust are parallel to the plate boundaries and are not coincident with the stress directions given by the accurately defined position of the related pole of rotation. In the Sumisu rift, the location of the zigzag rift pattern could be also related to the presence of a previous zone of weakness such as the intraoceanic island arc. Rift directions that develop within the oceanic rift system would be parallel to the rift borders and independent of the stress directions.

3.3. Quantification of the Spatial Distribution of the Two Families of Faults

Based on the previous assumptions, a systematic study of the directions of these two families of faults has been performed. For each fault that presents a linear trend across the surveyed bathymetric swath, the following parameters are collected: latitude, longitude, vertical offset, azimuth, and dipping direction. As many as 510 measurements have been performed from southern Japan to Taiwan (Fig. 9.15). Directions of faults change from N090° east of Taiwan to N040° southwest of Kyushu (Fig. 9.15). The distribution of faults
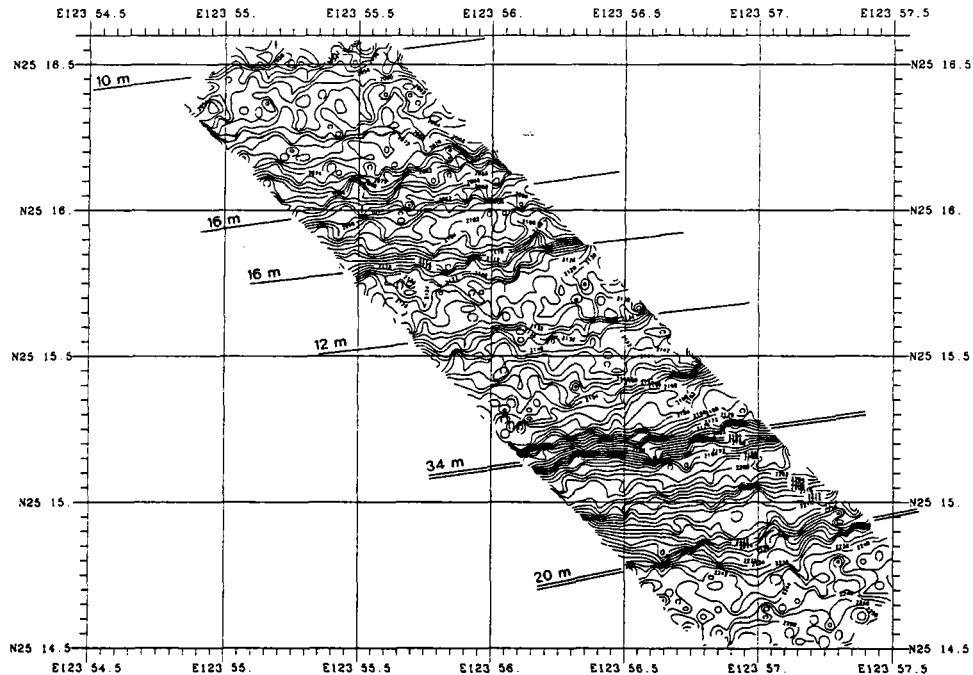
FIGURE 9.12. Sea Beam bathymetric map of a portion of profile 62 (middle Okinawa Trough) located in Fig. 9.2. plotted in Mercator projection and contoured every 2 m. Directions and vertical offset values of the normal faults are given. Large-offset normal faults are generally associated with the early Pleistocene phase of extension, but exceptions exist, as the 8-m-offset normal faults shows.

summed in 5° intervals of azimuths (Fig. 9.16) has been calculated for each of the four geographical boxes displayed in Fig. 9.15. These diagrams show that peaks of dominant fault directions change from 80–95° in box A, to 65–80° in box B, to 50–80° in box C, and to 40–80° in box D.

Figure 9.17 displays the direction of the faults as a function of the longitude. The continuous decrease of the azimuth as a function of the longitude is confirmed. The dispersion of azimuths around the mean value is ±20° at longitude 123°E (close to Taiwan) and ±30° at longitude 129°E (close to Japan). This observation confirms the existence of two families of faults that diverge in the northward direction as previously suggested.

In Fig. 9.17, the directions of the OT axis and of the trench axis are also displayed as a function of the longitude. All the directions of normal faults are located on the right-hand side of the direction of the trough axis and also preferentially on the right-hand side of the
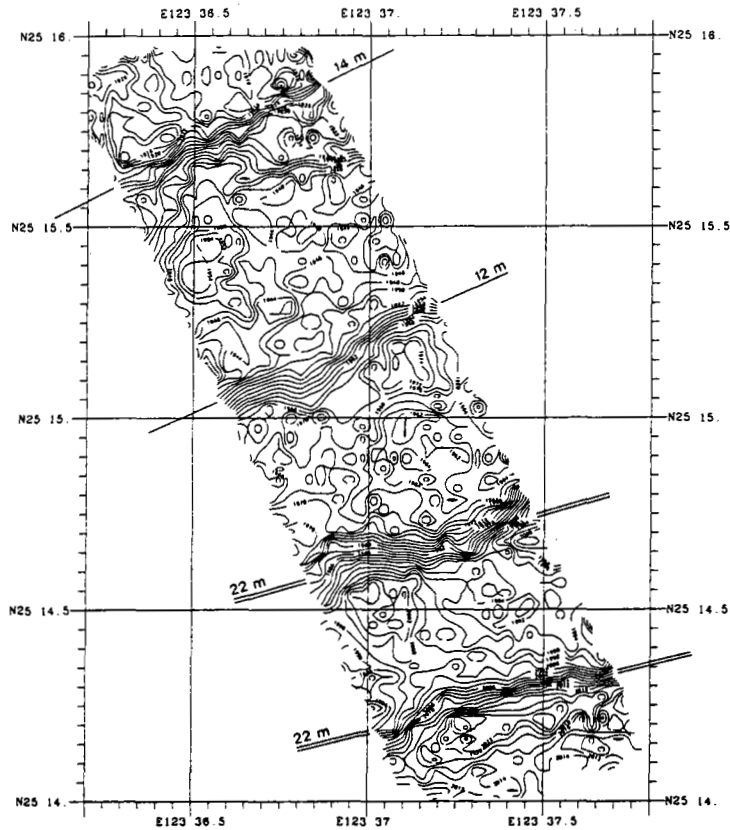
FIGURE 9.13. Sea Beam bathymetric map of a portion of profile 162 (southern Okinawa Trough) located in Fig. 9.2, plotted in Mercator projection and contoured every 2 m. Directions and vertical offset values of the normal faults are given. Normal faults belonging to the early Pleistocene and Recent phases of extension cannot be differentiated in the southern Okinawa Trough.

direction of the trench axis. This means that both the large normal faults related to Lower Pleistocene (as already noticed by Sibuet *et al.* 1987) and the late Pleistocene to Recent small offset normal faults are systematically offset with respect to the directions of the OT axis and continental slopes. The geodynamic context is different from the one of the Izu–Bonin arc and of the western Bay of Biscay in the sense that several tensional phases occur in the OT instead of a single tensional phase where rift features are parallel to the rift borders. Because the two families of normal faults belonging to the second and third phases of extension only differ by a maximum of 20° to 25° in direction, we have selected a few normal faults that clearly belong to one of the two families by using the following criteria.

Seismic data are used to identify large tilted blocks formed during the second phase of extension, bound by normal faults which present a significant vertical offset larger than a few hundred meters, and which display a significant topographic effect larger than 30 m (Fig. 9.18a).

Seismic data also unambiguously indicate Recent faults that affect the late Pleistocene to Recent sedimentary layers. Among them, we have selected normal faults characterized by small topographic vertical offsets and not related to possible deep normal faults bounding large tilted blocks formed during the second phase of extension (Fig. 9.18b).

With these specific criteria, the two families of faults are clearly discriminated. The mean direction of normal faults is estimated as a function of the longitude with an error of ±15° for faults of the second generation and ±10° for faults of the third generation (see mean direction of faults in the southern and northern OT; Table I, and in the four geographical

FIGURE 9.14. Sea Beam bathymetric map of a portion of profile 164 (southern Okinawa Trough) located in Fig. 9.2, plotted in Mercator projection and contoured every 2 m. Directions and vertical offset values of the normal faults are given. Normal faults belonging to the early Pleistocene and Recent phases of extension cannot be differentiated in the southern Okinawa Trough.

boxes; Figs. 9.15 and 9.16). The mean directions of faults related to tensional phases 2 and 3 and calculated from the selection of data shown in Fig. 9.18 correspond to the whole spectrum of directions displayed for each of the four geographical boxes (Figs. 9.15 and 9.16), except for the secondary peak, which appears in Fig. 9.18a between 60° and 75°. In fact, this peak corresponds to data collected west of 123°E (Fig. 9.15) on the northern OT continental slope, which changes trend in its southwestern termination.

Consequently, as the change of direction of faults seems to be progressive, it confirms, as previously seen, that the strain directions could correspond to the stress directions. In this hypothesis the extensional stress regime in the backarc basin would have the minimum principal stress $\sigma 3$ perpendicular to the mean directions of faults belonging to each of the two families. However, for both tectonic phases, $\sigma 3$ is not parallel to the future breakup line between the Okinawa platelet (defined by the Ryukyu arc and forearc) and the Eurasia plate (i.e., the trends of continental margins of the OT). This means that $\sigma 3$ has changed through time and that the initial tensional Miocene stress regime was different from the Lower Pleistocene and Recent regimes. We propose to examine if the two families of normal faults could be explained by single rotations.
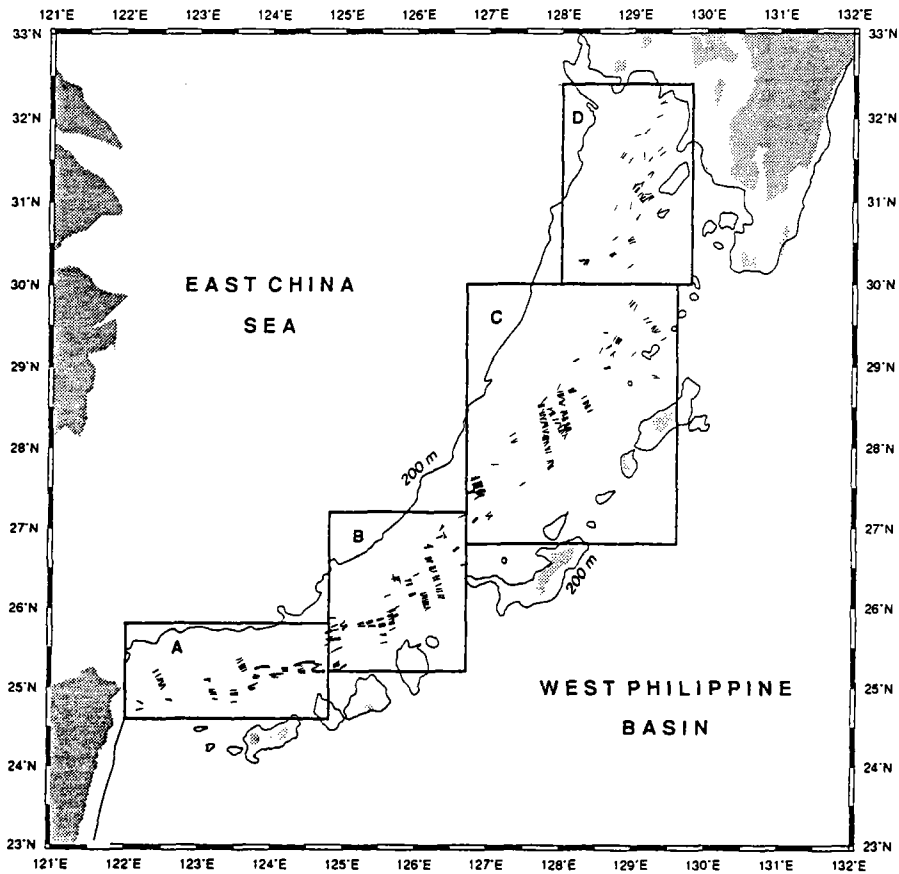
FIGURE 9.15. Directions of normal faults identified on large-scale Sea Beam maps contoured every 2 m. The POP1 data yielded 510 measurements (R/V *Jean Charcot* cruise, September–October 1984) and show a progressive change in direction from N090° east of Taiwan to N040° south of Japan.

4. KINEMATICS OF THE OKINAWA TROUGH OPENING

4.1. Determination of the Poles of Rotation Corresponding to the Early Pleistocene and Recent Tectonic Phases

From previous discussion, the orientation of the normal faults probably represents the stress regime for both the second and third tensional phases. Position of the poles of rotation can thus be computed for these two tensional phases. For each family of faults, the position of the pole of rotation has been computed by minimizing the error on a grid. The error σ at each point of the grid is equal to

$$\sigma = \sqrt{\frac{\sum_{n=1}^{N}(\theta_1 - \theta_2)^2}{N - 1}}$$

where θ_1 is the observed azimuth of a measurement, θ_2 is the azimuth of the segment connecting the computed point to the location of the measured point, and N is the total
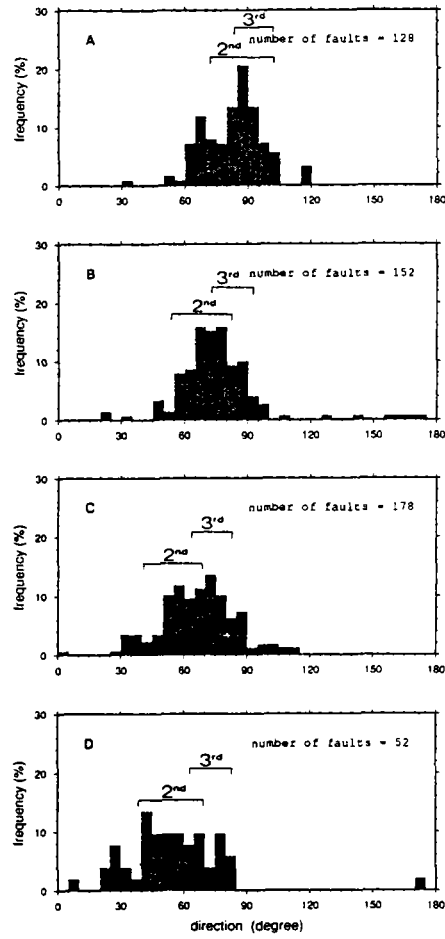
FIGURE 9.16. Distribution of fault directions by summing the faults within 5° intervals of azimuth for each of the four geographical boxes displayed in Fig. 9.15. Azimuths of normal faults belonging to the second and third phases of extension are from the mean curves of Figs. 9.18a and b.
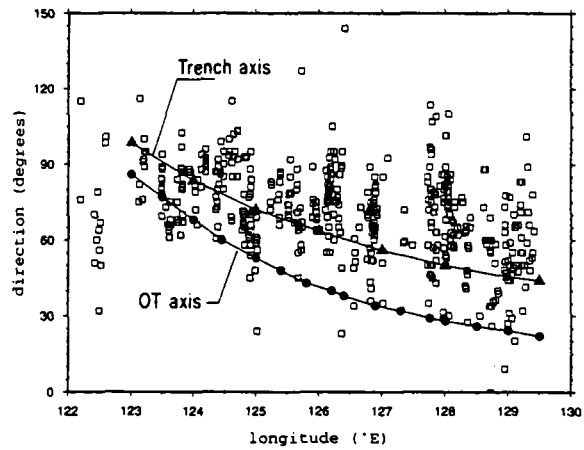
FIGURE 9.17. Directions of the normal faults as a function of the longitude (small open squares). Directions of the axis of the Okinawa Trough (black dots) and of the trench axis (black triangles) are also displayed as functions of the longitude. Directions of the normal faults are systematically deviated from the direction of the Okinawa Trough axis.
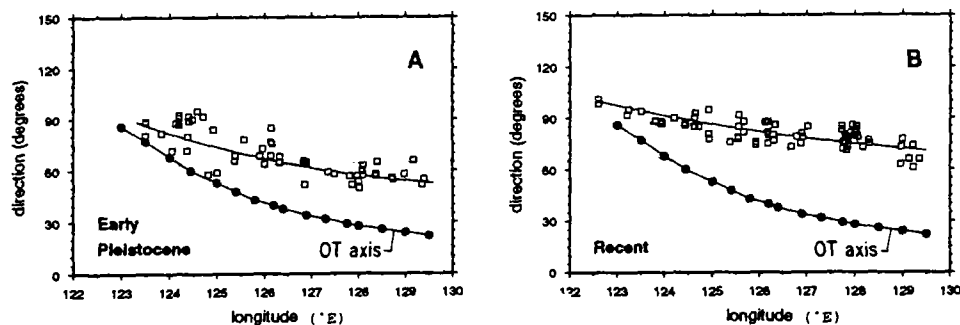
FIGURE 9.18. (a) Selected directions of normal faults belonging to the second phase of extension (early Pleistocene, Table I) as a function of the longitude (small open squares) and mean value (continuous line). Black dots represent the direction of the Okinawa Trough axis. (b) Selected directions of normal faults belonging to the third phase of extension (late Pleistocene to Recent, Table I) as a function of the longitude (small open squares) and mean value (continuous line). Black dots represent the direction of the Okinawa Trough axis.

number of measurements. The error has been computed every 0.2°, and the error values have been contoured and plotted with the GMT software package (Wessel and Smith, 1991). Poles of rotation corresponding to the second and the third generations of faults have been derived from 56 and 63 data points, respectively. The location of the pole of the second generation of faults (24.8°N, 121.6°E) lies in the eastern portion of the Ilan Plain (Fig. 9.19a). Consequently, extension in the southern OT and Ilan Plain would be weaker compared to the northern OT. This explains why large tilted fault blocks with significant offsets are observed in the northern OT and not in the southern OT. The location of the pole for the third generation of faults (24.6°N, 113.6°E) is about 800 km west of the previous one (Fig. 9.19b). A kinematic consequence is that the extension in the Ilan Plain was weak during the early Pleistocene but more active during the Recent phase. In fact, normal faults observed in the Ilan Plain affect the Plio–Pleistocene erosional surface. However, the Tatun and Kilung volcano groups, which are located in northern Taiwan behind the backarc basin but are related to the Ryukyu subduction system, are mostly of Quaternary age (Ho, 1986). High-heat-flow values (Yamano et al., 1989) and hydrothermal manifestations (Yamano et al., 1986) show that N075°-oriented volcanic ridges of the VAMP area located in the middle OT (Davagnier et al., 1987; Sibuet et al., 1987) are present-day to Recent features emplaced along trends that are in the direction of the pole of rotation of the third phase. This observation confirms the validity of the computed pole position and that present-day volcanism is emplaced along the rift direction of the third phase.

4.2. Determination of the Total Amount of Extension in the Okinawa Trough

It has been shown that extension occurs in the continental domain along the whole OT, from Taiwan to Japan. The bathymetric map (Fig. 9.2) shows that the OT is wider on the Japanese side, but the maximum water depth decreases toward the northeast; thus we do not know if the amount of total extension increases toward Japan. From available refraction and gravity data, we have established two crustal sections for the northern and southern OT, respectively, in order to quantify the amount of extension along these two transects.

Two techniques could be used to define the geometry of the Moho if part of the Moho depth is known: (1) By assuming that the crust is in local isostatic equilibrium, the geometry
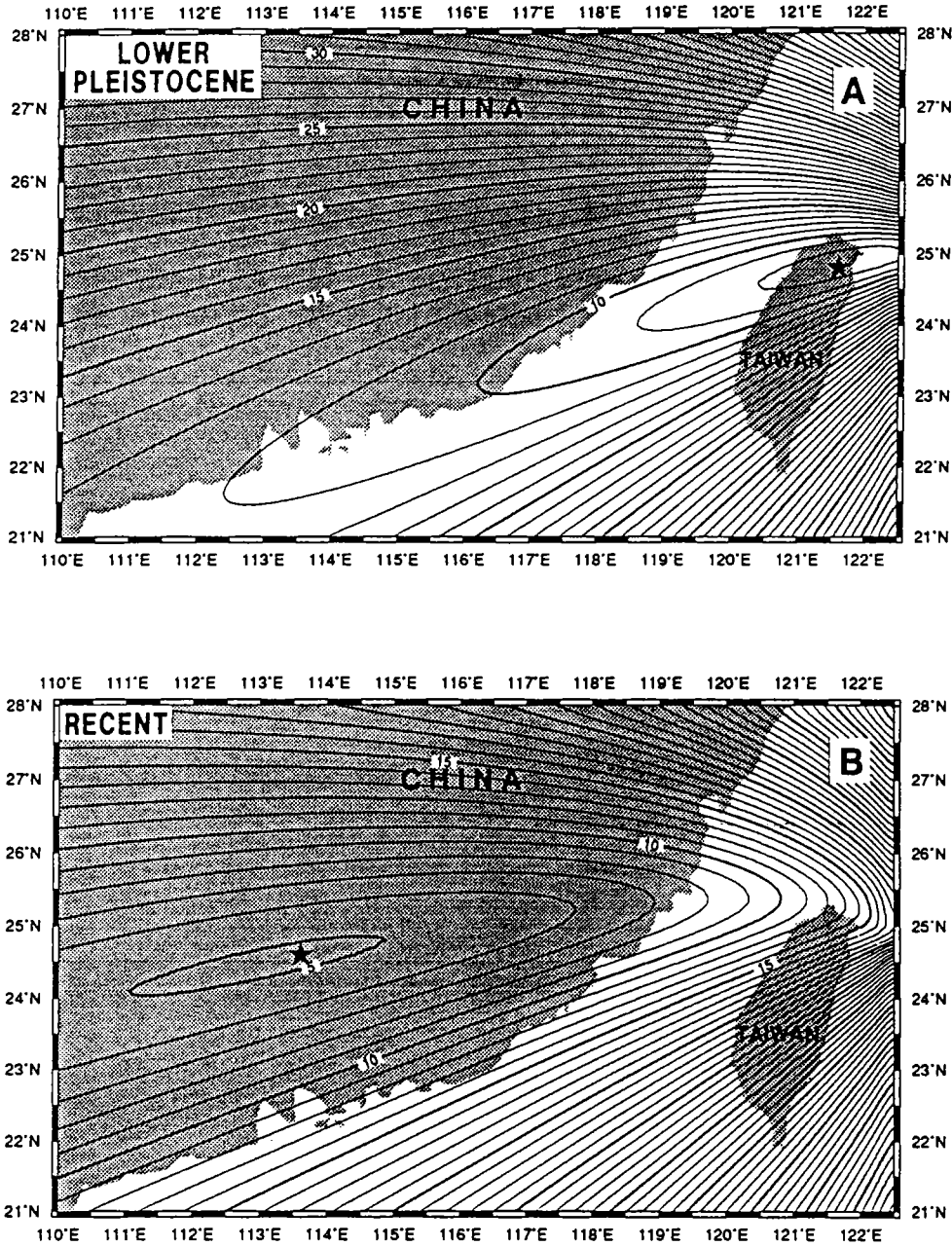
FIGURE 9.19. (A) Location of the pole of rotation (star) computed by minimization of the error on a 0.2° grid (24.8°N, 121.6°E). Data from 56 normal faults that unambiguously belong to the early Pleistocene phase of extension have been used in this calculation. Error values have been contoured and plotted by using the GMT software package (Wessel and Smith, 1991). (B) Location of the pole of rotation (star) computed by minimization of the error on a 0.2° grid (24.6°N; 113.6°E). Data from 63 normal faults which unambiguously belong to the late Pleistocene to Recent phase of extension have been used in this calculation. Error values have been contoured and plotted by using the GMT software package (Wessel and Smith, 1991).

of the Moho can be deduced by using an appropriate relationship between refraction velocities and densities. (2) If the gravity along the profile is known, the geometry of the Moho can be laterally extended by fitting the results of a two-dimensional gravity model with observed seismic refraction data.

We have used the first technique to obtain a model in local isostatic equilibrium, which was in agreement with the limited available refraction constraints. Then the calculated gravity values from this geometrical model have been compared with the observed gravity in order to provide geometrical models across the entire OT reasonably in agreement with both refraction and gravity data.

The seismic refraction experiment of Hirata *et al.* (1991) was conducted in the southern OT along profile I (Fig. 9.2). The Moho has been identified in the axial part of the trough at a depth of 18 km, with no evidence of existing oceanic crust beneath the central axis of the trough. However, in their ray-tracing modeling, Hirata *et al.* (1991) assumed that both the Moho and the boundary between the upper and lower crusts were flat outside of the trough axis. This assumption is not valid in the context of a narrow basin because it strongly violates the isostatic equilibrium principle. Consequently, we can only retain with caution a depth of 18 km for the Moho at the axis of the trough. Lee *et al.* (1980) reported refraction results along a profile parallel to the strike of the trough intersecting profile I. The P-wave velocity distributions in the crust are similar for both studies, except Lee *et al.* (1980) found that the Moho is at a depth of 15 km. Figure 9.20 presents models of profile I in local isostatic equilibrium with Moho depths beneath the axis of the southern OT at 15 and 18 km. Densities are obtained by using the theoretical relationship of Warner (1987) for sediments
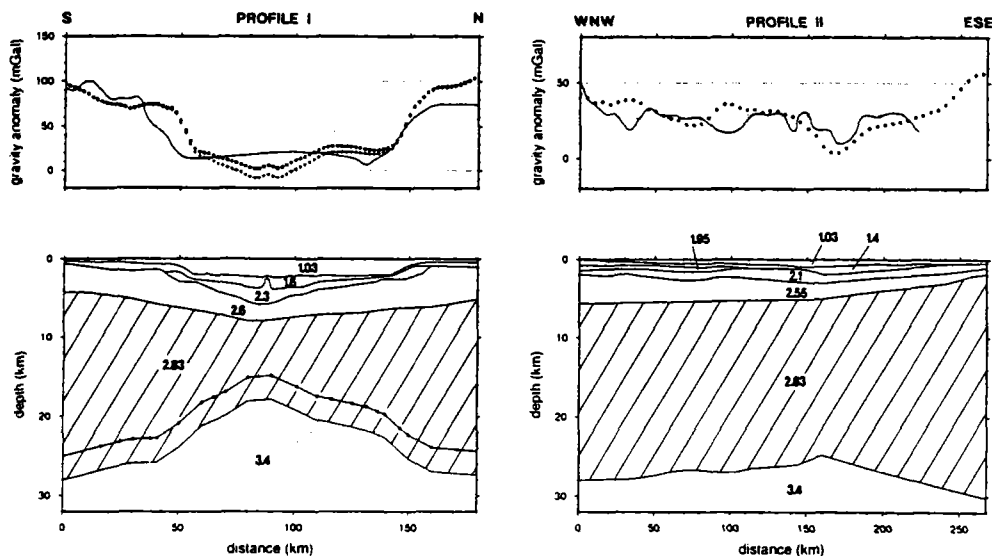

FIGURE 9.20. Crustal models in local isostatic equilibrium established from available refraction data along profiles I and II located in the southern and northern Okinawa Trough (Fig. 9.2). Densities are in g/cm³. The shallowest point of the Moho in profile I is at 18 km (continuous line) or at 15 km (continuous line with dots), depending on the interpretation of refraction data (Lee *et al.*, 1980; Hirata *et al.*, 1991). Hatched area corresponds to thinned continental crust. Observed gravity data (continuous line) and calculated gravitational attractions due to the geometrical structure (crosses for the Moho at 18 km and dots for the Moho at 15 km) are also shown. Same legends for profile II except that only one Moho position is provided.

and the velocity density relationship for crustal materials of Sibuet *et al.* (1990). The high value of the mantle density (3.4 g/cm³) has been chosen because continental rifting is still active and the whole lithosphere has not yet been heated. The geometrical model was established by using a reference hydrostatic column located in the axial portion of the trough. The deduced initial crustal thicknesses are 30.8 and 27.8 km, respectively, for axial Moho depths at 18 and 15 km. The observed gravity data are extracted from a free-air gravity anomaly chart of the Okinawa Trough and vicinity (Oshima *et al.*, 1988). The fit between the calculated and the observed gravity data is reasonably good except on both edges of the OT. Shallow Moho gives a better fit.

In the northern OT the refraction experiments of Iwasaki *et al.* (1990) in the western and central parts and Hayes *et al.* (1978) in the eastern part of the trough have been projected onto profile II (Fig. 9.2). The Moho has been identified in the western and central parts of the trough but not in the eastern part, where refraction data only provide information on the thickness of sediments and on the depth of the continental crust. Gravity data and density values are derived by using the same approaches as for profile I. The geometrical model is established by using a reference hydrostatic column located at 160 km where a Moho depth estimation is available. The deduced initial crustal thickness is 31 km, a value very close to the one obtained for profile I. The calculated gravitational attraction of this model in local isostatic equilibrium fits fairly well the general trend of the observed gravity data (Fig. 9.20).

If we assume that the extension is accommodated by stretching (pure shear) in the whole lithosphere, then knowing the initial thickness of the crust, the total amount of extension which affected the nonthinned continental lithosphere can be determined. It is the only way to get a rough estimate of the amount of extension in the OT. Note that this estimate is not significantly affected by the presence of dike intrusions in the OT. If the shallowest Moho is 15 km and the initial crustal thickness is 27.8 km, the amount of extension along profile I is 99 km—that is, 97 km perpendicularly to the axial direction of the trough. With a Moho at 18 km and an initial crustal thickness of 30.8 km, the amount of extension is 82 km—that is, 80 km perpendicularly to the direction of the trough at the location of profile I. For profile II, the total amount of extension is 74 km for an initial crustal thickness of 31 km.

For coherence of Moho depths along the entire OT, an amount of 80 km of extension has been assumed for the southern OT. This value is large compared to the width of the southern OT (100 km between the two continental slopes). However, the cross section of profile I (Fig. 9.20) shows that the Moho topography extends laterally, outside of the topographic expression of the OT located between 50 and 150 km. The existence of a thick pile of sediments above the continental crust is the reason for the slow decay of Moho depth to 31 km below the Eurasian platform. Consequently, part of the 80 km of extension is due to the thinning of the continental crust outside of the trough *sensu stricto*. The amount of extension is quite constant along the OT (Fig. 9.20), but the initial width of continental crust extended during the process of creation of the backarc basin is 100 km in the southeastern OT (along profile I) and 200 km in the northern OT (along profile II). This explains why the Moho depth increases from southern to northern OT.

Though a crude hypothesis has been made on the tensional mechanism to estimate the total amount of extension, an important indication is that the amount of extension across the OT does not increase from Taiwan toward Japan, as has been commonly implied in most of the geodynamic sketches except that of Vander Zouwen (1984), who proposed a pole of rotation located in southern Japan (Kyushu Island). The depth to Moho map of Jin *et al.*

(1983) grossly shows the northeastward increasing of the Moho depth and the increasing width of the trough. The Moho is at about 30-km depth beneath the East China Sea continental shelf. If we assume that the crustal thickness before rifting was 31 km, the total amount of extension along the OT is roughly constant or, to be more precise, slightly decreasing from 80 km at the location of profile I to 74 km at the location of profile II (Fig. 9.2). This means that the pole of rotation is located at about 90° from the OT location. From a kinematic point of view, if the poles of rotation of the second and the third phases of extension are both located west of Taiwan, the pole of rotation of the first phase of extension, which occurred in middle Miocene, was located northeast of the OT but far from the position given by Vander Zouwen (1984).

4.3. Determination of Parameters of the Total Rotation

Knowing the amount of extension perpendicular to the OT in two different places, we can obtain parameters of rotation only if a third constraint is available. This constraint comes from the shape of the continental slopes that bound the trough. At the base of slopes, between 1000 and 1500 m, a large bathymetric gradient could be followed on both edges of the OT (bathymetric chart of the middle and northern OT (Oshima et al., 1988) and bathymetric chart of the southern OT presented in this study). These two boundaries could be matched remarkably well because of their arcuate shapes and the presence of conjugate irregularities as, for example, at 26.2°N, 124.9°E and at 25.5°N, 125.3°E. The amount of extension has been maintained perpendicularly to the trough at 74 and 80 km in the northern and southern OT, respectively. In such conditions, the pole of rotation has been determined at 35°S, 50°N with a rotation angle of 0.77° (Table II). Figure 9.21 shows such a reconstruction with present-day contours and the rotated position of the Okinawa platelet. The rotated 1000-m isobath located north of the Ryukyu Islands fits very well with the conjugate isobath along the northern edge of the trough, except for the southwestern edge of the OT (west of 123.5°E), which has no bathymetric counterpart on the northwestern edge, and possibly for the southern segment located between 123.5°E and 124.5°E, which includes the two main islands of Iriomote Sima (24.3°N, 123.8°E) and Isigaki Sima (24.4°N, 124.2°E).

Consequently, east of 123.5°E or possibly east of 124.5°E, the curvature of the entire trough was not acquired during the formation of the backarc basin but was already in existence at the beginning of the formation of the trough and persisted through time. The main curvature of the trough is already given by the northeastern OT slope, which has not been significantly affected during the collision of Taiwan. The relative uniformity of the amount of extension along the trough (Fig. 9.21) also suggests a decoupling between the OT opening and the compressive tectonics in Taiwan, at least between profiles I and II located

TABLE II
Okinawa Platelet Motions with Respect to Eurasia

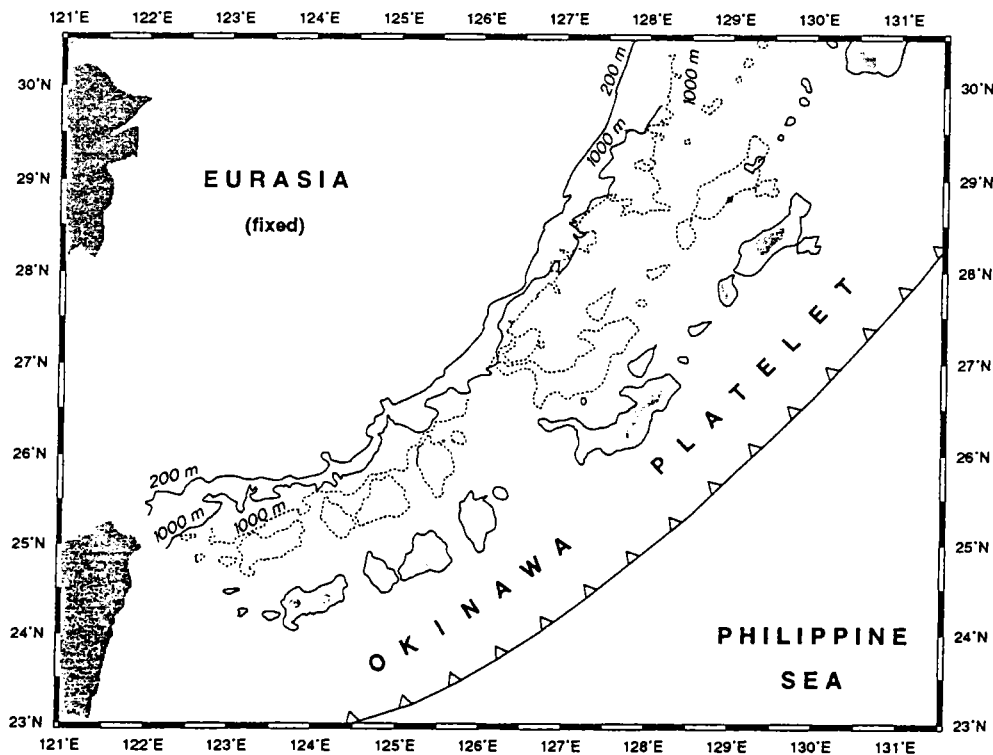| OT main tensional phases		Latitude (°N)	Longitude (°E)	Angle (°)
1st phase	Middle to late Miocene	37.6	144.0	−1.93
2nd phase	Early Pleistocene	24.8	121.6	1.58
3rd phase	Late Pleistocene to Recent	24.6	113.6	0.19
	Total extension	−35.0	50.0	0.77

FIGURE 9.21. Reconstructions of the Okinawa Trough opening. Present-day positions are in continuous lines. The Ryukyu Islands and their 200-m isobaths represent the Okinawa platelet, which extends as far as the trench axis (Fig. 9.4). The continuous line with open triangles shows the position of the trench. Eurasia is fixed. The dotted lines represent the present-day position of the Okinawa platelet at the closure of the Okinawa backarc basin before any tensional motion in the area occurred, i.e., in middle Miocene time. The parallelism of the 1000-m isobath of the Eurasian continental platform with the rotated 1000-m of the northwestern border of the Okinawa platelet shows the quality of the fit.

in Fig. 9.2. Another consequence of this reconstruction is that the mean azimuth of the relative motion of the Okinawa platelet with respect to Eurasia is N143°, which is quite similar to the mean direction of motion (N126°) of the Philippine Sea plate with respect to Eurasia (Seno and Maruyama, 1984). The decoupling of the tectonic evolutions of the backarc basin and of the collision in Taiwan is maintained through time, except for the southwestern portion of the trough, west of 123.5°E or 124.5°E, where the Okinawa platelet and the Ryukyu Trench change significantly in direction with respect to the rest of the OT. Numerous earthquakes occur over a maximum distance of 140 km from Taiwan in the EW forearc Nanao basin (Tsai, 1986). Focal mechanisms indicate a compressive motion which is related to the collisional processes in Taiwan (Kao and Chen, 1991; Cheng et al., 1992) and could explain the ESE-WNW orientation of the southwestern extremity of the Ryukyu forearc and trench and the narrowing of the backarc basin itself, though abnormally high tensional motions persist in the southern OT east of the Ilan Plain over a distance of 170 km as confirmed by the high earthquake density, focal mechanisms (Kao and Chen, 1991; Cheng et al., 1992), and seismic reflection profiles which display present-day normal faults parallel to the OT axis (Sibuet, 1991).

4.4. Trial to Quantify the Amount of Extension Corresponding to the Two Last Tensional Phases

To better define the last two phases of extension, we attempt to evaluate the horizontal offsets of faults related to each of the two phases across two transects of the OT. The amount of extension has been determined by assuming that the brittle surface deformation was representative of the crustal deformation following the method of Le Pichon and Sibuet (1981). Because pure shear is the assumed mechanism of extension, the surface extension is identical to crustal or lithospheric extensions. Though this method has been criticized in the past (Chenet *et al.*, 1983), in our opinion it is the only way to try to quantify the amount of extension. Horizontal offsets have been determined from the dip and the vertical offset of each fault and summed for all faults across the entire trough. Numerous seismic profiles of the POP1 cruise have been used for that purpose. Final estimates of the amount of extension perpendicular to the trough direction are given for two complete transects of the trough.

The Recent phase of extension is characterized by numerous small offset normal faults and also by the reactivation of normal faults that belong to the preceding phase of extension. Because the amount of extension cannot be estimated from faults that present a large topographic expression, but only from those faults which offset the sedimentary cover, this bias is eliminated by choosing only seismic sections where normal faults of the previous phase are buried, which is mainly in the southern and middle OT. The estimates of the cumulative extension amount on several OT cross sections are about 3 km in the southern OT and 5 km in the middle OT. Though there may be large errors, which could be a factor of 2 on these estimates, the final accepted estimate is 5 km in the middle OT (at 29°N, 128.5°E) which gives a 0.2° rotation angle for the last tensional phase (Table II).

Concerning the amount of extension that occurred in the second phase of extension (early Pleistocene), the only locations where such estimations can be done are in the middle or northern OT (example on profile 99, Fig. 9.6). Because of the high sedimentation rate, the subsequent thick sediments mask the tilted blocks relative to this phase in the southern OT. For badly defined blocks, the amount of extension has been estimated by using the downward prolongation of both the Plio–Pleistocene surface of the blocks and the normal faults that bound the blocks. Estimates performed in the middle and northern OT are similar and equal to 25 ± 10 km. Though the amount of error cannot be accurately defined, we retain 25 km of extension at 29.7°N, 129°E, which gives a 1.4° rotation angle for the second tensional phase (Table II).

4.5. Parameters of Rotations for the Three Tensional Phases

Parameters of the first phase of extension can be deduced from the total rotation and the two last rotations (Table II). Figure 9.22 shows the relative position of the Okinawa platelet (represented by the Ryukyu Islands and their 200-m isobaths) before extension (at the time of closure) and at the end of each of the first, second, and third (present-day position) phases of extension. As anticipated, the largest amount of motion corresponds to the first phase, which in fact is the least-documented phase from geological data. The corresponding pole of rotation is located in the northeastern prolongation of the OT, at about 1500 km beyond the northern extremity of the OT, which gives about 50 km of extension in the northern OT and 75 km of extension in the southern OT. From paleo-
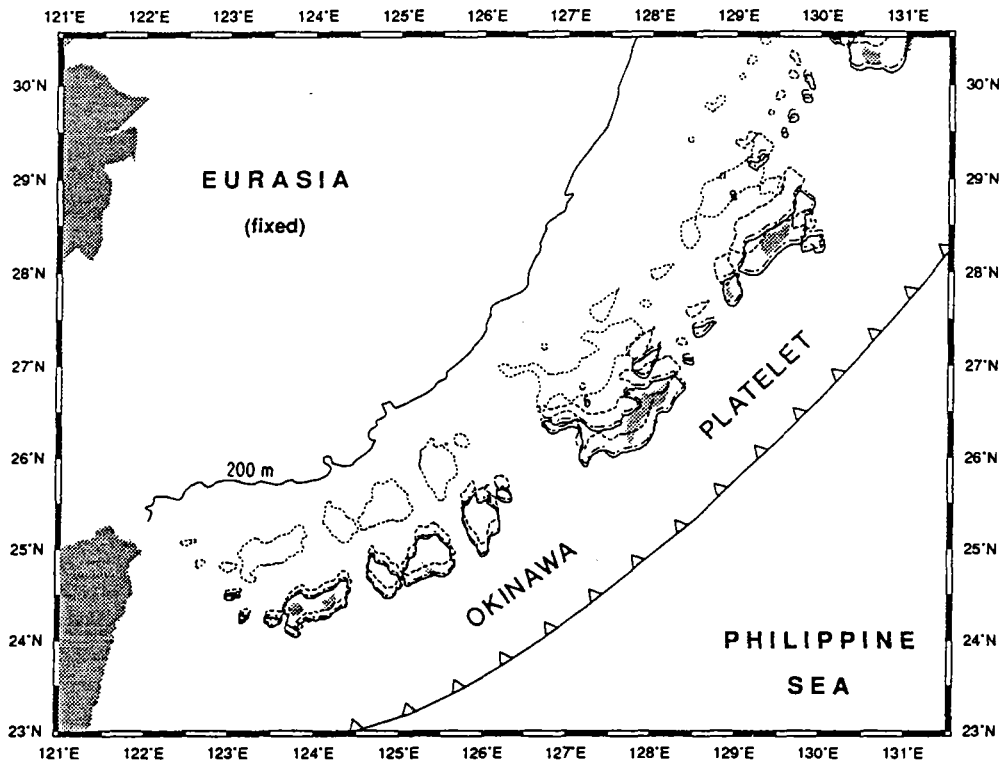
FIGURE 9.22. Reconstructions of the three extensional phases of the Okinawa Trough. Present-day positions are in continuous lines. The Ryukyu Islands and their 200-m isobaths represent the Okinawa platelet. The continuous line with open triangles shows the present-day position of the trench. Eurasia is fixed. The noncontinuous lines represent the position of the Okinawa platelet at the closure of the Okinawa backarc basin (about 15 Ma, dotted lines), at the end of the first tensional phase (about 7 Ma, dashed lines) and at the end of the second tensional phase (about 0.5 Ma, dotted and dashed lines).

magnetic constraints coming from the southeastern Ryukyu Islands, Miki *et al.* (1990) explain the motion of these islands (at least south of the Miyako depression) with respect to Eurasia by a clockwise rotation of 19° around a pole located in northern Taiwan (24.7°N, 121.7°E) for the portion of the Okinawa platelet located south of the Miyako depression. The amount of extension in the OT north of Isigaki Sima Island (Fig. 9.2, 24.4°N, 124.2°E) is 70 km, a value close to the one proposed in this study. However, using these parameters of rotation, the amount of extension would be 150 km near the Miyako depression and 340 km in the northern OT just south of Kyushu. Both values are unacceptable, which questions the validity of the interpretation of these paleomagnetic measurements. The most coherent interpretation of the 19° clockwise rotation of the southwestern portion of the Okinawa platelet would be to link this motion to the collision of the Luzon arc in Taiwan. Paleomagnetic measurements were performed on samples older than 10 Ma (Miki *et al.*, 1990), which do not give any information on the age of the rotation. We suggest that this rotation of the southwestern portion of the Okinawa platelet occurred during the collision in Taiwan (i.e., during the last 4 m.y.) and that the pole of rotation was not located in northern Taiwan

but close to or east of Iriomote Sima and Isigaki Sima Islands. This interpretation links the curvature of the southwestern Okinawa platelet west of 123.5°E or 124.5°E to the collision in Taiwan. The pole position of the OT total closure (Table II) also differs considerably from that proposed by Vander Zouwen (1984), which is located in Kyushu. That pole of rotation allows only a few kilometers of extension in the northern OT instead of several tens of kilometers as established in this study. To test the proposed kinematic evolution of the OT backarc basin, we examine newly compiled bathymetric and magnetic anomaly maps of the southern OT (Fig. 9.2).

5. NEWLY COMPILED BATHYMETRIC AND MAGNETIC DATA IN THE SOUTHERN OKINAWA TROUGH

Bathymetric and magnetic data from the National Geographic Data Center (NGDC) and new data acquired east and south of Taiwan by the Institute of Oceanography, National Taiwan University, have been compiled in the area east of Taiwan, in the OT, and in the Philippine Sea Basin.

5.1. New Bathymetric Map

Bathymetric data have been acquired in 95 different cruises (Fig. 9.23). The root-mean-squares (r.m.s.) error at the intersections of all tracklines is 119.3 m and the mean absolute value is 55.1 m. To avoid the appearance of pseudostructures, several cruises
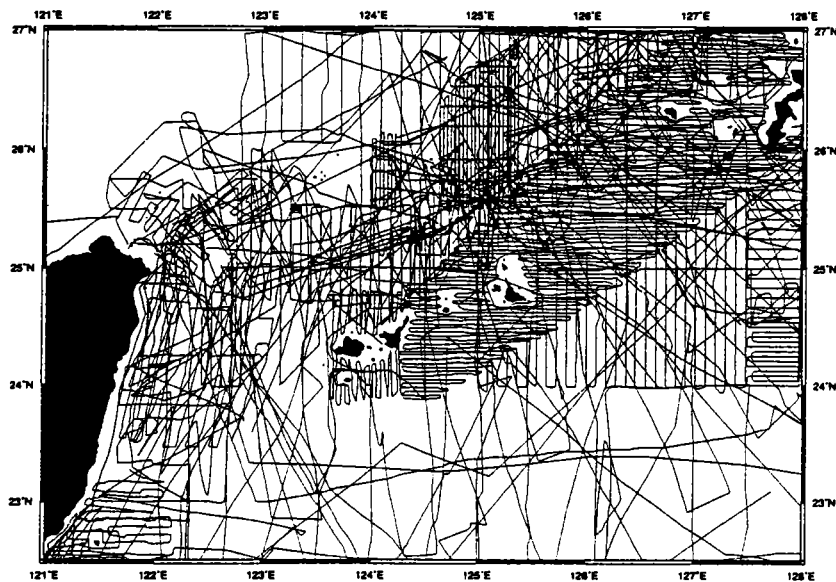
FIGURE 9.23. Tracklines show where bathymetric data have been acquired (95 cruises). Data have been collected by numerous institutions and are available through the National Geographic Data Center. Complementary data acquired east and south of Taiwan were made available by the Institute of Oceanography, National Taiwan University.

102

which give crossover errors larger than 200 m were removed first. The rest of the bathymetric data were adjusted by linear interpolation (Hsu, in press) to eliminate the crossover errors. Then data were gridded and contoured using the GMT software (Wessel and Smith, 1991). Figure 9.24 shows a portion of the bathymetric map over the southern OT, the direction of normal faults identified from Sea Beam data, together with offset and dip indications. Two major depressions located at about 25.2°N, 124°E and 25.8°N, 125.5°E in the southern OT are underlined by several segments of faults.

5.2. New Magnetic Map

Magnetic data have been acquired in 57 different cruises (Fig. 9.25). Magnetic anomalies are computed using the International Geomagnetic Reference Field (IGRF) 1990. The r.m.s. error at the intersections of all tracklines is 55.9 nT, and the mean absolute value is 38.8 nT. To avoid the appearance of pseudomagnetic features, we removed several cruises that give crossover errors larger than 100 nT and applied a regional correction to magnetic data of those cruises that do not have diurnal informations, using the general method of Regan and Rodriguez (1981). The remaining data have been adjusted by linear interpolation (Hsu, in press) to eliminate crossover errors. Then data were gridded and contoured with the GMT software (Wessel and Smith, 1991). A regional magnetic anomaly was extracted from the magnetic anomaly grid by second-order filtering and then was substracted from the initial grid to give the residual magnetic anomaly map (Fig. 9.26).
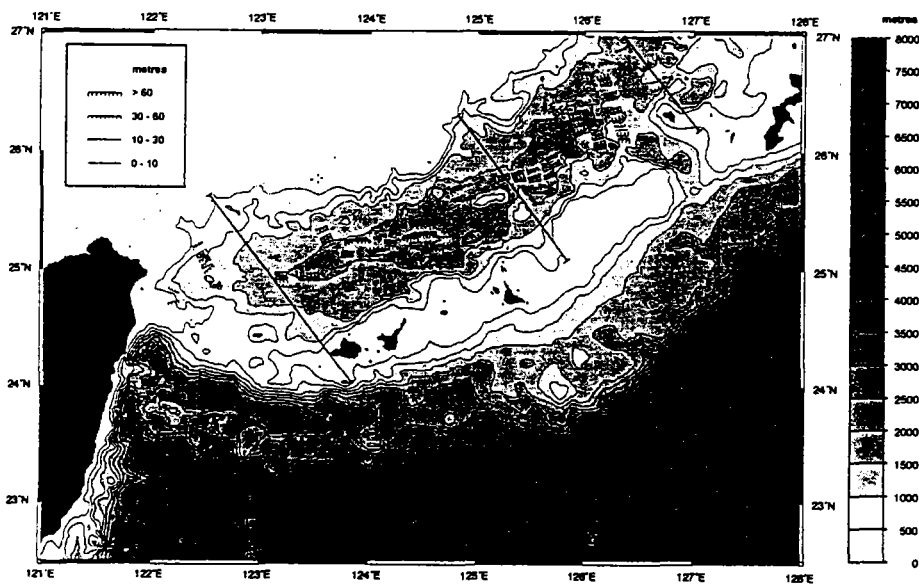
FIGURE 9.24. Bathymetric map of the southern Okinawa Trough in Mercator projection. Contours every 500 m. Gray scale on the right. Measurements of normal fault directions identified on Sea Beam data appear with indications of dips. Scale of vertical offsets in the upper left corner of the map. The N142° mean direction for the opening of the Okinawa Trough (Table II) shows the good correlation between topographic features located on either side of the trough, except for the southeastern portion of the Okinawa platelet, west of 123.5°E or 124.5°E, which has no morphologic counterpart on the northern continental slope of the Okinawa Trough.
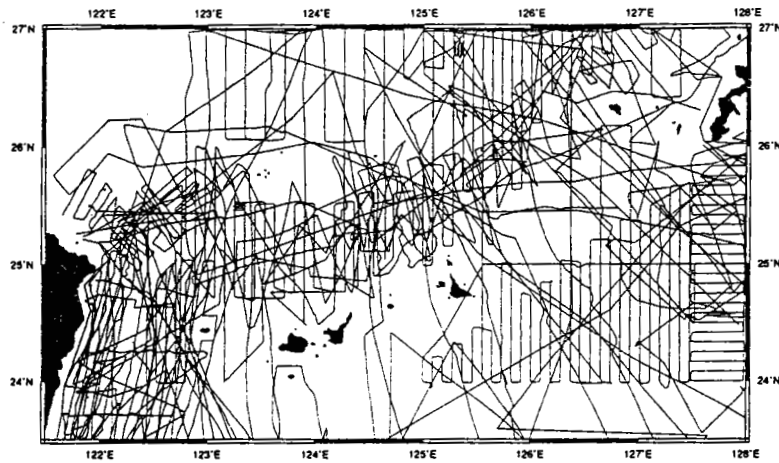
FIGURE 9.25. Tracklines show where magnetic data have been acquired (57 cruises). Data have been collected by numerous institutions and are available through the National Geographic Data Center. Complementary data acquired east and south of Taiwan were made available by the Institute of Oceanography, National Taiwan University.

5.3. DISCUSSION

A major feature of the residual magnetic anomaly map is the strong magnetic contrast between the OT backarc basin and the Okinawa platelet. The southern OT, defined by the 200-m isobath, is characterized by magnetic anomalies with magnitude of a few hundred nanoteslas and wavelengths of a few tens of kilometers. In contrast, the Okinawa platelet, defined by the 200-m isobath on the OT side and the trench axis, is characterized by weak magnetic anomalies, which confirm that the southern Ryukyu arc is a nonvolcanic arc
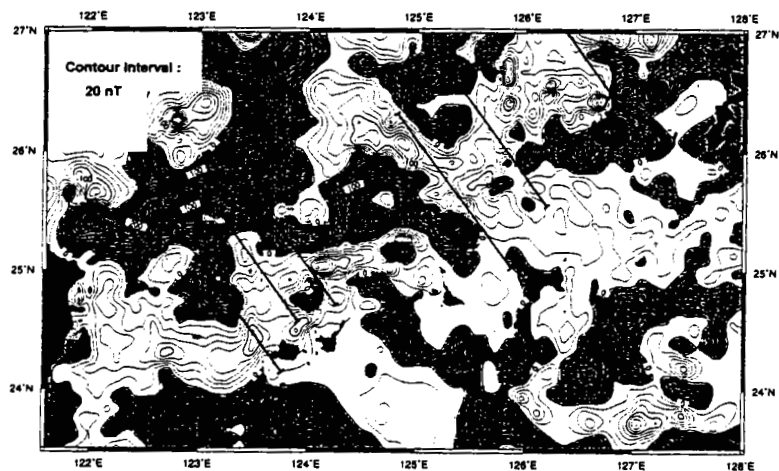
FIGURE 9.26. Residual magnetic anomaly map of the southern Okinawa Trough in Mercator projection obtained by subtraction of a regional field from the magnetic anomaly data. Contours every 20 nT. The N142° direction shows boundaries between areas of similar magnetic character.

104

(Letouzey and Kimura, 1986). However, except for the high-amplitude anomalies located northeast of Taiwan, which are linked to volcanics of the Taiwan Sinzi folded belt, the East China Sea continental margin is characterized by magnetic anomalies of similar wavelength but lower amplitude than in the OT. Two lines of interpretations can be proposed for the origin of the OT magnetic anomalies.

The initial continental domain, which was lately thinned and extended 80 km, belongs to the domain of the Taiwan Sinzi folded belt, where volcanics have been identified. As the initial continental domain has been extended by a factor of about 2 during rifting, an increase of the wavelength of magnetic anomalies and a reduction of the amplitude due to the subsidence of magnetic sources were anticipated. However, these were not observed.

As a result of tensional processes, the whole OT continental domain has been thinned and crustal and lithospheric thicknesses significantly reduced (Fig. 9.20). Products of partial melting initiated in the lower part of the lithosphere, just above the Benioff zone, probably come up through the lithosphere, lying as arc volcanic intrusions at different depths within the crust, and giving rise to significant magnetic anomalies. We tend to favor this hypothesis.

In an earlier magnetic compilation, Oshida *et al.* (1992) described relationships between magnetic anomalies and geologic features. They demonstrated that the numerous dipole-type anomalies observed along the southern side of the trough are linked to volcanic knolls that are considered as the southwestern extension of the Ryukyu volcanic arc (Ueda, 1986; Oshida *et al.*, 1988). Geochemical analyses performed on basaltic samples collected on these seamounts confirm the arc volcanic affinity of these seamounts (Sibuet *et al.*, 1986; Boespflug, 1990).

Because of the reduced amount of partial melting, only a small percentage of the crust would be composed of volcanics. It seems reasonable to assume that refraction data cannot resolve the presence of such crustal material. A major question concerns the mode of ascent of magmatism through the crust. Does the basaltic magma go indifferently or randomly through the crust? Or does it go preferentially along zones of weakness parallel to rift directions or transform directions? In addition to localized dipole anomalies linked to arc volcanism (Oshida *et al.*, 1992) along the southern side of the trough, a close examination of the shape of magnetic anomalies in the OT shows a good correlation between the location of the elongated magnetic anomalies and the axes of the two depressions already evidenced on the bathymetric map and where basaltic elongated ridges have been mapped and sampled (Sibuet *et al.*, 1987; Fig. 9.26). Oshida *et al.* (1992) modeled these magnetic anomalies with a normally magnetized crust (2.5 A/m), supporting the view that seafloor spreading has not started in the southern OT. In the southern OT only a few basaltic intrusions have been identified in these depressions (Fig. 9.3) where surface extension and consequent crustal extension are maximum. Thus, the residual magnetic anomaly map clearly shows a correspondence between magnetic anomalies and rift directions related to the last two phases of the OT opening. No correspondence seems to exist with rift directions of the first phase, oriented N052° from the kinematic analysis. Previous existing weak magnetic anomalies could have been obliterated by large anomalies related to the second and third phases of extension and, in any case, better developed because extension and partial melting increase with time.

The mean direction of the entire OT opening has been plotted on the bathymetric (Fig. 9.24) and residual magnetic anomaly (Fig. 9.26) maps. Though transform faults are not observed in the OT (Sibuet *et al.*, 1987), the N142° segments limit areas of similar magnetic character. A plausible interpretation of this observation is to relate magnetic anomalies and

associated crustal magmatic intrusions with different sections of the continental crust experiencing different tensional factors. Extension could be different in adjacent sections. For example, OT continental slopes are very steep on both sides of the section located between 123.8°E and 125.4°E (Fig. 9.26). Most of the extension occurs in the deepest part of the OT. In the adjacent southwestern section and extending to Taiwan, continental slopes are wider and the amount of extension in the deep part of the trough seems to be reduced compared with other sections. We consequently suggest that a link exists among partial melting, ascent of volcanic products within the crust, and amount of crustal extension.

6. CONCLUSIONS

The major conclusions concerning the structural and kinematic evolution of the OT are the following.

(1) The whole OT is still in a rifting stage as shown by refraction and magnetic data. The crustal thickness increases from 10 km in the deepest part of the southern OT to 30 km in the northern OT, close to Japan.

(2) The amount of extension across the OT has been estimated from refraction and gravity data. It slightly decreases from 80 km in the southern OT to 74 km in the northern OT.

(3) Three phases of extension are identified and their parameters of rotation are established: (a) The late Pleistocene to Recent phase of extension is characterized by normal faults with vertical offsets of a few meters and changing directions progressively along the OT. The amount of extension that occurred during this phase is about 5 km in the middle OT. (b) The early Pleistocene phase of extension is characterized by tilted blocks that affect late Pliocene–early Pleistocene sediments and change direction progressively along the OT. The difference in azimuths of these two last phases increases toward the northern OT. The amount of extension for this phase is estimated to be 25 km in the northern OT. (c) The middle to late Miocene phase of extension, poorly characterized from geological data, has been calculated from parameters of the total rotation and of the two last rotations. This first phase of extension is a major tectonic phase with about 50 km of extension in the northern OT and 75 km in the southern OT. The corresponding pole of rotation is located 1500 km northeast of Kyushu Island.

(4) Directions of normal faults of the last two phases correspond to the stress directions because of their progressive change along the OT axis resulting from a partial relaxation of the motion along zones of weakness active during previous tectonic phases.

(5) The proposed kinematic evolution of the OT differs considerably from previous reconstructions and raises questions concerning, for example, the interpretation of paleomagnetic measurements obtained in the southeastern Ryukyu Islands.

(6) The curved shape of the OT was acquired since the onset of the backarc basin extension except for the southwestern portion of the Okinawa platelet, west of 123.5°E or 124.5°E longitude, which has rotated 19° clockwise (Miki *et al.*, 1990) during the collision of Taiwan around a pole located east or close to the southern Ryukyu Islands.

(7) New bathymetric and residual magnetic anomaly maps are in agreement with the proposed kinematic evolution. Magnetic anomalies in the southern OT and geochemical analyses performed on collected basaltic samples suggest that part of the anomalies are linked to crustal arc volcanic intrusions emplaced close to the southern continental slope

of the OT and within topographic depressions located in the central part of the southern OT. For the remaining magnetic anomalies, we suggest a link among partial melting, ascent of volcanic products within the crust, and amount of crustal extension.

Acknowledgments

We thank Benoît Loubrieu, Alain Normand, and Michel Voisset for their help in processing Sea Beam data with the IFREMER TRISMUS software package, and Daniel Carré for drafting some figures. We acknowledge discussions with H. D. Needham about the kinematics of the early stage of ocean opening. The GMT software package was used to display some of the figures (Wessel and Smith, 1991). Brian Taylor gave us a lot of support and facilities for the submission and revision of this chapter and also numerous scientific comments on the first version of the manuscript.

REFERENCES

Boespflug, X. 1990. Evolution géodynamique et géochimique des bassins arrière-arcs. Exemples des bassins d'Okinawa, de Lau et Nord-Fidjien, Université de Bretagne Occidentale, Brest, France.

Chenet, P.-Y., Montadert, L., Gairaud, H., and Roberts, D. G. 1983. Extension ratio measurements on the Galicia, Portugal and northern Biscay continental margins: Implications for evolutionary models of passive continental margins, in *Studies in Continental Margin Geology* (J. S. Watkins and C. L. Drake, eds.), Am. Assoc. Petrol. Geol. Mem. **34**:703–715.

Cheng, S.-N., Lee, C.-T., and Yeh, Y. T. 1992. Seismotectonics of the Ryukyu arc, in *Proc. 4th Taiwan Symp. Geophys.*, Taipei, pp. 507–516.

Davagnier, M., Marsset, B., Sibuet, J.-C., Letouzey, J., and Foucher, J.-P. 1987. Mécanismes actuels d'extension dans le bassin d'Okinawa, *Bull. Soc. Géol. France* **8**:525–531.

Eguchi, T., and Uyeda, S. 1983. Seismotectonics of the Okinawa Trough and Ryukyu arc, *Mem. Geol. Soc. China* **5**:189–210.

Furukawa, M., Kondo, S., Miki, M., and Isezaki, N. 1991a. Report on DELP 1988 cruises in the Okinawa Trough. Part V: Measurement of the three components and total intensity of the geomagnetic field in the Okinawa Trough, *Bull. Earthquake Res. Inst., U. Tokyo* **66**:91–150.

Furukawa, M., Tokuyama, H., Abe, S., Nishizawa, A., and Kinoshita, H. 1991b. Report on DELP 1988 cruises in the Okinawa Trough. Part II: Seismic reflection studies in the southwestern part of the Okinawa Trough, *Bull. Earthquake Res. Inst., U. Tokyo* **66**:17–36.

Hayes, D. E., Houtz, R. E., Jarrard, R. D., Mrozowski, C. L., and Watanabe, T. 1978. Crustal structure, 1 sheet, scale 1:6,442,194, in *A Geophysical Atlas of the East and Southeast Asian Seas, Map Chart, MC25* (D.E. Hayes, ed.), Geological Society of America, Boulder, CO.

Hilde, T. W. C., Lee, C.-S., and Vander Zouwen, D. E. 1984. Tectonic and sedimentation history of Okinawa Trough: Implications for development of the East China and Yellow seas. Korea–U.S. Conference on the Yellow Sea.

Hirata, N., Kinoshita, H., Katao, H., Baba, H., Kaiho, Y., Koresawa, S., Ono, Y., and Hayashi, K. 1991. Report on DELP 1988 cruises in the Okinawa Trough. Part III: Crustal structure of the southern Okinawa Trough, *Bull. Earthquake Res. Inst., U. Tokyo* **66**:37–70.

Ho, C. S. 1986. A synthesis of the geologic evolution of Taiwan, *Tectonophysics* **125**:1–16.

Hsu, S.-K. in press. XCORR: A cross-over technique to adjust track data, *Comput. Geosci.*

Ishizaka, K., Yanagi, K., and Hayatsu, K. 1977. A strontium study of the volcanic rocks of the Myoko volcano group, central Japan, *Contrib. Mineral. Petrol.* **63**:295–307.

Iwasaki, T., Hirata, N., Kanazawa, T., Melles, J., Suyehiro, K., Urabe, T., Möller, L., Makris, J., and Shimamura, H. 1990. Crustal and upper mantle structure in the Ryukyu island arc deduced from deep seismic sounding, *Geophys. J. Int.* **102**:631–651.

Jarrard, R. D., and Sasajima, S. 1980. Paleomagnetic synthesis for Southeast Asia: constraints on plate motions, in *The Tectonic and Geologic Evolution of Southeast Asian Seas and Islands* (D. E. Hayes, ed.), Geophys. Monogr. Ser., Vol. 23, pp. 293–317, American Geophysical Union, Washington, DC.

Jin, X., Yu, P., Lin, M., Li, C., and Wang, H. 1983. Preliminary study on the characteristics of crustal structure in the Okinawa Trough (in Chinese with English abstract), *Oceanol. Limnol. Sin.* 14:105–116.

Kao, H., and Chen, W.-P. 1991. Earthquakes along the Ryukyu–Kyushu arc: Strain segmentation, lateral compression, and thermomechanical state of the plate interface, *J. Geophys. Res.* 96:21,443–21,485.

Kasahara, J., Nagumo, S., Koresawa, S., Ouchi, T., and Kinosita, H. 1985. Seismic features in the central Okinawa Trough—an active incipient rifting, Abstract for the 23rd General Assembly of IASPEI, Tokyo 1:279.

Kato, S., Katsura, T., and Hirano, K. 1982. Submarine geology off Okinawa Island, *Rep. Hydrogr. Res.* 17:31–70.

Kimura, M. 1985. Back-arc rifting in the Okinawa Trough, *Mar. Petrol. Geol.* 2:222–240.

Kimura, M., Kaneoka, I., Kato, Y., Yamamoto, S., Kushiro, I., Tokuyama, H., Kinoshita, H., Isezaki, N., Masaki, H., Oshida, A., Uyeda, S., and Hilde, T. W. C. 1986. Report on DELP 1984 cruises in the middle Okinawa Trough. Part V: Topography and geology of the central grabens and their vicinity, *Bull. Earthquake Res. Inst., U. Tokyo* 61:269–310.

Le Pichon, X., Huchon, P., and Barrier, E. 1985. Geoid and the evolution of the western margin of the Pacific Ocean, in *Formation of Active Ocean Margins* (N. Nasu, ed.), pp. 3–42, Tokyo, Terrapub.

Le Pichon, X., and Sibuet, J.-C. 1981. Passive margins: A model of formation, *J. Geophys. Res.* 86:3708–3710.

Lee, C. S., Shor, G. G., Jr., Bibee, L. D., Lu, R. S., and Hilde, T. W. C. 1980. Okinawa Trough: Origin of a back-arc basin, *Mar. Geol.* 35:219–241.

Letouzey, J., and Kimura, M. 1986, The Okinawa Trough: Genesis of a back-arc basin developing along a continental margin, *Tectonophysics* 125:209–230.

Ludwig, W., Murauchi, S., Den, N., Bull, P., Hotta, H., Ewing, M., Asanuma, T., Yoshii, T., and Sakajiri, N. 1973. Structure of the East China Sea–West Philippine Sea margin of southern Kyushu, *J. Geophys. Res.* 78:2526–2536.

Miki, M., Matsuda, T., and Otofuji, Y. 1990. Opening mode of the Okinawa Trough: Paleomagnetic evidence from the South Ryukyu arc, *Tectonophysics* 175:335–347.

Nagumo, S., Hinoshita, H., Kasahara, J., Ouchi, T., Tokuyama, H., Asamuma, T., Koresawa, S., and Akiyoshi, H. 1986. Report on DELP 1984 cruises in the Middle Okinawa Trough, Part II: Seismic structural studies, *Bull. Earthquake Res. Inst., U. Tokyo* 61:167–202.

Nash, D. F. 1979. The geological development of the north Okinawa Trough area from Neogene times to Recent, *J. Jpn. Assoc. Petrol. Technol.* 44:121–133.

Oshida, A., Midorikawa, Y., Kawabata, K., Kanazawa, J., Kimura, M., and Kato, Y. 1988. Submarine acoustic and geomagnetic surveys in the north of Yaeyama–Gunto, Ryukyu arc (RN86 and RN87 cruises), *Bull. Coll. Sci., U. Ryukyus* 46:123–138.

Oshida, A., Tamaki, K., and Kimura, M. 1992. Origin of the magnetic anomalies in the southern Okinawa Trough, *J. Geomagn. Geoelectr.* 44:345–359.

Oshima, S., Takanashi, M., Kato, S., Uchida, M., Okazaki, I., Kasuga, S., Kawashiri, C., Kaneko, Y., Ogawa, M., Kawai, K., Seta, H., and Kato, Y. 1988. Geological and geophysical survey in the Okinawa Trough and the adjoining seas of Nansei Syoto, *Rep. Hydrogr. Res.* 24.

Reches, Z. 1983. Faulting of rocks in three-dimensional strain fields. II: theoretical analysis, *Tectonophysics* 95:133–156.

Regan, R. D., and Rodriguez, P. 1981. An overview of the external field with regard to magnetic surveys, *Geophys. Surv.* 4:255–296.

Seno, T., and Maruyama, S. 1984. Paleogeographic reconstruction and origin of the Philippine Sea, *Tectonophysics* 102:53–54.

Sibuet, J.-C. 1991. The southern Okinawa Trough, in *Taicrust Workshop Proc.*, June 10–12, 1991, National Taiwan University, Taipei, Taiwan, R.O.C., pp. 117–126.

Sibuet, J.-C. 1992. New constraints on the formation of non-volcanic continental Galicia–Flemish Cap conjugate margins, *J. Geol. Soc. London* 149:829–840.

Sibuet, J.-C., Dyment, J., Bois, C., Pinet, B., and Ondréas, H. 1990. Crustal structure of the Celtic Sea and western approaches from gravity data and deep seismic profiles: Constraints on the formation of continental basins, *J. Geophys. Res.* 95:10,999–11,020.

Sibuet, J.-C., Letouzey, J., Barbier, F., Charvet, J., Foucher, J.-P., Hilde, T. W. C., Kimura, M., Ling-Yun, C., Marsset, B., Müller, C., and Stéphan, J.-F. 1987. Backarc extension in the Okinawa Trough, *J. Geophys. Res.* 92:14,041–14,063.

Sibuet, J.-C., Letouzey, J., Marsset, B., Davagnier, M., Foucher, J.-P., Bougault, H., Dosso, L., Maury, R., and Joron, J.-L. 1986. Tectonic evolution and volcanism of Okinawa Trough (abstract), *Am. Assoc. Petrol. Geol. Bull.* **70**:934.

Sibuet, J.-C., Monti, S., Réhault, J.-P., Durand, C., Gueguen, E., and Louvel, V. 1991. Quantification de l'extension liée à la phase pyréneenne et géométrie de la frontière de plaques dans la partie ouest du golfe de Gascogne, *C.R. Acad. Sci. Paris* **317**:1207–1214.

Sun, S. C. 1981. The Tertiary basins of off-shore Taiwan, ASCOPE, Manila.

Taylor, B., Klaus, A., Brown, G. R., and Moore, G. F. 1991. Structural development of Sumisu rift, Izu-Bonin arc, *J. Geophys. Res.* **96**:16,113–16,129.

Tsai, Y.-B. 1986. Seismotectonics of Taiwan, *Tectonophysics* **125**:17–37.

Tsuburaya, H., and Sato, T. 1985. Petroleum exploration well Miyakojima–Oki, *J. Jpn. Assoc. Petrol. Technol.* **50**:25–53.

Ueda, Y. 1986. Geomagnetic anomalies around the Nansei Soto (Ryukyu Islands) and their tectonic implications, *Bull. Volcanol. Soc. Jpn.* **31**:177–192.

Ujiie, H. 1980. Significance of "500 m deep island shelf" surrounding the southern Ryukyu Island arc for its Quaternary geological history, *Quat. Res.* **18**:209–219.

Uyeda, S. 1977. Some basic problems in trench-arc-back-arc-system, in *Island Arcs, Deep Sea Trenches and Back-Arc Basins* (M. Talwani and W. C. Pitman III, eds.), Maurice Ewing Ser., Vol. 1, pp. 1–14, American Geophysical Union, Washington, DC.

Uyeda, S., Kimura, M., Tanaka, T., Kaneoka, J., Kato, Y., and Kushiro, I. 1985a. Spreading center of the Okinawa Trough, *Tech. Rep. JAMSTEC*, pp. 123–142.

Uyeda, S., Nagumo, S., and Hilde, T. W. C. 1985b. Okinawa Trough—An early stage of continental margin rifting, in *1985 Geodynamics Symposium on Intraplate Deformation: Characteristics, Processes, and Causes*, Texas A&M University, College Station, TX.

Vander Zouwen, D. E. 1984. Structure and evolution of Southern Okinawa Trough, Master's thesis, Texas A&M University, College Station.

Warner, M. R. 1987. Seismic reflections from the Moho: The effect of isostasy, *Geophys. J. R. Astron. Soc. London* **88**:425–435.

Wessel, P., and Smith, W. M. F. 1991. Free software helps map and display data, *EOS, Trans. AGU* **72**:441–446.

Yamano, M., Uyeda, S., Foucher, J.-P., and Sibuet, J.-C. 1989. Heat flow anomaly in the middle Okinawa Trough, *Tectonophysics* **159**:307–318.

Yamano, M., Uyeda, A., Kinoshita, H., and Hilde, T. W. C. 1986. Report on DELP 1984 cruises in the Middle Okinawa Trough. Part IV: Heat flow measurements, *Bull. Earthquake Res. Inst., U. Tokyo* **61**:251–267.

Transition between the Okinawa Trough Backarc Extension and the Taiwan Collision:

New Insights on the Southernmost Ryukyu Subduction Zone

Les analyses de l'ensemble des données géophysiques dans la partie sud de la zone de subduction des Ryukyus ont permis d'indiquer que la région située à l'ouest de 123,5°E présente des failles dextres majeures orientées NW-SE, ce qui s'oppose au mécanisme du modèle de collision arc-continent engendrant l'ouverture du bassin d'Okinawa. Les structures identifiées dans cette région sont en faveur d'une collision arc-arc pour expliquer la surrection de Taiwan et la fermeture d'une partie du bassin arrière-arc d'Okinawa.

Transition between the Okinawa Trough Backarc Extension and the Taiwan Collision: New Insights on the Southernmost Ryukyu Subduction Zone

Shu-kun Hsu[1,2], Jean-Claude Sibuet[1] , Serge Monti[1] , Chuen-Tien Shyu[3] and Char-Shine Liu[3]

[1] Ifremer, Centre de Brest, BP 70, 29280 Plouzané, France
[2] GDR 910 du CNRS, Université de Bretagne Occidentale, BP 809, 29285 Brest, France
[3] Institute of Oceanography, National Taiwan University, Taipei, Taiwan, ROC

Abstract

Located between the Okinawa trough (OT) backarc basin and the collisional zone in Taiwan, the southernmost Ryukyu subduction zone is investigated. This area, including the southwestern portions of the OT and Ryukyu island arc (RA) and located west of 123.5°E, is named the "Taiwan-Ryukyu fault zone" (TRFZ). West of 123.5°E, the OT displays NNW-SSE structural trends which are different in direction from the ENE-WSW trending pattern of the rest of the OT. Using joint analysis of bathymetric, magnetic, gravity and earthquake data, three major discontinuities, that we interpret as right-lateral strike-slip faults (Faults A, B and C), have been identified. These faults could represent major decouplings in the southern portion of the Ryukyu subduction zone: each decoupling results in a decrease of the horizontal stress on the portion of the RA located on the eastern side of the corresponding fault, which allows the extension of the eastern side of OT to proceed more freely.

We demonstrate that the 30° clockwise bending of the southwestern RA and the consecutive faulting in the TRFZ are mainly due to the collision of the Luzon arc with the former RA. After the formation of Fault C, the counterclockwise rotated portion of the ancient RA located west of the Luzon arc was more parallel to the Luzon arc. This configuration should have increased the contact surface and friction between the Luzon arc and the ancient RA, which could have reduced the northward subduction of the Luzon arc. Thus, the westward component of the compressive stress from the collision of the Luzon arc should become predominant in the collisional system resulting in the uplift of Taiwan. Presently, because the most active collision of the Luzon arc has migrated to the

central Taiwan (at about 23°N; 121.2°E), the southwestern OT has resumed its extension. In addition, the later resistent subduction of the Gagua ridge could have reactivated the pre-existing faults A and B at 1 M.y. ago and present, respectively.

From 9 to 4 M.y., a large portion of the Gagua ridge probably collided with the southwestern RA. Because of its large buoyancy, this portion of the ridge resisted to subduct beneath the Okinawa platelet. As a result, we suggest that a large exotic terrane, named the Gagua terrane, was emplaced on the inner side of the present Ryukyu trench. Since that period, the southwestern portion of the Ryukyu trench was segmented into two parallel branches separated by the Gagua ridge: the eastern segment propagated westward along the trench axis while the western segment of the trench retreated along the trench axis.

Key words: arc-arc collision, backarc extension, along-axis propagating trench, trench segmentation, Gagua ridge, Luzon arc, Taiwan, Okinawa trough.

1. Introduction

The Okinawa trough (OT), located landward the Ryukyu island arc (RA), is a backarc basin developed in a continental domain (Figure 1) (Lee et al., 1980; Letouzey and Kimura, 1985; Sibuet et al., 1987). Because the OT terminates at the western limit of the Ilan plain (northeastern Taiwan), where the Lishan fault begins (Figures 1 and 2b), the initial formation of the OT was therefore frequently considered to be associated with the collisional process in Taiwan (Letouzey and Kimura, 1985; Suppe, 1984; Teng, 1990; Angelier, 1990). In other words, previous interpretations were based on an arc-continent collision model which suggests a continuous evolution from a compressional regime to an extensional regime, such as the lateral extrusion model of Letouzey and Kimura (1985). However, the existence of NS structural discontinuities found in the Ilan plain (Hsu et al., 1995b) raises fundamental questions about the collision-controlled models of the OT opening. A recent arc-arc collision model, proposed by Hsu and Sibuet (1995) and Hsu et al. (1995a), suggests that a former subduction zone extended from southwestern Taiwan to southern Japan prior to the uplift of Taiwan. In this hypothesis, Taiwan mountain building started after the closure of the oceanic domain located between the Luzon arc and the former RA. The Hsüeshan and the Backbone ranges, located on the western and eastern sides of the Lishan fault respectively, are therefore interpreted as the closure of a former backarc basin and the Tananao complex as part of the former Ryukyu arc.

The region of the present-day southernmost Ryukyu subduction zone is named the Taiwan-Ryukyu fault zone (TRFZ) (shaded zone in Figure 1). This region is located west

of 123.5°E and includes the southwestern portions of the OT and Ryukyu island arc (RA). Southwest of the TRFZ, the collisional processes dominates the uplift of Taiwan, while east of this zone, the OT tensional features are not or are only weakly affected by the Luzon arc collision, as evidenced by the regular shape of the Ryukyu subduction zone. The TRFZ still exhibits tensional features within the backarc basin as attested by active extensional focal mechanism of earthquakes (Yeh *et al.*, 1991; Cheng *et al.*, 1992). However, even if this area is not directly involved in the uplift processes in Taiwan, the abnormal curvature of the RA suggests that the Taiwan collision process has affected this area. Consequently, the TRFZ provides a natural laboratory to study the interplay between backarc extensional and collisional processes.

In this paper, we propose to compile new bathymetric and gravity maps which will be used, in addition to the already compiled magnetic map (Sibuet *et al.*, 1995), to jointly identify geologic boundaries. The interpretation of these features will help to better understand how and why the RA bends in its southwestern portion and why the OT disappears in northeastern Taiwan.

2. New Bathymetric Map

In this section, we present a new bathymetric map (Figure 2a). The digital data consist of 87 oceanic cruises extracted from the National Geophysical Data Center (NGDC) and the Institute of Oceanography of National Taiwan University data banks (Table 1, Figure 3 and Plate 1). First of all, a cross-over technique was applied (Hsu, 1995) to automatically calculate all the cross-over errors (XOEs) (Figure 4). From the XOE information we define

$$W_i = N / \sum_{j=1}^{N} (XOE_{i,j})^2$$

as the relative weighting function which represents the data quality of each cruise (Table 1). W_i is the weight for the ith cruise, $XOE_{i,j}$ is the jth XOE for the ith cruise, while N represents the total number of cross-over points (XOPs) for the ith cruise. To enhance the confidence of depth estimation and to avoid pseudo-features in the contour map generated from large XOEs along ship tracks, all the XOEs at the XOPs were eliminated, and a new value was assigned at each XOP, according to the relative weights of the two intersecting cruises. Between consecutive XOPs, the rest of the data was proportionally adjusted according to the newly computed values at the two XOPs (Hsu, 1995). The root-mean-square error (rms) for all the XOEs is 119.3 meters (Figure 4b). Cruises characterized by

115

average XOE values larger than 200 meters, an arbitrary defined truncated value, were removed. Remaining data were contoured by using the method of continuous curvature splines in tension (Smith and Wessel, 1990). However, because bathymetric data are not homogeneously distributed, the area located east of 123°E and south of 24°N was drawn by hand, taking into account the general trends given by the satellite derived marine gravity map (Sandwell et al., 1994). Except that, all the iso-contours were drawn automatically without human judgement. In addition, a Seabeam map of the area located near the southwestern Ryukyu trench and Gagua ridge intersection (22°20'N to 24°20'N and 122°50'E to 126°20'E, Matsumoto et al., 1993) was added. On land, the Digital Elevation Model (DEM) of Taiwan (Deffontaines et al., 1994; Lee, 1994) was added into the digital dataset. For compatibility with shipboard bathymetric data, DEM data were converted into the same geographic coordinate system. The spatial resolution of the DEM data is 500 m x 500 m in the horizontal plane and about 75 m in elevation (Deffontaines et al., 1994). This resolution is roughly similar to the one of the bathymetric map. A 3-D topographic model has also been produced (Figure 2b).

With respect to previously published bathymetric maps (e.g. Sibuet et al., 1987), the present bathymetric map is systematically more reliable because XOEs are zero. However, for local studies (e.g. the morphology of a canyon) detailed surveys are needed. The new major features which appear on the bathymetric and topographic maps (Figures 2a and 2b) are:

(1) West of 123.5°E, the OT gradually narrows and ends formally into the Ilan plain (Figure 2b). However, the backarc basin is prolonged by the deep valley corresponding to the Lishan fault. In the Hsu and Sibuet (1995) and Hsu et al. (1995a) hypothesis, the suture zone along the Lishan fault corresponds to the closure of an uplifted former backarc basin.

(2) The Gagua ridge is a pronounced linear feature trending N004° near the 123°E meridian. It is composed of a succession of seamounts and elongated ridges.

(3) The Nanao basin extends from Taiwan to 125°E. A major change in the direction of this basin appears at 123.6°E longitude. This change of direction is related to a N135° bathymetric trend cutting across the Nanao basin and extending to the RA.

(4) The region located between 125.7°E and 127.7°E is a positive topographic forearc feature of the RA. It is in the eastern prolongation of the Nanao basin and is also characterized by a poor magnetic anomaly, a strong gravity anomaly and low seismicity.

(5) Several pronounced bathymetric depressions trending NNE-SSW at 21°N; 122°E and NE-SW at 20°N; 122°E, separate the Luzon arc into several segments. These depressions have been interpreted as strike-slip faults (Karig, 1973) or thrust faults (Lewis and Hayes, 1989), implying that the Luzon arc is not a rigid feature. As the Luzon arc

progressively changes of direction from N345° at 20°-22°N to N020° east of Taiwan, we suggest that the EW depression located near 22.3°N; 121.5°E (between the islands of Lutao and Lanhsu) corresponds to a major discontinuity of the Luzon arc linked to a major change in stress conditions. Moreover, this depression is prolonged in the Gagua basin by a N070° feature, along which several earthquakes of magnitude larger than 6 indicate a dextral strike-slip motion. This motion is also confirmed by the marine gravity anomalies (Sandwell et al., 1995), which shows a right-lateral offset of the trends between the Lutao and Lanhsu islands. In addition, the bathymetric map shows that the eastern side of the Luzon arc seems to be limited by a linear feature trending NW-SE, roughly along the 4000-m isobath (21.5°N; 122°E).

(6) The width of the Luzon arc progressively decreases in the northward direction to almost zero at 24°N. Taking into account the geodetic information of Yu *et al.* (1995), it implies that the Luzon arc could have begun to subduct beneath Taiwan at least north of 23.5°N.

(7) In eastern Taiwan, the Longitudinal valley is considered as the suture zone between the former Ryukyu arc and the Luzon arc (Hsu et Sibuet, 1995; Hsu *et al.*, 1995a). This suture zone is probably connected to the Nanao basin, as shown by the continuity of the topographic depressions from the northern end of the Longitudinal valley to the western end of the Nanao basin.

(8) NW-SE directions which appear in the Philippine Sea close to the Ryukyu trench (between 125°E and 126°E) on the Japanese swath bathymetric survey (Matsumoto *et al.*, 1993) correspond to the oceanic rift fabric formed at the time of magnetic anomaly 20 (Hilde and Lee, 1984).

(9) Several new seamounts (S1 to S5) have been identified in the oceanic domain, close to the Ryukyu trench.

(10) West of 120°E, the continental margin is supposed to be a former subduction zone (Hsu and Sibuet, 1995 and Hsu *et al.*, 1995a). The location of the paleo-trench would correspond to the EW depression parallel to 21.3°N. This segment of paleo-trench could be connected to the Longitudinal valley through the southward offshore extension of the Longitudinal valley (i.e. the South Longitudinal trough) (Figure 2b).

3. New Gravity Anomaly Map

To determine the geological boundaries, new free-air and Bouguer gravity anomaly maps have been produced. The shipboard gravity data have been extracted from the NGDC data base. Gravity data have been acquired during 53 different cruises (Figure 5) and re-corrected by the IAG system 1967. After correction, the rms of the total XOEs is

14.4 mGal (Figure 6). Then, all the XOEs have been eliminated by linear adjustment to avoid linear pseudo-structures as previously mentioned. The free-air gravity anomaly map (Figure 7a) has been obtained by contouring the adjusted data with the GMT-free software (Wessel and Smith, 1991). To obtain the Bouguer anomaly (Figure 7b), the bathymetric and free-air gravity anomaly datasets were gridded in a similar manner (5'x5') and the water effect of each 5'x5' rectangular prism was replaced by a sedimentary prism of density 1.67 g/cm^3. Because of the limited extent of the bathymetric map, the edge effect is not corrected on the Bouguer anomaly map. However, this effect is limited to the borders of the map.

4. Identification of Three Major Discontinuities

To outline geological boundaries such as faults or contacts, a second-order enhanced analytical signal technique has been used (Hsu *et al.*, 1995b). This method helps to locate the geological boundaries by tracing the maximum amplitudes of second-order enhanced analytical signal which is composed of the curvature values of the two horizontal and the vertical derivatives of the potential field anomalies. The relationship between each maximum amplitude and the depth from the measured surface to the top surface of the boundary corresponds to a peak of a bell-shaped function and is expressed as:

$$|A_2|_{max} = \left| \sqrt{(\frac{\partial^2 G_x}{\partial z^2})^2 + (\frac{\partial^2 G_y}{\partial z^2})^2 + (\frac{\partial^2 G_z}{\partial z^2})^2} \right|_{max} = \frac{|2\alpha|}{d^3}$$

where G is the gravity (or the magnetic anomaly);

$$G_x = \frac{\partial G}{\partial x}; \quad G_y = \frac{\partial G}{\partial y}; \quad G_z = \frac{\partial G}{\partial z};$$

d is the distance to the top surface of the causative source;

α is a coefficient of ambient parameters such as the intensity, inclination and declination of magnetization or the density contrast of the gravity source.

For a simple estimation of the depth d, the amplitude ratio method (Hsu *et al.*, 1995b) is used:

$$d \cong \sqrt{2} \times \sqrt{\frac{|A_0|}{|A_2|_{max}}}$$

118

where $|A_0| = \left| \sqrt{(G_x)^2 + (G_y)^2 + (G_z)^2} \right|$

The major advantages of this technique are: (1) the interference effect between close anomalies is reduced; (2) the determined locations of maximum amplitudes are independent of ambient parameters (such as inclination and declination of magnetization); and (3) the determination of maximum amplitudes can be automatically achieved by examining every 9-point grid-cell (Blakely and Simpson, 1986). However, for real data, the topographic effect and the high frequency error render this method less powerful. For that reason, we have used both the gravity anomalies presented here and the magnetic anomalies (Figure 8) compiled by Sibuet et al. (1995) to determine the geological boundaries. In addition, to avoid contour artefacts due to an insufficient density of shipboard data, a low-pass gaussian filter of 15 km has been applied to the gridded data sets before applying the enhanced analytic signal method.

The locations and depths to the top surfaces of geological boundaries have been identifed by using both gravity and magnetic anomalies (Figures 9 and 10). For better understanding, the continuation of boundaries has been drawn by hand. A careful examination of the identified boundaries with the bathymetric map shows that the topographic effect is dominant, especially on the OT margins. Among the detected boundaries, three major structural boundaries (discontinuities) trending roughly NW-SE appear in the southwestern OT (Faults A, B and C in Figure 7a to Figure 12). For comparison these discontinuities are plotted at the same location on each figure. The enhanced analytic signals associated with the three discontinuities are weak but their existence is confirmed by the abrupt truncation of several roughly NE-SW trending boundaries. This phenomenon implies that either the contrast of physical properties on each side of these discontinuities is weak, or their throw is small. We interpret these three discontinuities as faults because they correspond to bathymetric offsets or changes in the direction on the northern RA margin (Figure 11), which suggests a dextral strike-slip motion along these faults. In addition, the northwestern ends of the three faults are connected with canyons (e.g. in regions C1 and C2 of Figure 11) which are generally consistent with the structural trends. These faults are likely to extend northwestward on the continental shelf up to about 26°N, taking into account the seismic interpretations of Huang et al.. (1992) and Chen and Watkins (1994) on the continental shelf of the northern Taiwan. Moreover, as shown by the epicentral distribution of the NEIC's (National Earthquake Information Center) earthquake data for magnitude greater than 4 from 1965 to 1992, the density of earthquakes varies from one side to the other side of each fault (Figures 12a and 12b). From the distribution of sedimentary patterns and focal

mechanisms of earthquakes, several authors (Wageman *et al.*, 1970, Karig, 1973; Yen, 1975; Wu, 1970 and 1978; Lallemand *et al.*, 1995) have also suggested a dextral strike-slip tectonic regime in the region around the southernmost RA.

The discovery of these right-lateral strike-slip faults provides a very important constraint for the tectonic evolution of the southernmost Ryukyu subduction zone because: (1) They are continuous features that extend from the arc to the backarc region and the continental shelf. As evidenced by the depths of the earthquakes, the faulting could reach 30 km deep in the crust (Figure 12b). (2) Though no transform faults or fracture zones have been observed in the whole Okinawa trough (Sibuet *et al.*, 1987), the NNW-SSE orientation of Faults A, B and C might suggest that these faults are reactivated backarc basin fracture zones because they are quite parallel to the theoretical direction of the OT fracture zones (Sibuet *et al.*, 1995). Nevertheless, because they are continuous features and could be produced by an external force (indentation process) acting on the RA (see later), it is more probable that they represent dextral strike-slip faults.

5. Indentation tectonics of the southwestern Ryukyu subduction zone

Because of data density and in order to reduce the topographic effect, a 20-60 km gaussian band-pass filter was applied to the gravity and magnetic maps. Two major provinces appear in the southern OT (Figures 13 and 14). In the eastern province (east of 123.5°E), the ENE-WSW structural trends are roughly parallel to the en-échelon extensional depressions located in the central trough. By contrast, features of the western province (west of 123.5°E) are mainly NNW-SSE oriented. These latter trends, roughly parallel to the identified Faults A, B and C, and the development of canyons help to define a distinct portion of arc and backarc region named the Taiwan-Ryukyu fault zone (TRFZ) (Figure 2a).

5.1. BENDING OF THE SOUTHWESTERN RYUKYU ARC

The morphology (Figure 11) shows that: (1) the two segments of bathymetric slopes located west of Faults A and B (segments S1 and S2) are roughly parallel and EW oriented; (2) the segment S3, located in the non-deformed area of the Okinawa trough, is oriented N60°. If we assume that the northern margin of the RA was formerly oriented N60°, then the western portion of the south RA was rotated clockwise of about 30° around a pole of rotation located east of Fault A, possibly near 24°N; 123.6°E (point P in upper diagram of Figure 11). We suggest that this rotation was mainly due to the collision of the Luzon arc with the RA and mostly occurred before the initial uplift of Taiwan. The angle

120

of rotation is, however, smaller than the total bending angle (about 50°) between the strike of the undeformed RA (parallel to segment S3) and the mean strike of the southernmost RA (west of 123.5°E). This means that part of the bending would have been accommodated by the dextral strike-slip motions along the Faults A, B and C.

Marine normal faults, generally N-S oriented, around the Miyako island (Figure 11) suggest an extensional regime east of 123.5°E, while around the Yonaguni island (at about 122.9°E, 24.4°N) the tectonic features are roughly EW oriented and the principal stress is roughly oriented NW-SE on this island (Kuramoto and Konishi, 1989). These observations suggest that, west of 123.5°E, the bent RA is still in a compressional regime.

Numerous earthquakes with compressional focal mechanisms (Cheng et al., 1992) occurs within the bent RA, south of segments S1 and S2 (Figures 12a and 12b). In contrast, north of segments S1 and S2, numerous earthquakes with extensional focal mechanism occur in the OT. The large density of earthquakes, with extensional and compressional mechanisms, is geographically restricted west of 123.5°E and is significantly different from the earthquake density of the rest of the Ryukyu subduction zone. The abnormal amount of extensional earthquakes in the southwestern OT could be due to different factors such as a pressure release due to faulting or a decrease of temperature. The latter possibility is suggested by weak heat flow values (generally less than 1 HFU) recorded in the southwestern OT (Lu et al., 1981) and the presence of a relatively low gravity anomaly in this area (Figures 7a and 7b).

5.2. BENDING MODEL OF THE SOUTHWESTERN RYUKYU ARC

Because the convergent rate near the bent RA (about 70 mm/yr) (Seno et al., 1993) is an order larger than the average rifting rate of the OT (about 7 mm/yr) (Sibuet et al., 1995), the progressive NW bending and faulting on the southwestern RA should have induced the progressive narrowing of the southwestern OT and the continental shelf region, which may explain the triangular form of the southwestern OT and Ilan plain (Figures 2b and 11). Thus, the western end of the OT in the Ilan plain would correspond to the complete closure of the OT backarc basin, due to the collision by the northern tip of the Luzon arc pushing and bending the southwestern RA in the N310° direction (i.e. the direction of convergence of the Philippine Sea plate relative to the Eurasia) (Figure 15). Because Faults A, B and C display consecutive dextral strike-slip motions toward Taiwan (right-lateral stepping), it suggests that the horizontal compressional stress acting on the southwestern RA gradually increased westward. Accordingly, the downward component of the subduction with respect to the horizontal component should reach its minimum value at the intersection of the western end of the Ryukyu trench (the Nanao basin) and the

northern end of the Longitudinal valley (in Taiwan). This indicates that the subduction system gradually evolved into a collisional system. However, based on the occurence of abnormal quantity of the extensional earthquahes in the southern OT (Cheng *et al.*, 1992) and in the Ilan plain (Tsai *et al.*, 1975; Yeh *et al.*, 1991), the low velocity upper mantle wedge under the Ilan plain deduced from a tomographic study (Rau and Wu, 1995) and the geodetic observations in northeastern Taiwan (Yu *et al.*, 1995), the extensional process within the southwesternmost OT has probably resumed after the Luzon arc has swept the whole southwestern RA. Presently, the collision of the Luzon arc mainly concentrates in central Taiwan (at about 23°N; 12.2°E) (Yu *et al.*, 1995).

A tentative model for the collision between the Luzon arc and the ancient RA is proposed in Figures 15 and 16. The initial collision between the Luzon arc and the ancient RA could occur near 123.5°E. The large buoyancy of the Luzon arc has subsequently indented and bent the ancient RA and shortened the southern OT, generating several dextral strike-slip faults (Faults A, B and C). When Fault C occurred, the counterclockwise rotated portion of the ancient RA located west of the Luzon arc was rather parallel to the Luzon arc and most of the southwestern portion of the backarc basin was rather closed. This situation should have increased the contact surface and friction between the Luzon arc and the ancient RA (present-day Tananao complex), starting the uplift of Taiwan. Likewise, as shown by the satellite derived structural map of Taiwan (see Tsai, 1986), dextral strike-slip faults and folds resulting from the Luzon arc collision are observed in northern Taiwan. Such a mechanism, which produces brittle deformation in terms of dextral strike-slip faults, can also be observed on sandbox experiments near the free border of a rigid indenter (Lu and Malavieille, 1994).

6. Gagua Ridge and Gagua terrane

The Gagua aseismic ridge is a pronounced NS trending feature located east of Taiwan along the 123°E meridian (Figures 1 and 2a). This linear ridge is composed of several adjacent seamounts and segments of ridges. A bathymetric difference of about 1000 m is observed between the two sides of the Gagua ridge (Figure 2a) which acts as a dam for the eastward transportation of sediments coming from eastern Taiwan. The oceanic domain located west of the Gagua ridge (Gagua basin) is under compression on the basis of earthquake focal mechanisms (Yeh *et al.*, 1991) but seismic data collected by the National Taiwan University do not display any sign of compression (S. Lallemand, personal communication). However, this question is still debated.

Because the collision of the Gagua ridge could also change local stress conditions on the RA, Faults A and B may have been reactivated. In this hypothesis, taking into account

the relative motion of the Philippine Sea plate with respect to the Eurasian plate (Seno *et al.*, 1993), Fault A may have been reactivated about 1 M.y. ago. Because each fault could release external contraint (stress) on its eastern side, the OT could rift or extend more freely on the eastern side.

THE HYPOTHESIS OF THE GAGUA TERRANE AND ALONG-AXIS PROPAGATING TRENCH

A peculiar forearc feature, about 250-km long, located near 24.5°N; 126°E, displays a strong positive gravity anomaly and low seismicity (Figures 7a and 12). These properties are similar to those of stable oceanic plateaus present in today's oceans (e.g. Ben-Avraham *et al.*, 1983). We suggest that this stable feature, named here the Gagua terrane, could be part of the former Gagua ridge. If we trace back the Gagua ridge along small circles of the Philippine Sea plate relative to the Eurasian plate, the Gagua ridge was roughly south of the Gagua terrane about 9-4 M.y. ago. Accordingly, the former Gagua ridge would have collided with the RA during this period and resisted to subduct beneath the Okinawa platelet. In this hypothesis, the Gagua terrane, which was scraped from the Philippine Sea plate, was finally accreted against the forearc about 4 M.y. ago. In the above consideration, the former Gagua ridge was a large oceanic ridge with a small tail like the today's Oki-Daito ridge in the Philippine Sea. However, in the absence of any information about the geological nature of the Gagua terrane, a possibility still exits that this exotic terrane was part of the former Luzon arc.

During the accretion of this exotic terrane, a segment of the former Ryukyu trench became a suture zone and a new segment of the trench might appear south of it. After the emplacement of the Gagua terrane, the Gagua ridge resumed to subduct and the Ryukyu trench was segmented into two portions. When the Gagua ridge moves northwestward with respect to the Eurasian plate, the eastern segment of the Ryukyu trench propagated westward along the trench axis while the western segment retreated westward (Figures 12a and 16). On the basis of the topographic continuity between the northern end of the Longitudinal valley and the western end of the Nanao basin and the extremely low values of the gravity anomaly in the Nanao basin, the western segment should locate somewhere near the Nanao basin; however, it is noted that the orientations of both the Nanao basin and the bent RA are rather parallel to the direction of the present-day NW motion of the Philippine Sea plate relative to Eurasia (Figure 11). The present-day position of the trench is, hence, difficult to identify west of the Gagua ridge. This implies that, west of the Gagua ridge, the portion of the former convergent boundary could be considered today as

a segment of transform margin, which explains why the Ryukyu trench is well recognized east of 123°E and poorly expressed west of the Gagua ridge. However, because a Benioff zone can be observed there (Figure 12b), a possibility still exists that a portion of the Luzon arc would have already subducted beneath the Ryukyu subduction zone before the collision started in Taiwan.

7. Conclusions

A new bathymetric map around Taiwan has been compiled by using available data and a careful analysis of their quality. With respect to previously published bathymetric maps, new features as seamounts and rift features belonging to the northwestern Philippine Sea domain have been identified, the morphology of the Luzon arc and associated features is better defined and a clear image of the Gagua ridge and the identification of the Gagua exotic terrane have been also evidenced on gravity and magnetic data.

The main points resulting from the interpretation of the geophysical data in the southernmost Ryukyu subduction zone are:

(1) The collision of the buoyant Luzon arc with the former Ryukyu subduction zone could start near 123.5°E. The subsequent collision has resulted in the indentation and faulting of the RA and the shortening of the corresponding portion of backarc basin. Before the uplift of Taiwan, the southwestern RA bent clockwise of about 30° around a pole located near 24°N; 123.6°E and several dextral strike-slip faults probably developed during this process.

(2) Based on a joint analysis of the bathymetric, magnetic, gravity and earthquake data, three major dextral strike-slip faults (Faults A, B and C) have been identified in the TRFZ. Faults A, B and C were active during the collision of the Luzon arc. Faults A and B were probably reactivated during the northward motion of the Gagua ridge.

(3) The southwestern OT can be divided into two different provinces separated by Fault A. East of Fault A, features, generally ENE-WSW trending, belong to the backarc extensional domain. West of Fault A, features are generally NW-SE trending, and are probably related to the Luzon arc collision with the Ryukyu arc and the later motion of the Gagua ridge.

(4) After the indentation and faulting of the Ryukyu subduction zone, the counterclockwise rotated portion of the ancient RA (Tananao complex) located west of the Luzon arc was probably more parallel to the Luzon arc. This configuration should have increased the contact surface and friction between the Luzon arc and the ancient RA just before the process of the Taiwan mountain building started.

124

(5) The 250-km long portion of margin located west of the Gagua ridge has probably evolved from an active margin before the Luzon arc indentation to a transform margin, as attested now by the parallelism between the Philippine Sea plate motion with respect to Eurasia and the orientation of this margin.

(6) The Gagua terrane is a peculiar forearc feature that we suggest to belong to the former Gagua ridge. In this hypothesis, the Gagua terrane was accreted against the forearc during the 9-4 M.y. period. After the emplacement of the Gagua terrane, the Gagua ridge subducted again and the trench was segmented into two portions.

Acknowledgements

References

Angelier, J., 1990, Geodynamic evolution of the eastern Eurasian margin (Foreword), Tectonophysics **83**, VII-X.

Ben-Avraham, Z., Nur, A., Jones, D. and Cox, A., 1981, Continental accretion: from oceanic plateaus to allochonous terranes, Science **213**, 47-54.

Blakely, R. J., and Simpson, R. W., 1986, Approximating edges of source bodies from magnetic or gravity anomalies, Geophysics **51**, 1494-1498.

Chen, T.-T. and Watkins, J. S., 1994, Structure and stratigraphy of south Pengchiahsu basin, northern offshore Taiwan, Petrol. Geol., Taiwan, **29**, 127-170.

Cheng, S.-N., Lee, C.-T. and Yeh, Y.-T., 1992, Seismotectonics of the Ryukyu Arc. Proceeding of the fourth Taiwan Symposium on Geophysics, Taiwan, 507-516.

Cordell, L., and Grauch, V. J. S., 1985, Mapping basement magnetization zones from aeromagnetic data in the San Juan Basin, New Mexico, *in* Hinze, W. J., Ed., The utility of regional gravity and magnetic anomaly maps: Soc. Explor. Geophys., 181-197.

Deffontaines, B., Lee, J.-C., Angelier, J., Carvalho, J. and Rudant, J.P., 1994, New geomorphic data on the active Taiwan orogen: A multisource approach, J. Geophys. Res. **99**, 20243-20266.

Hilde, T. W. C. and Lee, C.-S., 1984, Origin and evolution of the west Philippine basin: a new interpretation, Tectonophysics **102**, 85-104.

Hsu S.-K., 1995, XCORR: a cross-over technique to adjust track data, Computers & Geosciences, **21**, 259-271.

Hsu, S.-K. and Sibuet, J.-C., 1995, Arc-arc collision: mechanism of the Taiwan mountain building, Earth Planet. Sci. Lett., submitted.

Hsu, S.-K., Sibuet J.-C. and Monti, S., 1995a, Arc-arc collision vs. backarc extension: Taiwan mountain building, ACT international conference and 3rd Sino-French symposium on active collision in Taiwan, program and extended abstracts, 22nd-23rd March, 1995, Geol. Soc. China, Taiwan, R.O.C., 121-130.

Hsu, S.-K., Sibuet J.-C. and Shyu, C.-T., 1995b, High-resolution detection of geologic boundaries from potential field anomalies: an enhanced analytic signal technique, Geophysics, in press.

Huang, S.-T., Ting, H.-H., Chen, R.-C., Chi, W.-R., Hu, C.-C. and Shen, H.-C., 1992, Basinal framework and tectonic evolution of offshore northern Taiwan, Petrol. Geol. Taiwan, **27**, 47-72.

Karig, D.E., 1973, Plate convergence between the Philippines and the Ryukyu islands, Marine Geology **14**, 153-168.

Kuramoto, S. and Konishi, K., 1989, The southwest Ryukyu arc is a migrating microplate (forearc sliver), Tectonophysics **163**, 75-91.

Lallemand, S. E., Liu, C.-S. et Lin, S.-J., 1995, Behaviour of the Ryukyu forearc sliver in the wake of the indenting northern Luzon arc (east of Taiwan), ACT international conference and 3rd Sino-French symposium on active collision in Taiwan, program and extended abstracts, 22nd-23rd March, 1995, Geol. Soc. China, Taiwan, R.O.C., 167-175.

Lee, J.-C., 1994, Structure et déformation active d'un orogène: Taiwan, Thèse de Doctorat. Univ. Pierre et Marie Curie, Paris, 281pp.

Lee, C.-S., Shor, G.G., Jr., Bibee, L.D, Lu, R.S. and Hilde, T.W.C., 1980, Okinawa trough: origin of a back-arc basin, Marine Geology **35**, 219-241.

Letouzey, J. and Kimura, M., 1986, The Okinawa trough: genesis of a back-arc basin developing along a continental margin, Tectonophysics **125**, 209-230.

Lewis, S.D. and Hayes, D.E., 1989, Plate convergence and deformation, North Luzon Ridge, Philippines, Tectonophysics **168**, 221-237.

Lu, C.-Y. and Malavieille, J., 1994, Oblique convergence, indentation and rotation tectonics in the Taiwan mountain belt: insights from experimental modelling, Earth Planet. Sci. Lett. **121**, 477-494.

Lu, R.S., Pan, J.J. and Lee C.T., 1981, Heat flow of the southwestern Okinawa trough, Earth Planet. Sci. Lett. **55**, 299-310.

Matsumoto, T., Fujioka, K., Kimura, M., Kato, Y. and Aoki, M., 1993, Detailed bottom topography in the southwesternmost part of the Nanseishoto trench area, JAMSTECR **30**, 17-36 (in Japanese with English abstract).

Rau, R.-J. and Wu, F. T., 1995, Tomographic images of the lithospheric structure under Taiwan, Earth Planet. Sci. Lett., in press.

Sandwell, D.T., Yale, M.M. and Smith, W.H.F., 1994, ERS-1 geodetic mission reveals detailed tectonic structures, EOS **75**, Abstract, 155.

Sandwell, D.T., Yale, M.M. and Smith, W.H.F., 1995, Gravity anomaly profiles from ERS-1, Topex and Geosat altimetry, EOS **76**, Abstract, 89.

Seno, T., Stein, S. and Gripp, A.E., 1993, A model for the motion of the Philippine Sea plate with NUVEL-1 and Geological data, J. Geophys. Res. **98**, 17941-17948.

Sibuet, J.-C., Letouzey, J., Barrier, F., Charvet, J., Foucher, J.-P., Hilde, T.W.C., Kimura, M., Chiao, L.-Y., Marsset, B., Muller, C. and Stephan, J.-F., 1987. Back arc extension in the Okinawa trough, J. Geophys. Res. **92**, 14041-14063.

Sibuet, J.-C., Hsu, S.-K., Shyu, C.-T. and Liu, C.-S., 1995, Structural and kinematic evolutions of the Okinawa trough back-arc basin. Backarc basins: tectonics and magmatism, Taylor, B., Ed., Plenum Press, New-York, 343-379.

Smith W. H. F. and Wessel P., 1990, Gridding with continuous curvature splines in tension, Geophysics **55**, 293-305.

Sun, S. C., 1981, The Tertiary basins of off-shore Taiwan, ASCOPE, Manila.

Suppe, J., 1984, Kinematics of arc-continent collision, flipping of subduction, and back-arc spreading near Taiwan, Mem. Geol. Soc. China **6**, 21-34.

Teng, L.S., 1990, Geotectonic evolution of late Cenozoic arc-continent collision in Taiwan, Tectonophysics **183**, 57-76.

Tsai, Y.-B., 1986, Seismotectonics of Taiwan, Tectonophysics **125**, 17-37.

Wageman, J.M., Hilde, T.W.C and Emery, K.O., 1970, Structural framework of East China Sea and Yellow Sea, Am. Assoc. Pet. Geol. Bull. **54**, 1611-1643.

Wessel, P. and Smith, W. H. F., 1991, Free software helps map and display data, EOS **72**, 441-446.

Wu, F.T., 1970, Focal mechanisms and tectonics in the vicinity of Taiwan, Bull. Seism. Soc. Amer. **60**, 2045-2056.

Wu, F.T., 1978, Recent tectonics of Taiwan. *In*: S. Uyeda, R.W. Murphy and K. Kobayashi (Eds.), Geodynamics of the Western Pacific, J. Phys. Earth, Suppl. Issue, 265-299.

Yeh, Y.-H., Barrier, E., Lin, C.-H. and Angelier, J., 1991, Stress tensor analysis in the Taiwan area from focal mechanism of earthquakes, Tectonophysics **200**, 267-280.

Yen, T.P., 1975, Lithostratigraphy and geologic structure of Taiwan, Geol. Paleontol. S. E. Asia **15**, 303-323.

Yu, S.-B., Chen, H.-Y. and Kuo, L.-C., 1995, Velocity field of GPS stations in the Taiwan area, ACT international conference and 3rd Sino-French symposium on active collision in Taiwan, program and extended abstracts, 22nd-23rd March, 1995, Geol. Soc. China, Taiwan, R.O.C., 317-327.

FIGURE CAPTIONS

Fig. 1. Schematic context showing the intermediate zone (shaded zone) between the collision in Taiwan and the Okinawa trough (OT) backarc basin. OKT: Oita-Kumamoto tectonic line; RA: Ryukyu arc; RT: Ryukyu trench; MT: Manila trench; LF: Lishan fault; MD: Miyako depression; TC: Tokara channel; LA: Luzon arc; EU: Eurasian plate; PH: Philippine Sea plate. Dashed lines and open arrows represent the small circles and the directions of motions of PH with respect to EU, according to Seno et al. (1993).

Fig. 2a. New bathymetric map around Taiwan. Mercator projection. Contour interval 200 m. Data coverage is shown in Fig. 3. See black and white foldout. TRFZ: Taiwan-Ryukyu fault zone.

Fig. 2b. 3-D topographic relief of the area located between 21°N; 26°N and 119°E; 124°E. Note the gradual narrowing from the southwestern Okinawa trough to the Lishan fault.

Fig. 3. Bathymetric ships' tracks used in this study. The identification and data quality of each cruise are shown in Table 1. The shaded area corresponds to the Seabeam survey of Matsumoto et al. (1993) added in Fig. 2a.

Fig. 4a. Average XOE of bathymetric cruise data for each 0.5 x 0.5 square degree. Unit in meters.

Fig. 4b. Histogram of bathymetric XOEs for cruise data shown in Table 1.

Fig. 5. Gravity ships' tracks used in this study.

Fig. 6. Histogram of XOEs of gravity anomalies compiled in this study.

Fig. 7a. Free-air gravity anomaly map of the southwestern OT. Positive values are shaded. Note that the step-like form of the steepest slope from 24.3°N; 122°E to 24°N; 123.5°E also reveals the locations of the right-lateral faults based on the maximum horizontal-gradient method (Cordell and Grauch, 1985).

Fig. 7b. Bouguer gravity anomaly map of the southwestern OT. Each 5' x 5' rectangular prism of water was replaced by a sedimentary prism of density $1.67g/cm^3$.

Fig. 8. Magnetic anomaly map of the southwestern OT (after Sibuet et al., 1995). Positive values are shaded. Faults A, B and C are shown.

Fig. 9. Geological boundaries of the southwestern OT detected by second-order enhanced analytic signal of the Bouguer gravity anomaly (Hsu et al., 1995b). The shaded bathymetry is superposed. Faults A, B and C are shown. Note that locations of Faults A, B and C correspond to the abrupt change of several NE-SW trending boundaries.

Fig. 10. Geological boundaries of the southwestern OT detected by second-order enhanced analytic signal of the magnetic anomaly (Hsu *et al.*, 1995b). The shaded bathymetry is superposed. Faults A, B and C are shown. Note that locations of Faults A, B and C correspond to the abrupt change of several NE-SW trending boundaries.

Fig. 11. Bathymetric map of the southwestern OT (from digital data). Heavy lines are central grabens in the OT. Lines with crosses are small circles of the motion of the Philippine Sea plate with respect to the Eurasian plate. Cross interval is 0.92 M.y. (after Seno *et al.*, 1993). The shaded area is the RA. C1 and C2 indicate location of canyons.

Fig. 12a. Distribution of earthquakes (small circles) of magnitude larger than 4. Dashed lines correspond to segments S1, S2 and S3 defined in Fig. 9. 1: propagating trench. 2: trace of the former retreating trench.

Fig. 12b. Three-dimensional distribution of the earthquakes occurring in the TRFZ. (a) Plan view distribution, superposed with shaded bathymetry. (b) Earthquake depth distribution projected perpendicular to a meridian. Elliptical shaded area represents extensional mechanism due to back-arc extension. Slab shaded area represents the Benioff zone with compressional mechanism (after Cheng *et al.*, 1992). Note that Fault A separates two groups of earthquakes in the OT and the earthquake depth in the OT is around 25 km. (c) Earthquake depth distribution projected perpendicularly to a parallel. A large number of earthquakes occurs west of the Fault B.

Fig. 13. Filtered Bouguer gravity anomaly of the southwestern OT. The filtered wavelength is 20-60 km. Positive values are shaded. The bathymetry is superposed. Note that, west of 123.5°E, the structural trends of the OT are roughly NW-SE oriented while, east of 123.5°E, features are trending ENE-WSW.

Fig. 14. Filtered magnetic anomaly of the southwestern OT. The filtered wavelength is 20-60 km. Positive values are shaded. The bathymetry is superposed. Note that, west of 123.5°E, the structural trends of the OT are roughly NW-SE oriented while, east of 123.5°E, features are trending ENE-WSW. Results are similar to those of the filtered gravity anomaly.

Fig. 15. Schematic tectonic deformation and evolution of the south RA. Region I is the region largely affected by the collision of the Luzon arc in Taiwan. Region II is the region of dextral strike-slip faults slightly reactivated by the collision of the Gagua ridge. Region III is undeformed. (a) Before the deformation, the RA was roughly NE-SW trending and the oceanic domain of the Philippine Sea subducted beneath the Okinawa platelet. (b) East of the Luzon arc, the RA started to bend clockwise while west of the Luzon arc the former RA started to bend counterclockwise. The clockwise deformation is accompanied by the occurrence of dextral strike-slip faults.

(c) At the end of bending and faulting of the RA the western bent RA is rather parallel to the Luzon arc. This situation increased the friction between the two features and the uplift of Taiwan started at that time. (d) The collision of the Gagua ridge could have reactivated the dextral strike-slip fault A. (e) Present-day configuration of the RA. Fault B have been recently reactivated.

Fig. 16. Schematic evolution of the southwestern OT with the motions of the Luzon arc and Gagua ridge. (a) Initial opening of the OT. (b) Bending and faulting of the Ryukyu arc because of the collision of the Luzon arc. (c) Beginning of the Taiwan mountain building, emplacement of the Gagua terrane. (d) Propagation of the eastern segment of the Ryukyu trench along the trench axis and the retreat of the western segment. Fault A is reactivated. (e) Present-day situation. Fault B is reactivated. EU: Eurasian plate. PH: Philippine Sea plate. Open arrows indicate the motion of the PH with respect to the EU. The mean rifting direction in the OT, proposed by Sibuet *et al.* (1995), is plotted.

Table 1. Crossover analysis of bathymetric cruises used in this study.

Plate 1. New bathymetric map around Taiwan. Mercator projection. Contour interval 200 m. Tracklines and Seabeam surveys appear on the reverse side.

Fig. 1

Fig. 2a

133
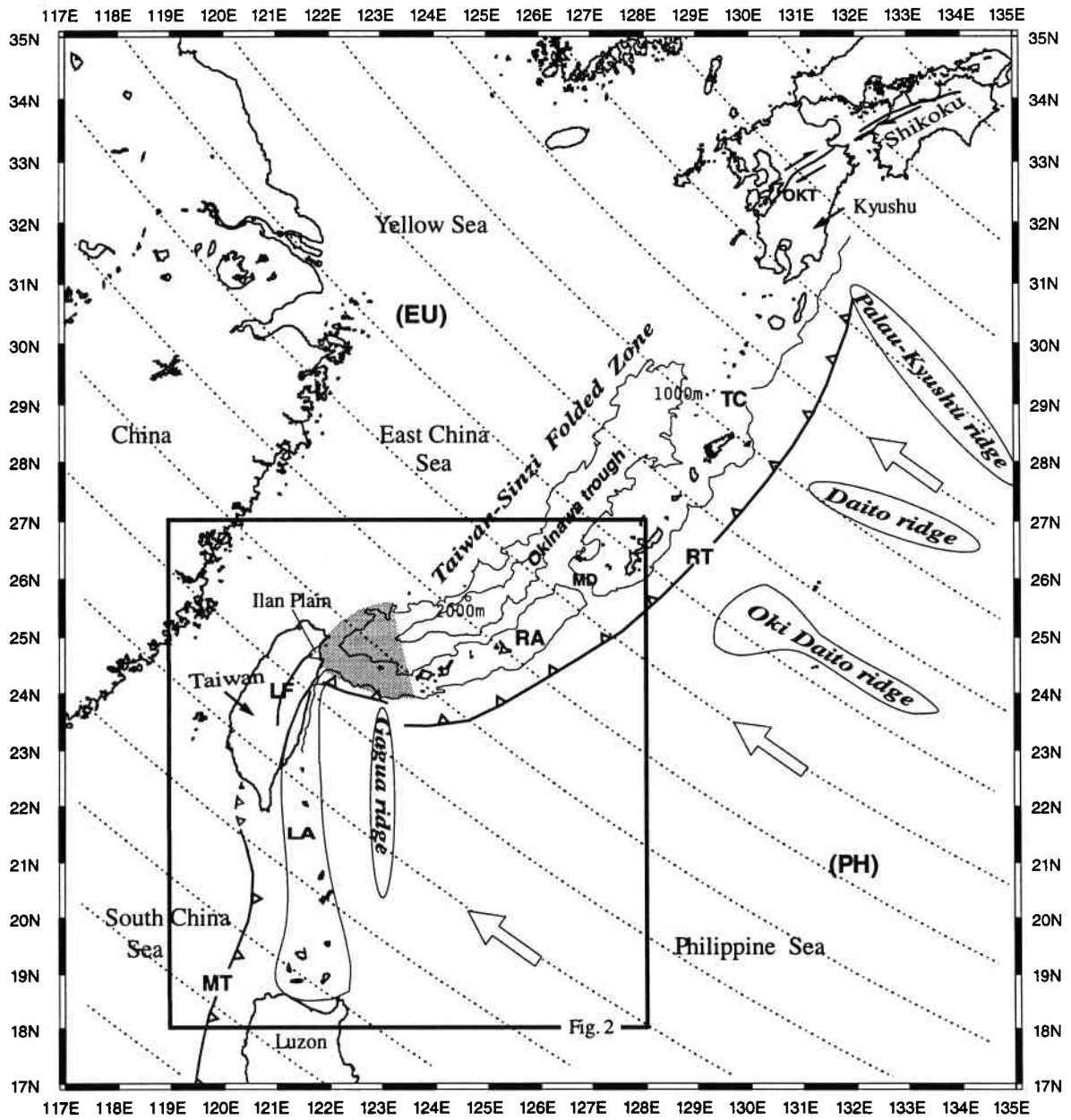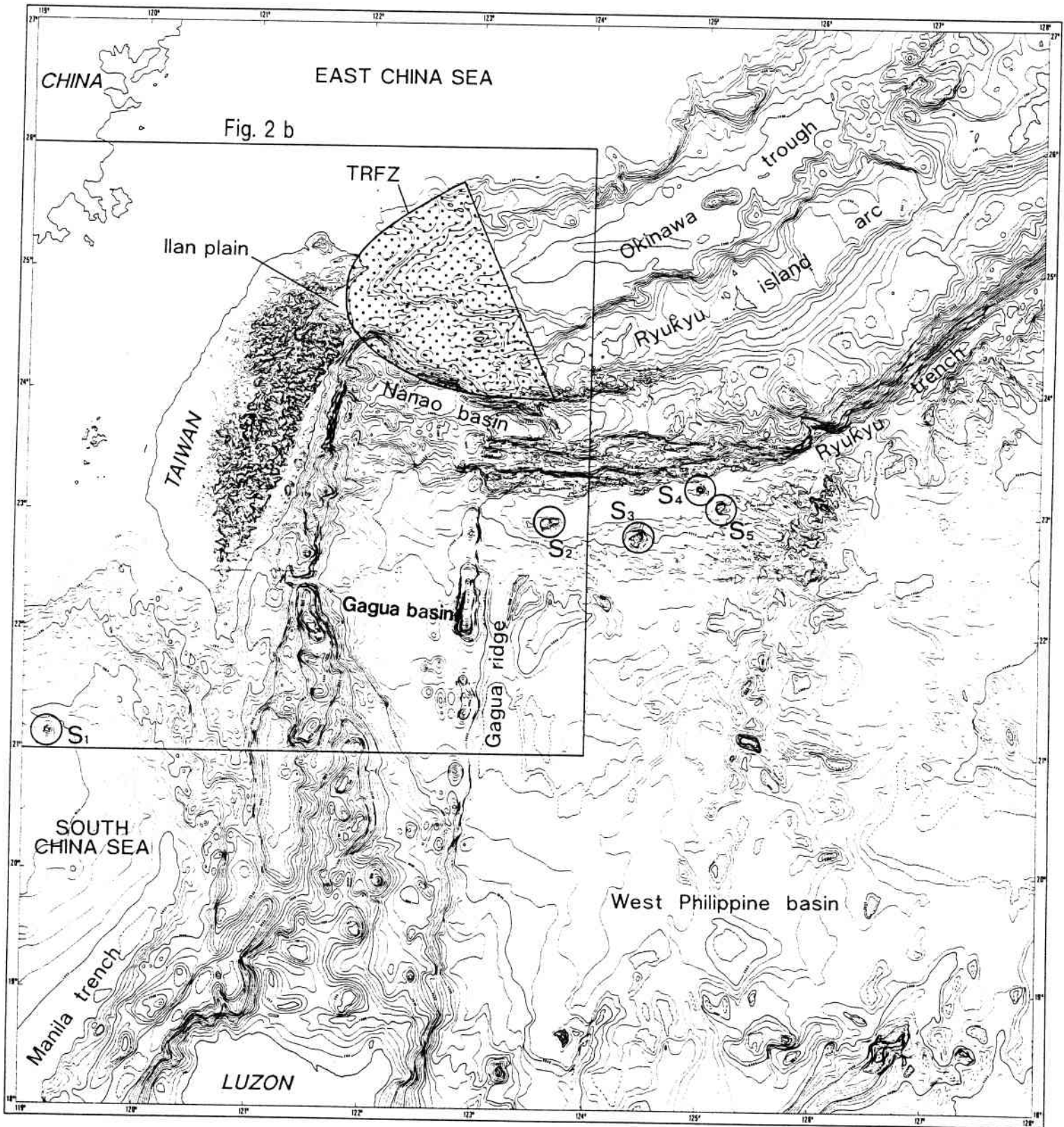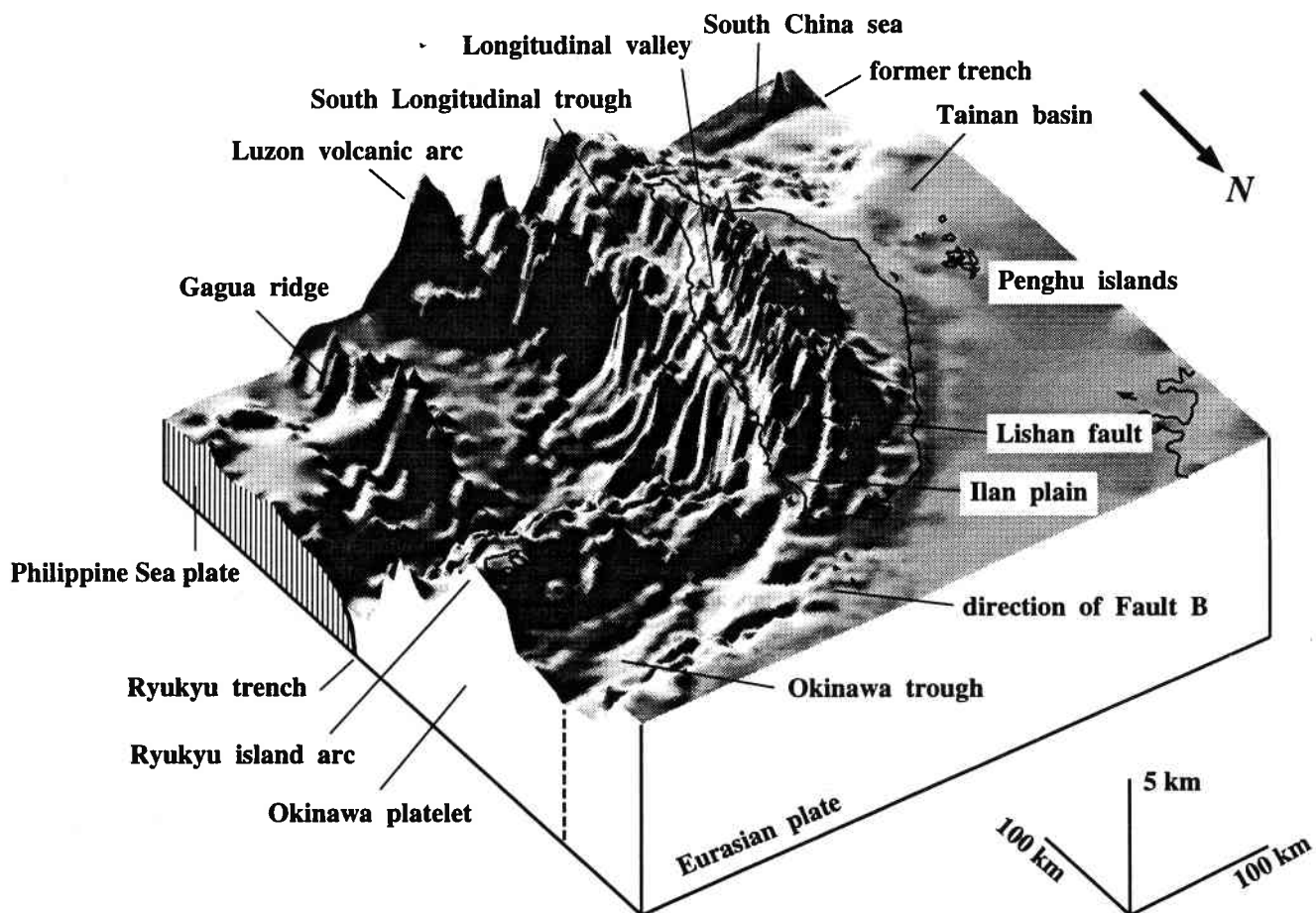
Fig. 2b

Fig. 3

Fig. 4a

Fig. 4b

138
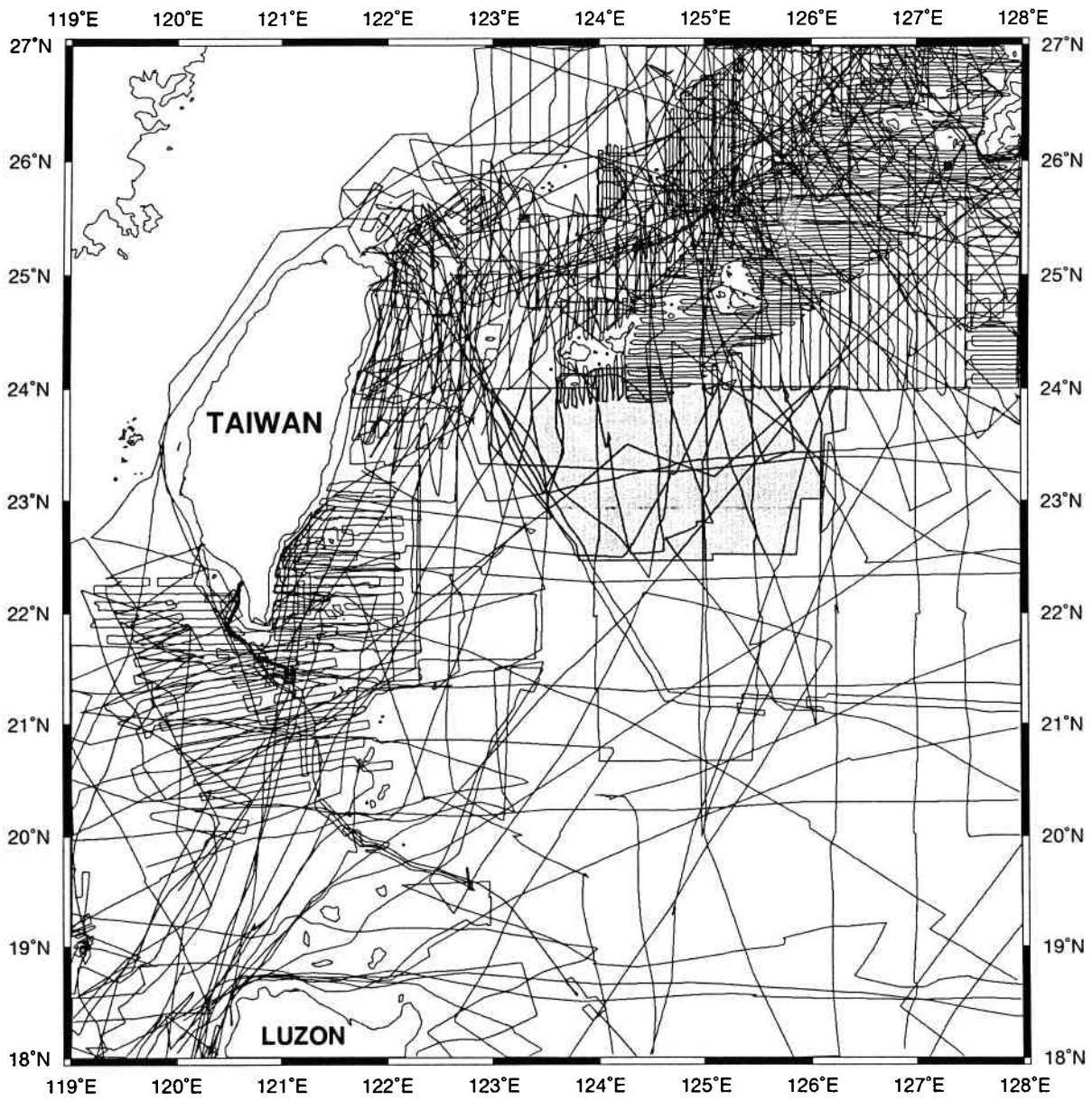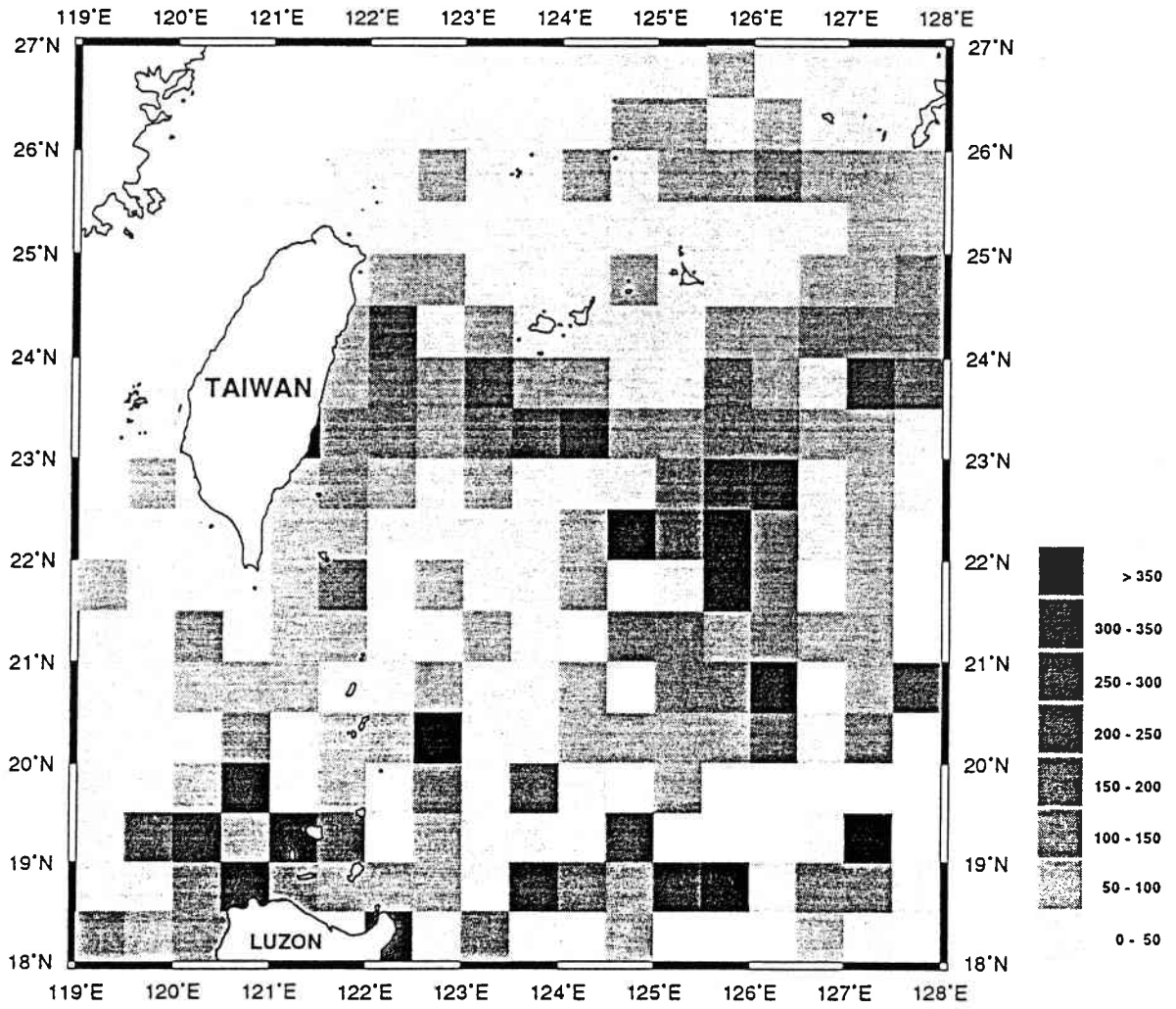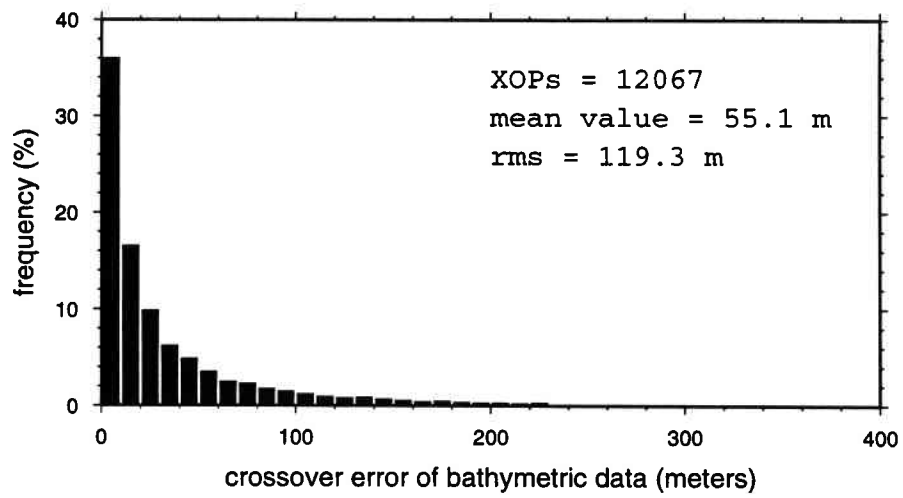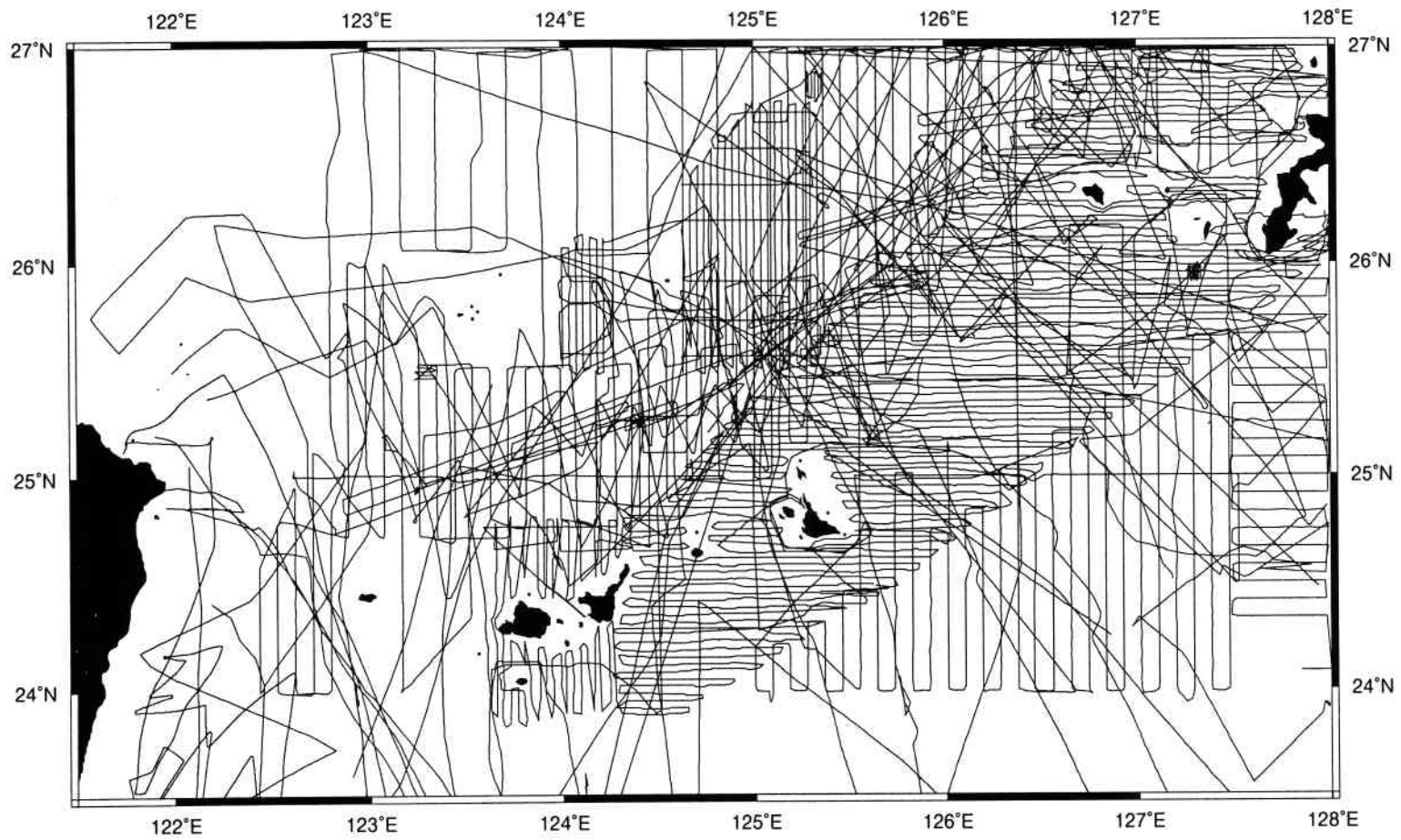
Fig. 5
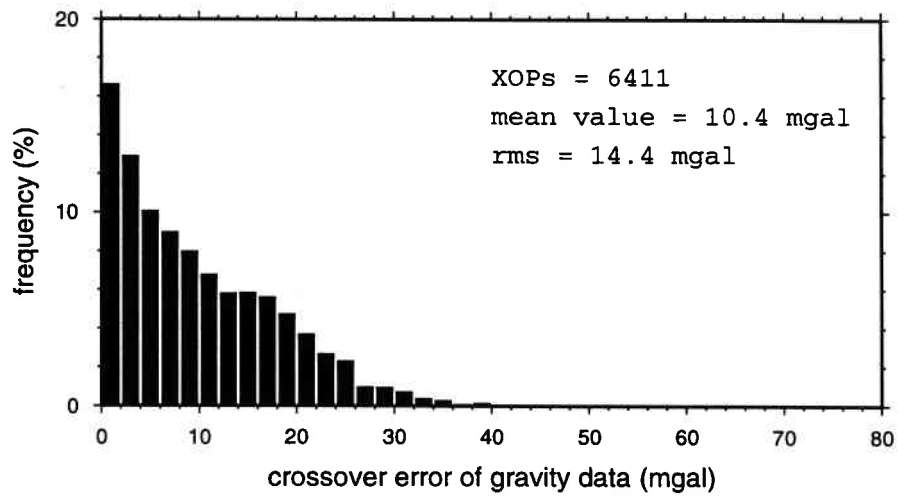
Fig. 6

Fig. 7a

Fig. 7b

Fig. 8

Fig. 9

143

Fig. 10

Fig. 11

Fig. 12a

b)

a)

c)

Fig. 12b

Fig. 13

Fig. 14

(a)

Fault B   Fault A

(b)

Fault C   Fault A
         Fault B

(c)

Fault C
    Fault B   Fault A

(d)

Fault C Fault B
         Fault A

(e)

I   II   III
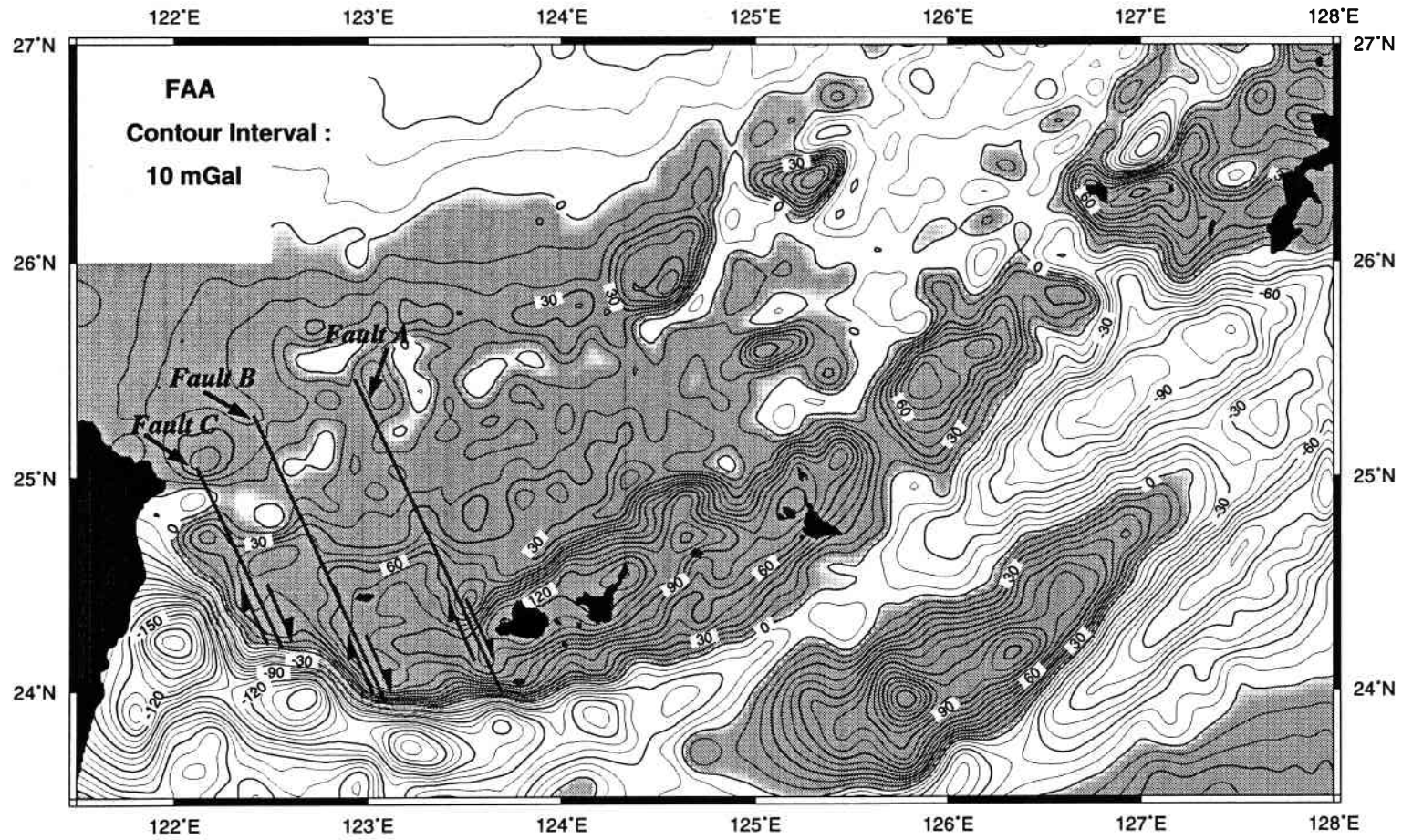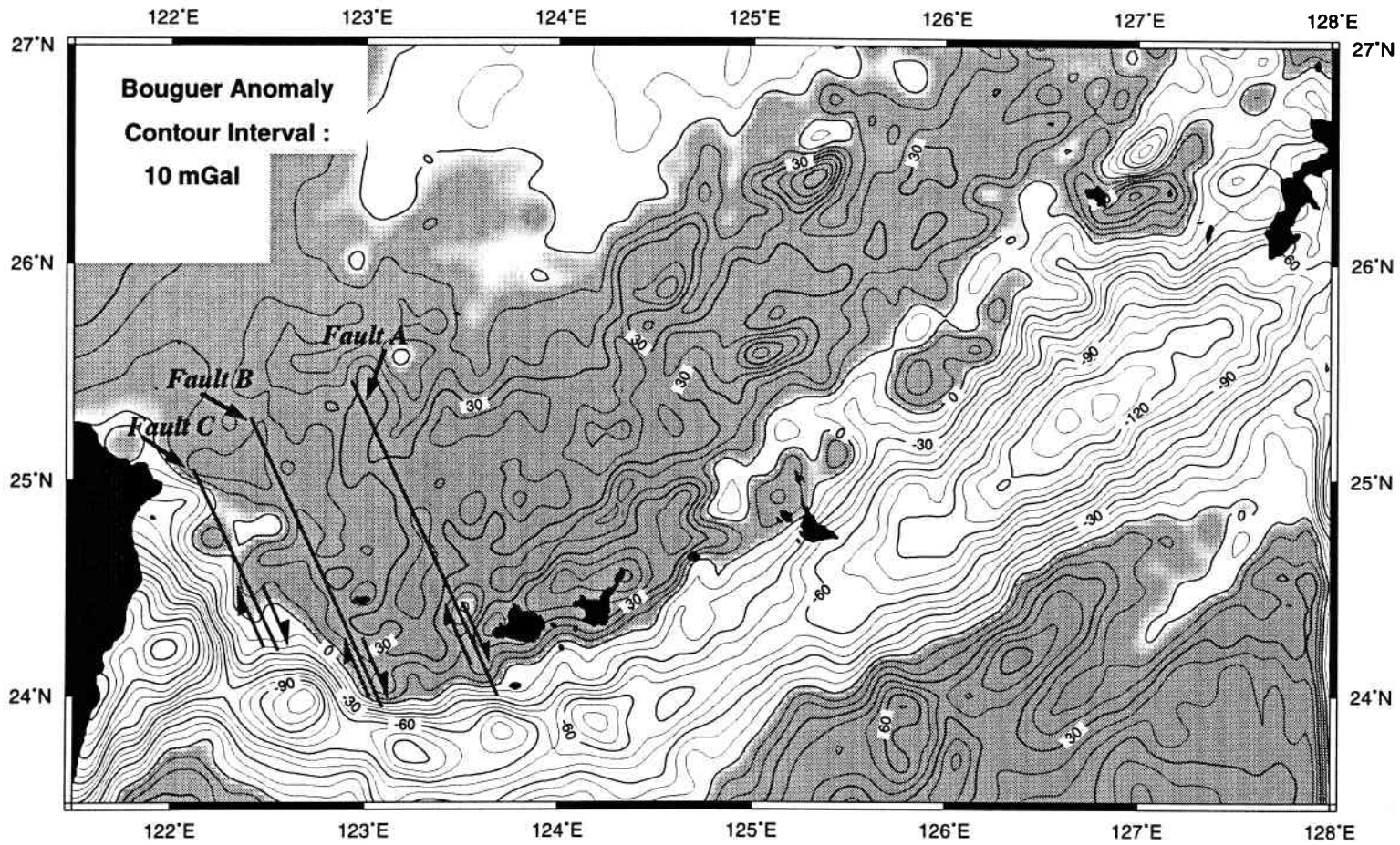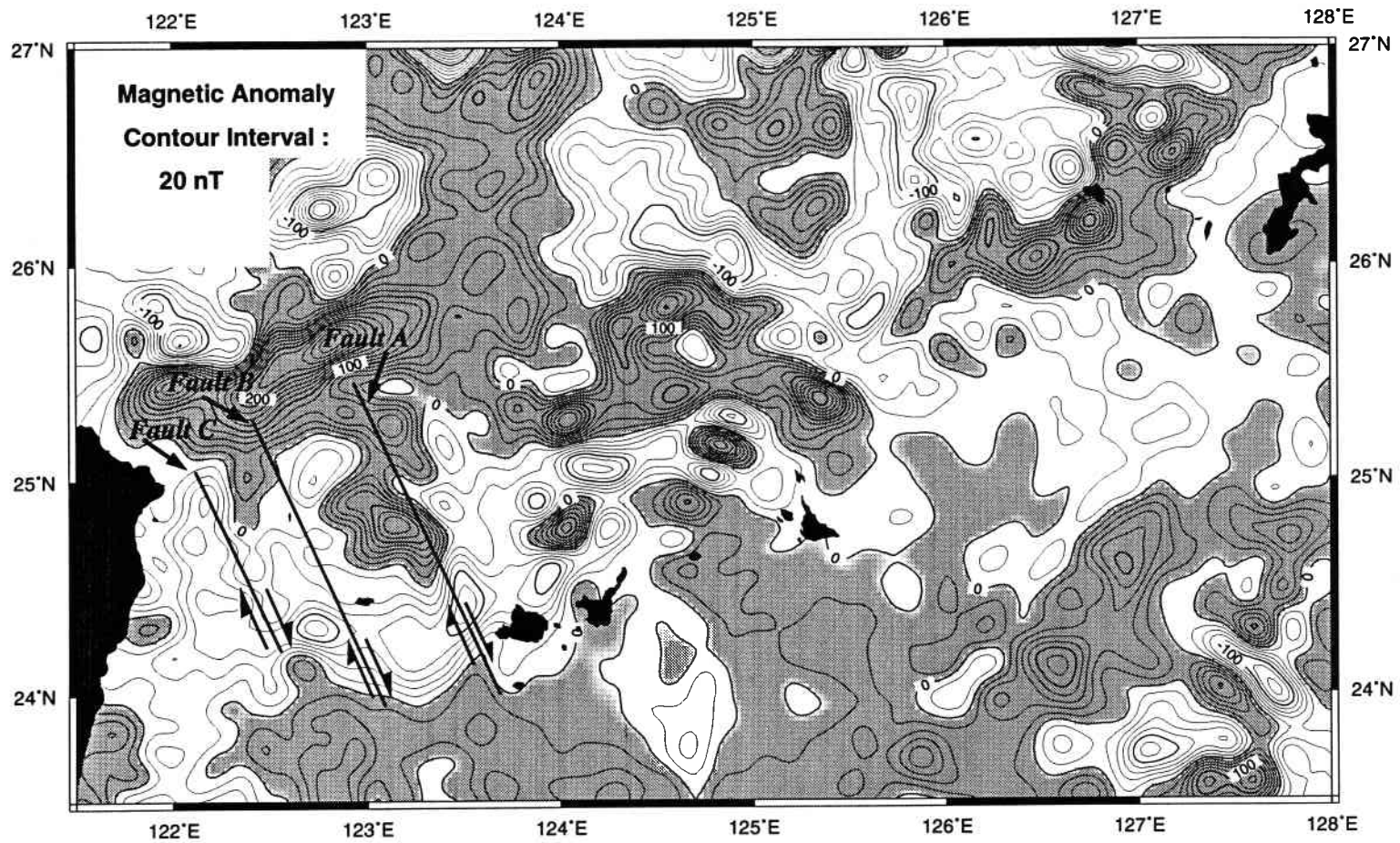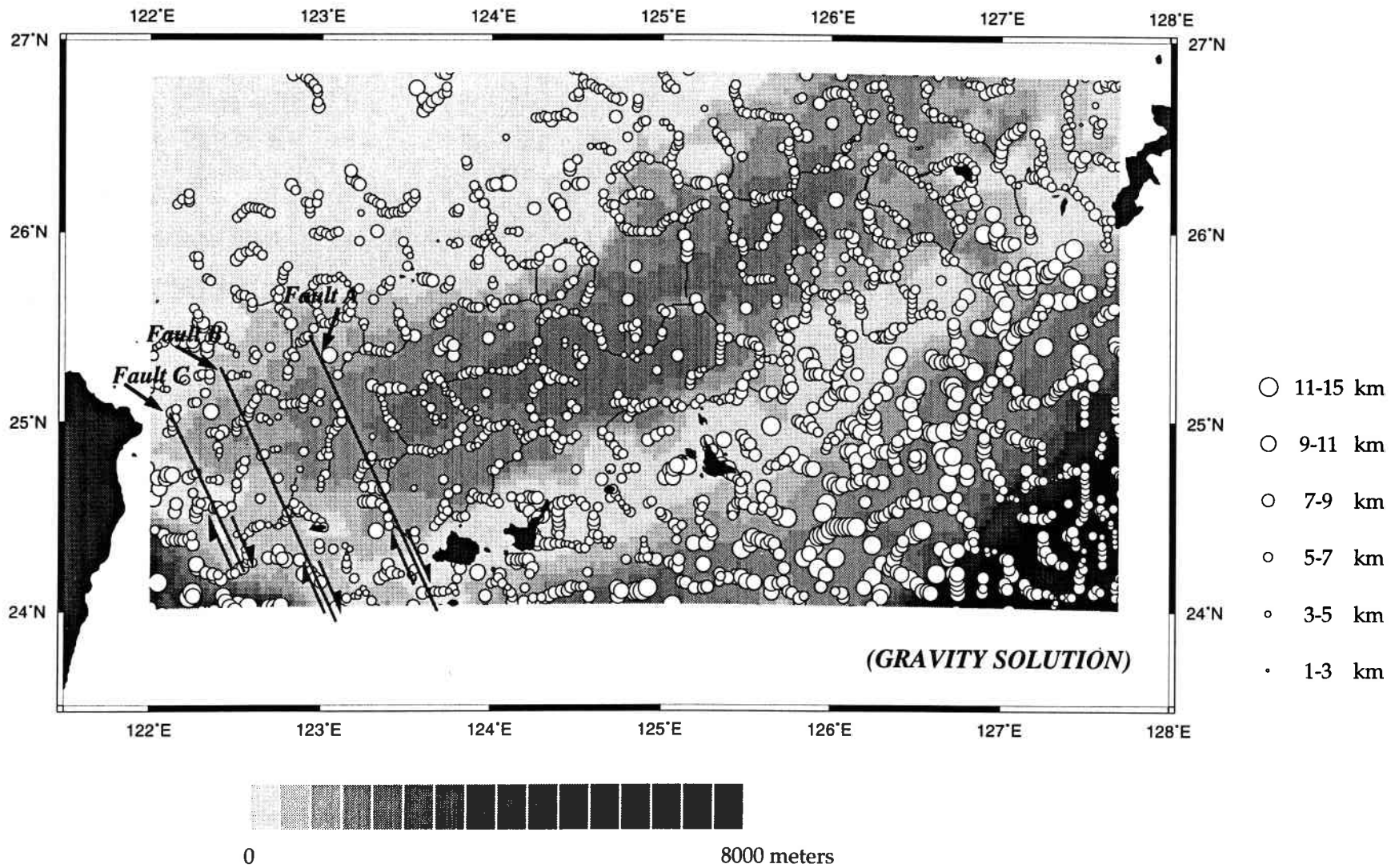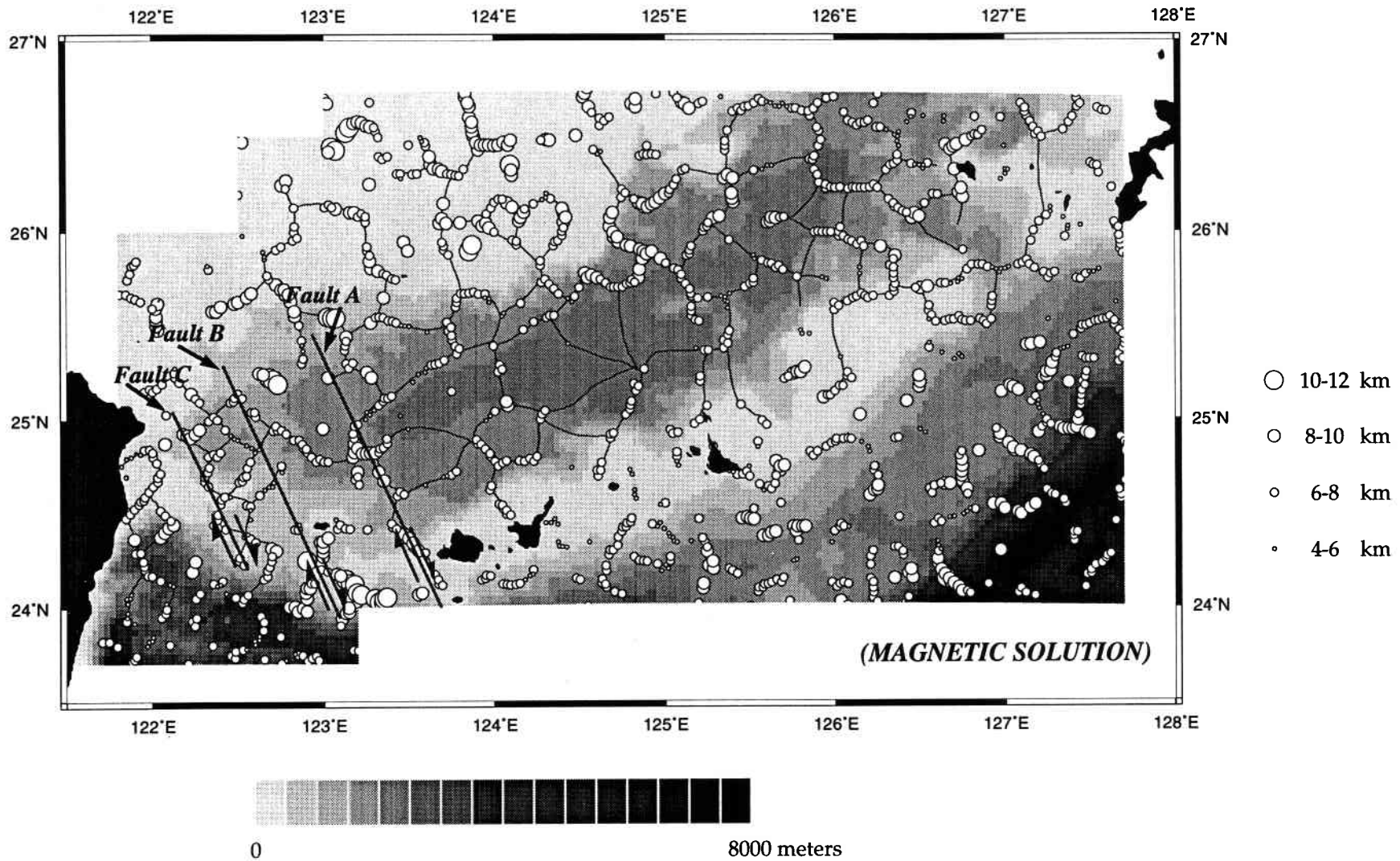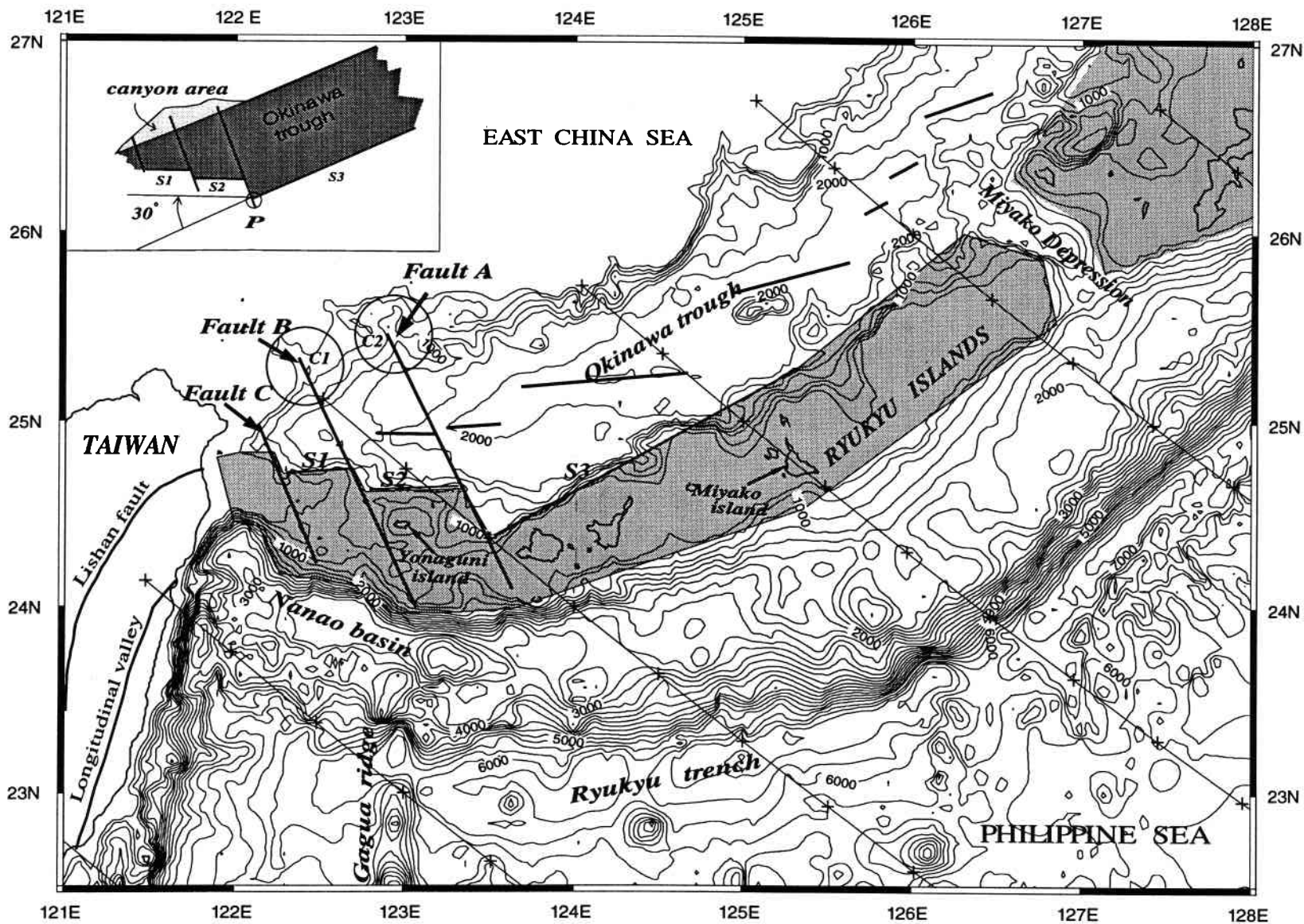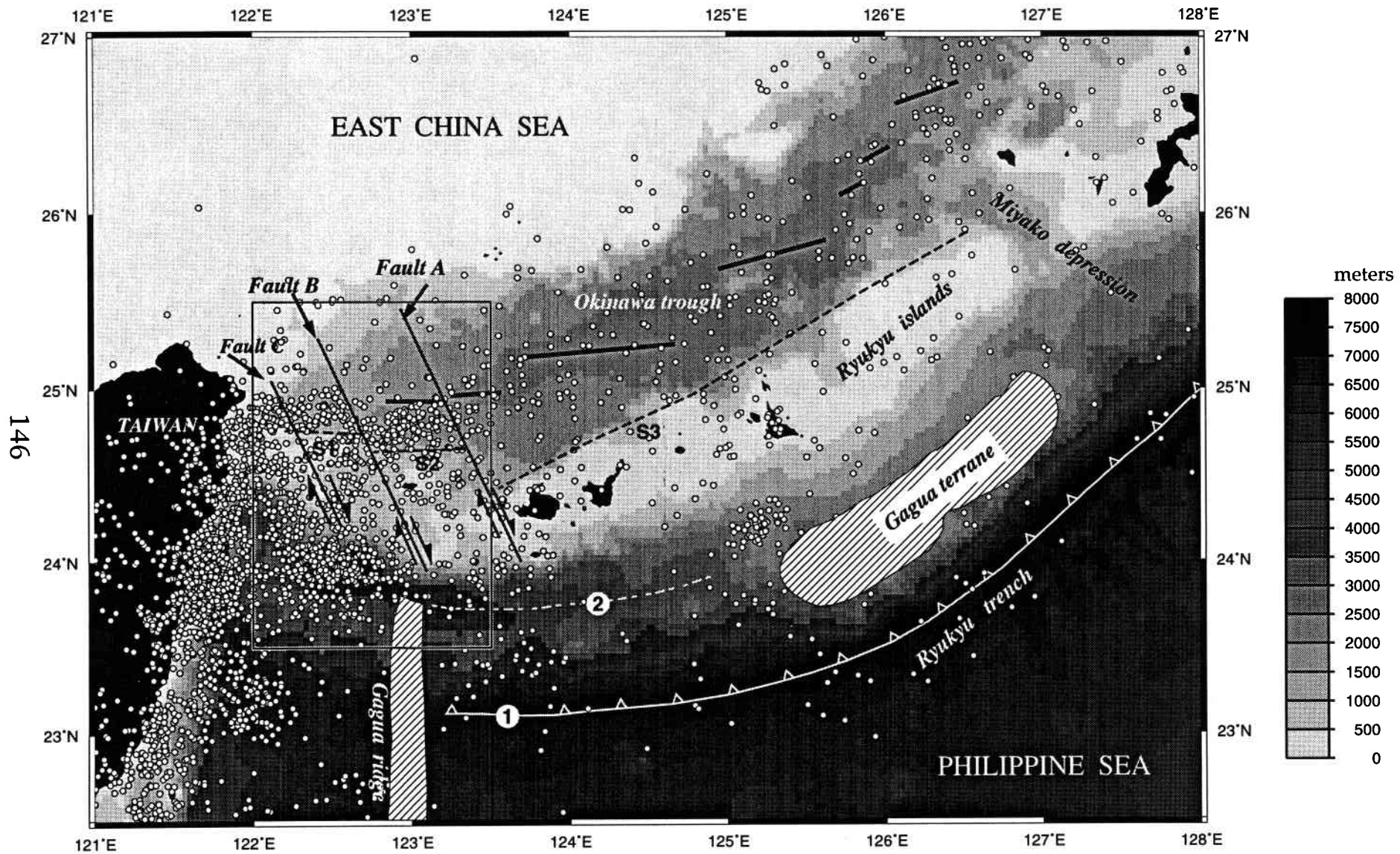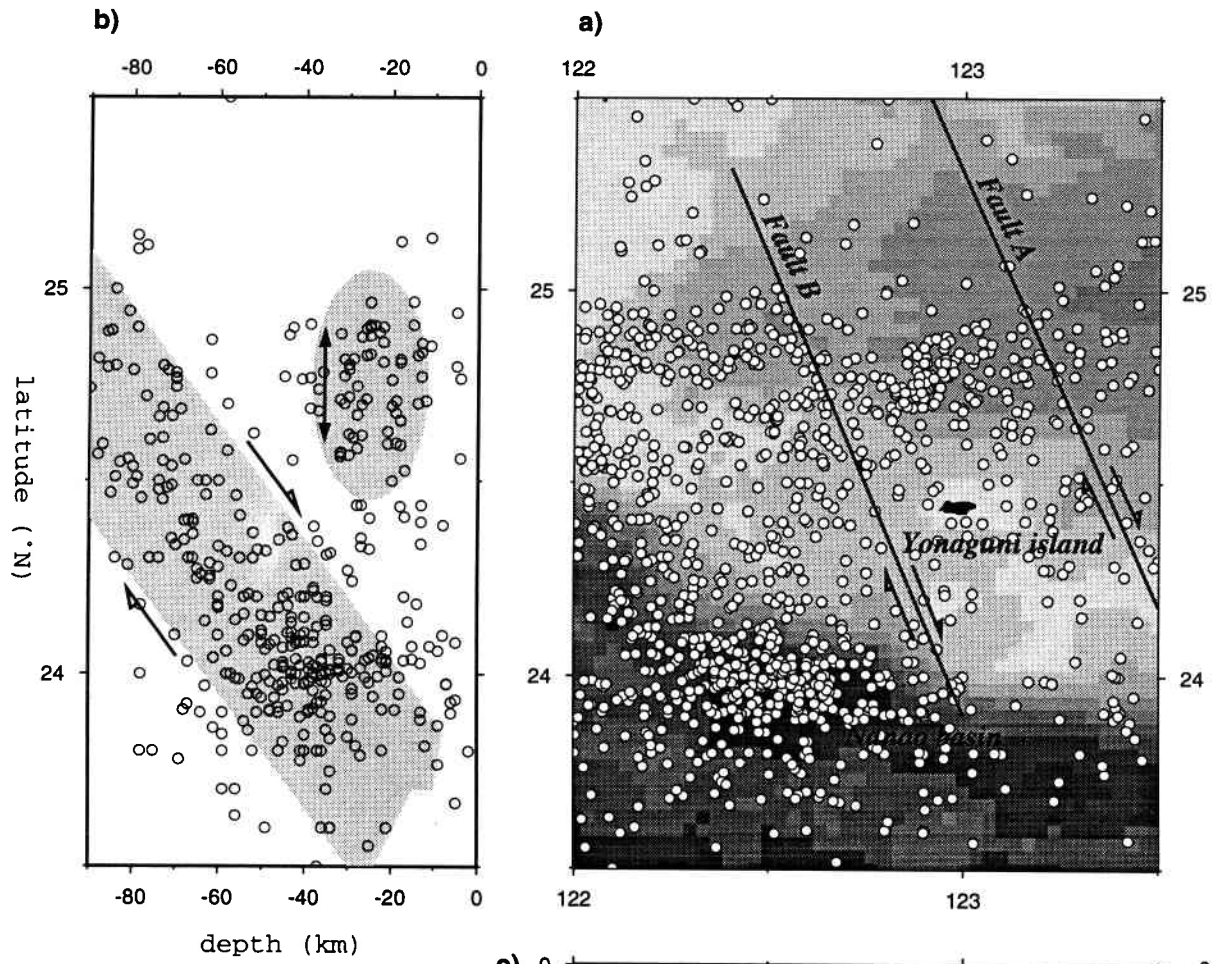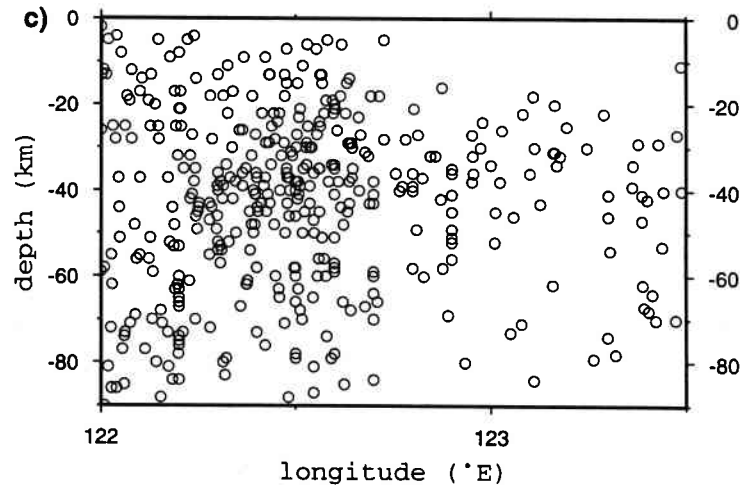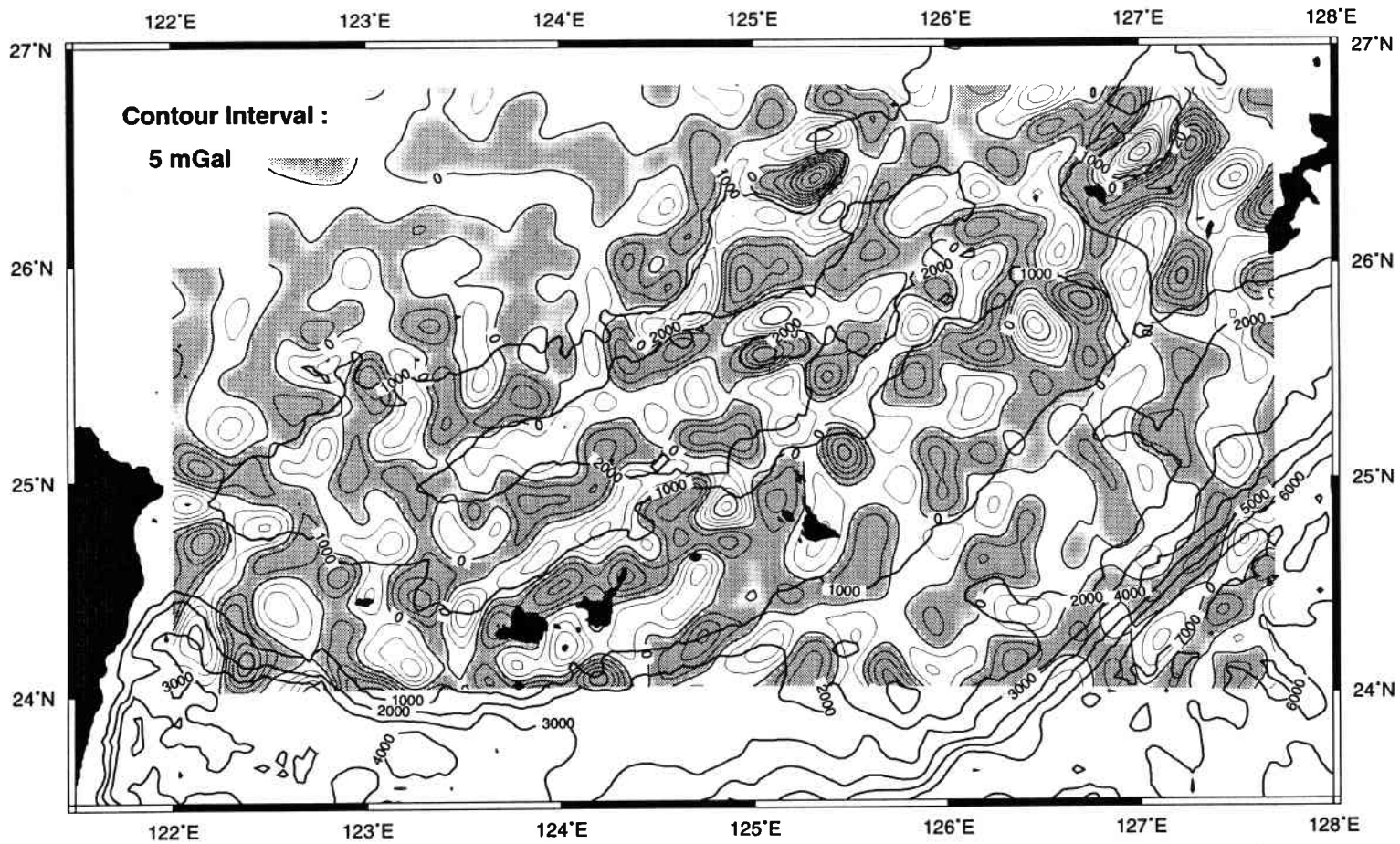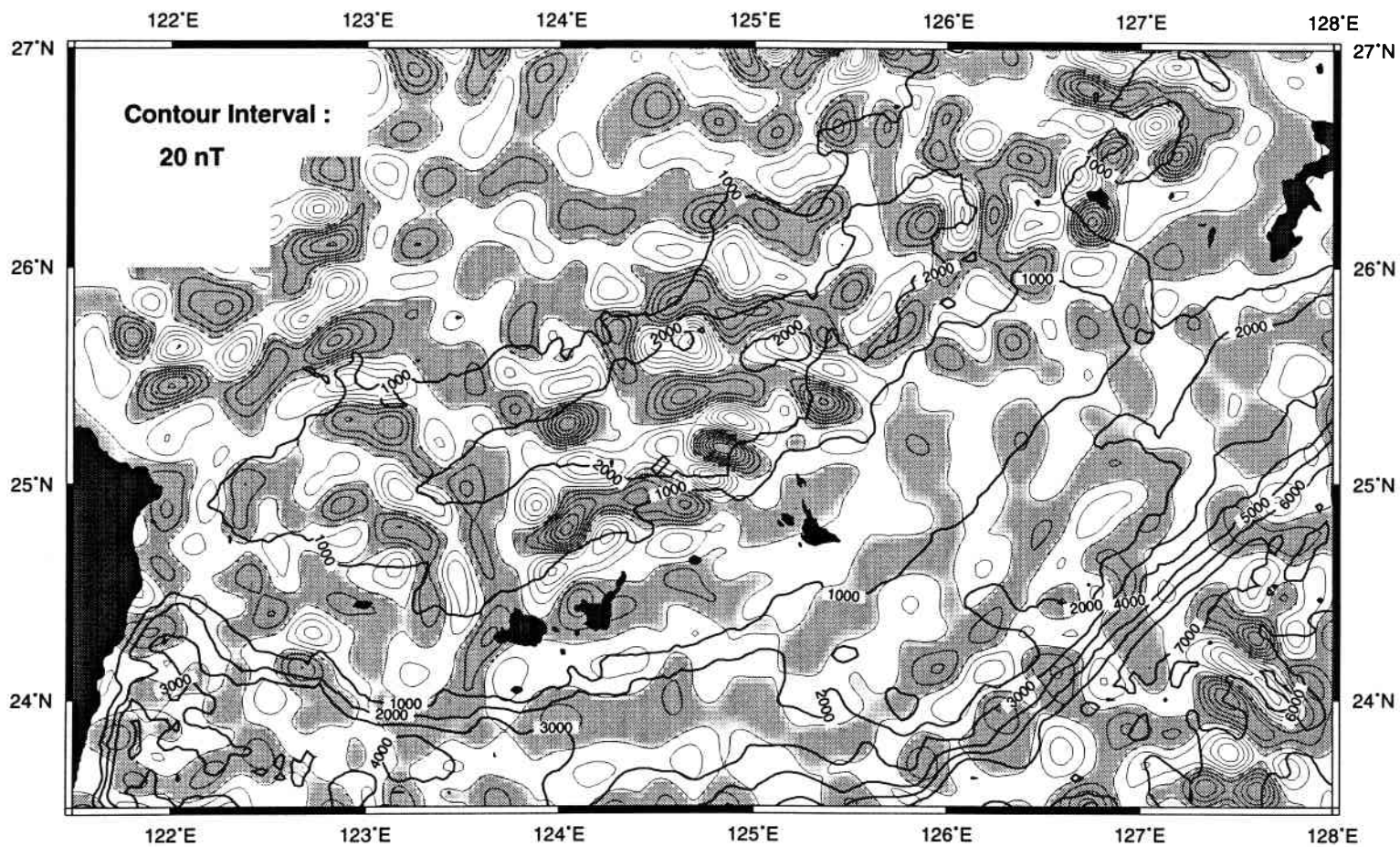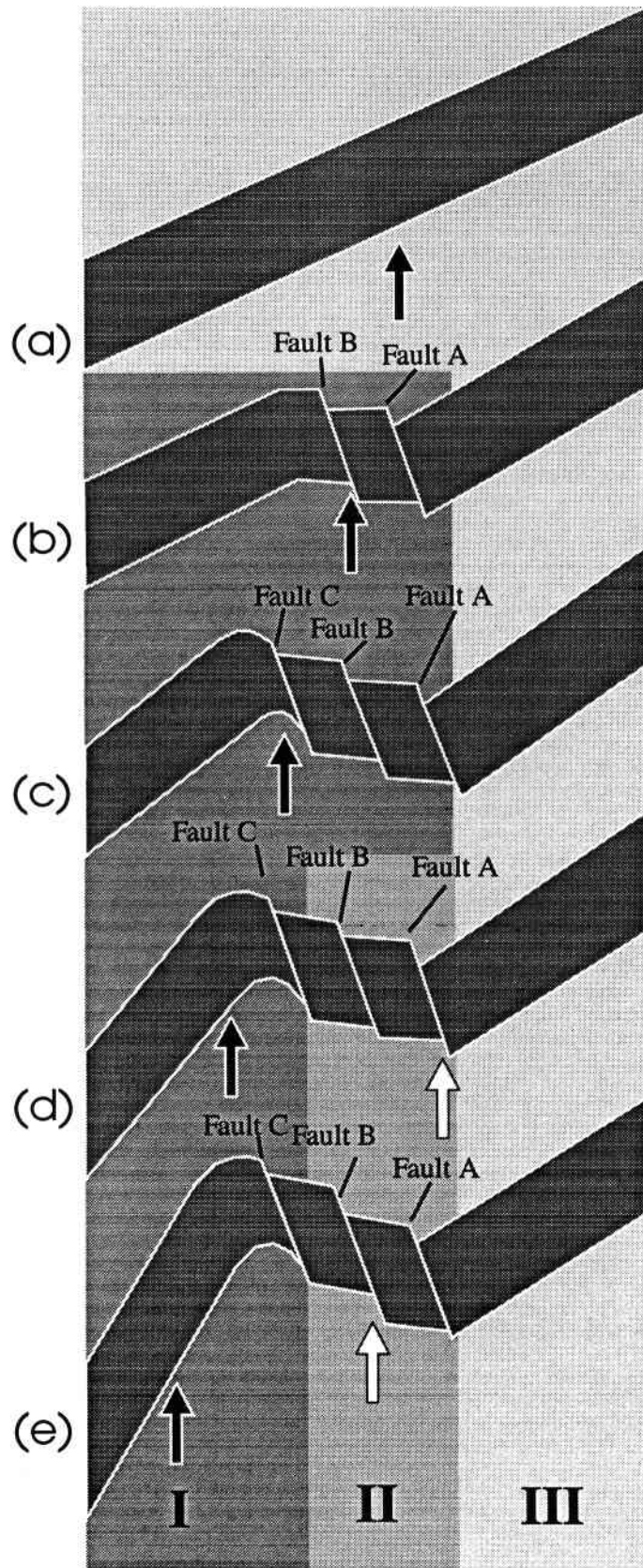
Fig. 15

↑ Luzon arc   ⇑ Gagua ridge

150
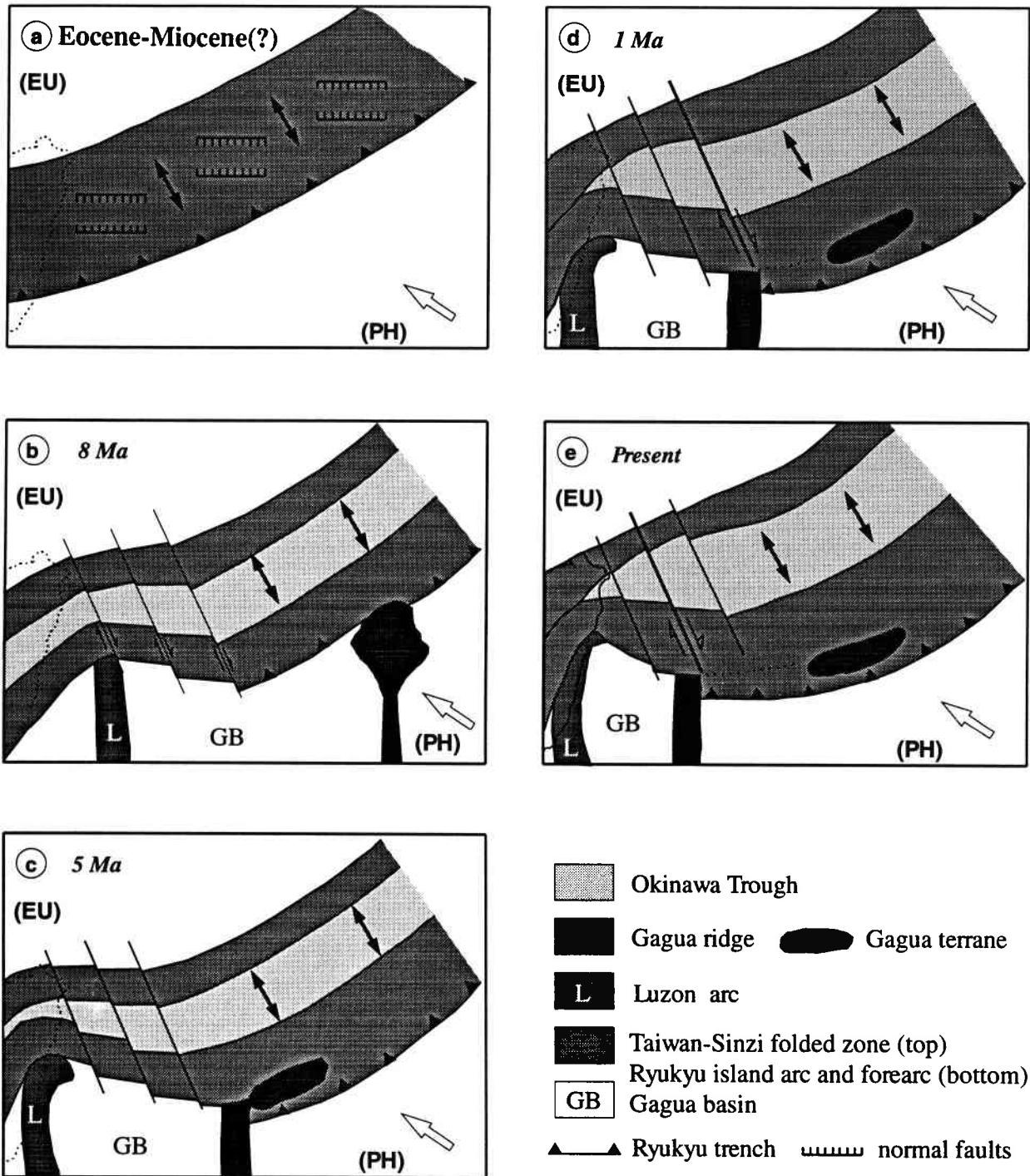
Fig. 16

TABLE 1.

cruise	start date	XOP (internal)	XOP (external)	average XOE(meters)	relative weight
84001311	Mai 14, 1984	0	80	57.8	0.715
84003211	Sept.21, 1984	61	1163	38.0	1.413
84004211	Oct. 18, 1984	66	439	56.0	0.776
84004711	Nov. 13, 1984	0	10	89.1	0.652
A2015L04	June 27, 1965	3	296	99.9	0.390
ANTAC21B	(unknown)	0	193	32.8	1.823
ANTP04MV	Aug. 28, 1970	3	69	108.2	0.241
C1217	Mai 28, 1969	1	124	97.2	0.444
C1404	Mai 9, 1971	0	314	47.1	1.128
C1710	Aug. 15, 1974	3	236	60.8	0.620
C1711	Sept. 16, 1974	0	114	52.8	1.225
C2006	Jan. 26, 1976	0	142	80.3	0.397
C2007	Dec. 3, 1976	16	402	32.9	2.145
C2008	Dec. 23, 1976	0	69	64.6	0.855
C2009	Jan. 5, 1977	3	91	84.8	0.559
DME10	June 27, 1973	0	25	97.9	0.289
DME24	Jan. 22, 1980	0	107	47.9	1.186
DSDP31GC	June 15, 1973	1	20	73.2	1.096
GH7501	Jan. 19, 1975	46	978	68.4	0.524
GH7505	July 16, 1975	7	186	50.8	1.030
HS7501	Apr. 10, 1975	125	171	30.9	3.533
HS7602	Apr. 12, 1976	231	1463	49.7	1.094
HS7603	June 4, 1976	137	592	35.9	2.861
HS8202	Apr. 10, 1982	160	758	47.5	0.824
HT8402	June 22, 1984	39	589	34.4	1.944
HT8403	Oct. 14, 1984	65	675	33.8	1.875
HT8502	Oct. 5, 1985	311	1862	43.6	1.128
HT8612	Dec. 5, 1986	12	113	54.0	1.457
HT8701	Oct. 9, 1987	11	63	86.6	0.633
HT861016	Oct. 16, 1986	0	5	53.2	1.513
HT861102	Nov. 2, 1986	0	33	36.9	3.016
HU939013	June 14, 1969	0	122	98.3	0.324
HUNT01HT	Oct. 6, 1969	1	160	96.1	0.325
INDP03WT	Mai 25, 1976	2	105	108.2	0.312
INDP05WT	July 8, 1976	23	173	29.9	2.297
INDP06WT	July 31, 1976	3	160	62.8	0.863
KH7104	Jan. 21, 1971	0	106	81.2	0.384
KH7201	Mai 11, 1972	0	63	161.8	0.167
KH7202	Jan. 25, 1972	2	351	80.7	0.554
KH7403	July 19, 1974	1	164	192.8	0.088
KH7501	Jan. 10, 1975	0	171	69.3	1.021
KH7502	Feb. 15, 1975	3	53	57.0	1.289
KH7505	Sept. 13, 1975	0	22	38.0	2.637
KH7605	Dec. 22, 1976	0	209	88.8	0.367
KH7802	Apr. 20, 1978	2	23	27.5	4.341
KH79	Jan. 27, 1979	2	351	59.5	0.641
MW8803	Mar. 12, 1988	352	399	29.4	2.247
MW9006	Mai 4, 1990	223	900	50.4	1.009
ODP124EJ	Jan. 9, 1989	30	89	138.4	0.132
ORI183	Oct. 11, 1988	6	157	103.6	0.173
ORI200	Mar. 15, 1989	0	101	117.2	0.290
ORI211	Mai 25, 1989	9	180	112.0	0.325
ORI222	Aug. 17, 1989	0	58	117.3	0.384
ORI232	Nov. 4, 1989	1	25	160.5	0.182
ORI279	Apr. 25, 1991	31	148	83.6	0.510

ORI291	Aug. 5, 1991	27	305	55.8	0.803
ORI298	Oct. 12, 1991	9	284	72.0	0.377
ORI325	July 26, 1992	132	169	36.5	0.817
ORI326	Aug. 1, 1992	43	188	29.2	1.859
ORI336	Nov. 22, 1992	87	86	39.3	0.558
POL6202	Apr. 4, 1962	0	14	62.4	1.498
POL7202	Mar. 7, 1972	18	443	94.3	0.263
SI939011	Feb. 13, 1969	2	264	69.1	0.505
ST	------, 1969	0	71	108.5	0.380
UM68	Oct. 16, 1968	0	115	104.4	0.301
UM69	Oct. 26, 1969	0	47	111.7	0.284
V2107	June 15, 1965	5	261	132.0	0.201
V2108	July 8, 1965	11	178	95.7	0.454
V2110	Aug. 8, 1965	0	42	166.9	0.133
V2405	Apr. 25, 1967	0	41	170.1	0.094
V2406	Mai 31, 1967	5	73	80.4	0.445
V2817	Aug. 13, 1971	9	468	58.2	0.802
V3310	Aug. 27, 1976	11	501	44.8	0.677
V3613	June 28, 1980	6	157	103.6	0.173

===

Is Taiwan the result of arc-continent or arc-arc collision?

Au lieu du modèle de collision arc-continent, nous présentons dans cette note un nouveau modèle de collision arc-arc pour expliquer la surrection de Taiwan. Ce nouveau modèle de collision arc-arc permet d'embrasser de nombreuses données géologiques et géophysiques. Ce modèle suggère que l'ancienne zone de subduction des Ryukyus s'étendait du sud-ouest de Taiwan au sud du Japon avant que la collision avec l'arc de Luzon ne commence.

Is Taiwan the result of arc-continent or arc-arc collision?

Shu-Kun Hsu[1,2,3] and Jean-Claude Sibuet[1]

[1] IFREMER, DRO/GM, Centre de Brest, BP 70, 29280 Plouzané, France
[2] GDR 910 du CNRS, Université de Bretagne Occidentale, BP 809, 29285 Brest, France
[3] Now at Institute of Oceanography, National Taiwan University, Taiwan, R.O.C.

Abstract

Conventionally, it was accepted that the formation of Taiwan results from the collision of the Luzon arc with the Eurasian continental margin. We suggest that Taiwan results from the collision of the Luzon arc with the former Ryukyu subduction zone. Before the collision, the latter extended a few hundred kilometres southwest of its present-day termination. In early to middle Miocene, the subduction became inactive in its southwest portion and the Manila trench migrated northeastward, giving rise to the formation of the Luzon arc. The collision started in late Miocene by closing the oceanic domain located between the Luzon arc and the former Ryukyu arc. Because the Luzon arc moved northwestward with respect to the former NE-SW trending Ryukyu arc, the oblique collision first resulted in the indentation on the south Ryukyu arc west of 123.5°E and the narrowing of the corresponding portion of the Okinawa trough prior to the uplift of Taiwan. Today, the Hsüehshan and Backbone Ranges represent the uplifted portion of the backarc basin and the Longitudinal valley corresponds to the suture zone between the former Ryukyu and the Luzon arcs.

In this model, we propose to link, though they are not of the same age, two truncated backarc basins: the active Okinawa trough to the northeast and the former active Tainan backarc basin to the southwest. The former backarc basin extended from southwest of Taiwan to southern Japan and could have been initiated near the paleo-location of Taiwan as early as Eocene-Oligocene times. The result of the collision is the truncation of the ancient backarc basin associated with the shortening, deformation and uplift of the ancient outer arc and related backarc region, which provides the fundamental mechanism of the Taiwan mountain building. This model is in agreement with a counterclockwise rotation of the portion of the Taiwan located west of the Coastal Range (belonging to the Luzon arc) and a clockwise rotation of the south Ryukyu arc. Earthquake focal mechanisms, geodetic observations and the distribution of the petrologic and structural features are also consistent with the proposed arc-arc collision model.

1. Introduction

Taiwan is located near the junction of the East China, the South China and the Philippine Seas (Fig. 1a). The Taiwan mountain belt is usually believed to be the result of the collision between the Luzon volcanic arc and the Eurasian continental margin (arc-continent collision model) [e.g. 1-6]. For most of the authors, the initial opening of the Okinawa trough is linked to

157

this collision and due to some lateral extrusion or block rotation at the western end of the Ryukyu arc [e.g. 4-8]. Nevertheless, an overview of the satellite derived marine gravity anomalies [9] shows that the Okinawa trough is probably linked to the Tainan basin on the basis of the similar amplitudes and general features of gravity anomalies (Fig. 1a). If this hypothesis is correct, a corresponding subduction zone should have existed before the uplift of Taiwan. The main consequence of this assumption is that Taiwan results from the collision of the Luzon arc with the former Ryukyu subduction zone extending at that time at least a few hundreds kilometres southwest of its present-day termination. In that case, instead of an arc-continent collision, the orogeny of Taiwan should be better described as a result of an arc-arc collision. In this paper, we will present geophysical and geological considerations which support this hypothesis.

2. Configuration of the former subduction zone (backarc basin, arc and trench)

The Chinese continental margin generally displays extensional features with predominant NE-SW trending basins [10,11]. However, only the Tainan basin and the Okinawa trough exhibit similar positive gravity signatures with relative lows along their elongated axes (Fig. 1a). Except for the striking northward shortening and the clockwise rotation of the southwestern portion of the Ryukyu subduction zone located between northeastern Taiwan and 123.5°E [12,13], the curvature of the Ryukyu subduction zone could be extended to the area surrounding the Tainan basin (Fig. 1a). The two roughly parallel NE-SW trending borders of the Tainan basin (black dashed lines in Fig. 1b) could be connected with the Yichu and Hsinhua-Chuko active faults located in southwestern Taiwan (numbers 2 and 3 in Fig. 1b). These two faults bound an onshore sedimentary basin located in the prolongation of the Tainan basin which disappears toward the northeast. The axis of this basin can be identified on the pre-Miocene basement relief map established from drilling data but disappears just south of Fault D (Fig. 2) [14]. The ancient arc associated with the ancient backarc basin in southwest Taiwan is poorly expressed; however, its position is revealed on the Bouguer anomaly map [15], which shows a NE-SW oriented local maximum in the northeastern prolongation of the suggested outer arc of the Tainan basin (red area located south of the black dashed lines in Fig. 1b).

In its southwestern portion, the Okinawa trough becomes narrow and disappears in the Ilan plain considered to be the westward termination of the present-day active backarc basin. The Lishan fault lies in the direct continuation of the backarc basin as shown by the presence of a deep valley located in the prolongation of the Ilan plain (Fig. 3). The Lishan fault, generally dipping southeastward for most of the authors [e.g. 2], separates similar argillite-slate facies of the Hsüehshan and Backbone Ranges (Fig. 2) [2]. These argillaceous sediments were deposited in an outer neritic to upper bathyal environment. We assume that they represent uplifted and metamorphosed sediments deposited in a former backarc basin. In this interpretation, the Lishan fault is the trace of a major normal fault of the backarc basin re-mobilised as a crustal thrust fault during later compression and the Hsüehshan and Backbone Ranges the two margins of the former backarc basin.

Considered as the suture zone of the ancient backarc basin, the Lishan fault can be traced from the Ilan plain to the Yushan mountain (Figs. 1b and 2) [2, 16-20]. However, its connection with the onshore Tainan basin shows a right-lateral offset of over 40 km (Fig. 2). This offset is underlined in the Bouguer anomaly map [15] and by geodetic observations [21], which show that

the region located on the northern side of the Yushan mountain is stable whereas on the southern side, the horizontal velocity field of the crust increases southward and eastward with respect to Eurasia. In other words, the present-day convergence linked to the collision of the Luzon arc is absorbed in southern Taiwan by thrusts and strike-slip faults whereas in the eastern portion of northern Taiwan, it should be accommodated by the subduction of the northern portion of the Luzon arc. Right-lateral strike-slip faults located on the western side of the Yushan mountain may be related to this offset (Fig. 2). By what mechanism this offset is produced remains a question. However, it might be related to heterogeneities in the arcs or backarc regions. For example, the inner arc seems to be absent along segment HH' (Fig. 1b).

The Longitudinal valley is the convergent boundary between the Philippine Sea and Eurasian plates [2]. In our model it corresponds to the suture zone between the former Ryukyu trench becoming inactive in Early to Middle Miocene and the former Manila trench active at the time of collision. To the east, the Coastal Range comprises volcanic and siliciclastic sequences and belongs to the Luzon arc [2]. To the west, the Tananao complex comprises metamorphic and sedimentary sequences above a Paleozoic/Mesozoic basement and belongs, in our hypothesis, to the Ryukyu arc and forearc system (Fig. 2) [22]. Because the Tananao complex consists of a metamorphic belt pair [23] - the high T low P Tailuko belt to the west and the low T high P Yuli belt to the east (Fig. 2) -, it indicates that the Philippline Sea plate subducted westward beneath the former Ryukyu arc.

South of the Tainan basin, in the northern South China Sea, a relatively low gravity anomaly, roughly parallel to 21.3°N (white dashed line in Figs. 1a and 1b), suggests that a subduction zone could have existed there. This subduction zone was probably bounded to the west by a NW-SE trending feature, which probably represents a former transform fault (indicated by two white arrows in Fig. 1a). The existence of this feature is also clearly evidenced in the magnetic anomaly map [24] and the ETOPO5 bathymetry.

In summary, prior to the formation of Taiwan, a continuous subduction zone existed from Japan to the southwest Taiwan. Today, the trace of the former Ryukyu trench follows the present-day Ryukyu trench, the Nanao basin, the Longitudinal valley and the base of the continental slope located south of the Tainan basin; the trace of the former backarc basin follows the Okinawa trough which ends in the Ilan Plain, the uplifted Hsüehshan and Backbone Ranges located on each side of the Lishan fault and the onshore and offshore Tainan basin (Fig. 1).

3. Earthquake relationship

Figure 4a shows the location of earthquakes and areas with similar type of focal mechanisms [19]. A large number of shallow earthquakes with compressional mechanism occurs in zone D (Fig. 4a), which suggests that the Nanao basin is a weak zone. By contrast, a large number of earthquakes with extensional mechanism occurs in the corresponding backarc region (zone E). This phenomenon could be ascribed to different factors such as the pressure release due to faulting and/or the input of cold material [12]. In zone C, numerous earthquakes with mostly compressional mechanisms are directly linked to the collision between the Luzon arc and the former Ryukyu arc. These earthquakes, especially those occurring along the Longitudinal valley with a sinistral motion, are linked to the oblique convergence of the Luzon arc with respect to the Tananao complex. In addition, a shallow Wadati-Benioff zone dipping eastward is observed in

zone C [25], which suggests that the Longitudinal valley marks the trace of the former former Manila trench which was active during the collision. The present-day Manila trench is, however, separated from this former segment of the Manila trench by a right-lateral strike-slip fault located south of Taiwan (Fig. 1). Along the Lishan fault backarc basin suture zone (zone F), earthquakes also exhibit compressional mechanisms. In zone B, earthquakes show mostly compressional mechanisms and could be related to the right-lateral offset, located between the onshore Tainan basin and the Lishan fault. In zone A, earthquakes with mainly extensional mechanisms characterise a still active, though weak, extensional domain including the former Tainan backarc basin and associated forearc region.

Accordingly, earthquakes occurring in the area of Taiwan could be ascribed to two principal factors: the extension of the backarc basin and the collision of the Luzon arc. Because the Luzon arc, considered to be part of the Philippine Sea plate [26], moves northwestward with respect to the Eurasian plate [27], the region located on the northwest side of the Luzon arc is under compressional regime while outside the region is mostly under extensional regime (Fig. 4b). Because the Luzon arc collision migrates southward [6], the southwesternmost Okinawa trough has probably resumed its extension after the northern tip of the Luzon arc has swept it [12] while southwestern Taiwan is still a region to be compressed and uplifted.

4. Tectonic evolution

From drilling data in the northern Okinawa trough, it is assumed that the present-day backarc extension began in middle Miocene [28]. However, the sedimentary units located on each side of the Lishan fault (Backbone and Hsüehshan Ranges, Fig. 2) were deposited under extensional regime in Eocene-Oligocene times and are under compression since late Miocene/Pliocene [e.g. 16]. Simultaneously, the Tainan basin started to subside in late Oligocene with ENE-WSW trending grabens formed during rifting [29]. Basaltic tuffs, tuff breccias and some lava flows are found in most of the Miocene sediments in Taiwan; however, in southern Taiwan, only sparsely small tuffaceous lenses are scattered in the late Miocene sediments [2]. Consequently, the opening of the former backarc basin(s) should have started near Taiwan in Paleogene. In addition, submarine volcanism occurred in several local centres of the former backarc basin [2] with basalts similar to those recovered in other backarc basins [30].

During Paleogene the former transform fault (Fig. 1a) probably connected the southern end of the former Ryukyu trench with the northern end of the Manila trench. This transform fault became inactive in early to middle Miocene and the former Manila trench migrated northeastward, giving rise to the formation of the Luzon arc. Simultaneously, the previously transform fault jumped futher northeast connecting the northern end of the Luzon arc with the southwestern end of the active Ryukyu arc located near 123.5°E. However, because of the relatively northwestward motion of the Luzon arc, this transform fault progressively diminished in length and disappeared when the collision between the two arcs began. The northeastward jump of the activity of the transform fault induced the cessation of the subduction between the southwest of Taiwan and the south Ryukyu subduction zone. This jump in the location of the subduction coincides with the end of the South China Sea opening and with a major plate kinematic reorganization.

Assuming that the shape of the former Ryukyu arc was regular and NE-SW oriented before the collision (Fig. 5) and that the SSE-NNW trending Luzon arc moved northwestward [27], the

initial collision between the two arcs was oblique. The indentation of the former Ryukyu arc and the narrowing of the Okinawa trough backarc basin occurred before the uplift of Taiwan. Because west of 123.5°E the Okinawa trough displays striking NW-SE structural trends and is quite different from the rest of the Okinawa trough which generally shows NE-SW trends, the arc-arc collision could have first occurred near 123.5°E, following the direction of convergence of the Philippine Sea plate relative to the Eurasian plate [12]. This implies that the convergent boundary between northern Taiwan and the bent Ryukyu arc became a transform boundary after the Luzon arc collision. This hypothesis could explain the pronounced bending of the Ryukyu arc and the triangular shape of the Okinawa trough west of 123.5°E. During the process of indentation of the former Ryukyu arc, the portion of arc and backarc region located west of the Luzon arc should have rotated counterclockwise and the eastern portion clockwise. This is in agreement with the counterclockwise motion in western Taiwan deduced from the paleostress study [31] and the clockwise rotation of the south Ryukyu arc deduced from paleomagnetic study [8], occurring during the last 10 My [8]. Thus, we interpret the clockwise rotation of the south Ryukyu arc as a consequence of the Luzon arc collision, rather than a consequence of the wedge-shaped opening of the Okinawa trough [8]. Several NW-SE trending dextral strike-slip faults, including Fault B, across the entire subduction zone were active during the indentation of the Ryukyu arc west of 123.5°E (Figs. 1 and 3) [12].

In addition, the collision and the consecutive accretion of the Coastal Range, a portion of the Luzon arc composed of Miocene-Pleistocene volcanic rocks [1,2], occurs in northern Taiwan and propagates southwestward, as suggested by Suppe [6]. As a consequence, an extensional regime could still exist in southern Taiwan with continuous subsidence and sedimentation thought collision occurred in northern Taiwan. This phenomenon accounts for the increased sedimentary thickness toward the south [4].

5. Conclusions

The axis of the Tainan basin, the area between the Yichu and the Hsinhua-Chuko faults, the Lishan fault, the axis of the Okinawa trough, the Oita-Kumamoto and the Median Tectonic Lines constitute a continuous feature which corresponds to the axis of a former system of backarc basins evolving into a shear zone in southern Japan (Fig. 5). The initial opening of the backarc basin probably occurred as early as Eocene-Oligocene near the paleo-location of Taiwan. The former Ryukyu arc-trench system was active from south of the Tainan basin to Japan. In early to middle Miocene, the subduction became inactive in its southwest portion and the former Manila trench migrated northeastward, giving rise to the formation of the Luzon arc. In late Miocene, because of the similar buoyancy, the southwestern portion of the former Ryukyu arc and the Luzon arc became to collide. The uplift of Taiwan started after the indentation of the south Ryukyu arc and the narrowing of the corresponding portion of the Okinawa trough and was followed by the closure of the oceanic lithosphere located between the Tananao complex (belonging to the former Ryukyu arc) and the Coastal Range (belonging to the Luzon arc). As a result, the former Ryukyu arc and associated backarc basin were partly squeezed, deformed and uplifted (Taiwan mountain building), leaving two independent backarc basins: the still active Okinawa trough and the almost inactive Tainan basin. The Longitudinal valley marks the suture zone between the former Ryukyu arc and the Luzon arc. The Ryukyu arc-trench system was collided and indented not only by the

Luzon arc but also by the Palau-Kyushu ridge (Fig. 5). This provides a simple mechanism, as suggested by Vogt [32], to explain the entire arcuated form of the Ryukyu arc.
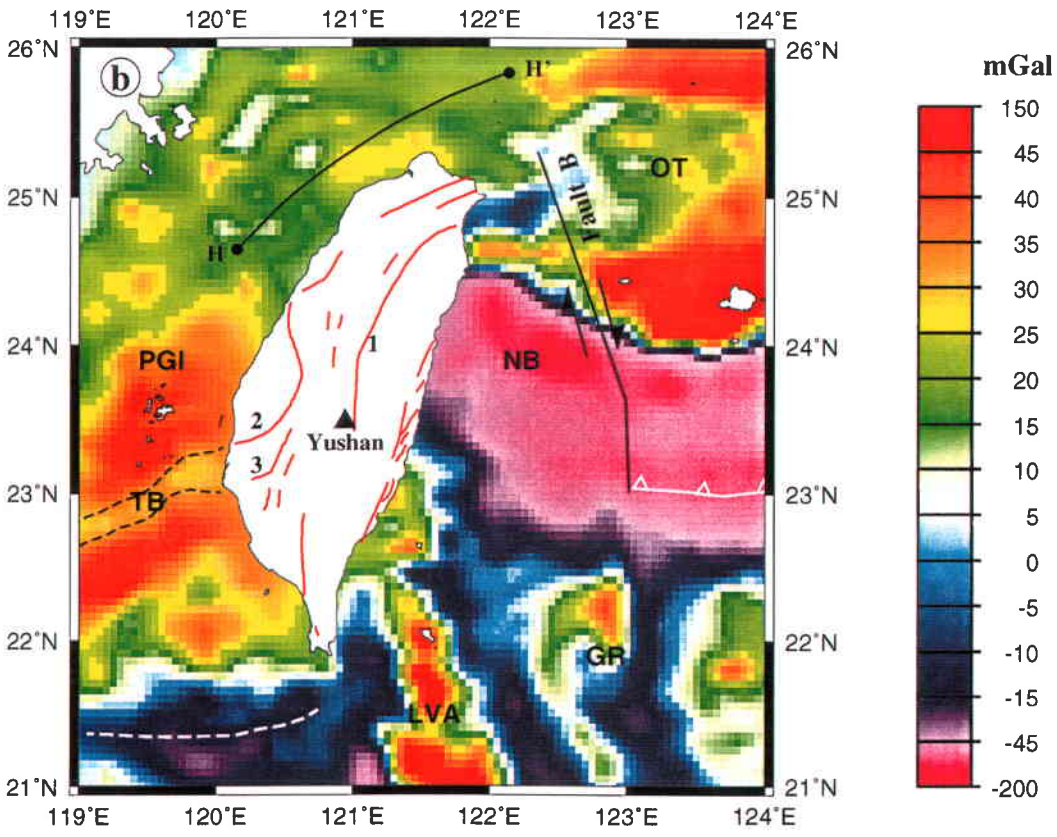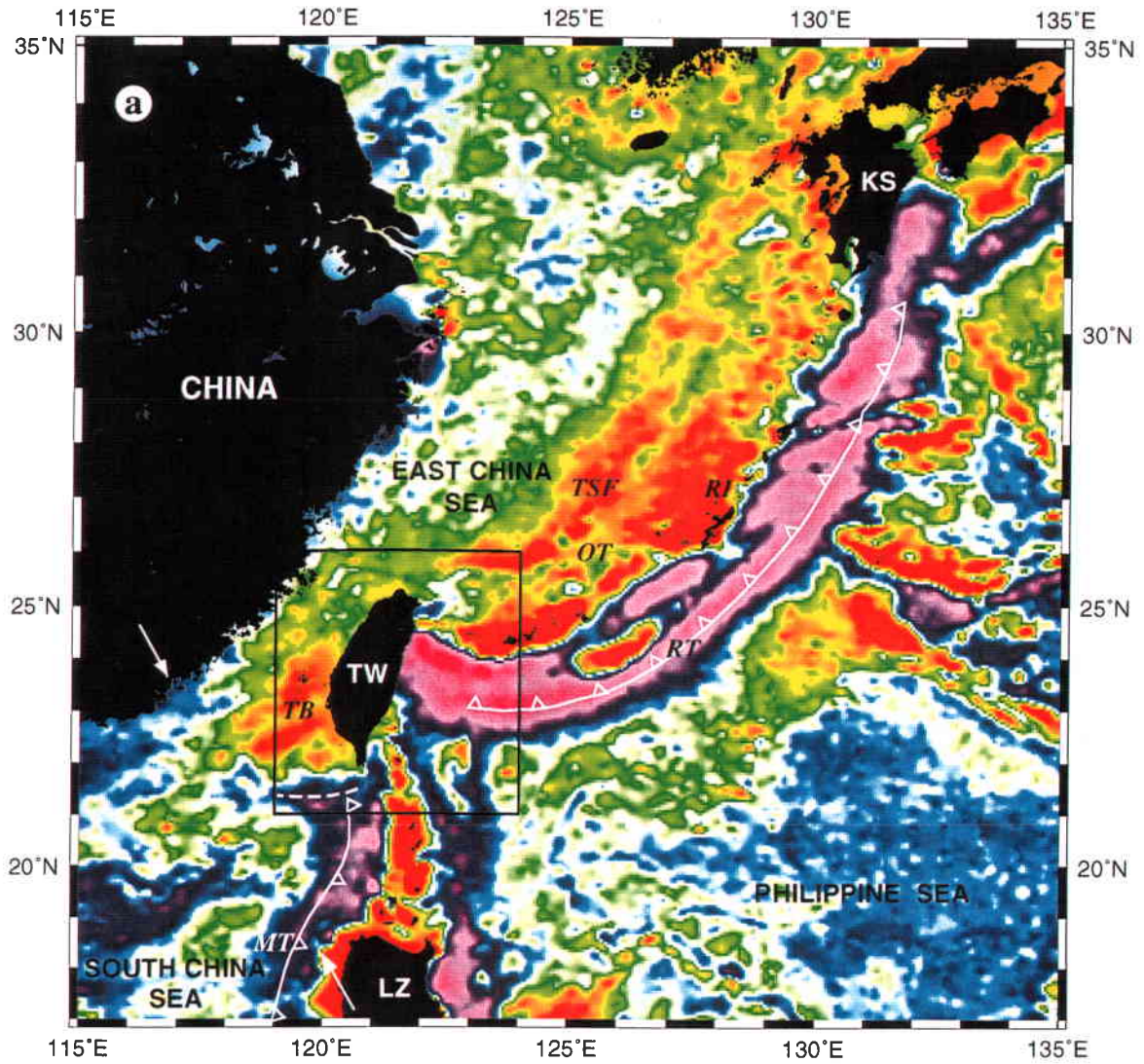
Acknowledgements

References

[1] C.-S. Ho, Tectonic evolution of Taiwan: Explanatory text of the tectonic map of Taiwan, Minist. Econ. Affairs, Rep. of China, 1982.

[2] C.-S. Ho, An introduction to the geology of Taiwan: Explanatory text of the geologic map of Taiwan, 2nd. Ed., 192 pp., Minist. Econ. Affairs, Rep. of China, 1988.

[3] C.-Y. Lu and J. Malavieille, Oblique convergence, indentation and rotation tectonics in the Taiwan Mountain Belt: Insight from experimental modelling, Earth Planet. Sci. Lett. 121, 477-494, 1994.

[4] L.S. Teng, Geotectonic evolution of late Cenozoic arc-continent collision in Taiwan, Tectonophysics 183, 57-76, 1990.

[5] J. Angelier, F. Bergerat, H.-T. Chu and T.-Q. Lee, Tectonic analysis and the evolution of a curved collision belt: the Hsuehshan Range, northern Taiwan, Tectonophysics 183, 77-96, 1990.

[6] J. Suppe, Kinematics of arc-continent collision, flipping of subduction, and back-arc spreading near Taiwan, Mem. Geol. Soc. China 6, 21-34, 1984.

[7] J. Letouzey and M. Kimura, The Okinawa trough: genesis of a backarc basin developing along a continental margin, Tectonophysics 125, 209-230, 1986.

[8] M. Miki, Two-phase opening model for the Okinawa trough inferred from paleomagnetic study of the Ryukyu arc, J. Geophys. Res., 100, 8169-8184, 1995.

[9] D.T. Sandwell and W.H.F. Smith, New global marine gravity map/grid based on stacked ERS-1, Geosat and Topex altimetry, EOS, AGU, Spring meeting, Abstract, 75, 321, 1994.

[10] H.-S. Yu, Structure, stratigraphy and basin subsidence of Tertiary basins along the Chinese southern continental margin, Tectonophysics 235, 63-76, 1994.

[11] J.M. Wageman, T.W.C. Hilde and K.O. Emery, Structural framework of East China Sea and Yellow Sea, Am. Assoc. Pet. Geol. Bull. 54, 1611-1643, 1970.

[12] S.-K. Hsu, J.-C. Sibuet, S. Monti, C.-T. Shyu and C.-S. Liu, Transition between the Okinawa trough backarc extension and the Taiwan collision: new insights on the southernmost Ryukyu subduction zone, Mar. Geophys. Res., (in press), 1996.

[13] J.-C. Sibuet, S.-K. Hsu, C.-T. Shyu and C.-S. Liu, Structural and kinematic evolutions of the Okinawa trough backarc basin, in Taylor, B., Ed., Backarc basins: tectonics and magmatism, Plenum, New-York, 343-379, 1995.

[14] C.-H. Tang, Late Miocene erosional unconformity on the subsurface Peikang high beneath the Chiayi-Yulin coastal plain, Taiwan, Mem. Geol. Soc. China 2, 155-168, 1977.

[15] Y.-H. Yeh and H.-Y. Yen, Gravity anomalies of Taiwan and their tectonic implications, TAICRUST workshop proceedings, June 10-12, 1991, Taipei, Taiwan, R.O.C., 175-184, 1991.

[16] J.-C. Lee, Structure et déformation active d'un orogène : Taiwan, Thèse de Doctorat. Univ. Pierre et Marie Curie, Paris, 1994.

[17] Y.-B. Tsai, C.-C. Feng, J.-M. Chiu and H.-B. Liaw, Correlation between microearthquakes and geologic faults in the Hsintien-Ilan area, Pet. Geol. Taiwan 12, 149-167, 1975.

[18] F.T. Wu, Recent tectonics of Taiwan, J. Phys. Earth 26 (suppl.), 265-299, 1978.

[19] Y.-H. Yeh, E. Barrier, C.-H, Lin and J. Angelier, Stress tensor analysis in the Taiwan area from focal mechanism of earthquakes, Tectonophysics 200, 267-280, 1991.

[20] S.-K. Hsu, J.-C. Sibuet and C.-T. Shyu, High-resolution detection of geologic boundaries from 3-D potential field anomalies: an enhanced analytic signal technique, Geophysics, (in press), 1995.

[21] S.-B. Yu, H.-Y. Chen, and L.-C. Kuo, Velocity field of GPS stations in the Taiwan area, ACT international conference and 3rd Sino-French symposium on active collision in Taiwan, program and extended abstracts, 22nd-23rd March, 1995, Geol. Soc. China, Taiwan, R.O.C., 317-327, 1995.

[22] K. Kizaki, Geology and tectonics of the Ryukyu islands, Tectonophysics, 125, 193-207, 1986.

[23] T.-P. Yen, The metamorphic belts within the Tananao schist terrain of Taiwan, Proc. Geol. Soc. China 6, 72-74, 1963.

[24] Magnetic anomaly map of east Asia, Geological survey of Japan and committee for co-ordination of joint prospecting for mineral resources in Asian offshore areas (CCOP), 1994.

[25] S.-N. Cheng, Stress distribution in Taiwan: a finite element analysis, M.S. thesis, National Taiwan University, 1988 (in chinese).

[26] T. W. C. Hilde and C.-S. Lee, Origin and evolution of the West Philippine basin: a new interpretation, Tectonophysics, 102, 85-104, 1984.

[27] T. Seno, S. Stein and A.E. Gripp, A model for the motion of the Philippine Sea plate with NUVEL-1 and Geological data. J. Geophys. Res. 98, 17,941-17,948, 1993.

[28] J.-C. Sibuet, J., Letouzey, F. Barrier, J. Charvet, J.-P. Foucher, T.W.C. Hilde, M. Kimura, L.-Y. Chiao, B. Marsset, C. Muller and J.-F. Stephan, Back arc extension in the Okinawa trough, J. Geophys. Res. 92, 14,041-14,063, 1987.

[29] S.-C. Sun and Y.-Y. Hsu, Overview of the Cenozoic geology and tectonic development of offshore and onshore Taiwan, Taicrust workshop proceedings (June 10-12), Taipei, Taiwan, Rep. of China, 35-47, 1991.

[30] X. Boespflug, Evolution géodynamique et géochimique des bassins arrière-arcs. Exemples des bassins d'Okinawa, de Lau et Nord-Fidjien, Université de Bretagne Occidentale, Brest, France, 354 p., 1990.

[31] J. Angelier, E. Barrier and H.-T. Chu, Paleostress trajectories related to collision in foothills fold-thrust belt of Taiwan, Mem. Geol. Soc. China 7, 201-217, 1986.

[32] P.R. Vogt, Subduction of aseismic ridges, Nature 241, 189-192, 1973.

Figure captions

Fig. 1. (a) Satellite derived marine gravity anomaly around Taiwan [9]. Note that, except for the bent region west of 123.5°E, the general curvature of the Ryukyu subduction zone (including the Ryukyu arc, the Okinawa trough and the Taiwan-Sinzi folded belt) can be extended to the Tainan basin and its continental margin. The two white arrows indicate a probable fossil transform fault. The white dashed line indicates a segment of the former Ryukyu trench. (b) Close-up of the region surrounding Taiwan. Active faults in Taiwan are plotted as red lines [18]. GR: Gagua ridge; KS: Kyushu island (south Japan); LVA: Luzon volcanic arc; LZ: Luzon; MT: Manila trench; NB: Nanao basin; OT: Okinawa trough; PGI: Penghu islands; RI: Ryukyu islands; RT: Ryukyu trench; TB: Tainan basin; TSF: Taiwan-Sinzi folded belt; TW: Taiwan; 1: Lishan fault; 2: Yichu fault; 3: Hsinhua-Chuko fault. Yushan is the highest mountain in Taiwan (about 4 km). The white dashed line indicates a segment of the former Ryukyu trench.

Fig. 2. General structural map of Taiwan modified from [2,14]. The pre-Miocene basement relief beneath the Coastal plain is shown in the box. Note that the onshore Tainan basin disappears south of Fault D. Right-lateral strike-slip fault zones on the western side of the Yushan mountain correspond to a right-lateral offset zone between the Lishan fault and the onshore Tainan basin.

Fig. 3. 3-D topographic diagram of the area shown in Fig. 1b. Note that the southeastern Okinawa trough ends in the Ilan Plain. In its southward prolongation, the Lishan fault is considered to be the suture of the former Okinawa trough backarc basin. The Longitudinal valley is the suture zone between the former Ryukyu arc and the Luzon arc.

Fig. 4a. Distribution of earthquakes of the magnitude greater than 4 and areas with similar focal mechanisms near Taiwan [19]. In general, zones A and E are extensional areas linked to backarc extension. Other zones are compressional areas linked to the arc-arc collision. LVA: Luzon volcanic arc. GR: Gagua ridge.

Fig. 4b. Schematic diagram showing areas under compressional regime (region C) due to the collision of the Luzon arc and under extensional regime (regions E) related to backarc extension. The extensional region E in northern Taiwan probably resumed its extension after the collision of the Luzon arc migrated southward. Solid circles and triangles represent thrusts or strike-slip mechanisms. Open circles represent normal fault mechanisms. Squares represent earthquakes associated with the subducted slab of the Philippine Sea plate [19].

Fig. 5. Simplified geological sketch showing the present-day position of the trench and backarc basin axis of the former Ryukyu subduction zone. 1: Tainan basin (former backarc basin); 2: Lishan fault (suture of the backarc basin); 3: Okinawa trough; 4: Oita-Kumamoto Tectonic Line; 5: Median Tectonic Line; 6: Ryukyu trench; 7: Former extension of the Ryukyu trench; 8: Fossil transform fault; 9: Manila trench; EU: Eurasian plate; PHS: Philippine Sea plate. The arrow indicates the direction of convergence of PHS with respect to EU. The dashed line between 6 and 7 corresponds to the position of the trench before the collision of the Luzon arc.
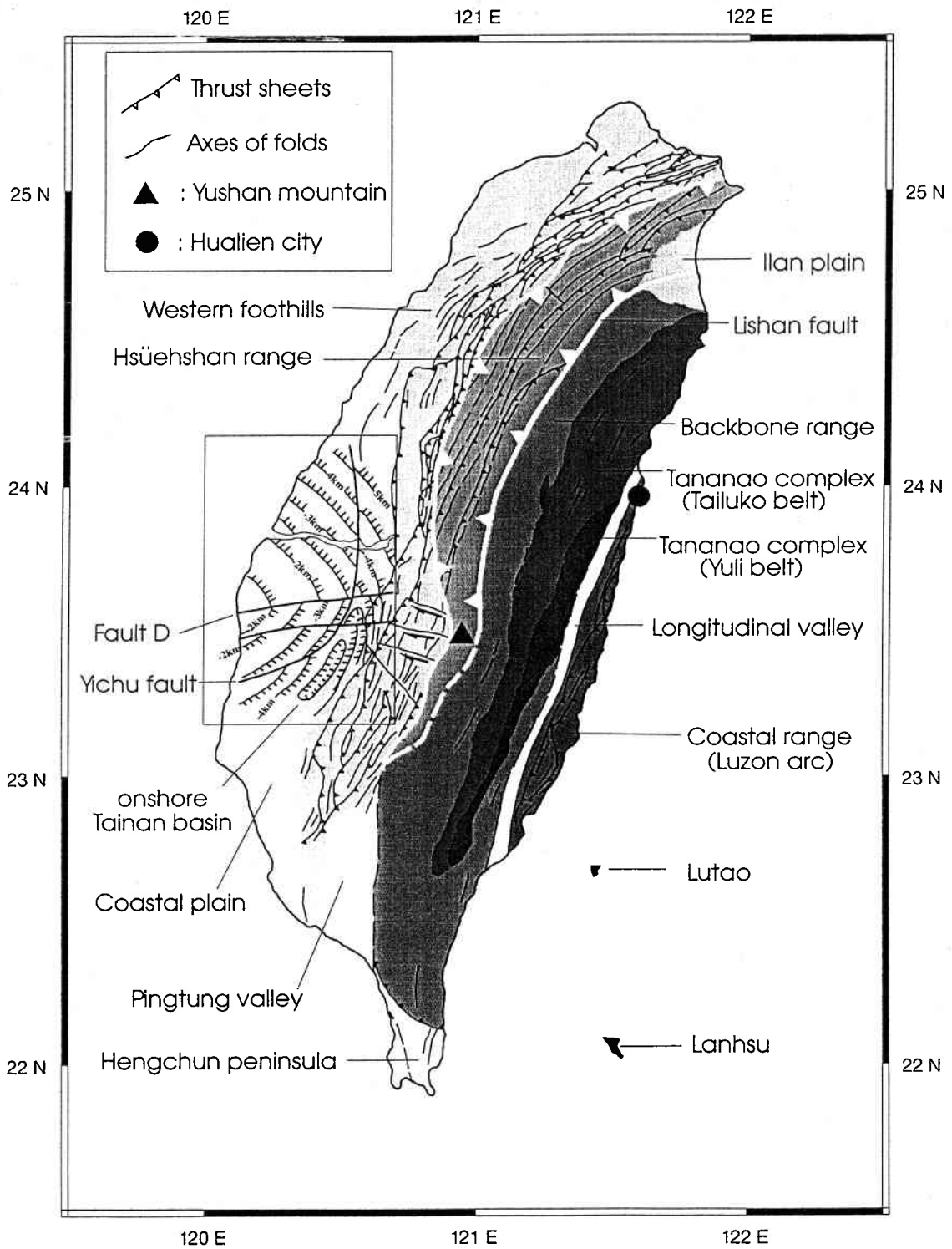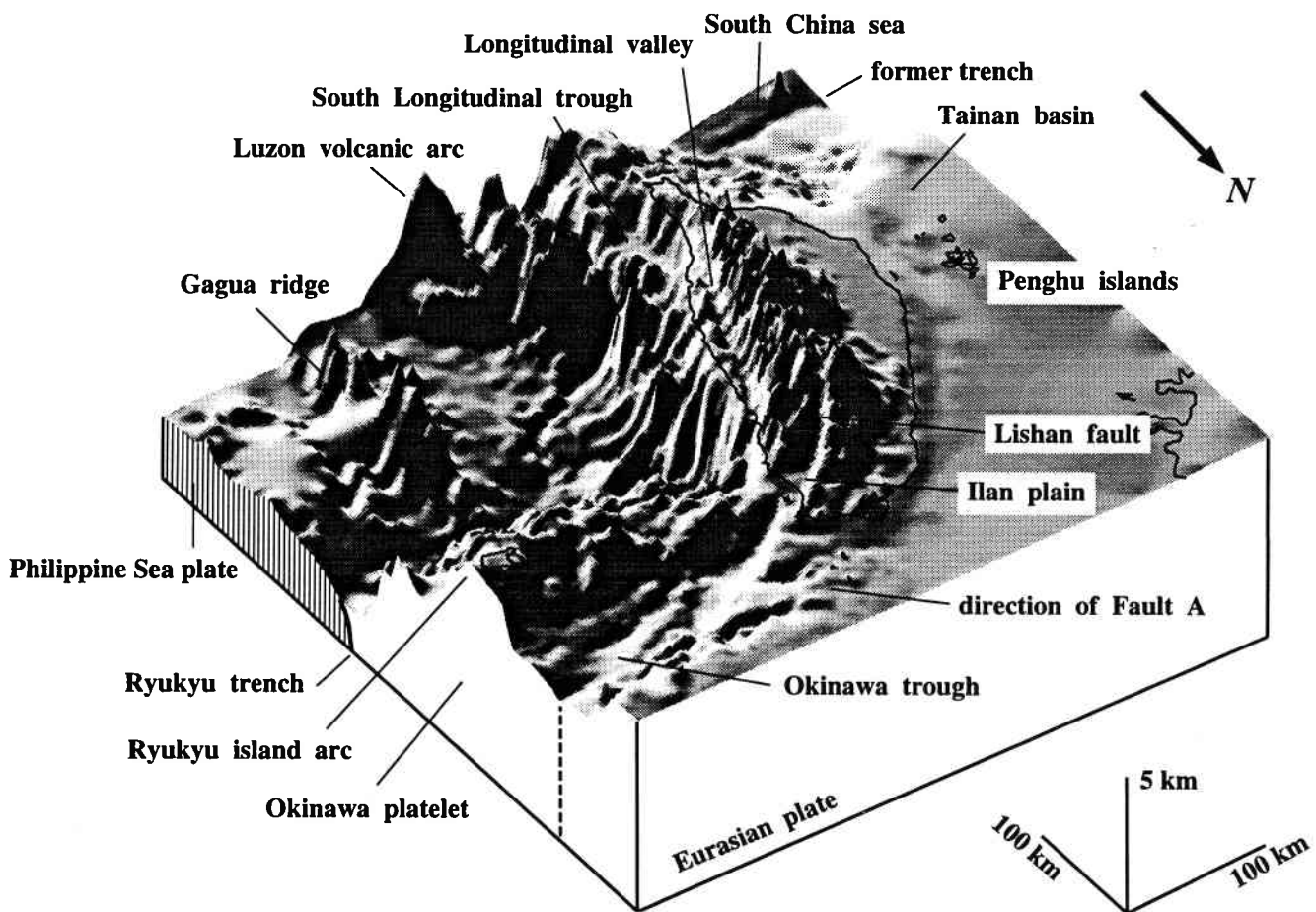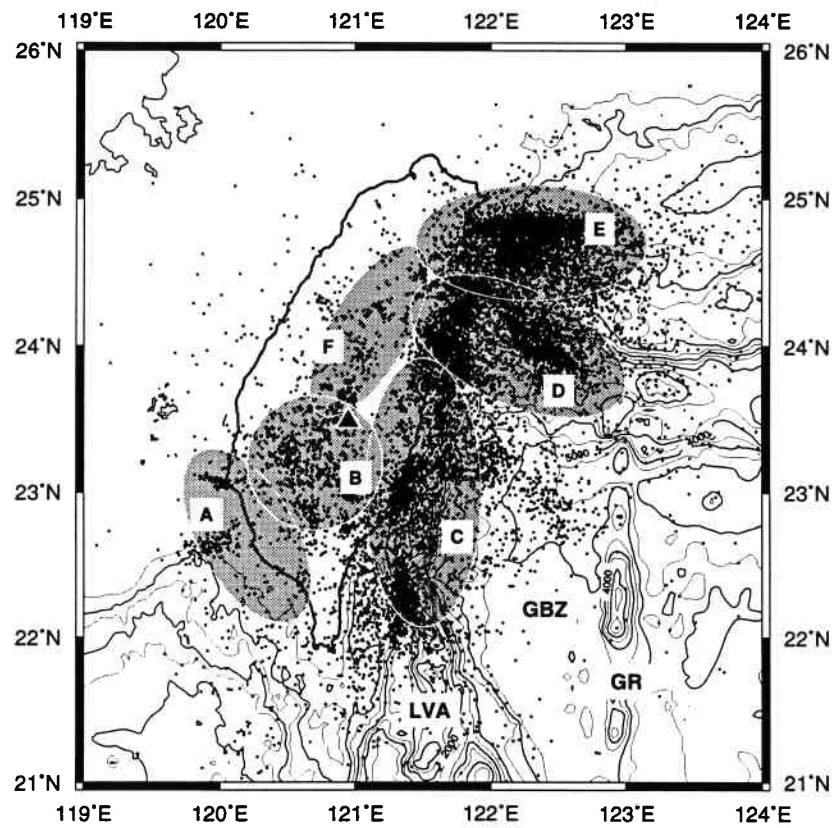
Fig. 2

Luzon volcanic arc
South Longitudinal trough
Longitudinal valley
South China sea
former trench
Tainan basin
N
Gagua ridge
Penghu islands
Philippine Sea plate
Lishan fault
Ilan plain
direction of Fault A
Ryukyu trench
Okinawa trough
Ryukyu island arc
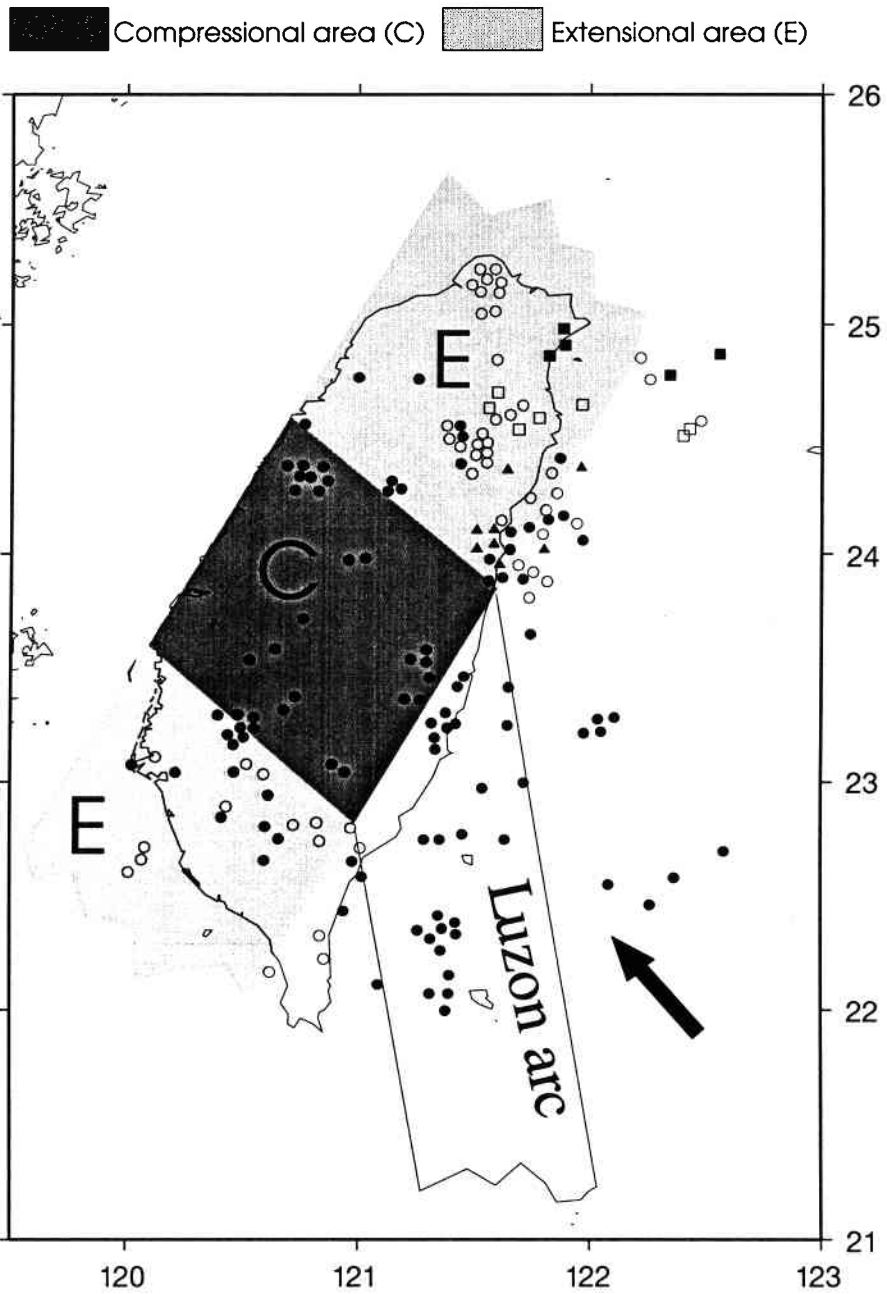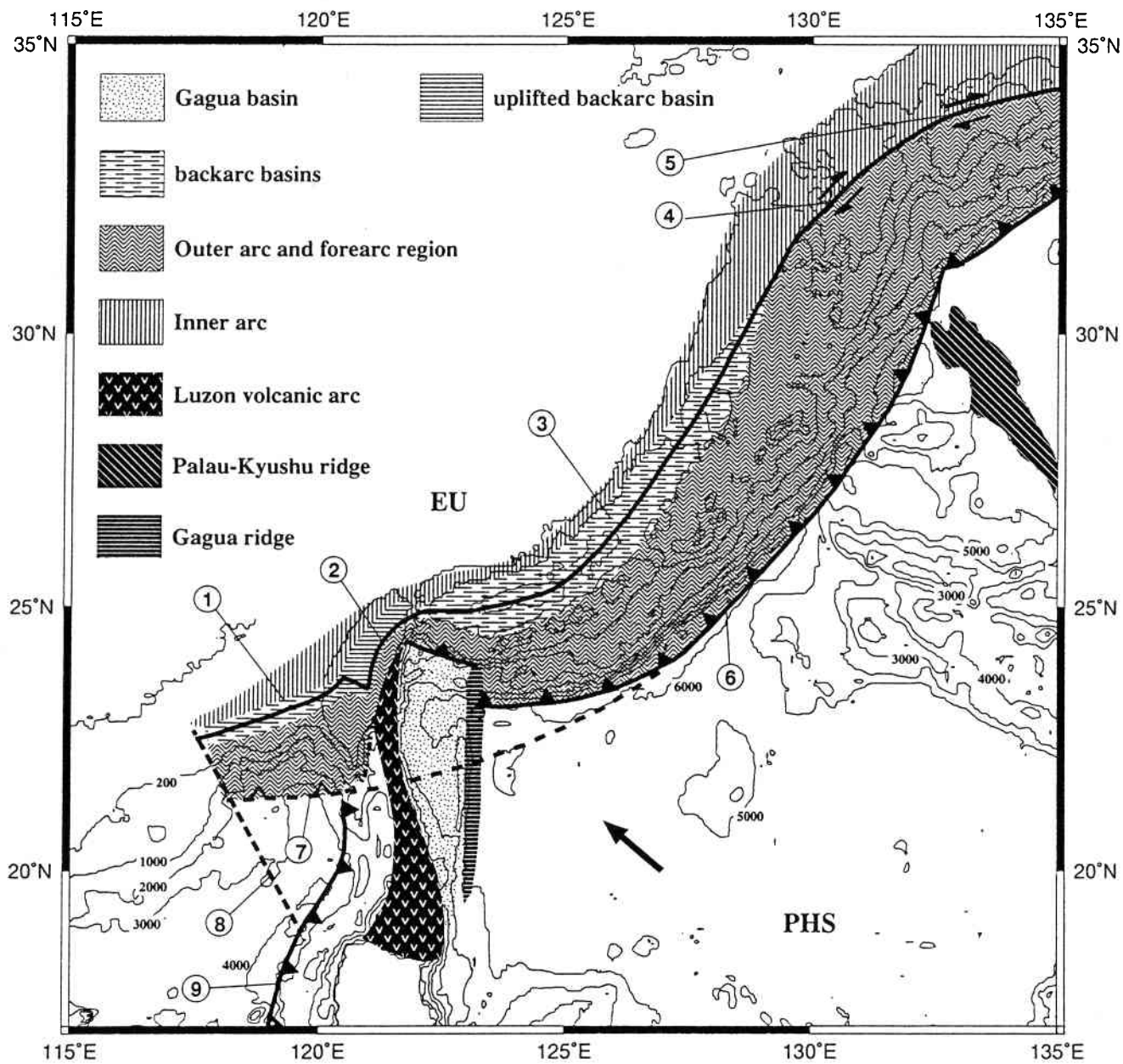Okinawa platelet
Eurasian plate
5 km
100 km
100 km

Fig. 3

Fig. 4a

Fig. 4b

Fig. 5

PARTIE II : COLLISION ACTIVE A TAIWAN

1. DESCRIPTION GÉNÉRALE

1.1. Contexte général

L'île de Taiwan, située au sud-est de l'Asie, se trouve à la frontière entre la plaque eurasiatique (EU) et la plaque de la Mer des Philippines (PH) (**Fig. 1**). L'importance de la séismicité de cette zone est due principalement à la convergence entre ces deux plaques. Cette convergence s'effectue à la vitesse de 71 mm/an selon un azimut d'environ 310° au voisinage de Taiwan (**Fig. 2**), et elle a évolué en collision depuis le Miocène/Pliocène (environ 8 Ma).

La séismicité a permis de déterminer la géométrie des zones de Wadati-Benioff (Tsai, 1986) : la plaque PH subducte sous l'arc des Ryukyus au nord-est de Taiwan et la plaque de la Mer de Chine du Sud subducte sous l'arc de Luzon appartenant à la plaque PH (**Figs. 3 et 4**). Ce contexte géodynamique complexe permet de considérer Taiwan comme un laboratoire naturel, particulièrement intéressant pour les géosciences.

A Taiwan, la Vallée Longitudinale est généralement considérée comme la frontière principale entre les plaques PH et EU (**Fig. 5**) (e.g. Ho, 1988). Selon les résultats géodésiques, le raccourcissement (ou la discontinuité de mouvement relative) dû à cette convergence entre les deux cotés de la vallée est de 20-30 mm/an selon la direction N315° ± 10° (Lee et Angelier, 1993 ; Yu et al., 1995), le reste du raccourcissement étant globalement absorbé dans l'île, à l'ouest de la Vallée Longitudinale.

1.2. Géologie générale de Taiwan

Taiwan est composée de cinq provinces géologiques principales (**Fig. 5**) (Ho, 1988) :

1) <u>La Chaîne Centrale Est</u> (i.e., le Complexe de Tananao qui comprend "*Yuli belt*" à l'est et "*Tailuko belt*" à l'ouest). Cette province correspond au socle métamorphique anté-tertiaire. Kizaki (1986) a suggéré qu'elle rejoint l'arc des Ryukyus dans sa partie nord.

2) <u>La Chaîne Centrale Ouest</u> qui comprend deux unités : le "*Backbone Range*" à l'est et le "*Hsuehshan Range*" à l'ouest. Elle est principalement composée d'une série d'argiles et de grès d'âge Eocène à Miocène. Ces deux unités sont
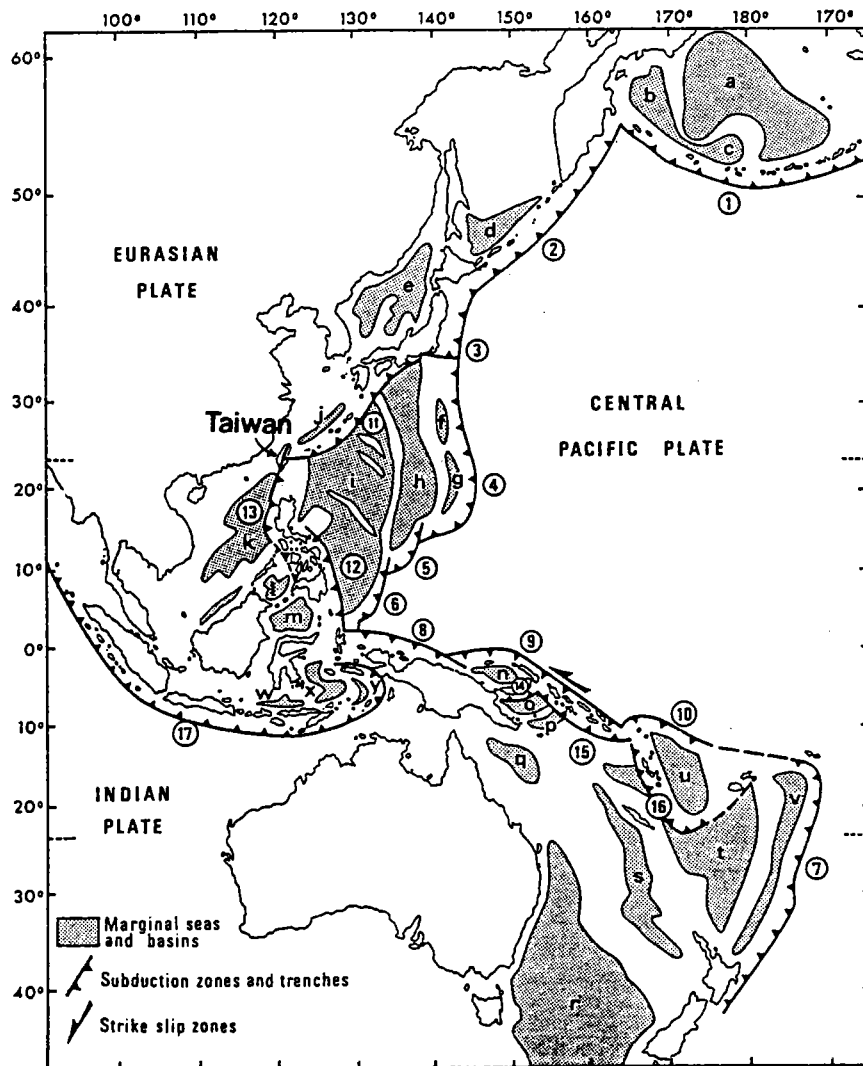
Fig. 1 : Les fosses, les arcs et les bassins marginaux dans le Pacifique Ouest (d'après Aubouin, 1990). [*1-16 = Fosses et subductions dans le Pacifique Ouest.* 1-10 = limite du Pacifique Central (subductions à vergences vers le continent (1-7), décrochement principal (8-10)) : 1 = fosse des Aléoutiennes ; 2 = fosse des Kouriles ; 3 = fosse du Japon ; 4 = fosse des Bonins et des Mariannes ; 5 = fosse de Yap ; 6 = fosse de Palau ; 7 = fosse des Tonga-Kermadec ; 8 = fosse de Nouvelle Guinée ; 9 = fosse Ouest-Mélanésienne ; 10 = fosse de Vitiaz ; 11 = fosse des Ryukyus ; 12 = fosse des Philippines. *13-16 = Fosses et subductions du Pacifique Occidental.* 13 = fosse de Manille ; 14 = fosse de Nouvelle Bretagne; 15 = fosse des Solomon ; 16 = fosse des Nouvelles Hébrides. 17 = *Fosses et subduction dans l'océan Indien* (i.e. fosse de Java). a-y *Bassins marginaux.* a = bassin des Aléoutiennes ; b = bassin du Kamtchakta ; c = bassin de Bowers ; d = bassin d'Okhotsk ; e = mer du Japon ; f = bassin des Bonins ; g = bassin des Mariannes ; h = bassin de Parce-Vela ; **i = Bassins des Philippines Ouest ; f+g+h+i = Mer des Philippines ; j = bassin d'Okinawa ; k = Mer de Chine du Sud ;** l = Mer de Sulu ; m = bassin des Célèbes ; n = Mer de Bismarck ; o = bassin des Solomon ; p = bassin de Woodlark ; q = Mer de Corail ; r = Mer de Tasmanie ; s = bassin de Nouvelle Calédonie ; t = bassin Sud-Fidjien ; u = bassin Nord-Fidjien ; v = bassin de Lau-Havre ; w = bassin des Flores ;
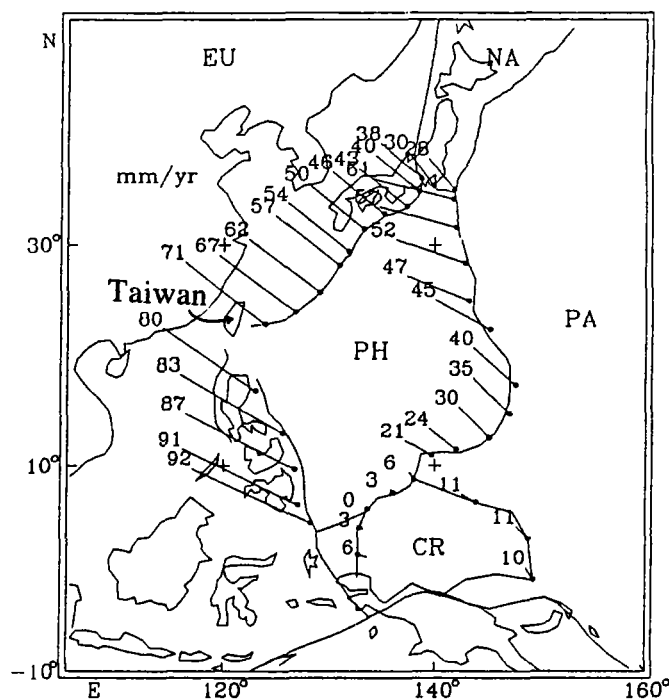
Fig. 2 : Vitesses relatives autour des plaques PH et EU (d'après Seno et al., 1993). Les azimuts sont indiqués par des barres, et les taux sont indiqués en millimètres par an. Le long des frontières EU-PH et NA-PH, les mouvements de PH par rapport à EU ou à NA sont indiqués ; le long des frontières PA-PH et PA-CR, les mouvements de PA par rapport à PH ou à CR sont indiqués ; et le long de la frontière CR-PH, les mouvements de CR par rapport à PH sont indiqués. PA : plaque Pacifique ; PH : plaque de la Mer des Philippines ; EU : plaque eurasiatique ; CR : plaque des Caroline ; NA : plaque Nord-Américaine.

séparées par la faille de Lishan, une structure topographique très marquée située au nord de 23°N.

3) Les "*Western Foothills*" (i.e., les sédiments de la partie occidentale). Cette province représente la zone de plissements et de chevauchements récents, datée du Néogène et généralement non-métamorphisée.

4) La Plaine Côtière ("*Coastal plain*") qui est composée d'alluvions quaternaires.

5) La Chaîne Côtière ("*Coastal range*") qui est séparée de la Chaîne Centrale par la Vallée Longitudinale. Elle fait partie de l'arc de Luzon.

Le degré de métamorphisme diminue au fur et à mesure que l'on s'éloigne de la Vallée Longitudinale vers l'ouest (i.e., du Complexe de Tananao vers les *Western Foothills*) (Ho, 1988).
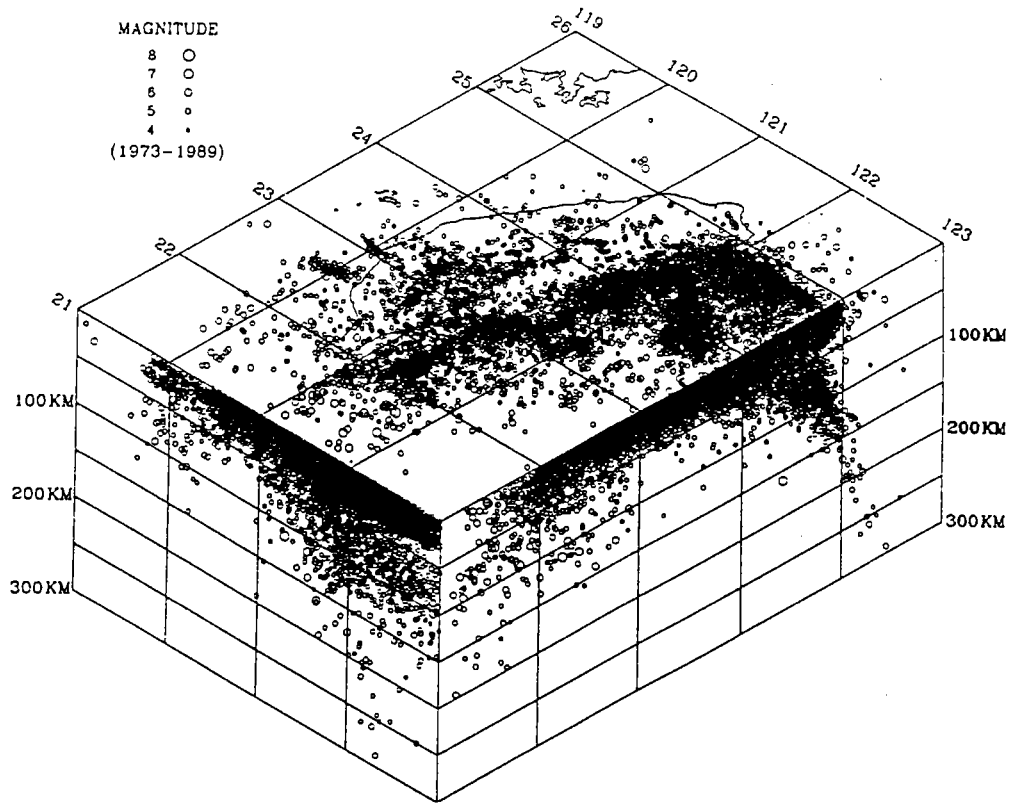
Fig. 3 : Répartition des séismes de magnitude ML $\geq$ 4 dans la région de Taiwan, de 1973 à 1989 (d'après Yeh et al., 1991).
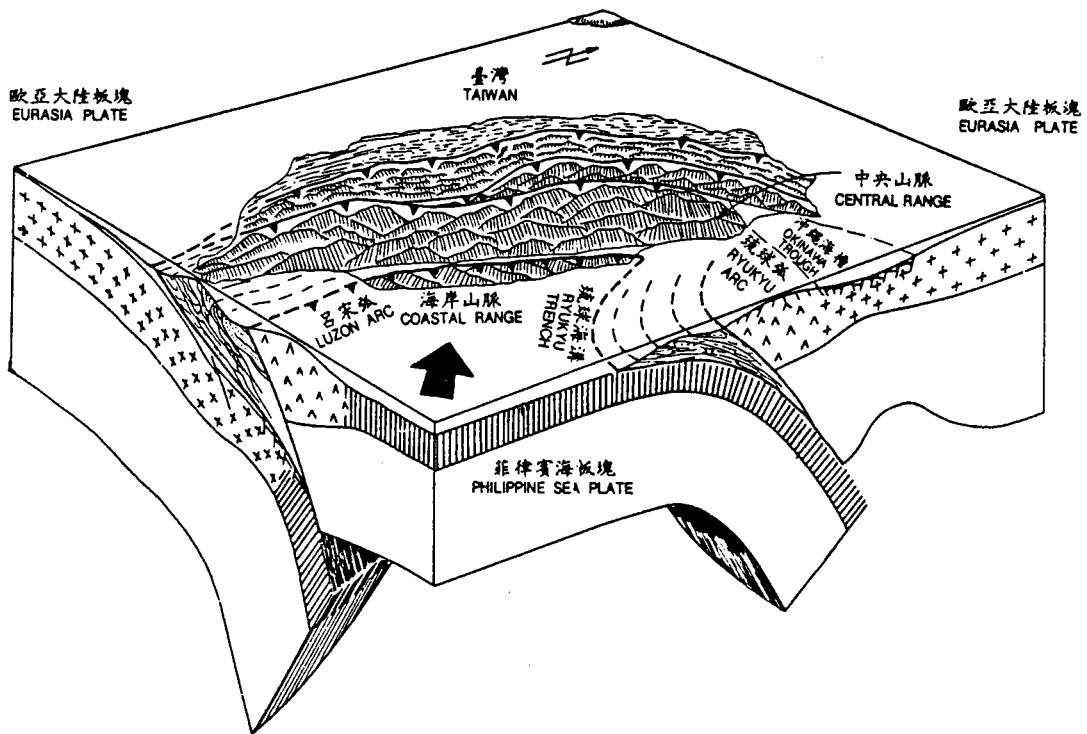
Fig. 4 : Bloc diagramme schématique montrant la collision arc-continent et le cadre tectonique de Taiwan (d'après Angelier, 1986).
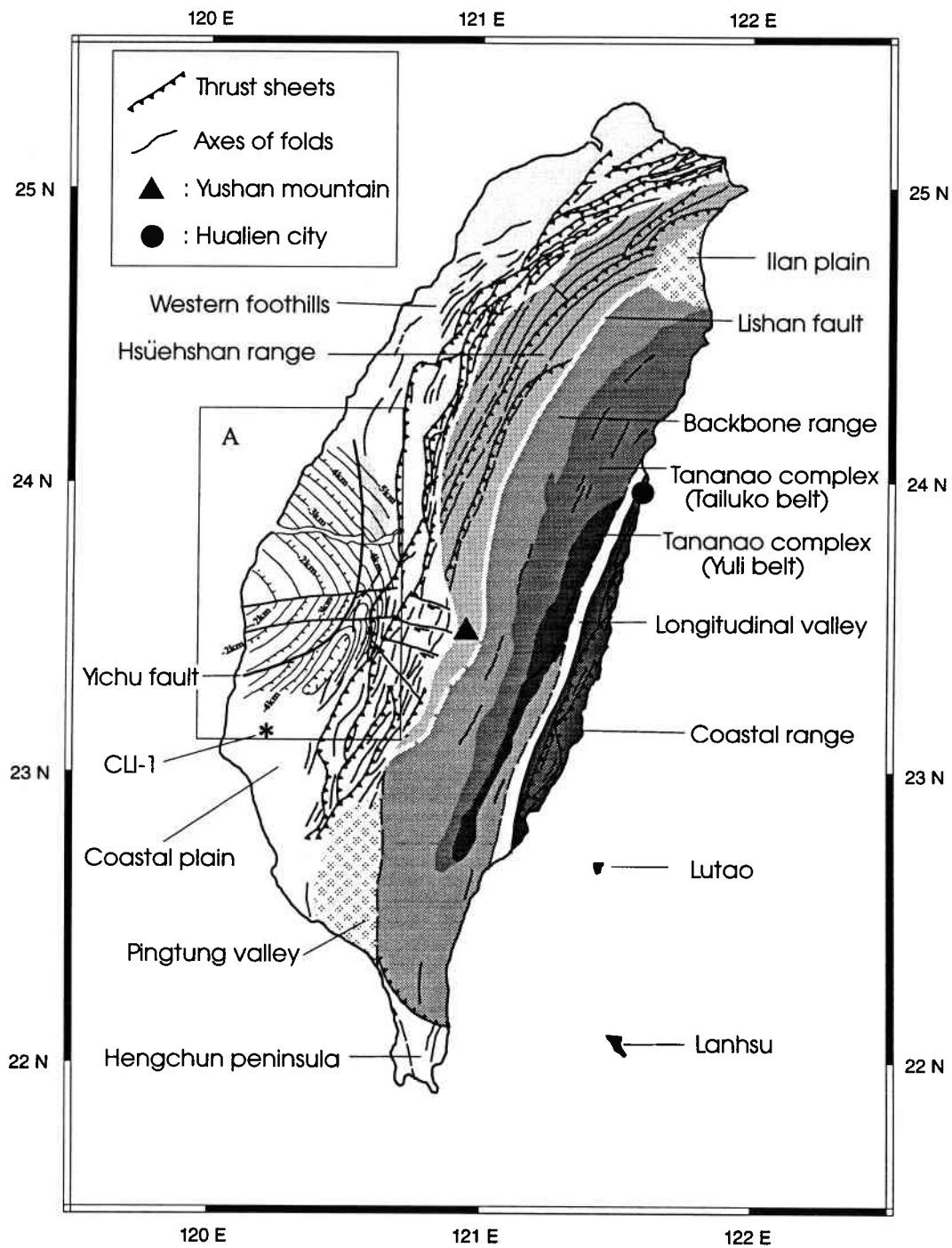
Fig. 5 : Carte tectonique générale de Taiwan (d'après Ho, 1988). Les iso-contours du relief du socle pré-Miocène (dans la fenêtre A) ont été obtenus d'après les données de forages (Tang, 1977).
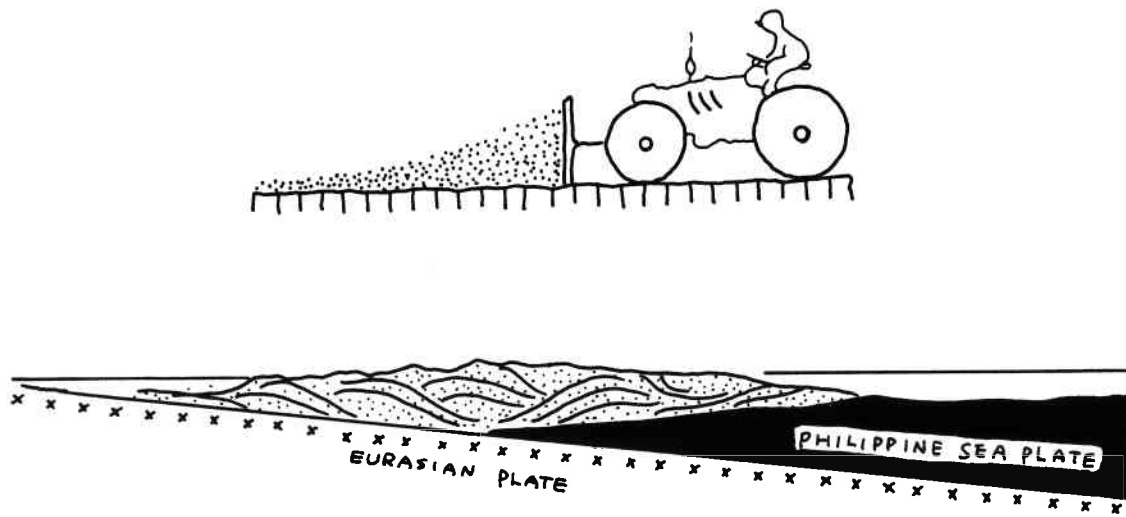
Fig. 6 : (en haut) Schéma de formation d'un prisme d'accrétion par un bulldozer (d'après David et al., 1983). (en bas) Coupe de l'orogène de Taiwan selon le modèle de "Coulomb-wedge" (d'après Suppe, 1981).

1.3. Surrection de Taiwan (le modèle de collision arc-continent)

Afin d'expliquer la formation de Taiwan, plusieurs modèles de formation ont été proposés (e.g., Suppe, 1981 ; Teng, 1990 ; Lu et Malavielle, 1994 ; Chemenda et al., 1995). L'orogène de Taiwan a été initialement expliqué en termes de géosynclinal (Ho, 1967). En revanche, Chai (1972) interprète la surrection de Taiwan comme le résultat d'une collision arc-continent, entre la marge continentale chinoise et l'arc de Luzon appartenant à la plaque PH. Cette hypothèse est généralement acceptée (e.g. Ho, 1988 ; Angelier, 1990). Suppe (1981) et Davis et al. (1983), par exemple, ont décrit l'orogène de Taiwan comme dû à l'accumulation des sédiments de la marge continentale résultant de la poussée de la plaque PH (**Fig. 6**). L'ouverture du bassin arrière-arc d'Okinawa serait associée à cette collision (**Fig. 7**) (e.g. Teng, 1990).

Le modèle de collision arc-continent peut expliquer certains phénomènes géologiques à Taiwan, notamment les plissements et les chevauchements observés dans les *Western Foothills* à l'ouest de Taiwan. Cependant, certains phénomènes géologiques

178
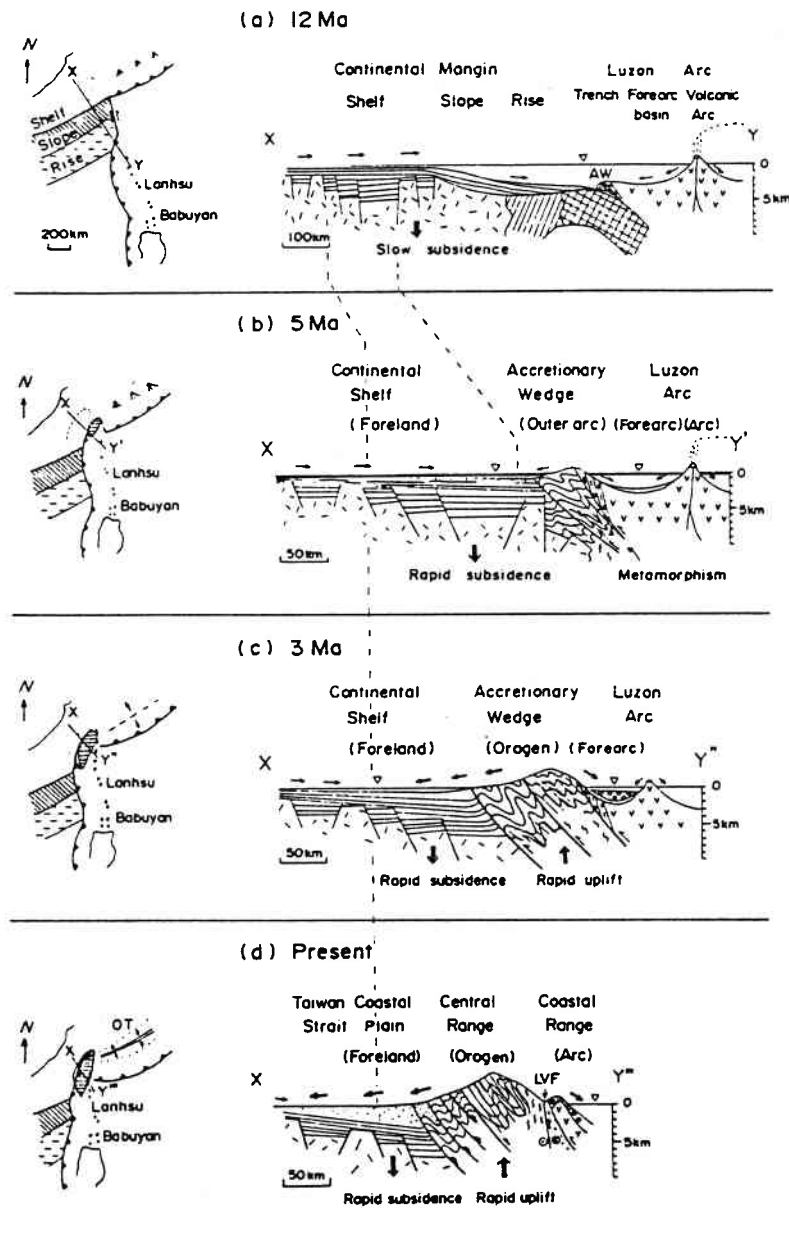
Fig. 7 : Evolution cinématique de la collision cénozoïque à Taiwan (Teng, 1990). Notons que d'après ce modèle, l'ouverture du bassin d'Okinawa serait un effet de la collision. OT : bassin d'Okinawa.

au niveau de Taiwan ne paraissent pas compatibles avec ce modèle. Par exemple,

1) Viallon et al. (1986) et Hu et al. (1995a) ont montré qu'une collision seule ne pouvait pas créer l'extension et l'ouverture du bassin d'Okinawa, bien que les modèles de collision arc-continent suggèrent que la collision soit le moteur de l'ouverture initiale du bassin d'Okinawa (**Fig. 7**) (e.g. Suppe, 1984 ; Letouzey et Kimura, 1986 ; Teng, 1990). De même, des discontinuités structurales majeures affectant toute la croûte et orientées NW-SE ont été identifiées entre le bassin sud d'Okinawa et Taiwan (Hsu et al., 1995b). La présence de ces discontinuités remet en cause les modèles qui proposent un mécanisme continu depuis la compression à Taiwan jusqu'à l'extension correspondant à l'ouverture du bassin d'Okinawa.
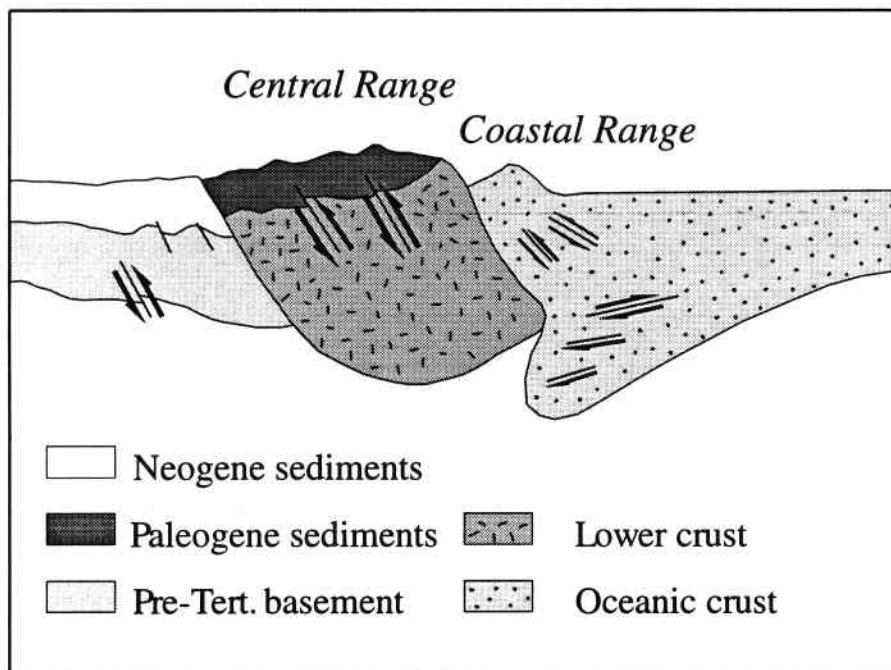
Fig. 8 : Modèle lithosphérique pour expliquer la collision à Taiwan (Wu et al., 1995).

2) Selon le modèle de collision arc-continent, Taiwan est principalement composée de sédiments plissés et soulevés. Cependant, les résultats de tomographie à Taiwan ont montré que non seulement la croûte sous la Chaîne Centrale était épaisse, mais que la partie inférieure de cette croûte était caractérisée par une vitesse élevée des ondes P (Wu et al., 1995). Ainsi, au lieu que ce soit les sédiments qui jouent le rôle principal pour la surrection de Taiwan, Wu et al. (1995) proposent que toute la croûte continentale ait été comprimée et soulevée (**Fig. 8**).

2. LES FRONTIÈRES MAJEURES ENTRE LES PLAQUES PH ET EU

Faute de données suffisantes, les frontières entre les plaques PH et EU ont souvent été controversées au niveau de Taiwan (**Fig. 9**). Avant de proposer notre nouveau modèle expliquant l'orogène de Taiwan, il est important de discuter les frontières possibles en tenant compte des données récentes.

2.1. Où se situe la frontière entre les deux plaques au niveau de Taiwan ?

Une frontière en subduction étant marquée par l'apparition d'ophiolites et de mélanges, Biq (e.g. 1969 ; 1977) a suggéré que l'actuelle frontière entre les plaques PH et EU se situait au niveau de la Vallée Longitudinale où se trouve le mélange de Lichi (**Fig. 10**). Cette interprétation est corroborée par les données de séismicité (Tsai, 1978 ; 1986). Yen (1963) a aussi montré, en tenant compte des données géologiques et géochimiques, que la majeure partie de la croûte de Taiwan présente un caractère continental, tandis que la Chaîne Côtière située à l'est de la Vallée Longitudinale est caractérisée par une croûte d'arc (e.g. Biq, 1981 ; Ho, 1988 ; Chen, 1995). En effet, on peut considérer que la croûte située sous la Chaîne Centrale Est pourrait être du même type que celle de l'arc des Ryukyus (Ho, 1988 ; Chen, 1991), car les basaltes analysés montrent une affinité d'arc volcanique (Chen, 1991).

En revanche, certains auteurs ont considéré que la faille de Lishan serait la frontière majeure entre les deux plaques (Suppe, 1981 ; 1984 ; Lu et Hsü, 1992). Lu et Hsü (1992) ont suggéré que le mélange de Kenting, daté du Miocène supérieur selon Chi (1982) et Pelletier (1985) et apparaissant dans la péninsule de Hengchun au sud de Taiwan (**Fig. 11**), représenterait la zone de suture d'une ancienne subduction. Cette suture et sa
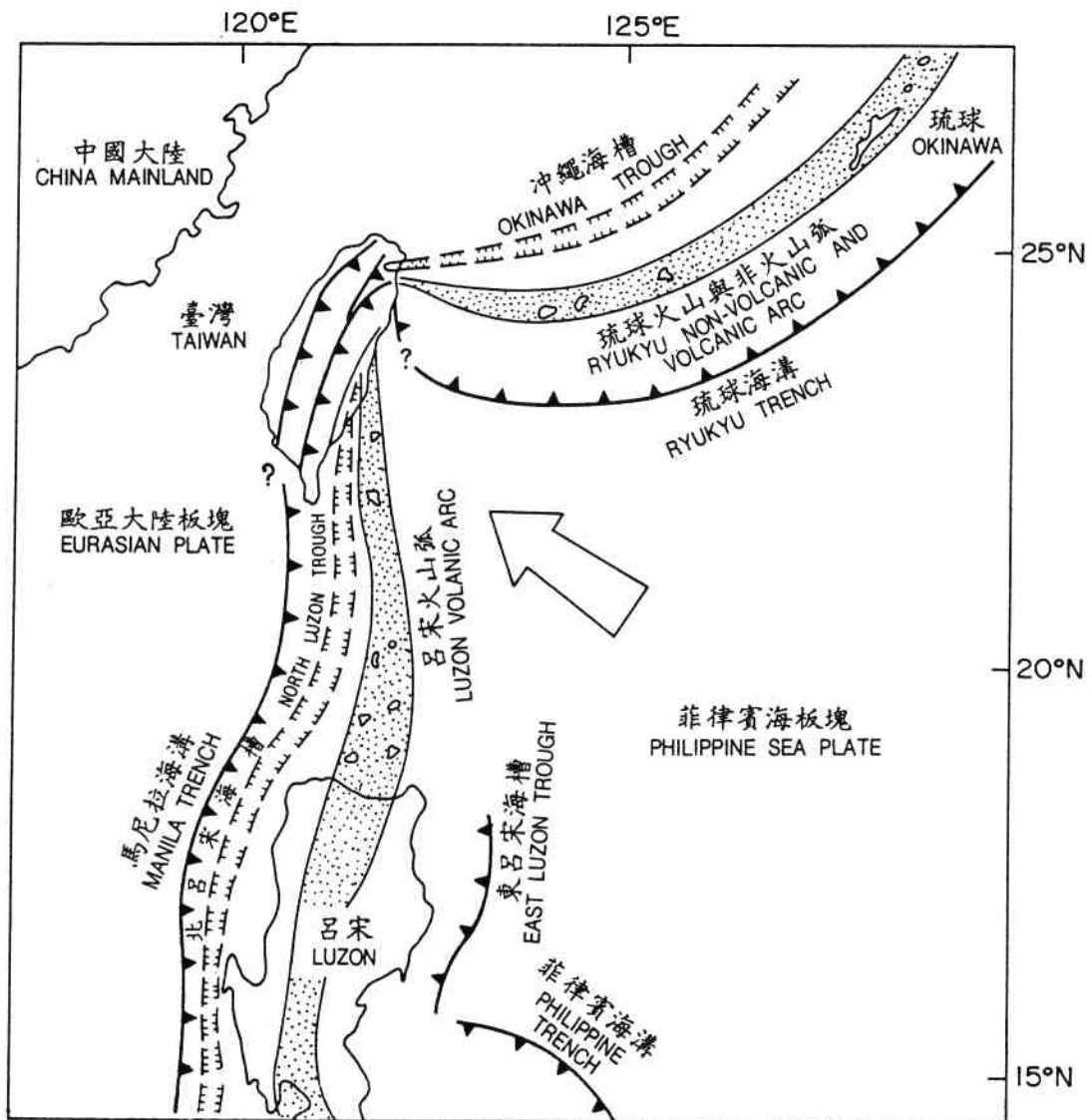
181

Fig. 9 : Cadre tectonique au Cénozoïque dans la région de Taiwan et ses environs, montrant l'interaction entre la plaque océanique Philippine et la plaque eurasiatique ainsi que les relations structurales entre Taiwan, l'arc des Ryukyus et l'arc de Luzon. Les problèmes controversés se trouvent principalement au sud-ouest et au nord-est de Taiwan.
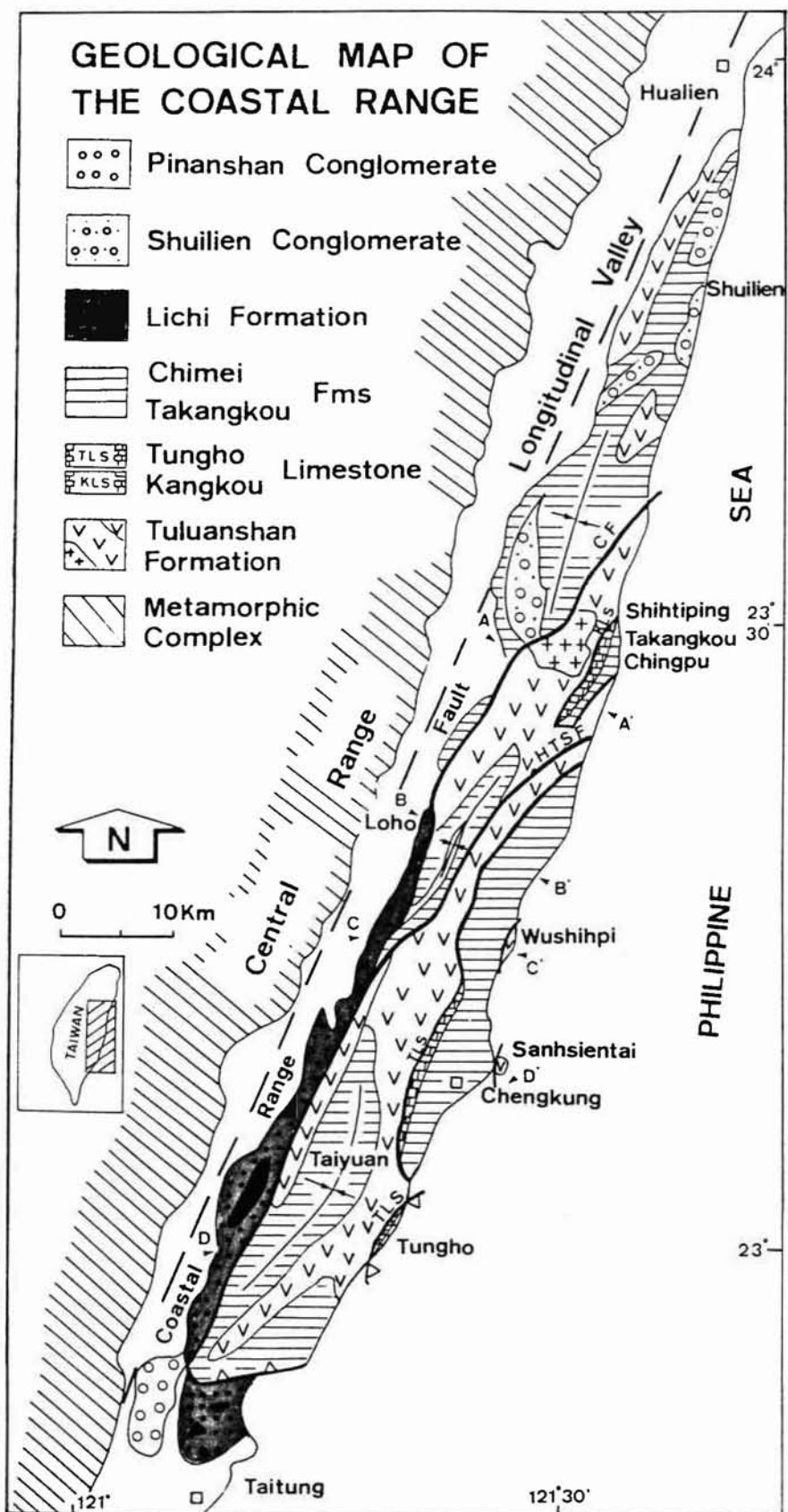
182

GEOLOGICAL MAP OF
THE COASTAL RANGE

Pinanshan Conglomerate

Shuilien Conglomerate

Lichi Formation

Chimei Takangkou Fms

Tungho Kangkou Limestone

Tuluanshan Formation

Metamorphic Complex

Fig. 10a : Géologie générale de la Chaîne Cotière (Huang et al., 1995b).

183

prolongation vers le nord, le long de la faille de Lishan, correspondrait à la frontière entre les plaques PH et EU. Dans le modèle de Lu et Hsü (1992), une ancienne zone de subduction, liée au mélange de Kenting, existerait avant la collision de l'arc de Luzon au Pliocène.
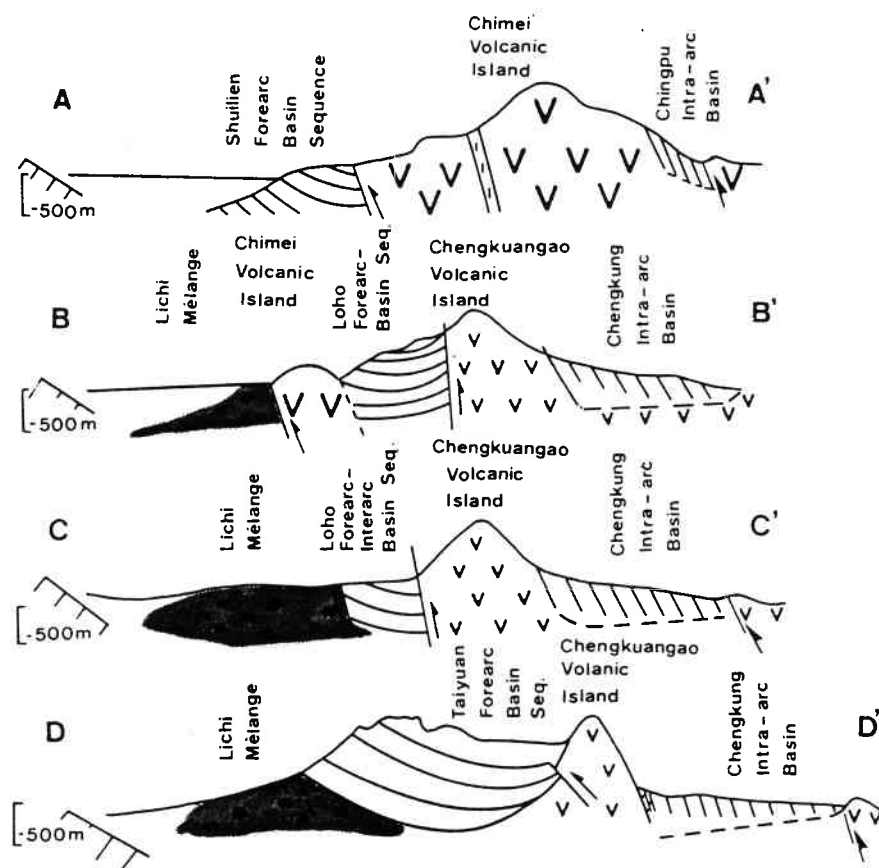
Fig. 10b : Coupes structurales à travers la Chaîne Côtière (Huang et al., 1995b).

La nature de la faille de Lishan est complexe : elle correspondrait à une faille normale majeure reprise en faille inverse et très probablement en décrochement (Lee, 1994). L'évolution tectonique le long de la faille de Lishan peut être décrite en quatre étapes principales **(Figs. 12 et 13)** (Lee, 1994).

i) **Eocène-Oligocène :** les sédiments se déposent dans un bassin affecté par de nombreuses failles normales. Par conséquent, cette période est caractérisée par un régime en extension.

184

ii) Miocène inférieur : la région est toujours en régime extensif mais la subsidence est plus faible qu'au Paléogène.

iii) Miocène moyen à supérieur-Pliocène : il s'agit d'un grand changement de régime avec passage d'un régime extensif à un régime compressif. Les failles normales préexistantes auraient rejoué en failles inverses et en décrochements.

iv) Quaternaire-Actuel : la Chaîne Centrale de Taiwan s'est soulevée rapidement.

En ce qui concerne le modèle de Lu et Hsü (1992), les considérations géologiques (Yen, 1975 ; Kizaki, 1986), ainsi que la nouvelle compilation bathymétrique que nous avons effectuée (Hsu et al., 1995b) montrent une continuité entre le complexe de Tananao et la partie sud-ouest de l'arc des Ryukyus. Cette continuité est aussi marquée sur la carte des anomalies de gravité de Taiwan sur laquelle on peut observer la présence de maximums relatifs à proximité de 24,5°N ; 121,8°E **(Fig. 14)**. D'autre part, en étudiant la micro-séismicité, Tsai et al. (1975) ont montré que la faille de Lishan se poursuit jusqu'à la terminaison occidentale du bassin d'Okinawa dans la plaine d'Ilan. La prolongation vers le nord de la faille de Lishan pourrait donc être mise en cause en tant que suture d'une ancienne zone de subduction.

Cette continuité entre la faille de Lishan et le bassin d'Okinawa nous a conduit à proposer que le bassin d'Okinawa actuel et le bassin sédimentaire localisé sous la faille de Lishan existaient avant la surrection de la Chaîne Centrale Ouest (Hsu et Sibuet, 1995). De plus, la continuité du mélange de Kenting jusqu'à la faille de Lishan ne peut pas constituer une ancienne zone de subduction. En effet, au sud de Yushan, la prolongation de la faille de Lishan n'est pas identifiable du point de vue structural (Ho, 1988) ou séismologique (Wu, 1978). De plus, selon le champ de vitesse géodésique à Taiwan **(Fig. 15)**, la vitesse relative de la croûte est assez stable au nord de Yushan, alors qu'au sud, elle augmente de l'ouest vers l'est et du nord vers le sud (Yu et al., 1995). Cette situation pourrait provoquer ou bien des cisaillements décrochants dextres, notamment à proximité de Yushan **(Fig. 5)**, ou bien des chevauchements. Ainsi, la faille de Hengchun située près du mélange de Kenting **(Fig. 11)**, dans la péninsule de Hengchun, peut difficilement être connectée à la faille de Lishan. Des décrochements dextres au moins mettent en cause cette continuité proposée par Lu et Hsü (1992). De plus, selon les données de paléontologie, le mélange de Kenting aurait été mis en place au Pléistocène (~1 Ma, Huang et al., 1995a).

En résumé, il semble que la frontière majeure entre les deux plaques se trouve bien dans la Vallée Longitudinale qui représente la suture actuelle correspondant à l'ancienne
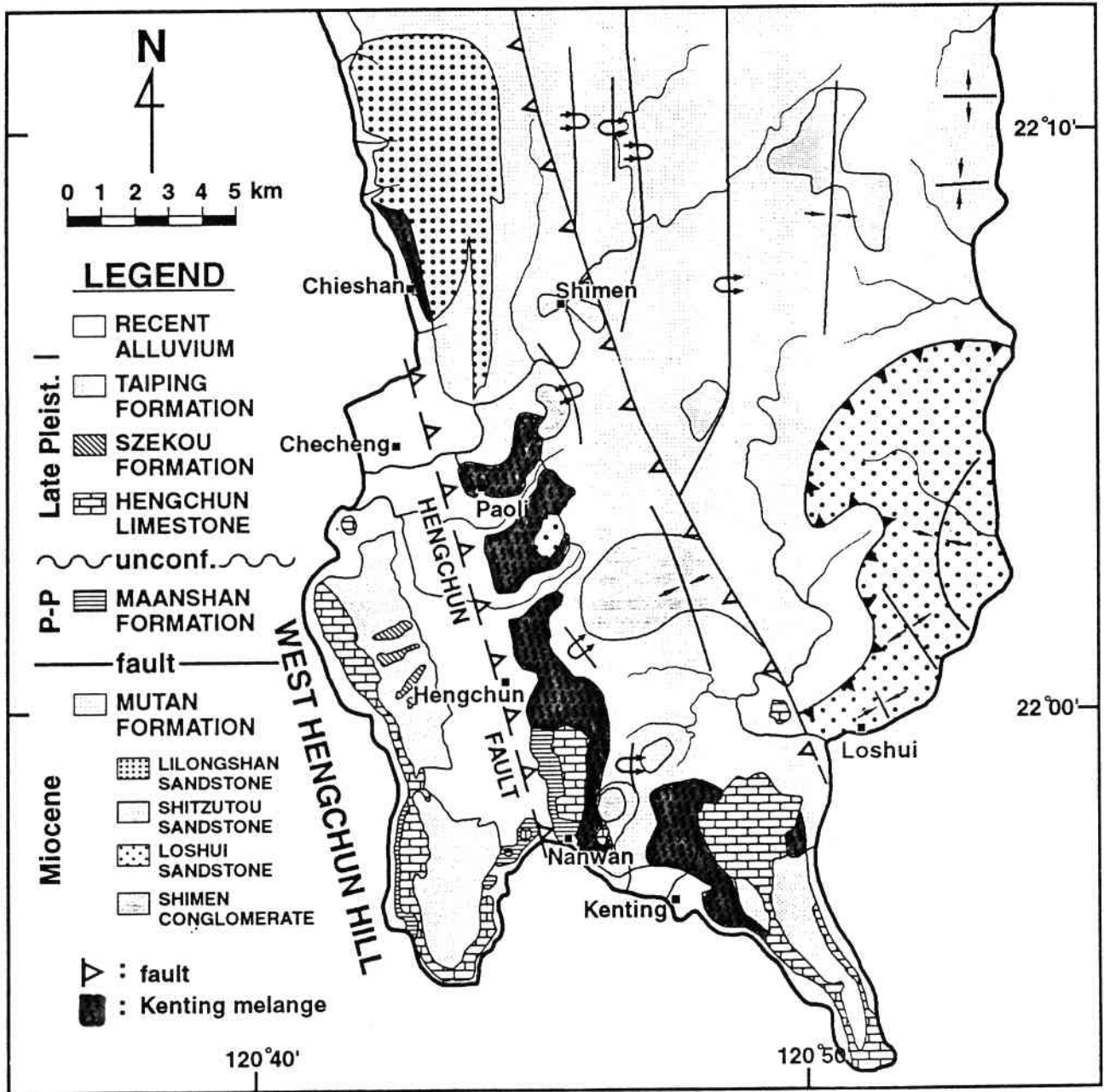
Fig. 11 : Carte géologique de la péninsule de Hengchun avec localisation du mélange de Kenting (Huang et al., 1995).
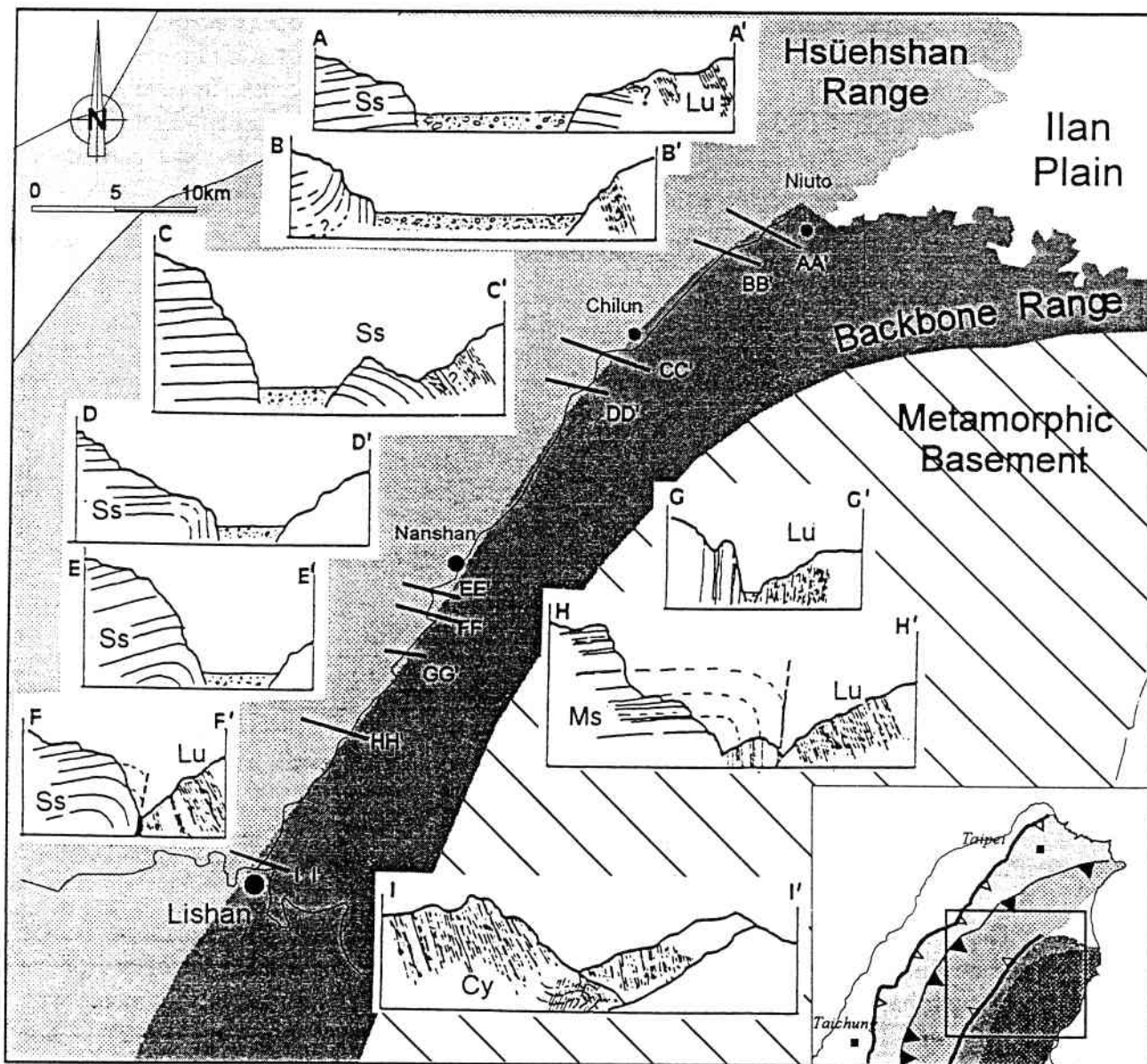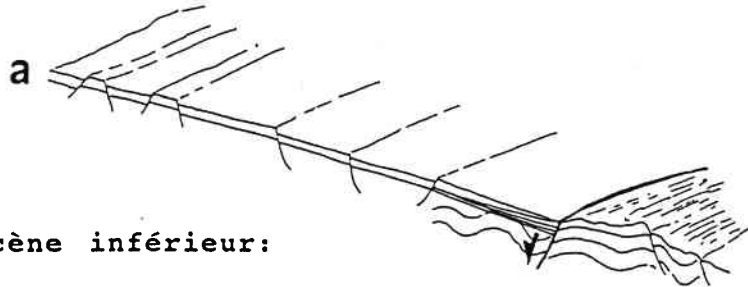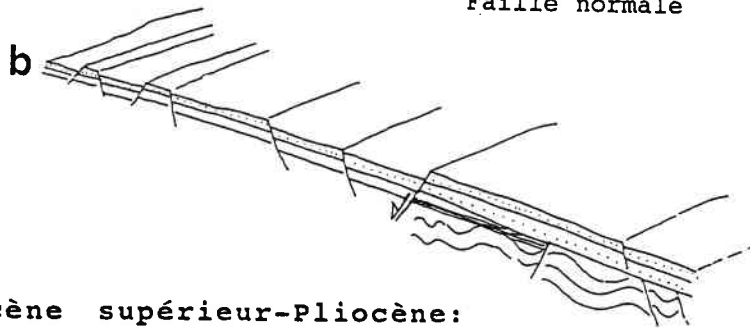
186

Fig. 12 : Profils schématiques traversant la faille de Lishan (Lee, 1994). Notons que la vallée se rétrécit du nord vers le sud. Ss : " grès Szeleng" ; Ms : "grès Meichi" ; Cy : "Formation de Chiayang" ; Lu : "Formation de Lushan".
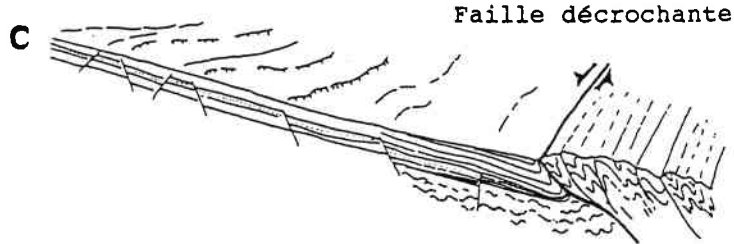
Eo-Oligocène:

a

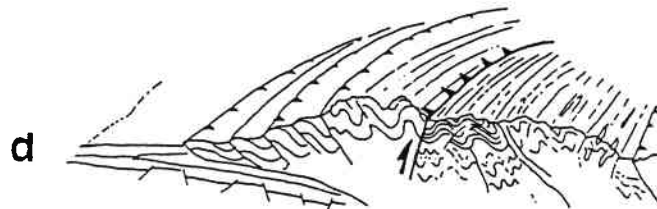Miocène inférieur:

Faille normale

b

Miocène supérieur-Pliocène:

Faille décrochante

c

Quaternaire:

Rétrochevauchement

d

Fig. 13 : Evolution tectonique de la faille de Lishan depuis le Tertiaire inférieur. (a) Eo-Oligocène : la faille de Lishan était probablement une faille normale majeure dans le socle métamorphique. Cette faille majeure était liée à un bassin extensif (b) Miocène inférieur : une phase tectonique calme avec une subsidence régulière. (c) du Miocène supérieur au Pliocène : la faille de Lishan est une faille normale qui rejoue en faille inverse (d) Quaternaire : rétrochevauchement à vergence ouest de la faille de Lishan. (Lee, 1994).
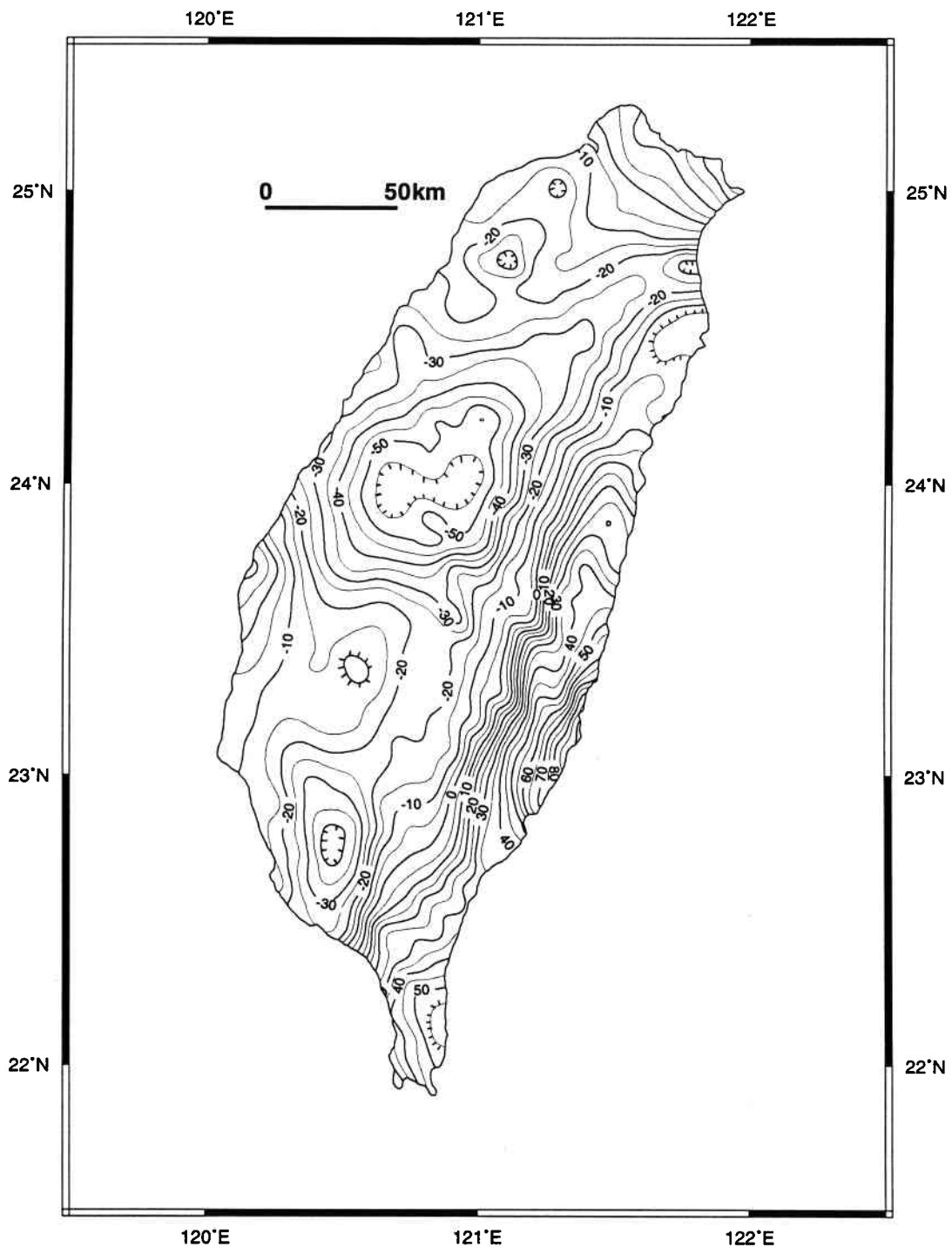
Fig. 14 : Anomalie de Bouguer à Taiwan (Yeh et Yen, 1991).

189
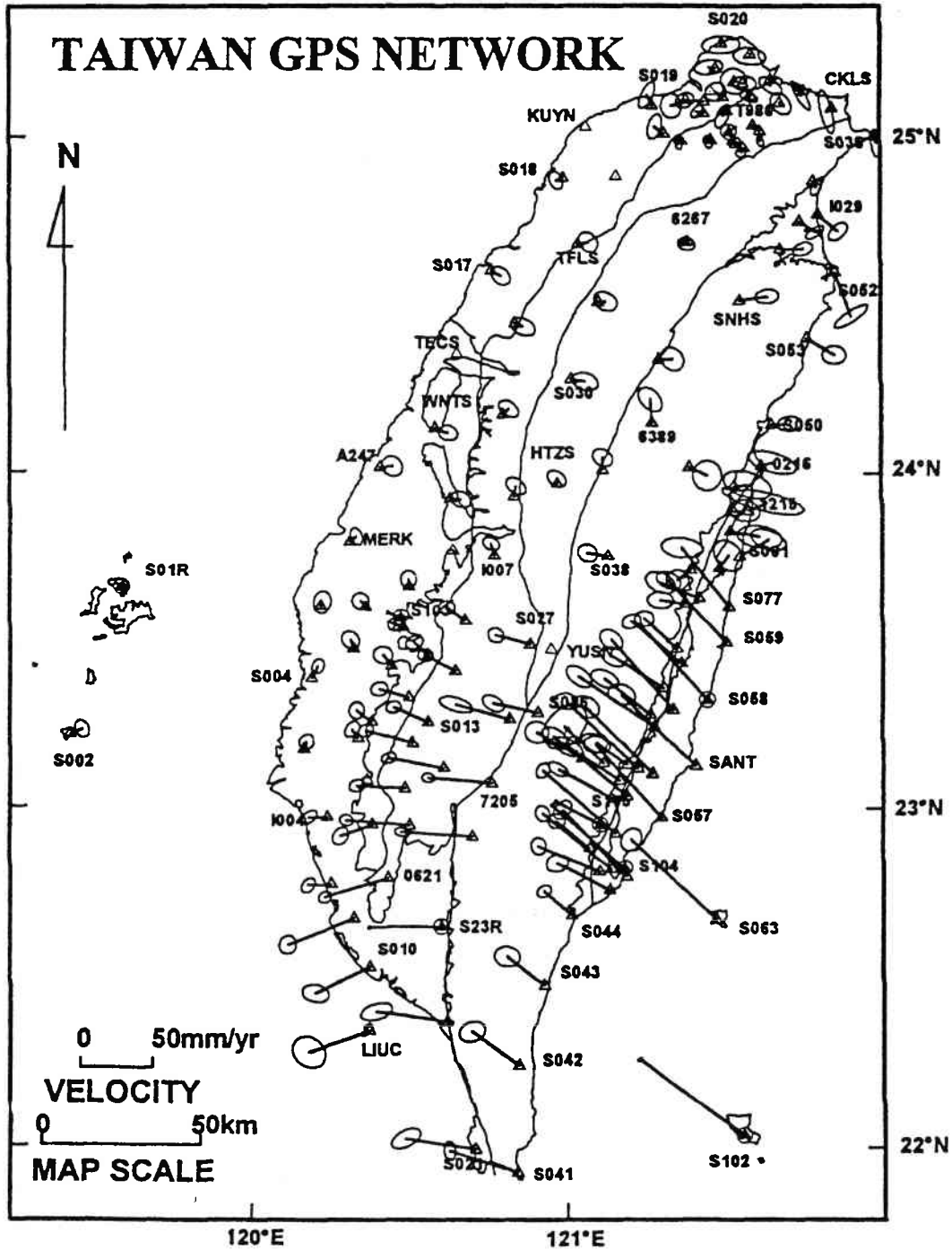
Fig. 15 : Réseau GPS de Taiwan et champ de vitesse. Les triangles blancs représentent les stations GPS relevées annuellement, les triangles noirs à l'intérieur des cercles représentent les stations à enregistrement continu. Les vitesses des stations sont rapportées à la station Paisha (S01R). L'ellipse de confiance à 95% se situe à la pointe de chacun des vecteurs vitesses (Yu et al., 1995).
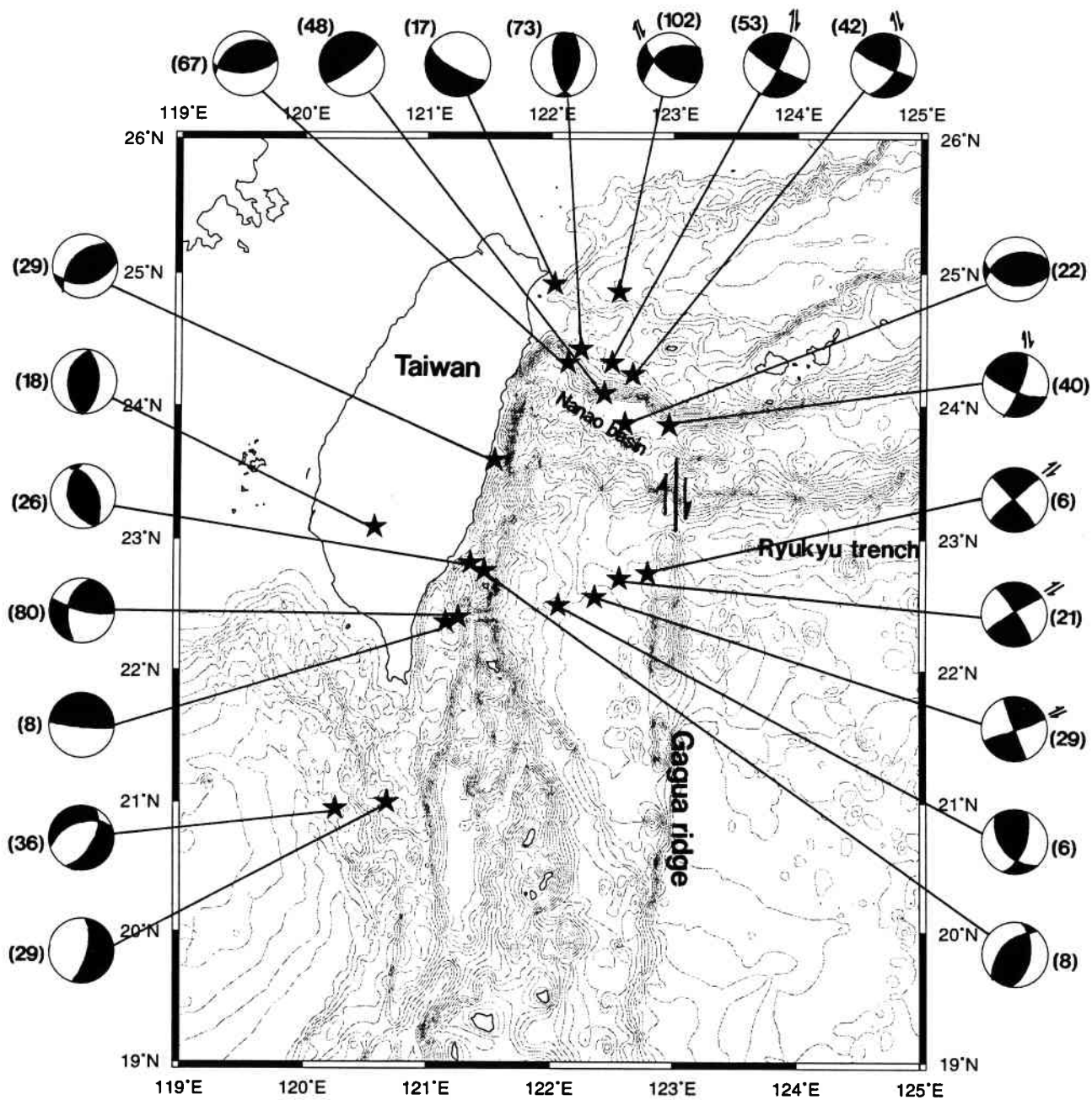
190

Fig. 16 : Récapitulation des mécanismes au foyer des grands séismes (M>6) entre 1963 et 1975 (d'après Wu, 1978), superposés à la bathymétrie au voisinage de Taiwan (Hsu et al., 1995b). Des décrochements dextres dans l'arc des Ryukyus sont suggérés.

191
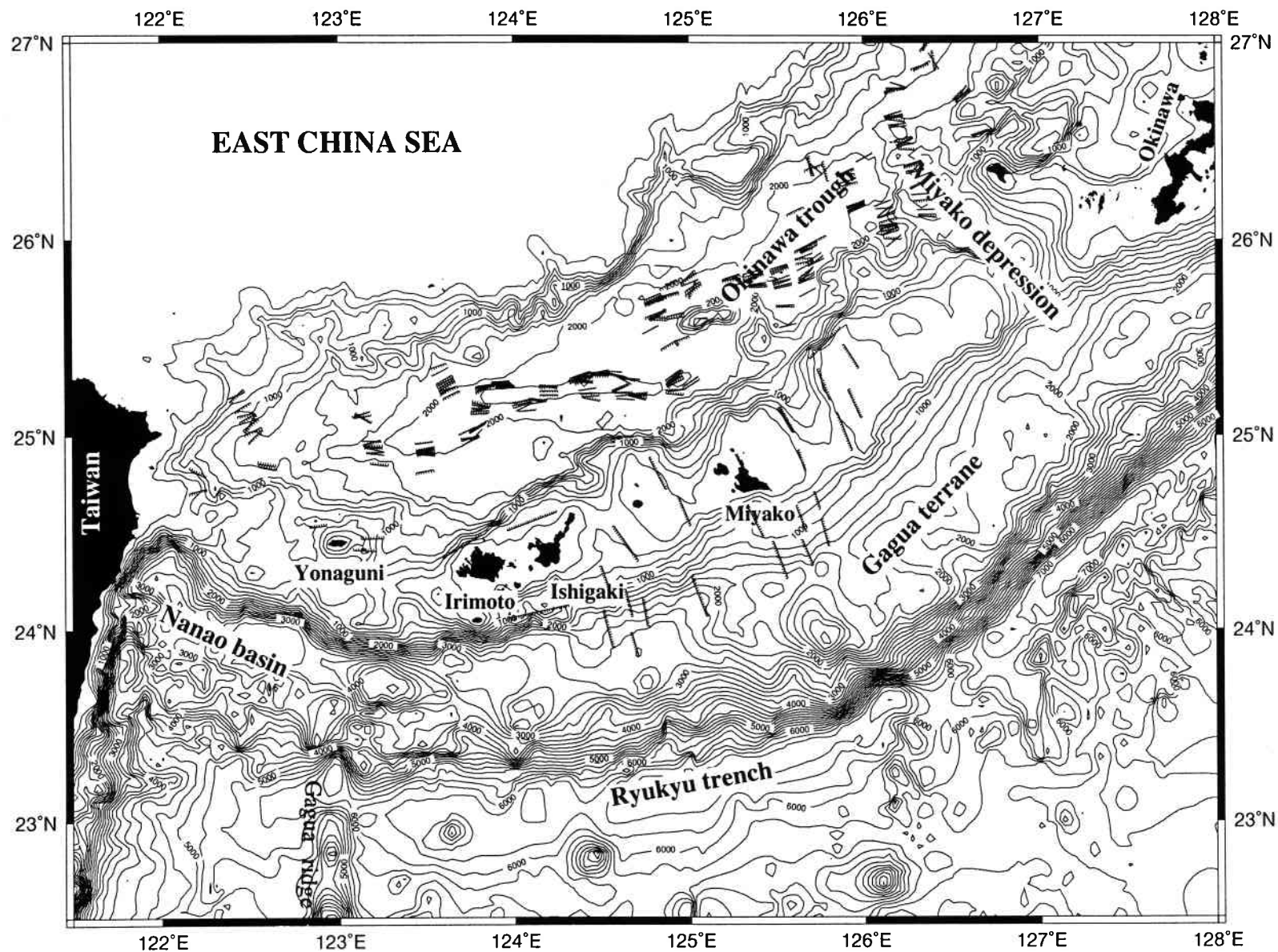
Fig. 17 : Carte bathymétrique du bassin sud d'Okinawa. Des failles normales ainsi que leurs orientations sont reportées (traits à barbules) (d'après Sibuet et al., 1995 ; Kuramoto et Konishi, 1989).

zone de subduction. La limite de la plaque PH suit la Vallée Longitudinale et rejoint la fosse des Ryukyus clairement exprimée à l'est de la ride de Gagua. Entre Taiwan et la ride de Gagua cette frontière de plaque est cependant plus difficile à mettre en évidence.

2.2. Y-a-t-il une dislocation dans la partie sud-ouest de la fosse des Ryukyus ?

La prolongation ouest de la fosse des Ryukyus demeure un problème très controversé. Certains auteurs pensent que la fosse des Ryukyus pourrait s'étendre jusqu'à Taiwan (e.g. Suppe, 1984 ; Kuramoto et Konishi, 1989 ; Teng, 1990 ; Kamata et Kodama, 1994). Au contraire, à partir des mécanismes au foyer des séismes, Wu (1970 ; 1978) a proposé l'existence d'une faille décrochante située à la longitude de 123°E, le long de la ride de Gagua (**Fig. 16**). Malgré cette controverse, des études sur la distribution des sédiments ont également montré des mouvements dextres au voisinage de la partie sud-ouest de l'arc des Ryukyus (Wageman et al., 1970 ; Karig, 1973 ; Yen, 1975 ; Kizaki, 1978 ; Lallemand et al., 1995). En outre, on peut observer que les directions des structures sous-marines autour de l'île de Miyako (entre 124°E et 126°E) sont généralement NNW-SSE alors que les directions des structures autour de l'île de Yonaguni (i.e. à l'ouest de 123,5°E) sont plutôt E-W (**Fig. 17**) (Kuramoto et Konishi, 1989). Ces observations suggèrent un changement dans la direction des contraintes de part et d'autre de la longitude 123,5°E dans l'arc des Ryukyus avec la présence éventuelle d'une faille.

L'analyse de l'ensemble des données géophysiques dans la partie sud-ouest de la zone de subduction des Ryukyus montre (Hsu et al., 1995b) :

- à l'est de 123,5°E, les structures dans le bassin d'Okinawa sont parallèles à la direction générale du bassin, tandis qu'à l'ouest de 123,5°E, les structures sont plutôt orientées NW-SE.

- trois décrochements dextres majeurs orientés NW-SE ont été identifiés à l'ouest de 123,5°E (à travers l'arc des Ryukyus et le bassin d'Okinawa).

Ainsi, des discontinuités tectoniques importantes devraient exister à l'ouest de 123,5°E et les contraintes horizontales devraient croître de l'est vers l'ouest. Il est donc probable que la collision entre l'arc de Luzon et l'arc des Ryukyus ait commencé à proximité de 123,5°E. Ensuite, la collision aurait provoqué la rotation de la partie située à l'ouest de 123,5°E de l'arc des Ryukyus d'environ 30° dans le sens des aiguilles d'une montre et aurait engendré des failles décrochantes dextres orientées NW-SE (Hsu et al., 1995b). Le début de la collision pourrait être datée à environ 10 Ma, correspondant à celle

de la rotation de l'île de Ishigaki déterminée par les données paléomagnétiques (Miki, 1995). A l'est de l'île de Ishigaki, la rotation faible de la déclinaison paléomagnétique n'a pas de signification tectonique (Miki, 1995). Postérieurement, la collision de la ride de Gagua avec l'arc des Ryukyus aurait pu faire rejouer les décrochements dextres. De plus, la modélisation analogique de l'effet de la collision entre deux blocs de rigidité différente entraîne l'apparition de décrochements dextres dans le "coin libre" **(Fig. 18)** (Lu et Malavielle, 1993).
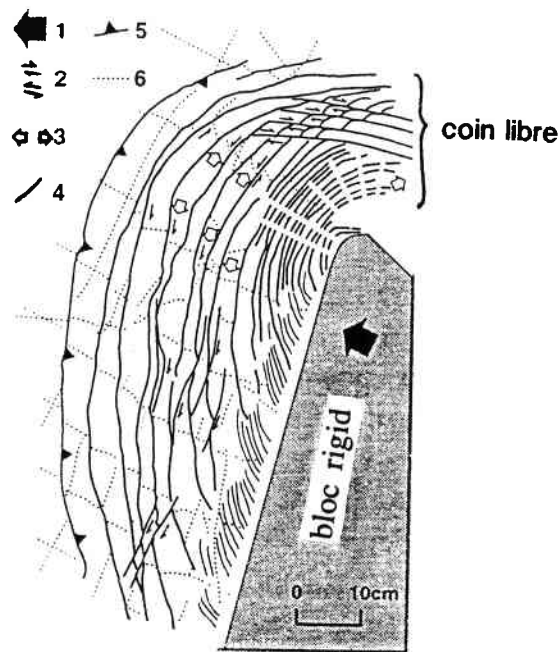
Fig. 18 : Modélisation analogique d'un poinçon (d'après Lu et Malavieille, 1994). On peut observer que les décrochements dextres sont concentrés au coin libre. 1 : direction du mouvement du poinçon. 2 : contrainte horizontale. 3 : extension. 4 : chevauchement oblique. 5 : chevauchement. 6 : repères des coordonnées.

Après le balayage de l'arc des Ryukyus par l'extrémité nord de l'arc de Luzon, la frontière de convergence à l'ouest de 123,5°E au voisinage du bassin de Nanao est pratiquement parallèle à la direction de convergence de la plaque PH par rapport à la plaque EU. Cette portion de marge pourrait donc être actuellement une portion de marge en cisaillement. Or, la présence d'une zone de Wadati-Benioff suggère, qu'au voisinage du bassin de Nanao, il existait une ancienne fosse. D'ailleurs, la carte bathymétrique met

en évidence la connexion morphologique entre la terminaison ouest du bassin de Nanao et la terminaison nord de la Vallée Longitudinale. De plus, l'anomalie de gravité dans le bassin de Nanao est extrêmement faible, ce qui suggère l'existence d'une ancienne fosse. En revanche, aucune continuité bathymétrique de la fosse des Ryukyus n'est observée à l'ouest de la ride de Gagua. La prolongation de la fosse des Ryukyus vers l'ouest n'est donc pas évidente.

Une hypothèse possible serait que la fosse des Ryukyus aurait été segmentée en deux parties, il y a environ 4 Ma, lors de la collision de l'ancienne ride de Gagua avec la zone de subduction des Ryukyus (Hsu et al., 1995b). Le segment Ouest de la zone de subduction diminuerait de longueur alors que le segment Est se propagerait vers l'ouest (Hsu et al., 1995b).

Dans cette hypothèse, une structure majeure, appelée *"Gagua terrane"*, est caractérisée par une anomalie positive gravimétrique de forte amplitude, dans l'avant-arc des Ryukyus. Cette structure est relativement aséismique **(Fig. 19)** et similaire aux plateaux océaniques ou aux rides aséismiques (Ben-Avraham et al., 1981). Nous formulons l'hypothèse qu'elle faisait initialement partie de la ride de Gagua. En tenant compte de la vitesse de la convergence entre les deux plaques PH et EU (Seno et al., 1993), il y a 9-4 Ma, la ride de Gagua se trouvait juste au sud de la position actuelle de cette structure (voir Fig. 11 de Hsu et al., 1995b). Autrement dit, cette structure aurait pu être mise en place à cette période et se serait séparée de la ride de Gagua il y a 4 Ma environ. Le *"Gagua terrane"* est limitée à l'est par la dépression de Miyako **(Fig. 17)**. La collision de la ride de Gagua avec l'arc des Ryukyus aurait pu entraîner le cisaillement initial à l'origine de cette dépression qui correspond à une des coupures majeures de l'arc des Ryukyus.

2.3. Où se situe la prolongation nord de la fosse de Manille ?

Au sud de Taiwan se pose la question de la prolongation vers le nord de la fosse de Manille. Ce problème peut être abordé à partir des données de tectonique, de séismicité, des anomalies gravimétriques et des anomalies magnétiques. En 1990, une mission océanographique sur le N/O *Moana Wave* a été effectuée au sud de Taiwan. Au cours de cette campagne les données d'imagerie par sonar latéral (*Sea MARC II*) et bathymétrie tri-dimensionnelle associées, de sismique réflexion et de 3,5 kHz ont été collectées.

Les résultats montrent qu'au sud de Taiwan la région est caractérisée par un prisme d'accrétion (e.g. Reed et al., 1992 ; Lundberg et al., 1995) marqué par la présence de
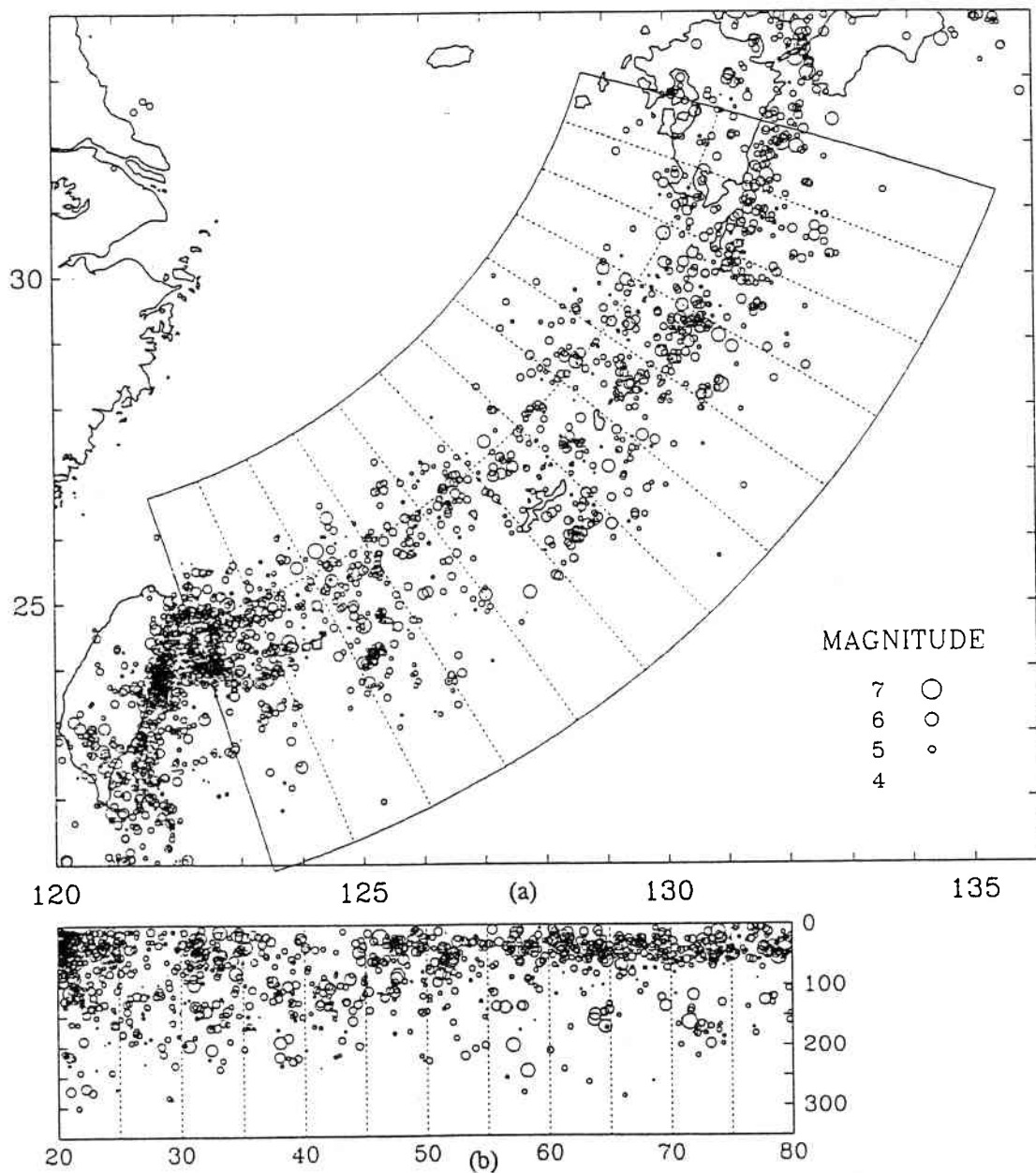
Fig. 19 : Distribution des séismes autour de l'arc des Ryukyus entre 1960 et 1991. Les séismes avec des magnitudes supérieures ou égales à 4 sont représentés (Cheng et al., 1989). (en haut) Distribution des épicentres, la ligne pointillée le long du bassin d'Okinawa indique la profondeur de 150 km pour la zone de Wadati-Benioff ; (en bas) Distribution des hypocentres qui sont projetés sur un axe parallèle à l'arc. Les abscisses sont reportées à partir du Sud. On peut observer qu'il y a une diminution de la densité des séismes entre 24°N-26°N et 126°E-128°E. Noter également une forte densité des séismes entre Taiwan et le méridien 123,5°E.

196
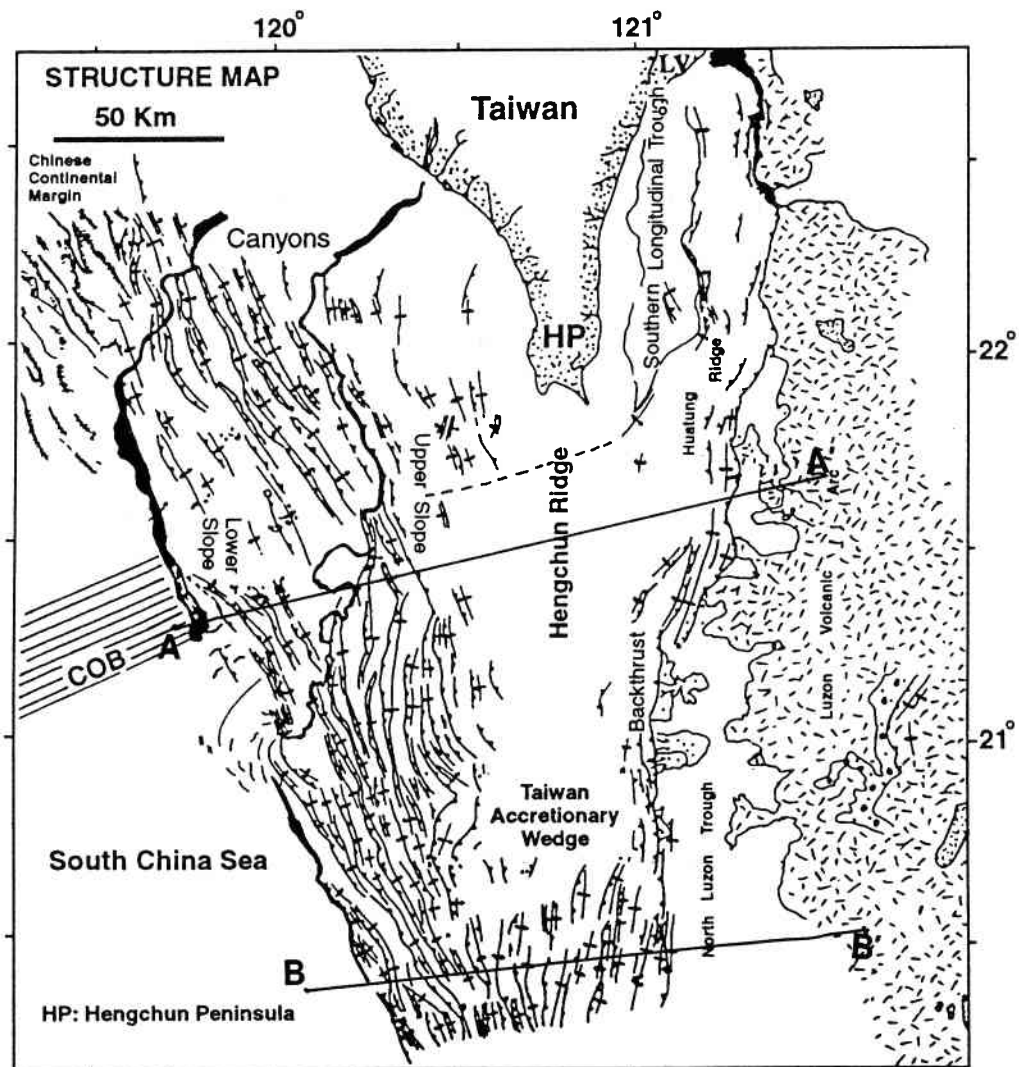
Fig. 20a : Carte structurale dans la région des levés SeaMARC et de sismique. Noter les orientations NNW-SSE des chevauchements le long des marges Est et Ouest du prisme d'accrétion (Reed et al., 1992). Noter également la discontinuité suggérée au sud de Taiwan (ligne pointillée).
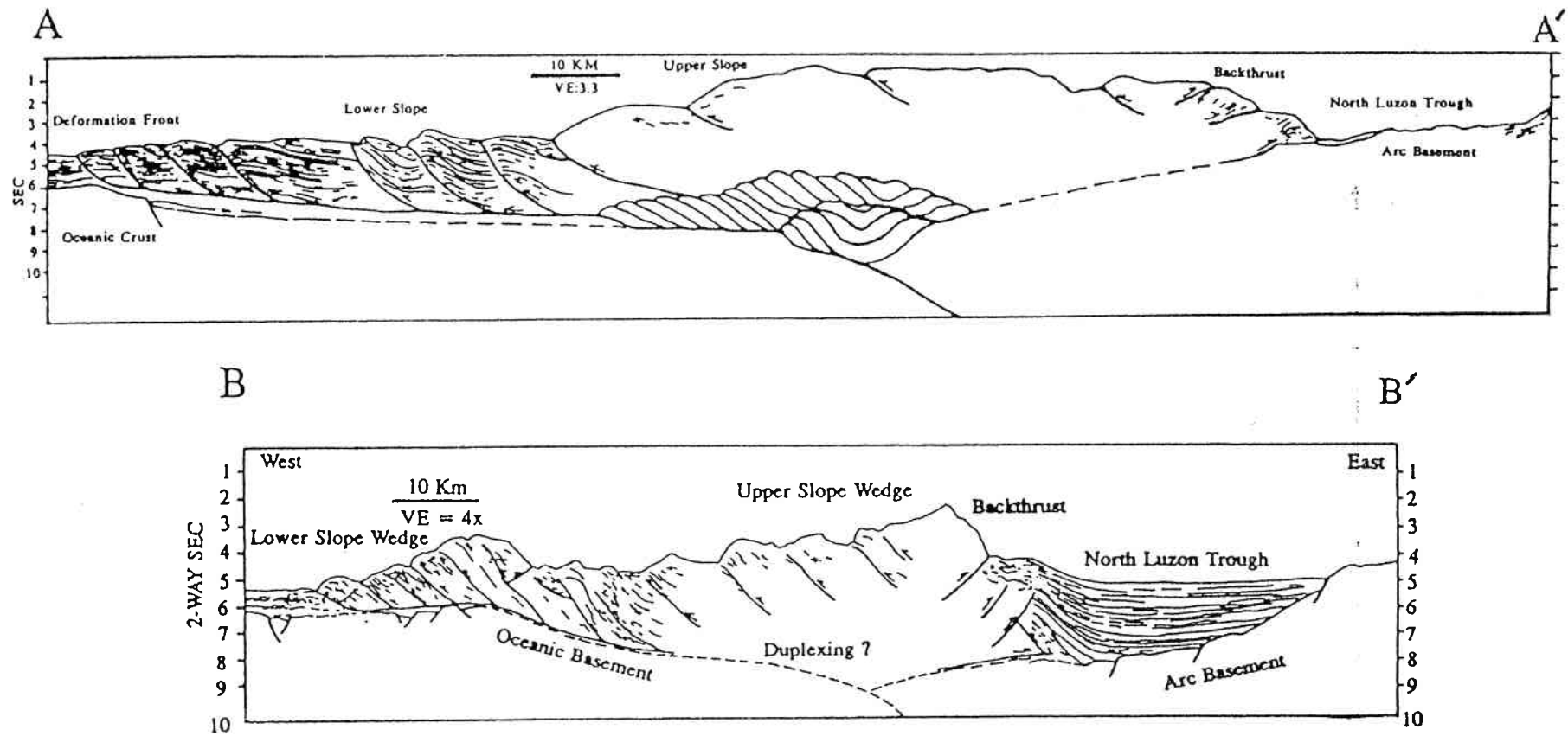
197

Fig. 20b : Interprétations des coupes sismiques selon les profils AA' et BB' localisés sur la Fig. 20a.
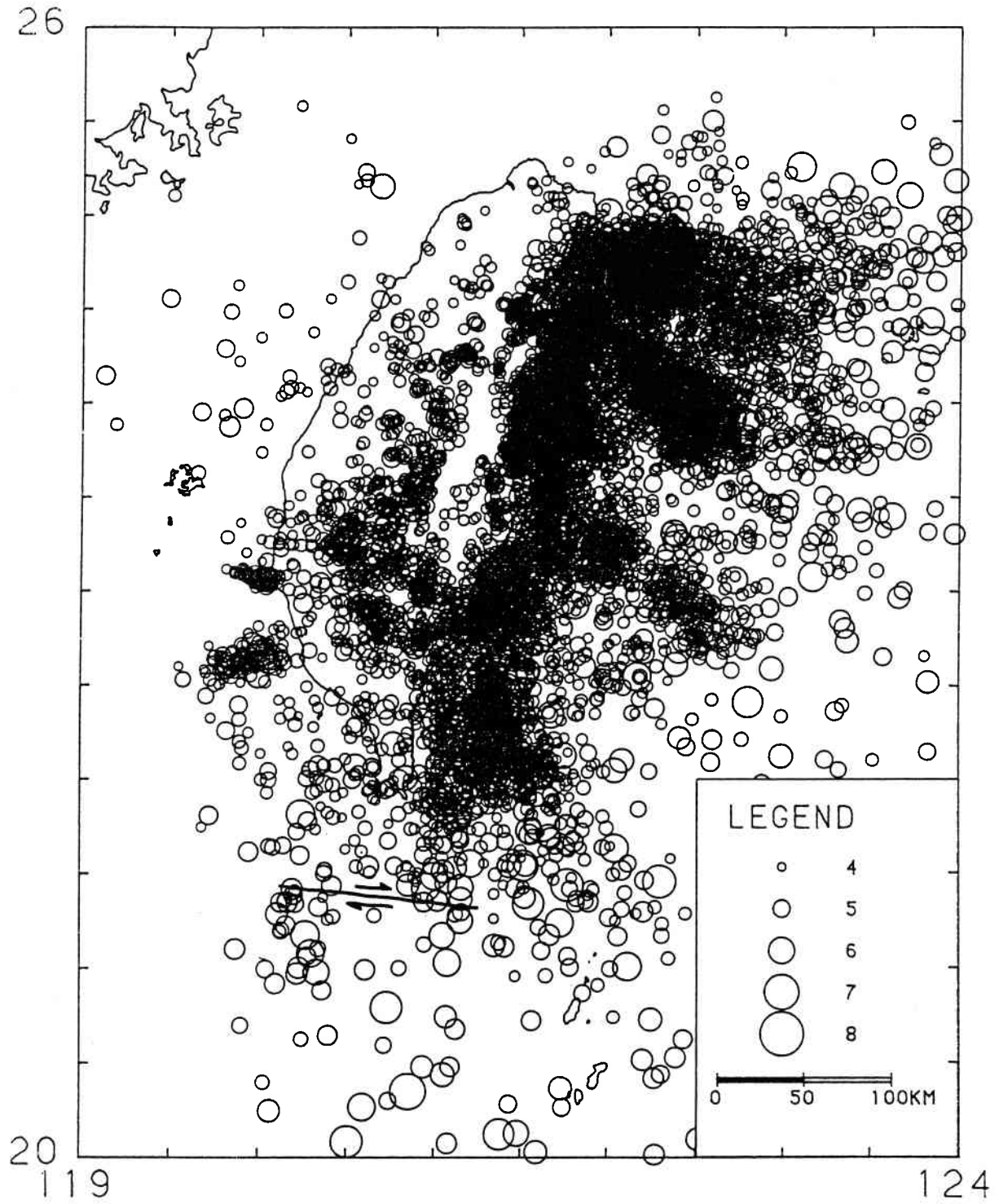
198

Fig. 21 : Epicentres des séismes enregistrés entre 1973 et 1988 (Cheng et Yeh, 1991). Noter la discontinuité suggérée au niveau de 21,5°N.
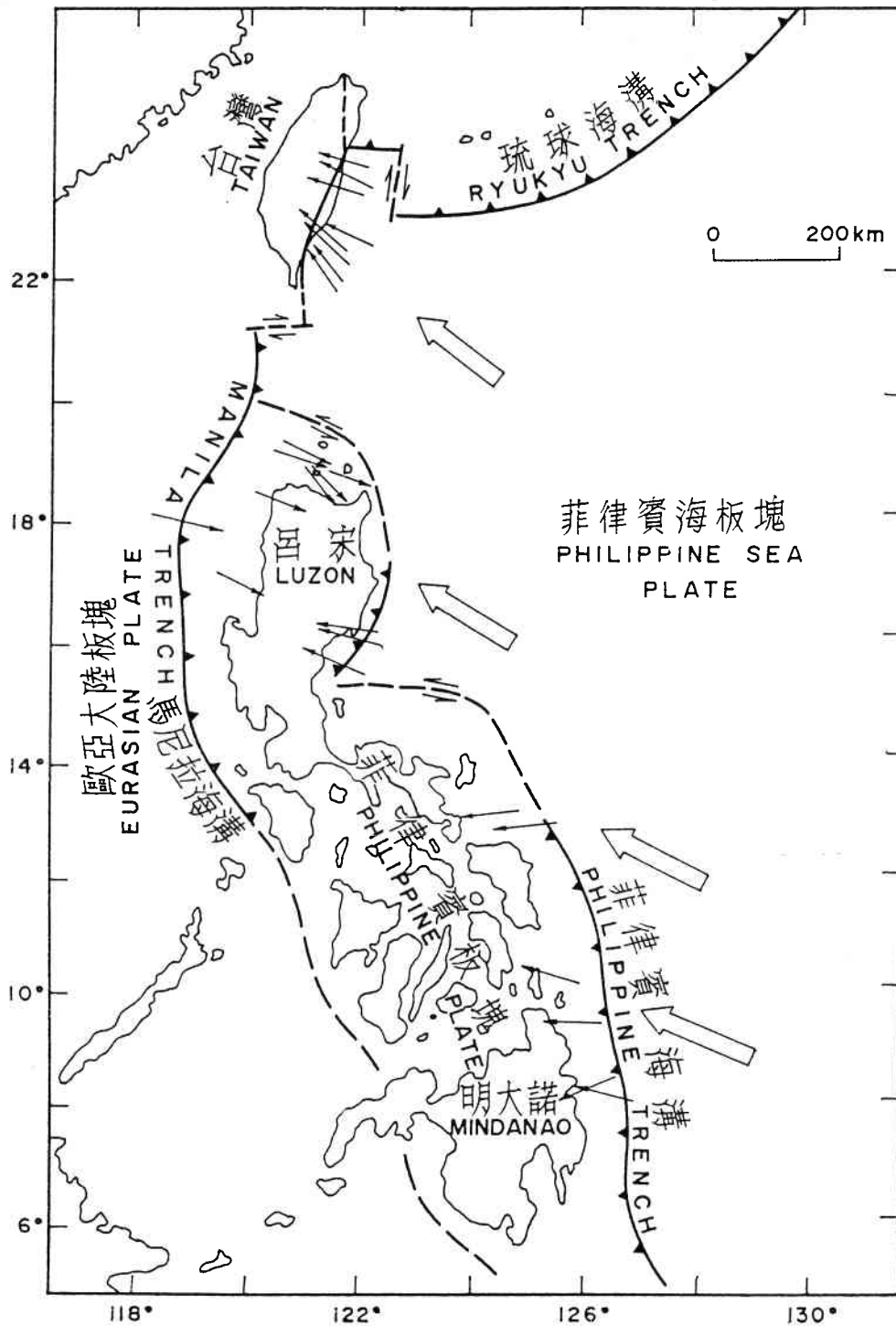
199

Fig. 22 : Les frontières tectoniques déterminées par les mécanismes des séismes entre Taiwan et les Philippines (Lin et Tsai, 1981). Les petites flèches représentent les vecteurs de déplacement le long des frontières.
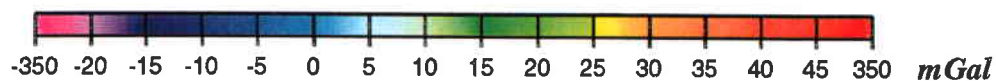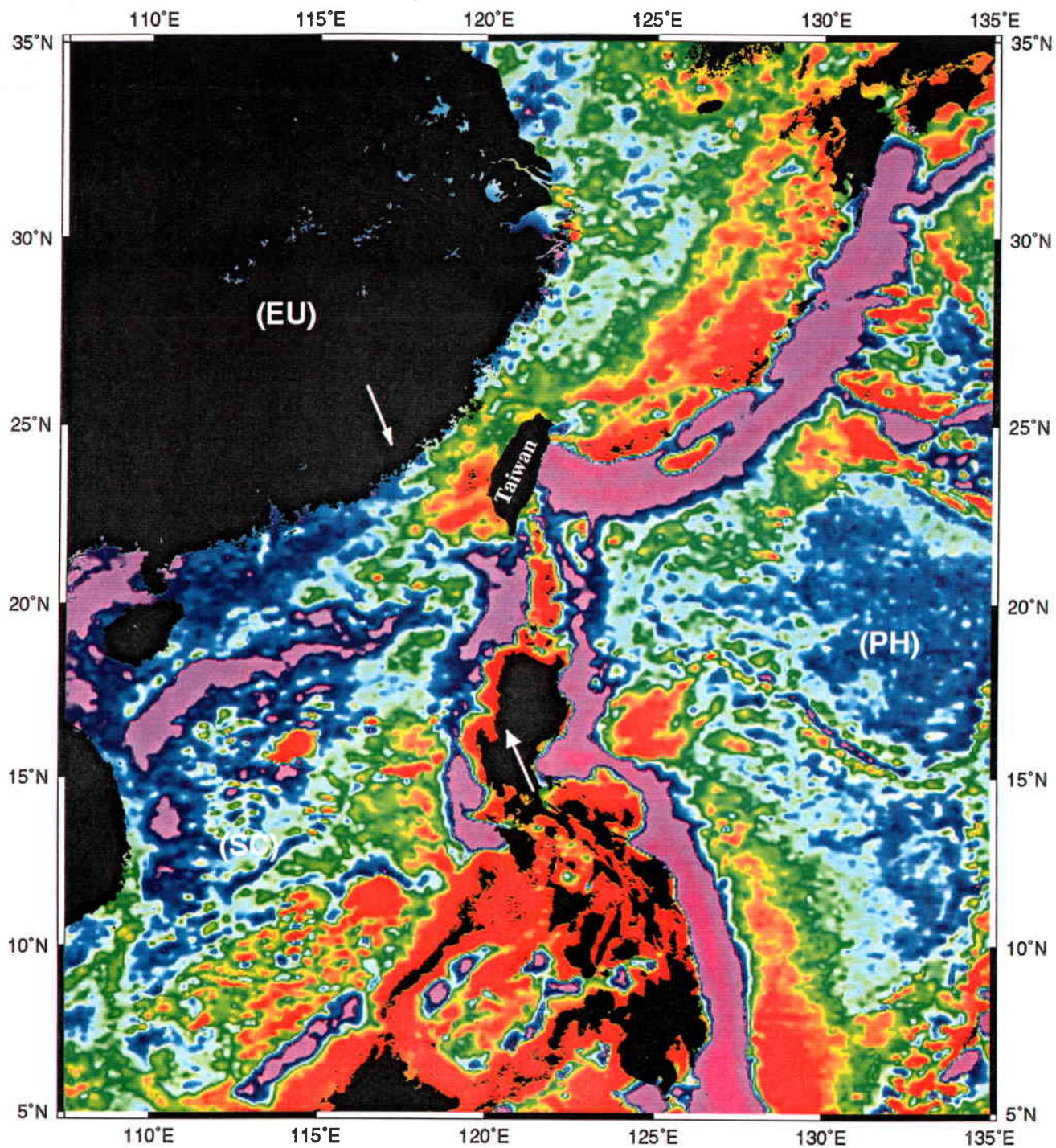
Fig. 23 : Anomalie gravimétrique dérivée de l'altimétrie satellitaire (Sandwell et Smith, 1994). Noter l'alignement orienté NW-SE à l'extrémité occidentale du bassin de Tainan (indiqué par les deux flêches blanches) séparant la Mer de Chine du Sud et l'ancienne zone de subduction au sud de Taiwan. Noter aussi la direction NE-SW de la dorsale fossile dans la mer de Chine du Sud, située par 12°N ; 113°E et orientée N052°. EU : la plaque eurasiatique. PH : la plaque de la Mer des Philippines. SC : la Mer de Chine du Sud.

chevauchements parallèles à la direction de la fosse de Manille (**Figs. 20a et 20b**). Il est donc tentant de suggérer une prolongation de la fosse de Manille en direction de Taiwan. Cependant, il existe une discontinuité située par 21,5°N ; 120,5°E et orientée ENE-WSW. Cette discontinuité est notamment marquée par un changement de direction du canyon de Pingtung (Liu et al., 1993). A partir des données magnétiques, l'existence d'une zone de transition dans le socle magnétique a également été suggérée (Liu et al., 1992). Reed et al. (1992) ont montré qu'à l'ouest de 122°E cette zone de transition était la frontière entre les croûtes océanique et continentale. Du point de vue de la séismicité, Tsai (1986) et Cheng et Yeh (1991) ont montré que la zone de Wadati-Benioff associée à la fosse de Manille s'estompait progressivement vers le nord et qu'au nord de 21,5°N, la zone de Wadati-Benioff n'existait plus (ou du moins ne pourrait plus être identifiée). Au nord de 21,5°N, la plupart des séismes est plutôt concentrée entre 121°E et 122°E, ce qui permet de mettre en évidence un changement dans la distribution des séismes superficiels (**Fig. 21**). Ceci est également corroboré par l'existence d'un décrochement dextre,
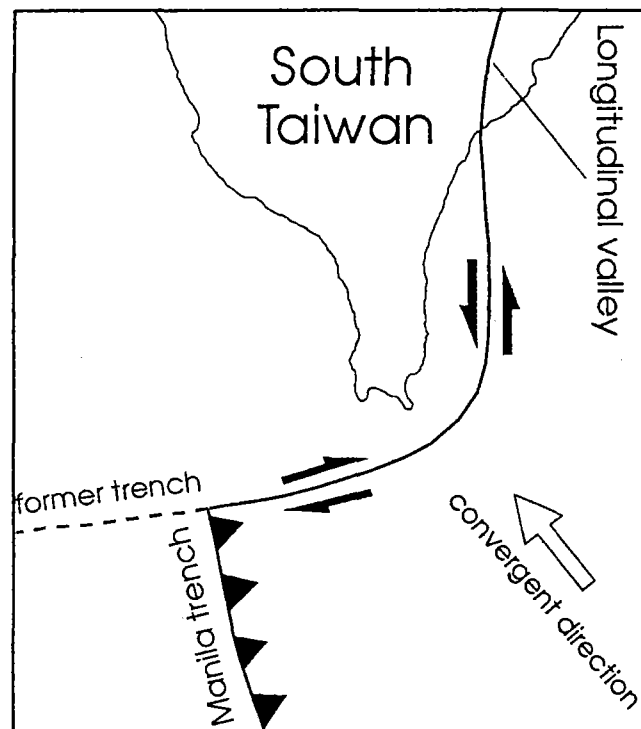

Fig. 24 : Frontière tectonique suggérée dans le sud de Taiwan. La flèche indique la direction de la convergence de la plaque de la Mer des Philippines.

déterminé par les mécanismes au foyer des séismes superficiels au sud de Taiwan (**Fig. 22**) (Lin et Tsai, 1981). De plus, la carte des anomalies de gravité, dérivée des données d'altimétrie satellitaire permet de mettre en évidence la présence de cette discontinuité caractérisée par une amplitude très faible quasi parallèle à la latitude 21,5°N (**Fig. 23**) (e.g. Sandwell et Smith, 1994 ; Sandwell et al., 1995). Au nord de cette discontinuité, la région est marquée par une amplitude élevée de la gravité. La discontinuité suggérée à 21,5°N pourrait représenter la connection de la fosse de Manille actuelle avec la zone de suture correspondant à la Vallée Longitudinale (**Fig. 24**). Avant la collision de l'arc de Luzon avec Taiwan, l'ancienne fosse de Manille était probablement continue, jusqu'au nord de l'arc de Luzon (**Fig. 25, 3Ma**).

Il est donc probable que l'actuelle fosse de Manille *stricto sensu* ne se poursuive pas au delà de cette discontinuité. En revanche, l'ancienne fosse de Manille se serait progressivement fermée depuis le nord et s'arrêterait aujourd'hui aux environs de 21,5°N. Or, la collision actuelle au sud de Taiwan a provoqué un front de déformation qui s'observe sur la carte structurale jusqu'à 22,5°N (**Fig. 20a**). Ces structures sont généralement orientées N330° et sont à peu près parallèles à la direction de Taiwan (**Fig. 20a**). Cette déformation récente jouerait principalement dans les sédiments des couches superficielles (**Fig. 20b**) et pourrait correspondre à l'absorption d'une partie de la convergence entre les plaques PH et EU, non absorbée sur l'île de Taiwan (cf. **Figs. 15 et 20a**) (Lallemand et al., 1995).

3. MODÈLE DE COLLISION ARC-ARC

L'apport de données récentes sur une région permet, naturellement, de mieux appréhender sa géologie et de proposer un modèle intégrant l'ensemble des observations. Depuis quelques années, à Taiwan, la quantité de données acquises à terre a été plus importante que celle obtenue en mer autour de Taiwan. Faute de connaissances suffisantes en mer, ceci ne permettait pas de contraindre correctement les modèles proposés. Par exemple, basé uniquement sur la distribution des séismes, Tsai (1986) a suggéré la présence d'un point triple au sud de Taiwan (Tsai, 1986). Néanmoins, si l'on reporte les épicentres des séismes sur la nouvelle carte bathymétrique (voir Fig. 4 de Hsu et Sibuet, 1995), il semble qu'une des frontières du point triple supposé, liée à une forte densité des séismes à proximité de 22,5°N ; 120°E et orientée NE-SW, serait plutôt liée à la présence d'une faille normale, située dans l'ancien avant-arc lié au bassin de Tainan. De plus, le long de cette frontière, on observe un changement dans les mécanismes au foyer des séismes : extension au sud-ouest et compression au nord-est. L'existence d'un point triple

à l'endroit où Tsai (1986) l'a proposé semble donc peu probable.

A l'aide des données bathymétriques, gravimétriques et magnétiques compilées récemment (Sandwell et Smith, 1994 ; Sandwell et al., 1995 ; Hsu et al., 1995b), nous avons proposé le modèle de collision arc-arc (Hsu et Sibuet, 1995). La surrection de Taiwan serait due à la collision entre l'arc de Luzon et l'ancien arc des Ryukyus, consideré comme une structure fossile au moment de la collision. La différence principale entre le modèle de collision arc-continent et le modèle de collision arc-arc est que l'arc de Luzon entre en collision avec une zone de subduction (arc et bassin arrière-arc) fossile, et non avec une marge continentale passive classique.

La collision entre les deux arcs aurait probablement débuté dans la partie sud de l'arc des Ryukyus actuel (à proximité de 123,5°E), l'arc de Luzon ayant joué le rôle de poinçon le long de la direction de convergence entre les plaques PH et EU (Hsu et al., 1995b). Ensuite, l'île de Taiwan se serait initialement formée par compression du bassin arrière-arc situé de part et d'autre de la faille de Lishan, au Miocène supérieur-Pliocène (Lee, 1994). Le mélange de Lichi aurait été mis en place le long de la Vallée Longitudinale plus récemment, il y a 3-4 Ma (Barrier et Müller, 1984). Notons qu'il n'y a plus d'activité volcanique au sud de l'arc des Ryukyus depuis le Miocène supérieur (Kizaki, 1986) et que l'arc lié au bassin de Tainan est recouvert par des sédiments épais. Il est donc probable que la subduction, du sud de Taiwan au sud de l'ancien arc des Ryukyus, ait cessé avant que la collision arc-arc ne commence. La marge active serait donc devenue passive avant le début de la collision arc-arc.

3.1. Cinématique

La plupart des auteurs suggèrent l'existence d'une proto-mer de Chine du Sud au début du Tertiaire (Holloway, 1982 ; Rangin, 1989 ; Lee et Lawer, 1992 ; Teng, 1992) située entre la marge nord de la Mer de Chine du Sud (qui comprenait, à cette époque, le banc de Reed, le banc de Macclesfield et une partie du bloc Palawan) et la marge sud de la Mer de Chine du Sud (Bornéo et Sud Palawan). Ce proto-océan était en cours de disparition avec le fonctionnement d'une zone de subduction, soit à vergence nord située au sud de la proto-mer de Chine du Sud (Williams et al., 1988), soit à vergence sud située au nord de la proto-mer de Chine du Sud (e.g. Teng, 1992). Selon cette dernière hypothèse, une zone de subduction continue (la zone de subduction des Ryukyus) fonctionnait au Crétacé supérieur-Tertiaire inférieur et s'étendait de l'Indochine au sud du Japon.

L'anomalie magnétique 11 (32 Ma) est l'anomalie la plus ancienne repérée en mer de Chine du Sud (Briais et al., 1989). La proto-mer de Chine du Sud se serait donc fermée au Tertiaire inférieur, avant que le rifting de la marge nord de la Mer de Chine du Sud, qui se situerait entre la marge actuelle et les bancs de Reed et Macclesfield et la partie nord du bloc Palawan, ne se développe. Entre 20 Ma et 13 Ma, une zone de subduction à vergence nord fonctionnait au sud de la Mer de Chine du Sud (**Fig. 25a**, 20 Ma). Au nord de la Mer des Philippines, la zone de subduction des Ryukyus pouvait s'étendre vers l'ouest jusqu'au sud-ouest de la position actuelle de Taiwan. Ces deux zones de subduction étaient connectées par une faille transformante sénestre qui matérialisait la limite entre les plaques PH et de la Mer de Chine du Sud (**Figs. 23 et 25**). Dans ce contexte, les bassins du plateau continental chinois (Rivière des Perles, Tainan, Taihsi, Pengchiahsu et Taiwan) peuvent être considérés comme des bassins arrière-arcs dont le rifting se serait terminé au Tertiaire inférieur.

Entre 20 et 13 Ma (**Fig. 25b**), une nouvelle migration de la zone de subduction des Ryukyus et un changement de la frontière entre la plaque PH et la plaque de la Mer de Chine du Sud marquent un réarrangement complet de la cinématique de cette région. La zone de subduction située au sud de la Mer de Chine du Sud se serait arrêtée de fonctionner au nord de Palawan mais s'étendrait plus au nord-est à cette époque. La fosse de Manille apparaîtrait et l'arc de Luzon commencerait à se former à partir de cette époque. Selon cette hypothèse, une portion de la plaque PH serait incorporée à la Mer de Chine du Sud. Cette portion de plaque séparée de la plaque PH pourrait correspondre à une croûte océanique "piégée" entre l'île de Taiwan et l'île de Luzon (Sarewitz et Karig, 1986). L'ouverture de la Mer de Chine du Sud était terminée à ~16 Ma (Briais et al., 1989).

Vers 8 Ma (**Fig. 25c**), la grande faille transformante sénestre serait pratiquement résorbée. L'arc de Luzon entrerait en collision avec la zone de subduction des Ryukyus en arrière de laquelle se développe le bassin arrière-arc d'Okinawa depuis 12 Ma (Sibuet et al., 1987 ; 1995) ou Eocène/Miocène (Hsu et Sibuet, 1995).

Vers 3 Ma (**Fig. 25d**), la collision de l'arc de Luzon avec la portion de la zone de subduction fossile des Ryukyus est largement réalisée.

Actuellement (**Fig. 25e**), la surrection de Taiwan est rapide. La partie nord de Taiwan s'éloigne de l'influence de la collision de l'arc de Luzon, tandis que la partie sud de Taiwan la subit fortement.

Dans le schéma cinématique proposé, la zone de subduction des Ryukyus s'étendait de l'Indochine au Japon au Crétacé terminal/Tertiaire inférieur, puis jusqu'à 13 Ma du sud-ouest de Taiwan au Japon, puis de l'est de Taiwan au Japon, depuis 13 Ma
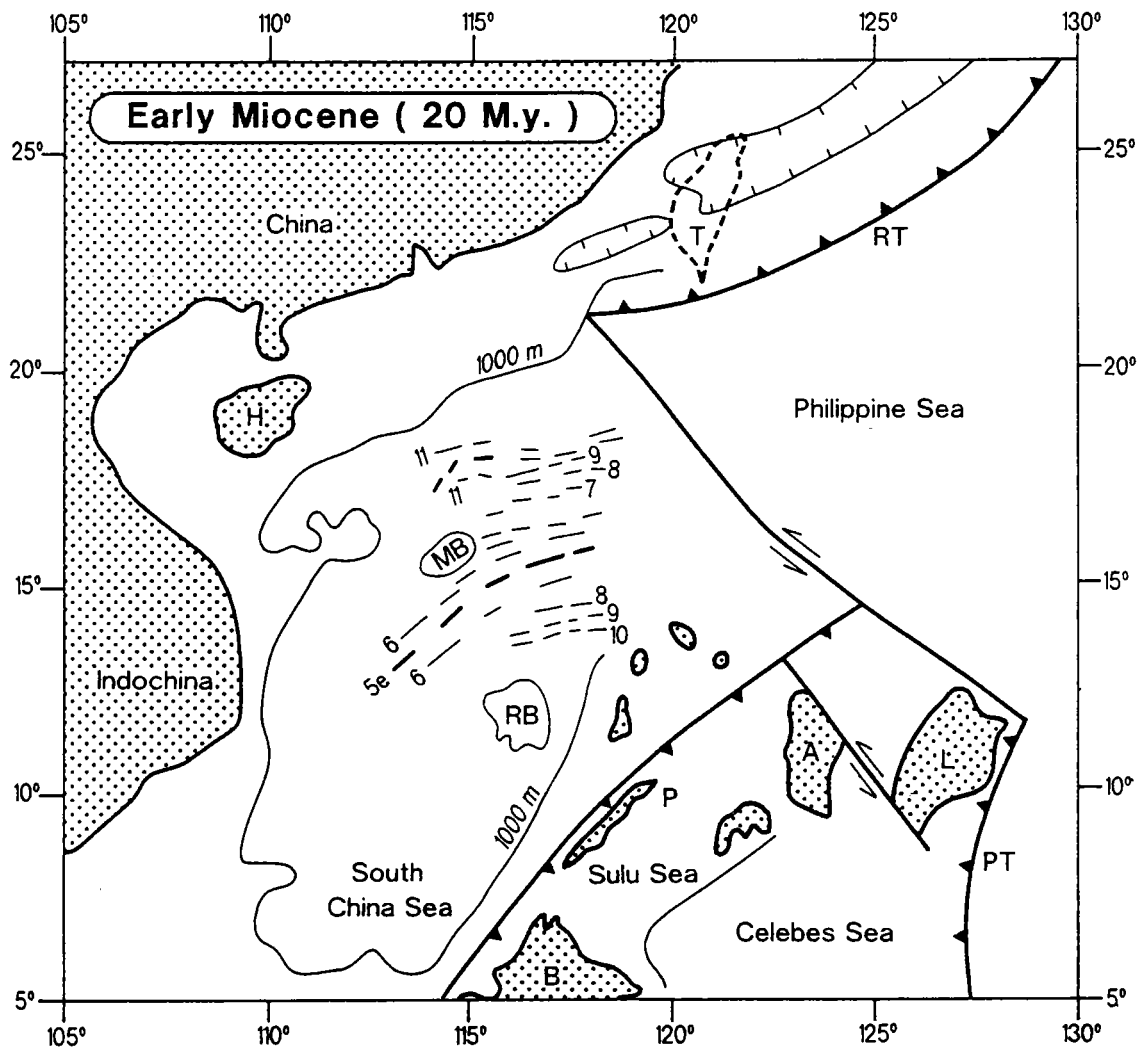
Fig. 25a : Reconstruction du sud-ouest de l'Asie, il y a 20 Ma Voir signification des symboles dans la légende de la Fig. 25e.
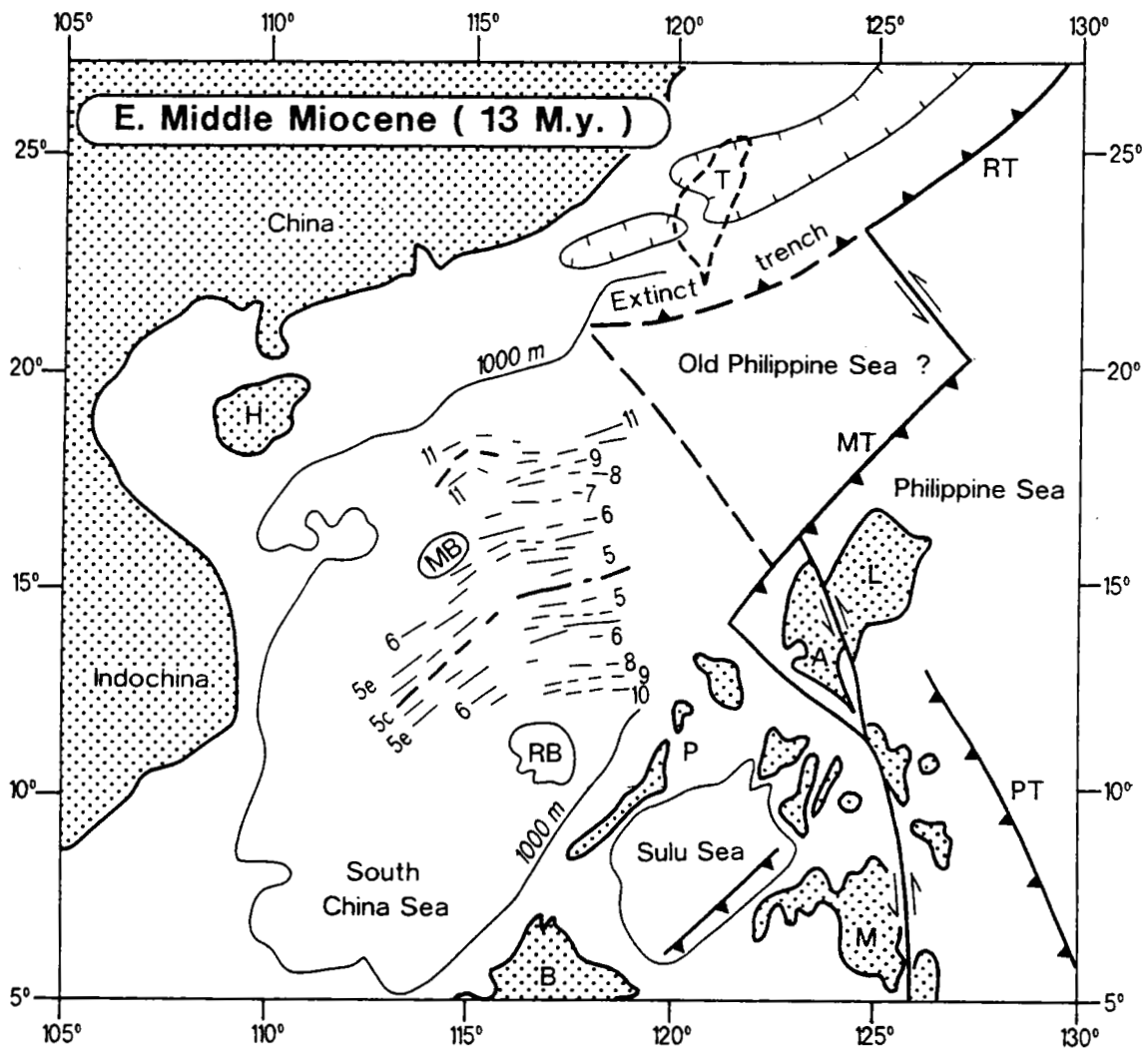
Fig. 25b : Reconstruction du sud-ouest de l'Asie, il y a 13 Ma Voir signification des symboles dans la légende de la Fig. 25e.
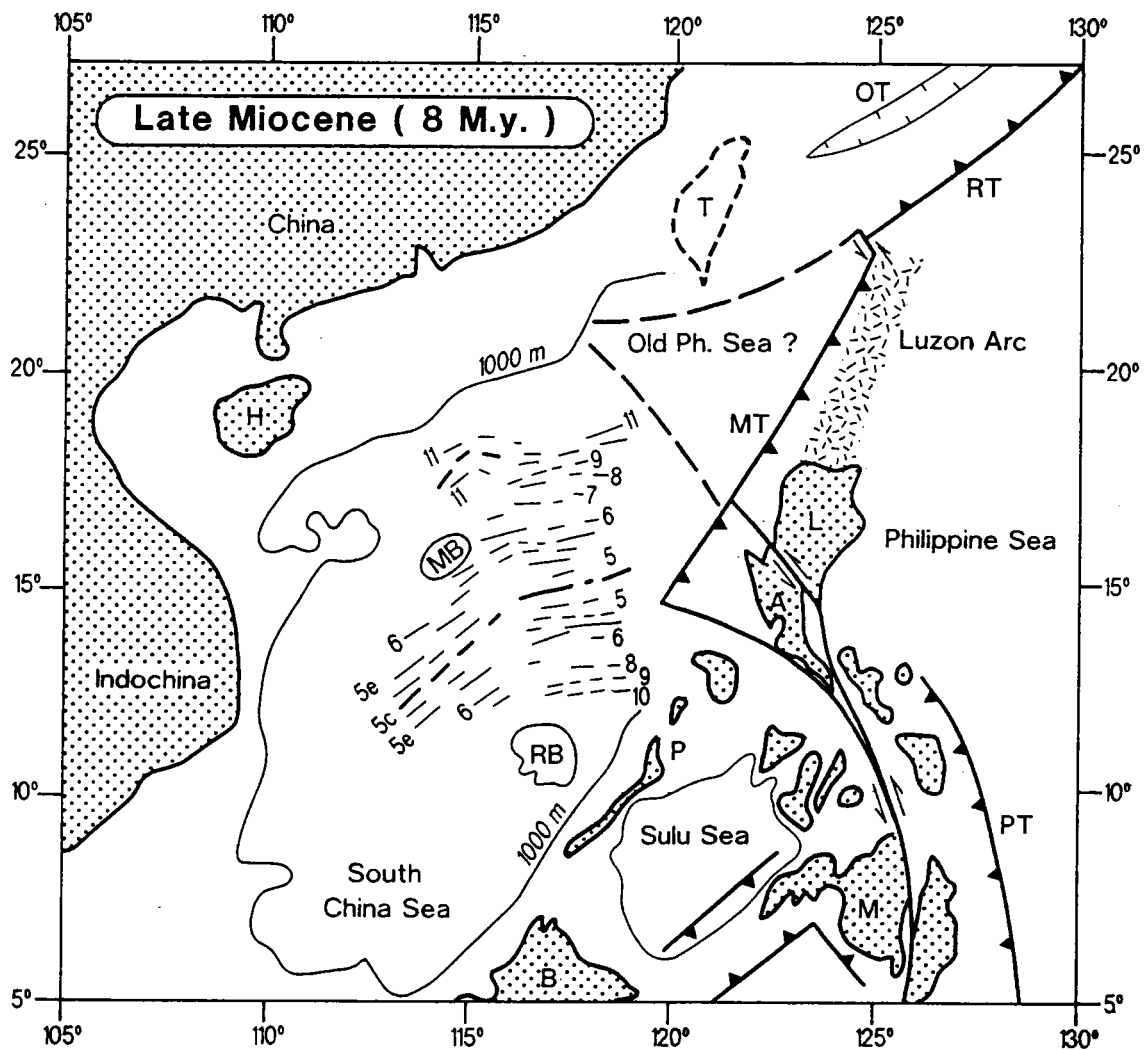
Fig. 25c : Reconstruction du sud-ouest de l'Asie, il y a 8 Ma Voir signification des symboles dans la légende de la Fig. 25e.
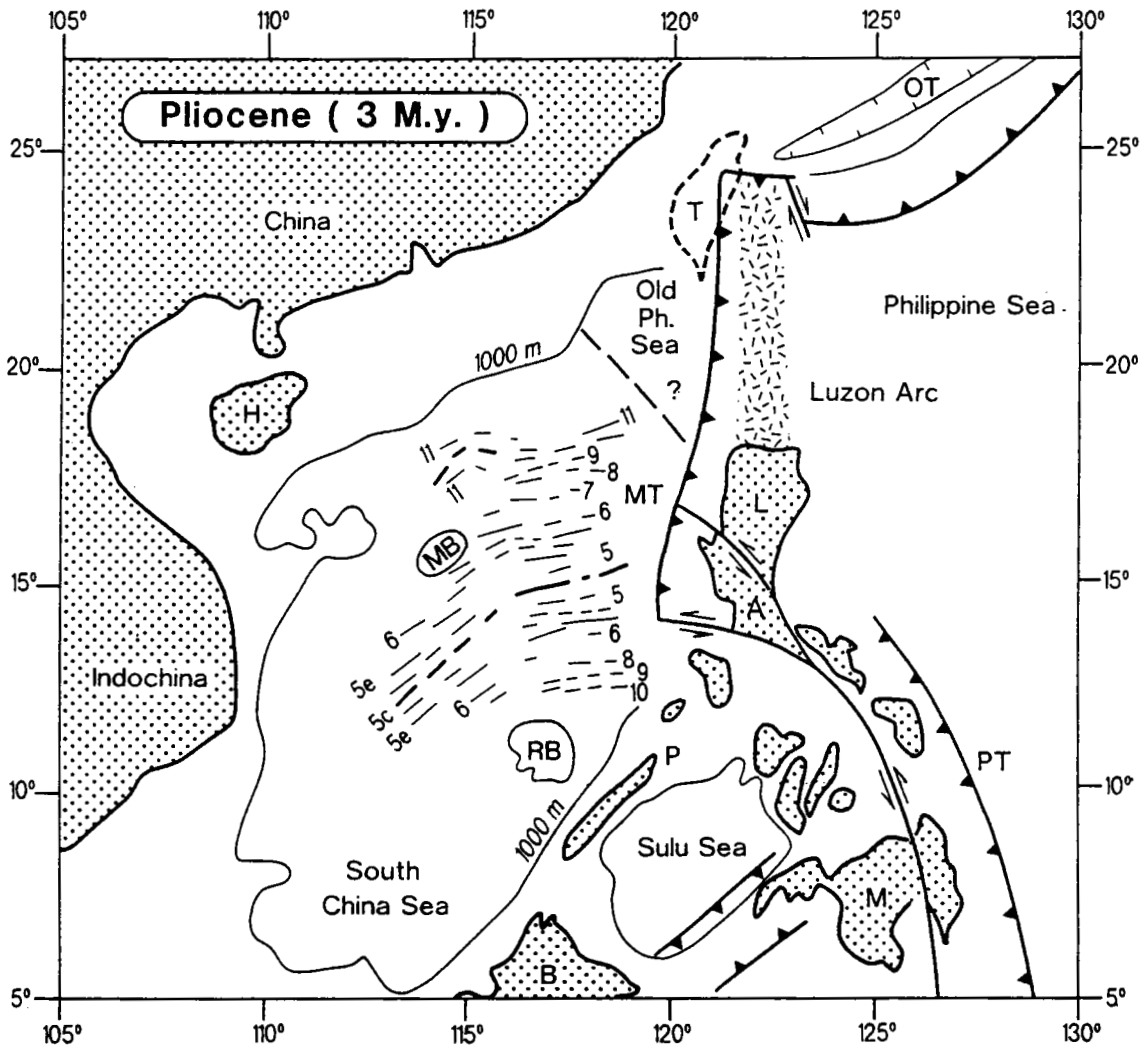
208

Fig. 25d : Reconstruction du sud-ouest de l'Asie, il y a 3 Ma Voir signification des symboles dans la légende de la Fig. 25e.
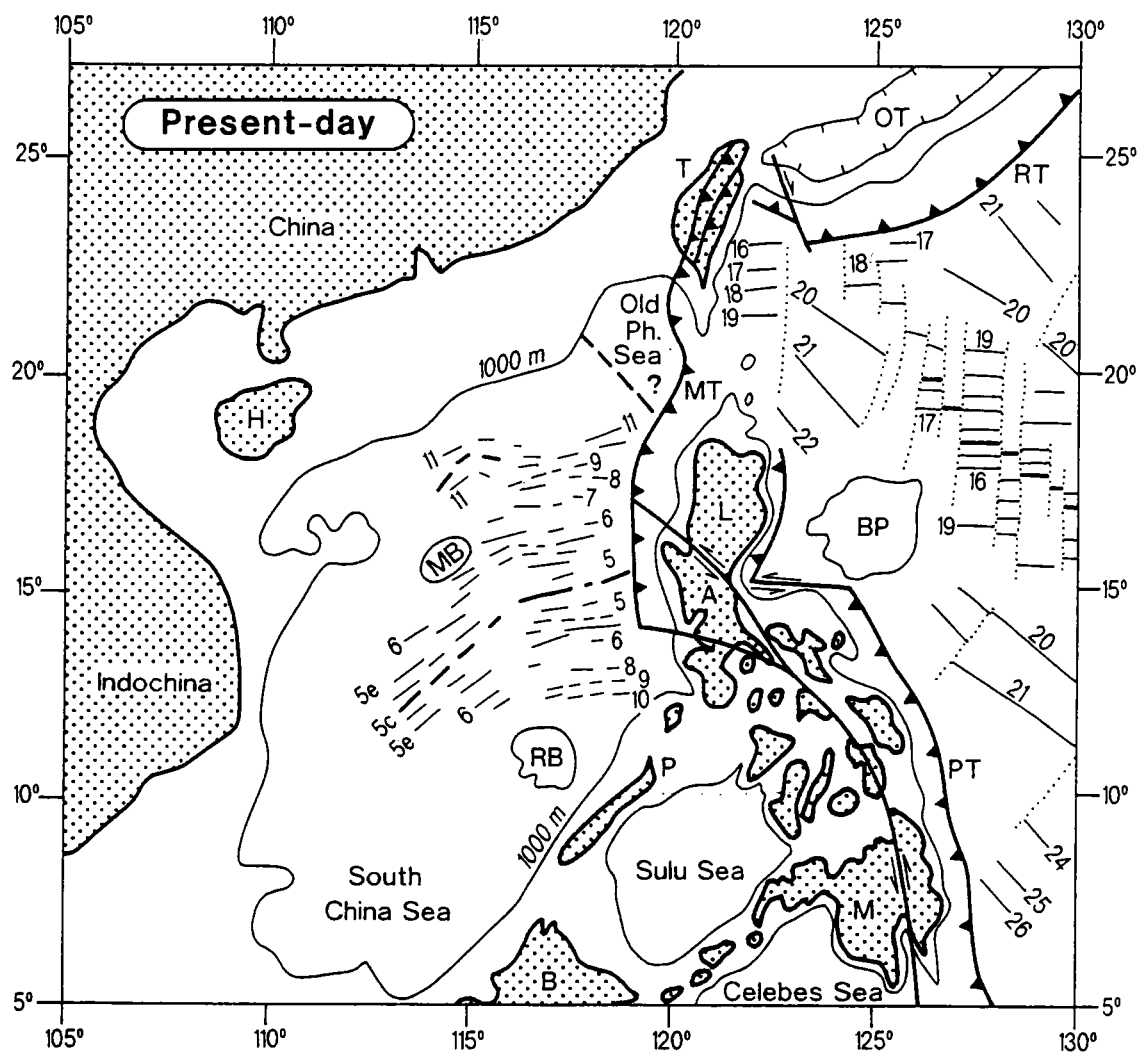
209

Fig. 25e : Contexte géodynamique actuel du sud-ouest de l'Asie. Isochrones magnétiques d'après Briais et al. (1989) pour la Mer de Chine du Sud et Hilde et Lee (1984) pour la Mer des Philippines. Signification des symboles : A : Bloc de Luzon central ; B : Bornéo ; BP : plateau de Benham ; H : Hainan ; L : Luzon ; M : Mindanao ; MB : banc de Macclesfield ; MT : fosse de Manille ; OT : bassin d'Okinawa ; P : Palawan ; PT : fosse des Philippines ; RB ; banc de Reed ; RT : fosse des Ryukyus ; T : Taiwan

210

En revanche, pour Angelier (1990), par exemple, la zone de subduction des Ryukyus est active de l'est de Taiwan au Japon, depuis une vingtaine de million d'années. Selon cette hypothèse, il n'est pas exclu que la zone des Ryukyus fonctionnait de l'Indochine au Japon au Crétacé terminal/Tertiaire inférieur. En d'autres termes, la portion de marge située entre le sud-est de Taiwan et l'est de Taiwan aurait été active jusqu'au Tertiaire inférieur.

Quelle que soit l'hypothèse retenue, l'arc de Luzon entrerait en collision avec une ancienne zone de subduction plus ou moins âgée comprenant un système arc-bassin arrière-arc, et non pas avec une marge passive typique (où le plateau continental ne présente pas, en règle générale, de bassins sédimentaires parallèles à la direction de la marge).

3.2. Configuration de l'ancien arc des Ryukyus

Dans cette section, nous mettons en évidence la position possible de l'ancien arc des Ryukyus, qui serait composé de la partie actuelle de l'arc des Ryukyus, d'une partie de Taiwan correspondant à la Chaîne Centrale Est (le complexe de Tananao) et de l'ancien arc situé juste au sud du bassin de Tainan. De même, les bassins arrière-arcs correspondraient au bassin d'Okinawa, au bassin situé sous la Chaîne Centrale Ouest et au bassin de Tainan.

Sur la **Fig. 23**, nous constatons que l'arc des Ryukyus peut être identifié par sa signature gravimétrique. De même, les caractéristiques gravimétriques de l'ancien arc et de l'avant-arc liés au bassin de Tainan sont similiares à celles de l'arc des Ryukyus. D'un point de vue gravimétrique, il est donc possible que le bassin de Tainan ait la même origine que le bassin d'Okinawa.

A partir de la carte des données gravimétriques de Taiwan, une densité moyenne de 2,57 g/cm^3 a été rétirée pour obtenir la carte des anomalies de Bouguer (**Fig. 14**) (Yeh et Yen, 1991). Sur cette carte, un maximum local situé près de 23,3°N ; 120,5°E suggère l'existence d'une structure de forte densité à l'aplomb de cette anomalie. Son orientation NE-SW permet de supposer que l'ancien arc situé au sud du bassin de Tainan pourrait se prolonger au sud-ouest de Taiwan. Afin de déterminer avec précision les limites de cette structure, nous avons appliqué la méthode du signal analytique haute-résolution (Hsu et al., 1995a). A l'aide des frontières identifiées au préalable (failles ou contrastes), nous avons essayé de localiser la position possible de l'ancien arc sous l'île de Taiwan (**Fig. 26**). La limite des structures identifiées par cette méthode permet de cartographier
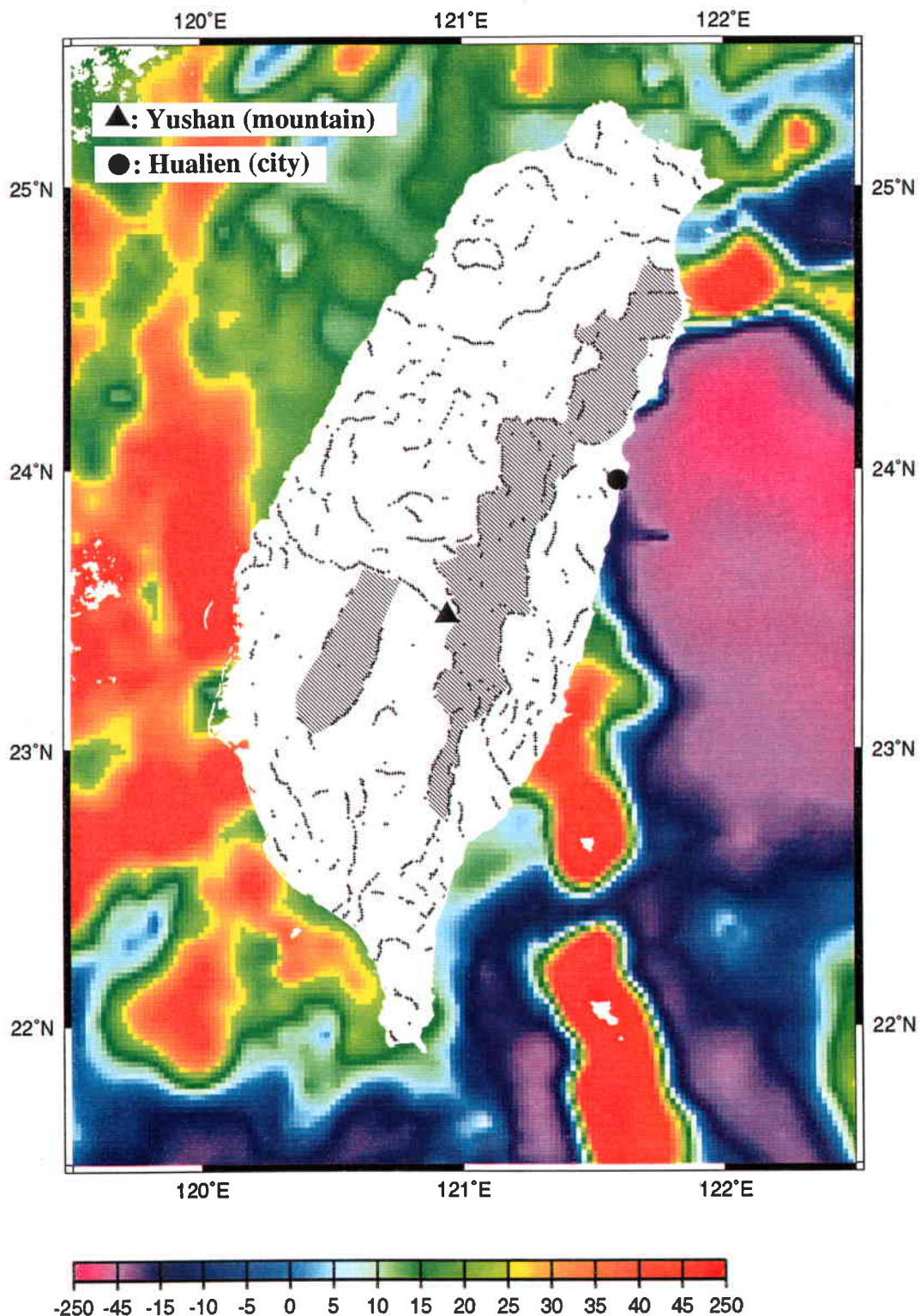
Fig. 26 : Frontières géologiques automatiquement identifiées par la méthode du signal analytique de haute-résolution (Hsu et al., 1995a) à l'intérieur de Taiwan. Croix : position des frontières identifiées par l'anomalie de Bouguer (Fig. 14). Les régions hachurées pourraient correspondre à l'arc fossile des Ryukyus. Celle située à l'est correspond au Complexe de Tananao qui rejoint, au nord, l'arc des Ryukyus. Celle située à l'ouest correspond à la prolongation nord-est de l'arc lié au bassin de Tainan. Noter la discontinuité orientée N295°, près de Yushan. L'anomalie gravimétrique dérivée de l'altimétrie satellitaire (Sandwell et al., 1995) est cartographiée à l'extérieur de Taiwan.

clairement l'extension du Complexe de Tananao à partir des données gravimétriques. Au nord, à proximité de 24,5°N ; 121,8°E, se situe la connexion entre le complexe de Tananao et la partie sud-ouest de l'arc des Ryukyus. Au sud-ouest de Taiwan, une partie de l'ancien arc (région hachurée à l'ouest sur la Fig. 26) se trouverait au voisinage de 23,3°N ; 120,5°E. Cependant, les données géologiques ne permettent pas d'identifier cette structure comme étant clairement une portion d'arc. La position possible de l'ancien arc des Ryukyus (du sud-ouest de Taiwan au sud du Japon) n'est donc que suggérée par les données gravimétriques. De plus, il faut remarquer que la connexion entre les deux structures hachurées de la Fig. 26, interprétées comme les reliques de l'ancien arc des Ryukyus, n'est pas évidente. Il faut noter également la présence d'une discontinuité orientée N295° située à l'ouest de Yushan **(Fig. 26)**. Le modèle numérique de terrain (M.N.T.) de Taiwan ainsi que les cartes morphologiques filtrées à grandes longueurs d'onde (Lee, 1994 ; Deffontaines et al., 1994) révèlent, également, la présence de cette discontinuité. De plus, cette discontinuité est confirmée par les observations géodésiques **(Fig. 15)** (Yu et al., 1995). L'origine de cette importante discontinuité située près de 23,5°N et la séparation de l'ancien arc au sud de Yushan restent cependant toujours des énigmes.

D'un point de vue pétrologique, le complexe de Tananao peut être considéré comme un arc fossile (Biq, 1981 ; Ho, 1988 ; Chen, 1991). En revanche, il n'y a pas de manifestation volcanique au niveau de l'ancien arc lié au bassin de Tainan. Le bassin de Tainan est recouvert par des sédiments depuis le Miocène moyen **(Fig. 27)** (Sun et Hsu, 1991 ; Lee et al., 1993a), ce qui suggère que la partie sud-ouest de l'ancienne zone de subduction des Ryukyus aurait été abandonnée depuis le Miocène moyen. Pour le moment, la seule donnée géologique, qui permet de lier les parties de l'ancien arc séparées par la discontinuité à 23,5°N, est la présence d'une épaisse couche de calcaire métamorphique forée à 4512 mètres de profondeur dans la Plaine Côtière (CLI-1 dans **Fig. 5**). Cette unité ne contient pas de fossiles mais les données de géochimie montrent qu'elle pourrait être de même nature que les calcaires de la Chaîne Centrale Est (Jahn et al., 1981 ; Ho, 1982). En tout cas, la connexion géologique entre le complexe de Tananao et l'ancien arc situé au sud du bassin de Tainan reste à établir.

3.3. Relation avec le champ de vitesse géodésique à Taiwan

Une carte du champ de vitesse horizontale géodésique a été établie par rapport à la station de Paisha (S01R), à partir des mesures géodésiques du GPS (*Global Positioning*

System) réalisées sur l'île de Taiwan par Yu et al. (1995) **(Fig. 15)**. Au nord de la discontinuté située au niveau du 23,5°N, la croûte est relativement stable alors qu'au sud de cette discontinuité, les vecteurs augmentent en amplitude de l'ouest vers l'est et du nord vers le sud. Ce phénomène permet d'expliquer les raccourcissements et les soulèvements en termes de décrochements dextres et de chevauchements dans le sud de Taiwan **(Fig. 5)**. Au sud de cette discontinuité, ce phénomène est notamment accompagné par un groupe de séismes dont les mécanismes sont généralement de type compressif. La croûte se déplace vers l'ouest et sa surrection pourrait aussi expliquer la migration (~20 km/Ma) des canyons situés au large du sud-ouest de Taiwan **(Figs. 28a et 28b)** (Lee et al., 1995a).

Pour comprendre la distribution du champ de vitesse à Taiwan, en particulier au sud, une modélisation numérique a été réalisée par Hu et al. (1995b). En supposant que le *Peikang High* est une région stable et résistante, et que le déplacement de la plaque PH est le moteur de la convergence **(Fig. 29)**, alors on peut constater que la région intermédiaire, moins rigide, se déforme de façon divergente et que la vitesse de déplacement diminue au voisinage de *Peikang High* (Hu et al., 1995b). Cette modélisation permettrait d'expliquer la déformation au sud de 23,5°N. En revanche, au nord de 23,5°N, la déformation observée est relativement faible, ce qui est en contradiction avec les résultats de cette modélisation simple.

Puisque le champ de vitesse est stable au nord de 23,5°N, une interprétation possible serait que la portion de l'arc de Luzon située au nord de 23,5°N commencerait à subducter sous l'arc des Ryukyus. Ceci est d'ailleurs suggéré par la carte bathymétrique et les données gravimétriques qui montrent la terminaison en pointe de l'arc de Luzon vers le nord. L'autre interprétation possible serait qu'au nord de 23,5°N, l'ancien bassin arrière-arc situé à l'ouest du complexe de Tananao était déjà fermé au voisinage de Yushan. Le témoignage de cette fermeture serait le rétrécissement morphologique de la vallée le long de la faille de Lishan. Ainsi, au nord de la discontinuité, l'ancien bassin arrière-arc situé sous la Chaîne Centrale Ouest pourrait être une région assez rigide par rapport à la région située au sud de cette discontinuité. Cette interprétation est corroborée par l'existence de fortes vitesses des ondes P sous la Chaîne Centrale (Wu et al., 1995) ainsi que par une séismicité faible, à l'exception d'une séismicité plus importante le long de la faille de Lishan.

De plus, à partir des images satellitaires, l'existence de failles décrochantes dextres et de failles inverses a été montrée au nord de 23,5°N **(Fig. 30)** (MRSO, 1982). Cela suggère que la partie nord de Taiwan aurait déjà subi la contrainte principale due à la collision de l'arc de Luzon, sachant que la convergence est actuellement concentrée au
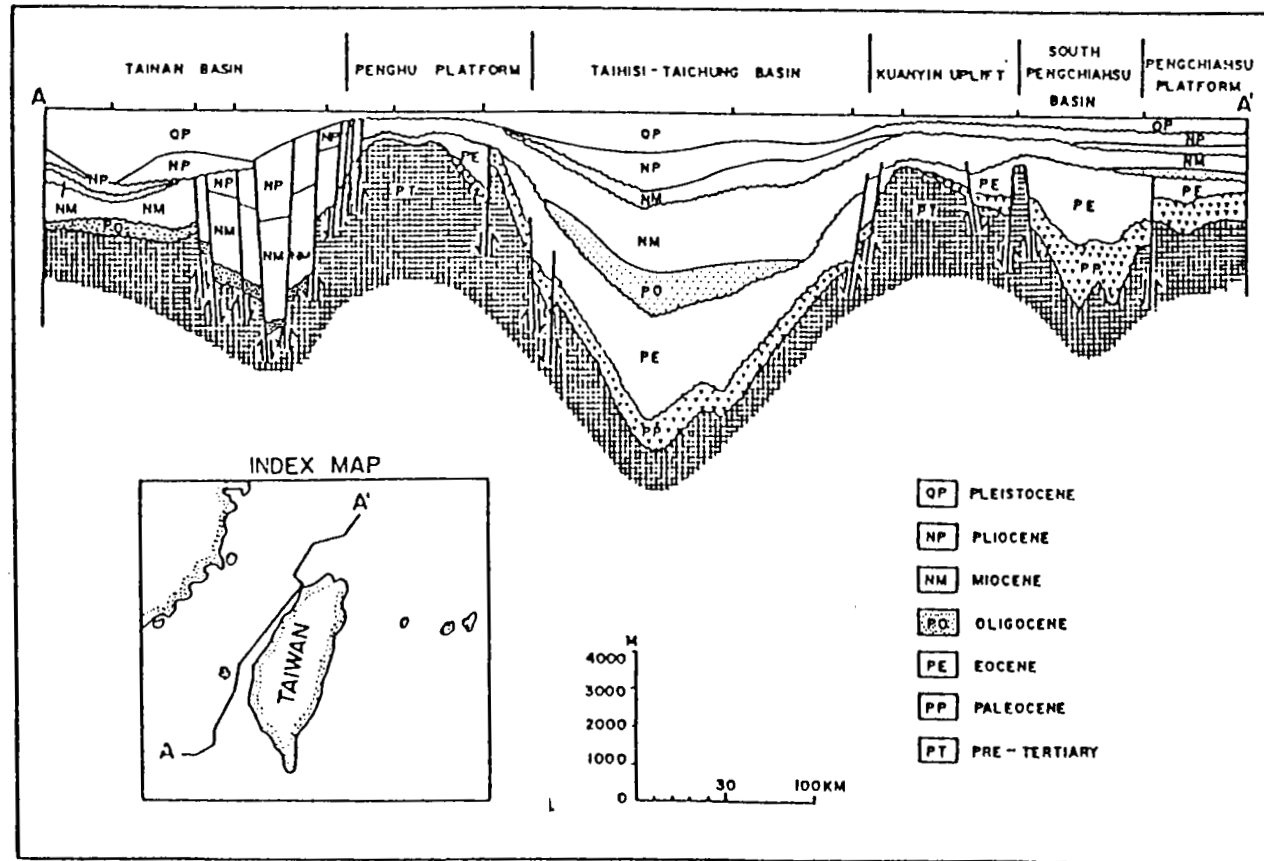
Fig. 27 : Coupe sismique à l'ouest de Taiwan. Notons qu'à partir du Miocène l'épaisseur des sédiments dans le bassin de Tainan est devenue importante.
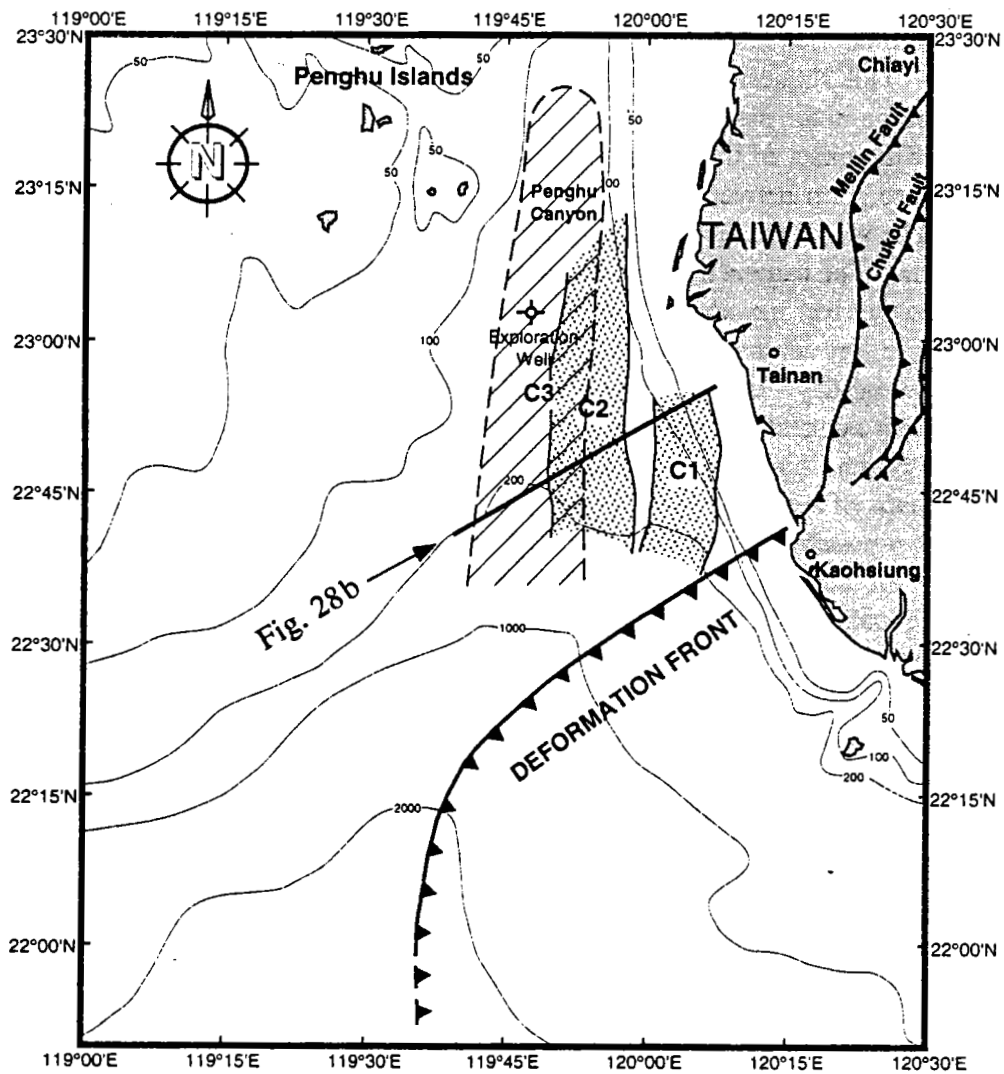
Fig. 28a : Localisation des trois systèmes de canyons dans les sédiments Plio-Pléistocènes. Contours bathymétriques en mètres (Lee et al., 1995a).
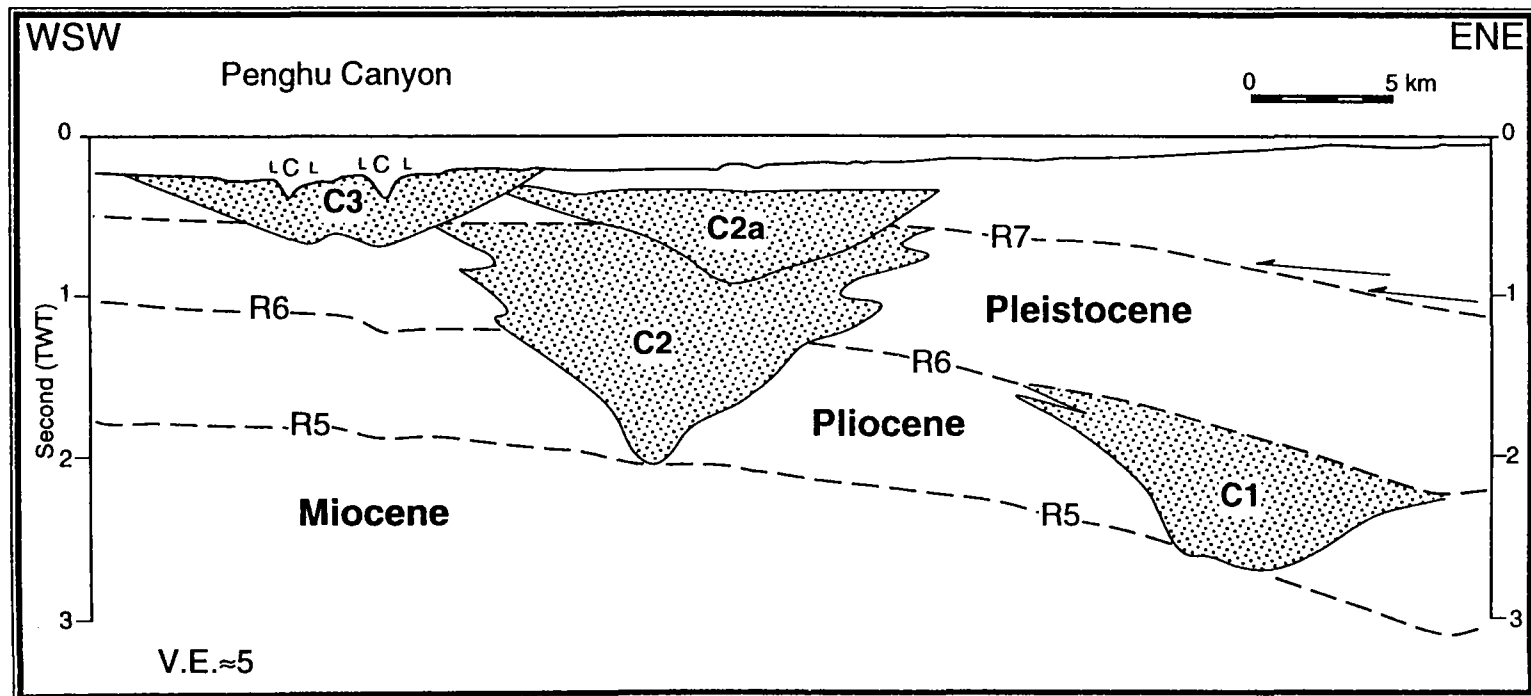
216

Fig. 28b : Interprétation du profil localisé sur la Fig. 28a. C = chenal et L = levée (Lee et al., 1995a).
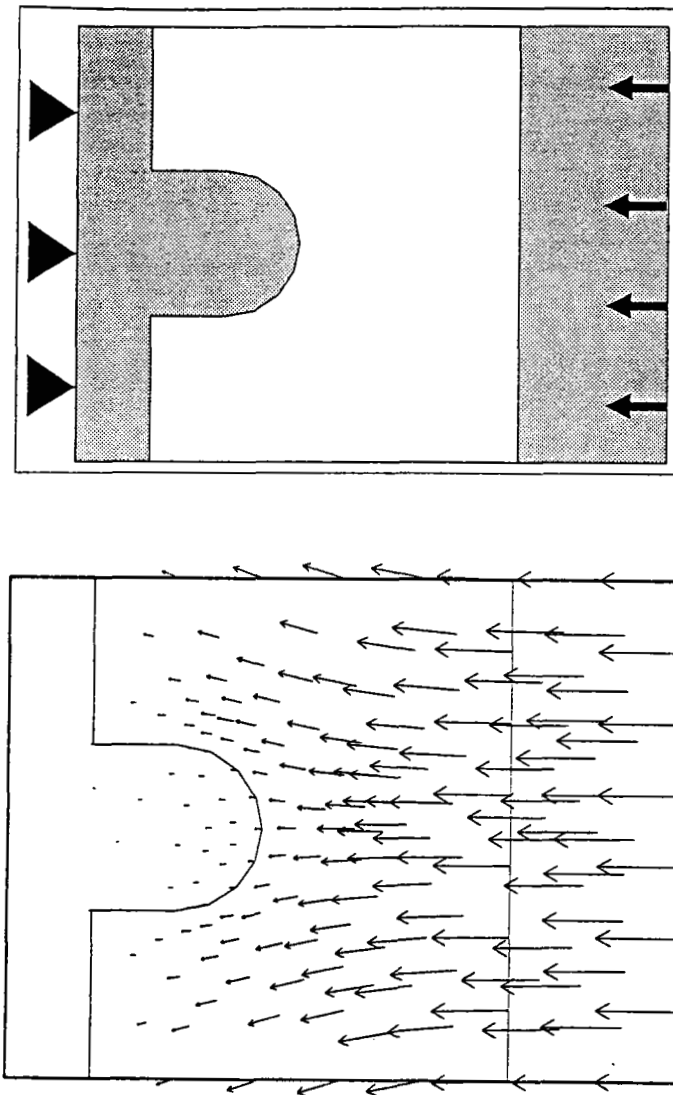
Fig. 29a : Modèle en éléments finis et champ de vitesse. On peut noter la divergence du champ et la diminution de la quantité de déplacement près du môle. Le module de Young est de 60 MPa pour le sous-domaine rigide (en gris) et de 5 MPa pour la zone fragile (en blanc). Le coefficient de Poisson pour les deux sous-domaines est de 0,25 (Hu et al., 1995b).

Peikang High

Philippine Sea plate

0 ___ 50 mm/yr   0 _____ 50 km

VELOCITY   MAP SCALE

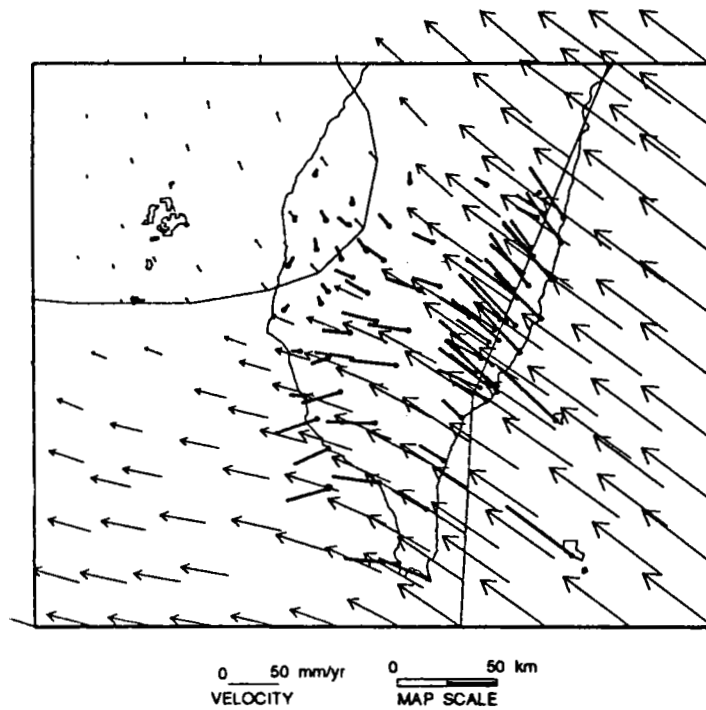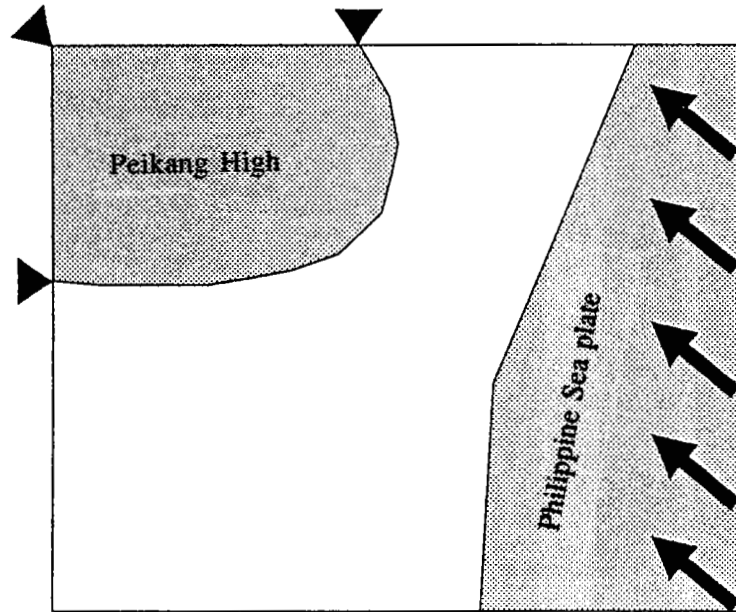**Fig. 29b :** Modélisation du champ de vitesse géodésique au sud de Taiwan (Hu et al., 1995b). Notons qu'au nord les vitesses géodésiques provenant du modèle ne correspondent pas à celles observées. Les flèches représentent les valeurs de la modélisation. Les traits avec un point à l'origine matérialisent les données observées.
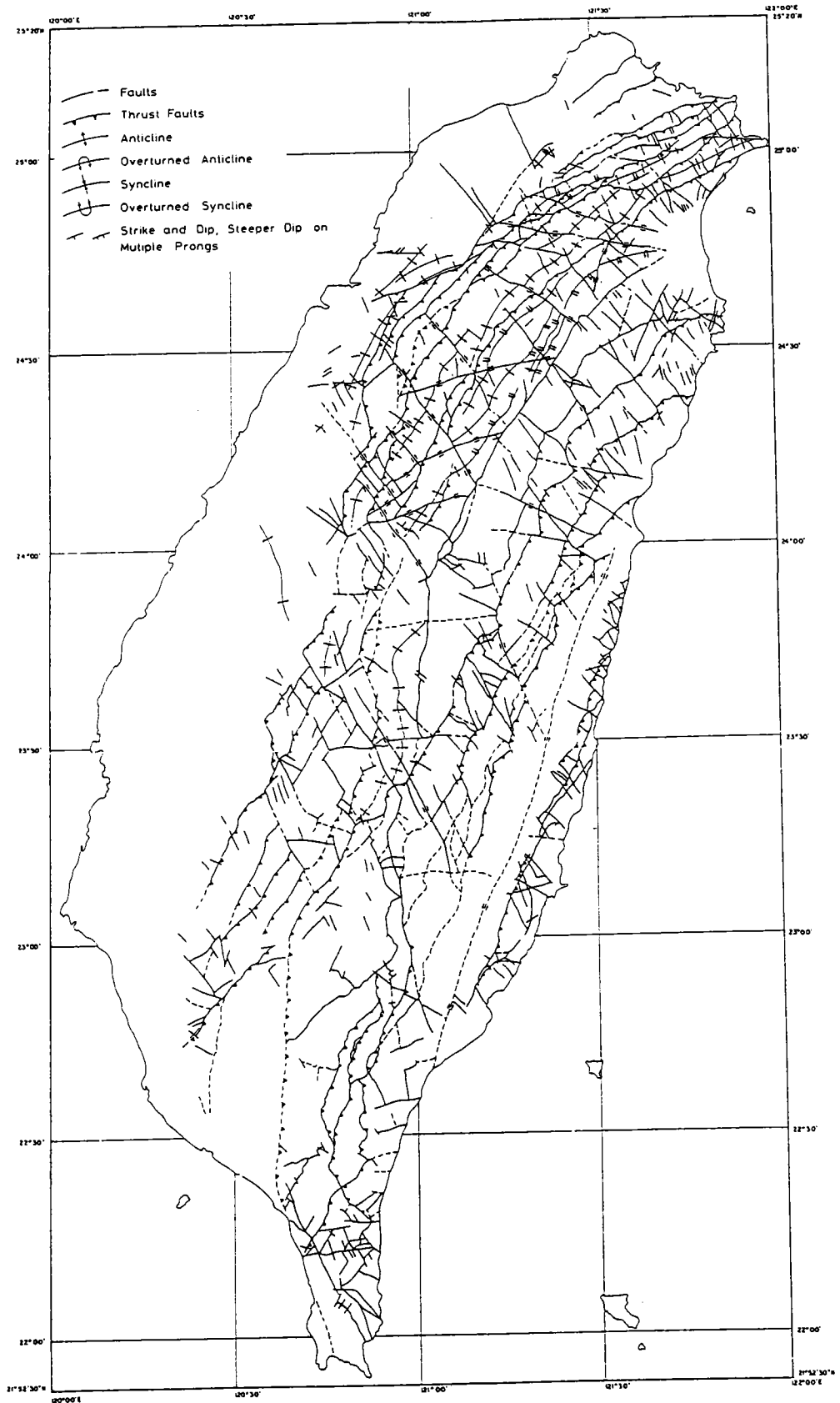
219

Fig. 30 : Interprétation structurale des images radar de Taiwan (MRSO, 1982).

220

niveau de 23°N ; 121,2°E (**Fig. 15**). L'extension dans la plaine de Ilan et dans la partie sud-ouest du bassin d'Okinawa aurait probablement repris après la collision due au balayage de l'arc de Luzon.

3.4. Relation avec la distribution des grands séismes

La relation entre le modèle que nous proposons et la distribution des séismes est décrite dans l'article de Hsu et Sibuet (1995). En résumé, sous l'influence de la collision de l'arc de Luzon, au milieu de l'île de Taiwan apparaît plus particulièrement des mécanismes en compression, et en extension en dehors de cette zone (**Fig. 31**). Dans cette section, nous comparons le modèle avec la distribution de grands séismes dans la région de Taiwan. Sur la **Fig. 32a**, les accélérations terrestres sont estimées par les grands séismes de magnitude (M) supérieure à 6, enregistrés entre 1898 et 1988 dans la région de Taiwan (Table 1) (Cheng et Yeh, 1989). Les intensités de séisme (ou accélérations ressenties en surface) dues aux grands séismes dans la région de Taiwan sont réparties en cinq régions principales (**Fig. 32a**). Ces régions pourraient être essentiellement considérées comme des zones de faiblesse, c'est à dire là où les contraintes maximales accumulées dans ces régions sont le plus facilement libérées.

- La région I, correspondant au prolongement à terre du bassin de Tainan, est actuellement soumise à la compression de l'arc de Luzon (**Figs. 15 et 32a**). Ce bassin arrière-arc préexistant n'est pas encore complètement fermé et est recouvert par d'épais sédiments quaternaires.

- La région II, correspondant à la plaine d'Ilan, représente, en revanche, une région qui aurait déjà subi la collision de l'arc de Luzon. Le régime extensif, témoigné par la nature des mécanismes au foyer des séismes, est probablement lié à une reprise de l'ouverture du bassin d'Okinawa (Hsu et al., 1995b). Dans le sud de cette region, les séismes le long de la faille de Lishan montrent, au contraire, un régime compressif. Des décrochements pourraient accommoder le changement de type de mécanismes. Notons que la collision arc-arc s'est propagée du nord verd le sud.

- La région III est localisée au nord-ouest de la Chaîne Centrale Ouest et est un bassin sédimentaire, situé entre le *Peikang High* (H1) et le *Kuanyin High* (H2) (**Fig. 32b**). Ainsi, pour comprendre la présence des grands séismes dans cette région, il faut noter que l'ancien bassin arrière-arc, situé au niveau de la Chaîne Centrale Ouest, est bien fermé au voisinage de Yushan. L'emplacement particulier de la région III permet de suggérer que la contrainte due à la collision de l'arc de

221
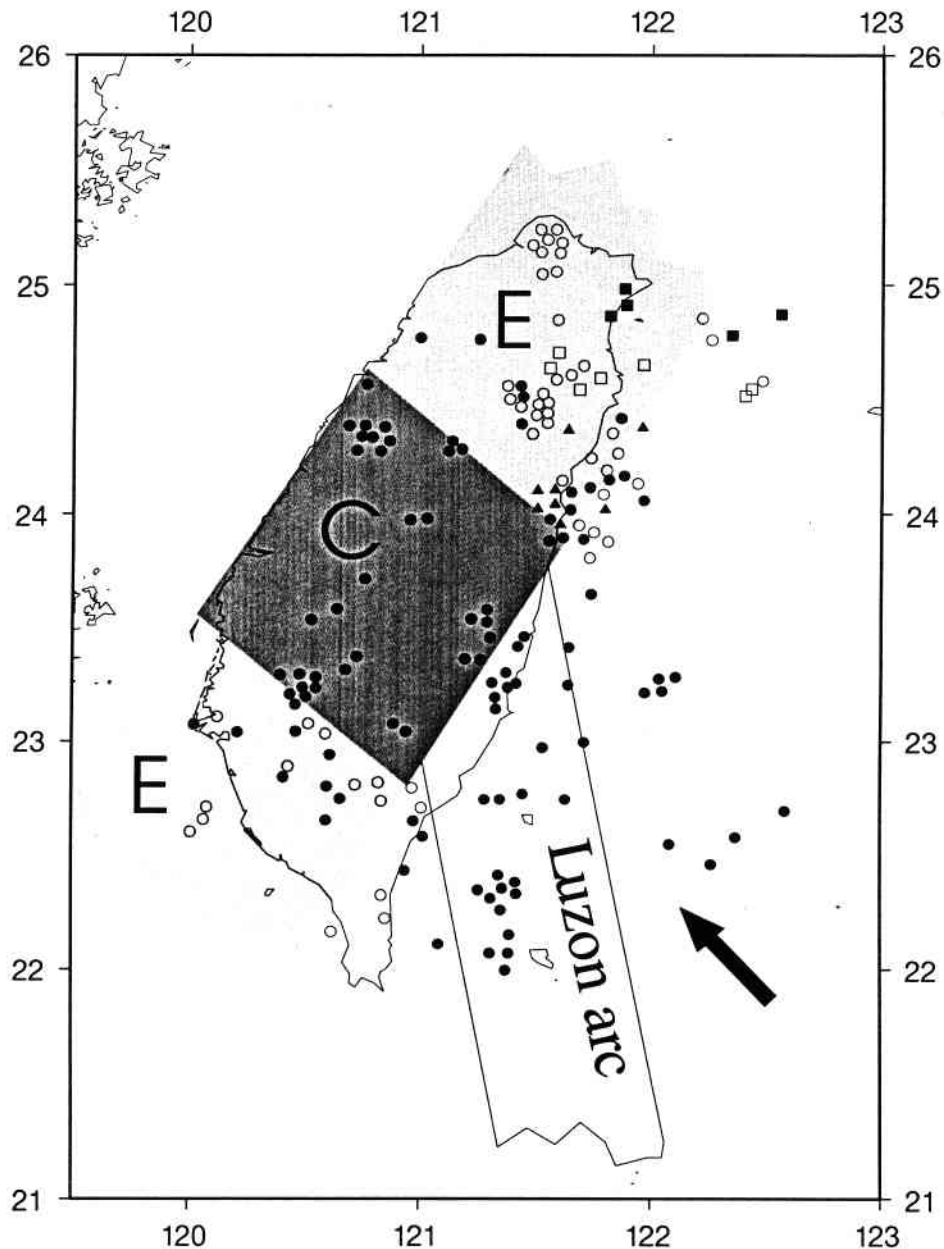
Fig. 31 : Schéma expliquant la distribution des régimes des mécanismes au foyer dans la région de Taiwan dus à la collision de l'arc de Luzon. Les triangles et les ronds noirs représentent les mécanismes en chevauchement et en décrochement. Les ronds blancs représentent les mécanismes en faille normale. Les carrés représentent les séismes associés à la plaque plongeante de la Mer des Philippines. C : région avec mécanismes de type compressif. E : région avec mécanismes de type extensif.

Earthquake Intensity:

80 - 250 gal   > 250 gal
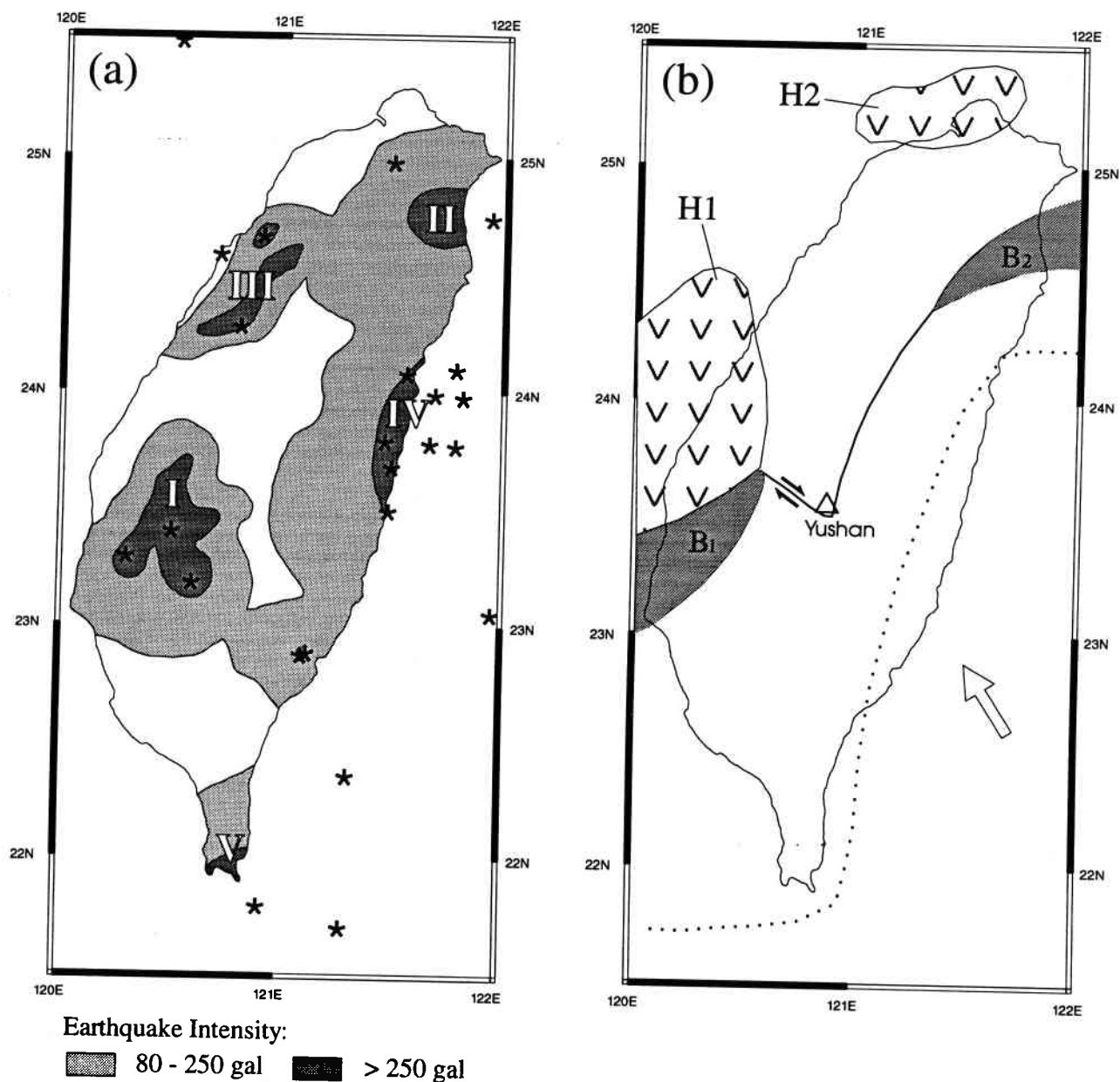
Fig. 32 : (à gauche) Contour des intensités des 23 premiers séismes de la Table 1 dont la magnitude est supérieure à 6 (Cheng et Yeh, 1989). (à droite) Configuration simplifiée de l'ancienne zone de subduction des Ryukyus au niveau de Taiwan. B1 et B2 représentent deux bassins arrière-arcs non totalement fermés par la collision de l'arc de Luzon. Entre *Peikang High* (H1) et *Kuanin High* (H2) la lithosphère serait moins rigide que celle où se trouvent H1 et H2. La ligne en pointillée indique la position de l'ancienne fosse.

Luzon (dans la direction NW-SE) pourrait ainsi être transmise et accumulée dans cette zone.

- L'apparition des grands séismes dans les régions IV et V montre que la zone suturée de l'ancienne zone de subduction est une zone de faiblesse (la ligne pointillée sur la **Fig. 32b**).

No.	Year	M	D	H	M	Lat.	Lon.	Depth	M
		Time (U.T.)				**Hypocenter**			
01	1906	3	16	22	42	23.583	120.533	-	7.1
02	1909	4	14	19	54	25.0	121.5	80.0	7.3
03	1927	8	24	18	9	23.3	120.3	-	6.6
04	1935	4	20	22	2	24.3	120.8	5.0	7.1
05	1935	4	20	22	26	24.7	120.9	-	6.2
06	1935	7	16	16	19	24.6	120.7	30.0	6.4
07	1941	12	16	20	19	23.4	120.5	10.0	7.1
08	1943	10	22	16	1	23.8	121.5	5.0	6.4
09	1943	11	23	21	51	24.0	121.7	0.0	6.0
10	1951	10	21	21	34	23.8	121.7	0.0	7.3
11	1951	10	22	3	29	24.1	121.8	20.0	7.1
12	1951	11	26	6	38	22.9	121.1	0.0	6.4
13	1951	11	29	14	25	22.9	121.0	-	6.0
14	1955	4	4	11	12	21.8	120.9	5.0	6.8
15	1957	2	23	20	26	23.8	121.8	30.0	7.3
16	1957	10	19	18	29	23.7	121.5	10.0	6.7
17	1959	8	15	8	57	21.7	121.3	20.0	6.9
18	1964	1	18	14	4	23.2	120.6	20.0	6.5
19	1972	4	24	9	57	23.5	121.5	3.0	6.9
20	1978	7	23	14	42	22.352	121.329	6.1	6.7
21	1986	1	16	13	4	24.763	121.961	10.2	6.5
22	1986	5	20	5	25	24.082	121.592	15.8	6.5
23	1986	11	14	21	20	23.992	121.833	13.9	6.7
24	1989	8	3	11	31	23.078	122.010	5.6	6.4
25	1989	8	21	23	12	23.963	122.437	8.1	6.1
26	1994	2	1	22	44	24.747	122.693	115.6	6.1
27	1994	5	23	15	16	23.863	122.636	5.5	6.0
28	1994	5	24	4	0	23.827	122.603	4.5	6.6
29	1994	6	5	1	9	24.462	121.838	5.3	6.2
30	1995	6	25	6	59	24.588	121.690	44.0	6.5

Table 1 : Les grands séismes enregistrés dans la région de Taiwan depuis 1906. Les 23 premiers séismes sont été pris en compte pour estimer les intensités des séismes à l'intérieur de Taiwan (voir Fig. 32) (d'après Cheng et Yeh, 1989 ; W.-B. Cheng, communication écrite, 1995).

Notons que le taux de convergence le plus important le long de la Vallée Longitudinale (entre les deux plaques) se trouve au voisinage de 121,2°E ; 23°N (**Fig. 15**). Cependant les grands séismes se produisent plutôt dans la région I (i.e. région située dans l'alignement de la zone au taux de convergence le plus important) et non pas au voisinage de la partie de la zone suturée. Ainsi, le bassin arrière-arc se serait fermé, en premier, avant le soulèvement complet de Taiwan. Ce qui confirme, en d'autres termes, que la lithosphère sous le bassin arrière-arc était moins épaisse.

3.5. Processus de la surrection de Taiwan

En tenant compte des interprétations précédentes, la surrection de Taiwan pourrait être décrite en cinq étapes (**Fig. 33**) :

1) Il y a 20 Ma, l'ancienne position de Taiwan était sous l'influence du régime extensif du bassin arrière-arc. La plaque PH subducte sous la plaque EU.

2) Il y a 13 Ma, la subduction de la partie sud-ouest de l'ancienne fosse des Ryukyus aurait cessé et la fosse de Manille aurait migré vers le nord-est, ce qui aurait engendré la formation de l'arc de Luzon.

3) Entre 13 et 8 Ma, le contact entre l'arc de Luzon et l'arc fossile des Ryukyus apparaît à proximité de 123,5°E. A l'ouest de 123,5°E, l'ancien arc des Ryukyus aurait été indenté par l'arc de Luzon le long de la direction de convergence de la plaque PH par rapport à la plaque EU. A 8 Ma, la compression dans l'ancien bassin arrière-arc débuterait.

4) Il y a 3 Ma, la surrection de Taiwan est en partie réalisée. En premier lieu, le bassin arrière-arc, situé sous la Chaîne Centrale Ouest, a été comprimé et soulevé car sa lithosphère était peu épaisse. Les anciennes failles normales du bassin arrière-arc ont été reprises de façon préférentielle en failles inverses (par exemple, la faille de Lishan). Le mélange de Lichi est apparu le long de la Vallée Longitudinale (i.e. la frontière de convergence entre l'arc de Luzon et l'ancien arc des Ryukyus).

5) Actuellement, la collision arc-arc est active dans la partie centrale de Taiwan (23°N ; 121,2°E). L'ancien arc (ou le complexe de Tananao) a été comprimé et soulevé.
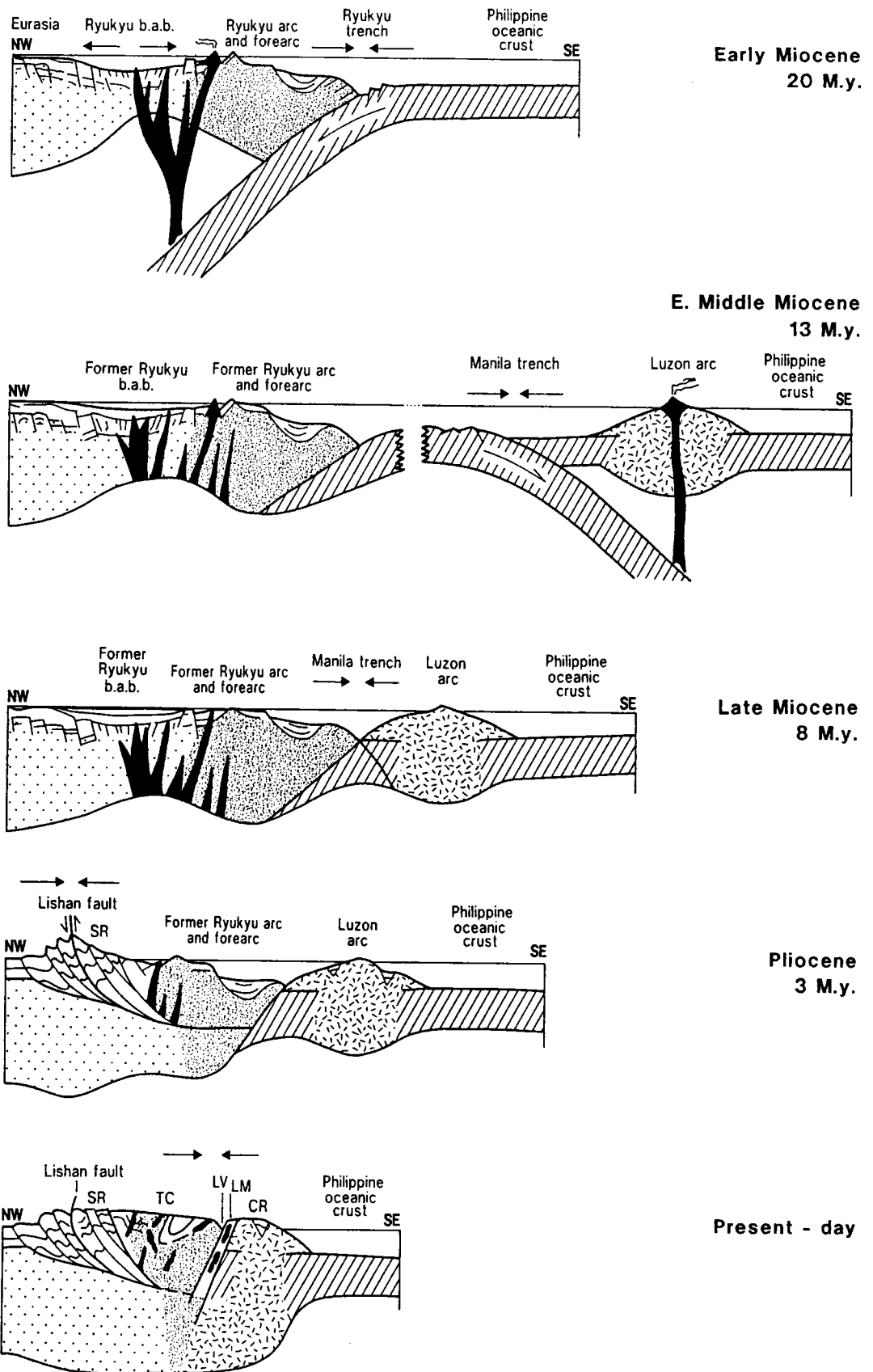
Fig. 33 : Modèle simplifié de l'évolution de la collision arc-arc à Taiwan de 20 Ma à l'actuel.

4. CONCLUSIONS

L'objectif de ce travail était de mieux comprendre les processus de la collision active à Taiwan. L'analyse des données géophysiques et géologiques réalisée dans ce travail et par d'autres auteurs a permis :

- de localiser la position de l'ancien arc des Ryukyus à partir des données gravimétriques dérivées des données altimétriques (e.g. Sandwell et Smith, 1994) ou mesurées à terre (Yeh et Yen, 1991).

- de montrer une répartition des mécanismes au foyer en compression entre 23°N et 24°N, au niveau de la région en contact avec l'arc de Luzon, et en extension en dehors de cette zone.

- de mettre en évidence la présence d'une discontinuité orientée N295° au niveau de Yushan (à 23,5°N) à partir des données structurales et gravimétriques. L'existence de cette discontinuité est corroborée par la distribution du champ de vitesse géodésique (Yu et al, 1995). Elle délimite une région à champ de vitesse stable au nord, d'une région où le champ de vitesse augmente de l'ouest vers l'est et du nord vers le sud, au sud.

- de révéler la présence de vitesses élevées des ondes P sous la Chaîne Centrale (Wu et al., 1995).

- de montrer que la région le long de la faille de Lishan est passée d'un régime extensif à un régime compressif au Miocène supérieur-Pliocène (Lee, 1994).

- de mettre en évidence des décrochements majeurs orientés NW-SE, entre le nord-est de Taiwan et 123,5°E. L'orientation de l'arc des Ryukyus à l'ouest de 123,5°E est quasi parallèle à la direction de la convergence entre les plaques PH et EU (Hsu et al., 1995b).

- de révéler que la fosse de Manille disparaît à 21,5°N de latitude et serait connectée à la Vallée Longitudinale par un décrochement dextre.

- de montrer que la partie de la zone de subduction des Ryukyus située à l'ouest de l'arc de Luzon a subi une rotation anti-horaire (e.g. Angelier et al., 1986) et la partie est a subi une rotation dans le sens horaire (e.g. Lee et al., 1991 ; Miki, 1995 ; Hsu et al., 1995b).

Ces observations nous ont conduit à proposer un nouveau modèle de collision arc-arc pour expliquer la surrection de Taiwan. Les principaux résultats sont :

i) L'ancienne zone de subduction des Ryukyus aurait fonctionné jusqu'à environ 13 Ma, du sud-ouest de Taiwan au sud du Japon.

ii) Ensuite, la partie sud-ouest de la zone de subduction des Ryukyus, située entre le bassin de Tainan et la partie sud-ouest de l'arc des Ryukyus, serait devenue inactive. La migration de la fosse de Manille vers le nord-est aurait permis la formation de l'arc de Luzon.

iii) La collision entre l'arc de Luzon et l'arc inactif des Ryukyus aurait commencé aux environs de la longitude 123,5°E. A l'ouest de 123,5°E, l'arc des Ryukyus aurait été indenté par l'arc de Luzon dans la direction N310°. Cet épisode correspond au stade de pré-surrection de Taiwan.

iv) La surrection de l'île de Taiwan aurait commencé vers 8 Ma, avec la compression de l'ancien bassin arrière-arc localisé à l'emplacement actuel de la Chaîne Centrale Ouest suivi de la compression entre l'arc fossile des Ryukyus (Complexe de Tananao) et l'arc de Luzon.

Il reste bien sûr de nombreux problèmes géologiques à éclaircir ; en particulier, l'origine de la discontinuité majeure située au nord-ouest de Yushan et le problème de la connexion des structures correspondant à l'arc fossile des Ryukyus du sud du bassin de Tainan au Complexe de Tananao.

5. RÉFÉRENCES

Angelier, J., 1986. Préface, Tectonophysics, 125, p. 4.

Angelier, J., 1990. Geodynamic evolution of the eastern Eurasian margin (Foreword), Tectonophysics, 183, VII-X.

Angelier, J., Barrier, E. et Chu, H.-T., 1986. Plate collision and paleostress trajectories in a fold-thrust belt: the Foothills of Taiwan, Tectonophysics, 125, p. 161-178.

Aubouin, J., 1990. The west Pacific geodynamic model, Tectonophysics, 183, p.1-7.

Barrier, E. et Müller, C., 1984. New observations and discussion on the origin and age of the Lichi mélange, Mem. Geol. Soc. China, 6, p. 303-326.

Ben-Avraham, Z., Nur, A., Jones, D. et Cox, A., 1981. Continental accretion: from oceanic plateaus to allochonous terranes, Science, 213, p. 47-54.

Biq, C., 1969. Role of gravitational gliding in Taiwan tectogenesis, Bull. Geol. Surv. Taiwan, 20, p. 1-39.

Biq, C., 1977. The Kenting melange and the Manila trench, Proc. Geol. Soc. China, 15, p. 191-222.

Biq, C., 1981. Collision, Taiwan-style, Mem. Geol. Soc. China, 4, p. 91-102.

Briais, A., Patriat, P. et Tapponnier, P., 1989. Reconstructions of the South China Basin and implications for Tertiary tectonics in Southeast Asia, Earth Planet. Sci. Lett., 95, p. 307-320.

Chai, B. H. T., 1972. Structural and tectonic evolution of Taiwan, Amer. Jour. Sci., 272, p. 389-422.

Chemenda, A. I., Yang, R. K., Hsieh, C.-H. et Groholsky, A. L., 1995. The result from 3-D physical modeling of the Taiwan collision, ACT international conference and 3rd Sino-French symposium on active collision in Taiwan, program and extended abstracts, 22nd-23rd March, 1995, Geol. Soc. China, Taiwan, R.O.C., p. 33-40.

Chen, P.-Y., 1991. Basaltic-andesitic volcanic rocks from the areas of Changshinchiao and Hsiangyang, southern E-W cross island highway, Taiwan, Spec. Publ. Centr. Geol. Surv., 2, p. 1-3.

Chen, C.-S., 1995, Geoelectric structures along the plate boundary: the Longitudinal valley, Taiwan, ACT international conference and 3rd Sino-French symposium on active collision in Taiwan, program and extended abstracts, 22nd-23rd March, 1995, Geol. Soc. China, Taiwan, R.O.C., p. 49-56.

Cheng, S.-N. et Yeh, Y.-T., 1989. Catalog of the earthquakes in Taiwan from 1604 to 1988, Inst. Earth Sciences, Academia Sinica, 255pp.

Cheng, S.-N. et Yeh, Y.-T., 1991. Seismotectonics of the Taiwan-Luzon region as evidenced from seismicity and focal mechanism of earthquakes, TAICRUST workshop

proceedings, June 10-12, 1991, Taipei, Taiwan, R.O.C., p. 219-226.

Cheng, S.-N., Lee, C.-T. et Yeh, Y.-T., 1992. Seismotectonics of the Ryukyu Arc. Proceeding of the fourth Taiwan Symposium on Geophysics, Taiwan, p. 507-516.

Chi, W.-R., 1982. The calcareous nannofossils of the Lichi melange and the Kenting melange and their significance in the interpretation of plate-tectonics of Taiwan, Ti-Chi, 4, p. 155-194. (en chinois).

Davis, D., Suppe, J. et Dallen, F. A., 1983. Mechanics of fold-and-thrust belts and accretionary wedges, J. Geophys. Res., 88, p. 1153-1172.

Deffontaines, B., Lee, J.-C., Angelier, J., Carvalho, J. et Rudant, J.P., 1994. New geomorphic data on the active Taiwan orogen: A multisource approach, J. Geophys. Res. 99, p. 20243-20266.

Hilde, T. W. C. et Lee, C.-S., 1984. Origin and evolution of the west Philippine basin: a new interpretation, Tectonophysics, 102, p. 85-104.

Ho, C.-S., 1967. Structural evolution and major tectonic forms of Taiwan, Proc. Geol. Soc., 10, p. 3-24.

Ho, C.-S., 1982. Tectonic evolution of Taiwan: explanatory text of the tectonic map of Taiwan, The Ministry of Economic Affairs, Taipei, Taiwan, R.O.C., 126 pp.

Ho, C.S., 1988. An introduction to the geology of Taiwan: Explanatory text of the geologic map of Taiwan, 2nd, Minist. Econ. Affairs, Rep. of China, 192 pp.

Holloway, N. H., 1982. North Palawan block, Philippines - its relation to Asian mainland and role in evolution of South China Sea, Am. Assoc. Pet. Geol. Bull., 66, p. 1355-1383.

Hsu, S.-K. et Sibuet, J.-C., 1995. Is Taiwan the result of arc-continent or arc-arc collision?, Earth Planet. Sci. Lett., sous presse.

Hsu, S.-K., Sibuet J.-C. and Shyu, C.-T., 1995a. High-resolution detection of geologic boundaries from 3-D potential field anomalies: an enhanced analytic signal technique, Geophysics, sous presse.

Hsu, S.-K., Sibuet, J.-C., Monti, S., Shyu, C.-T. et Liu, C.-S., 1995b. Transition between the Okinawa trough backarc extension and the Taiwan collision: new insights on the southernmost Ryukyu subduction zone, Mar. Geophys. Res., sous presse.

Hu, J.-C., Angelier, J., Lee, J.-C., Chu, H.-T., et Byrne, D., 1995a. Kinematics of convergence, deformation and stress distribution in the Taiwan collision area: 2-D finite-element numerical modelling, Tectonophysics, sous presse.

Hu, J.-C., Angelier, J., Yu, S.-B. et Lu, C.-Y., 1995b. An interpretation of the GPS velocity field of southern Taiwan based on numerical modelling, ACT international conference and 3rd Sino-French symposium on active collision in Taiwan, program and extended abstracts, 22nd-23rd March, 1995, Geol. Soc. China, Taiwan, R.O.C., p.

141-149.

Huang, C.-Y., Lin, C.-W., Wu, W.-Y. et Chang, C.-P., 1995a. Geological significance of the Lichi and Kenting melanges in Taiwan, ACT international conference and 3rd Sino-French symposium on active collision in Taiwan, program and extended abstracts, 22nd-23rd March, 1995, Geol. Soc. China, Taiwan, R.O.C., p. 151-155.

Huang, C.-Y., Yuan, P. B., Song, S.-R., Lin, C.-W., Wang, C., Chen, M.-T., Shyu, C.-T. et Karp, B., 1995b. Field guide to the tectonics of short-lived intra-arc basins in the arc-continent collision terrane of the Coastal Range, eastern Taiwan, ACT international conference and 3rd Sino-French symposium on active collision in Taiwan, post conference field trip, p. 32-50.

Jahn, B.-M., Liou, J. G. et Nagasawara, H., 1981. High-pressure metamorphic rocks of Taiwan: REE geochemistry, Rb-Sr ages and tectonic implication, Mem. Geol. Soc. China, 4. p. 497-520.

Kamata, H. et Kodama K., 1994. Tectonics of an arc-arc junction: an example from Kyushu island at the junction of the southwest Japan arc and the Ryukyu arc, Tectonophysics, 233, p. 69-81.

Karig, D. E., 1973. Plate convergence between the Philippines and the Ryukyu islands, Marine Geology, 14, p. 153-168.

Kizaki, K., 1978. Tectonics of the Ryukyu island arc. In S. Uyeda, R.W. Murphy and K. Kobayashi (Eds.), Geodynamics of the Western Pacific, J. Phys. Earth, Suppl. Issue, p. 301-307.

Kizaki, K., 1986. Geology and tectonics of the Ryukyu islands, Tectonophysics, 186, p. 193-207.

Kuramoto, S. et Konishi, K., 1989. The southwest Ryukyu arc is a migrating microplate (forearc sliver), Tectonophysics, 163, p. 75-91.

Lallemand, S. E., Liu, C.-S. et Lin, S.-J., 1995. Behaviour of the Ryukyu forearc sliver in the wake of the indenting northern Luzon arc (east of Taiwan), ACT international conference and 3rd Sino-French symposium on active collision in Taiwan, program and extended abstracts, 22nd-23rd March, 1995, Geol. Soc. China, Taiwan, R.O.C., p. 167-175.

Lee, J.C., 1994. Structure et déformation active d'un orogène: Taiwan, Thèse de Doctorat, Univ. Pierre et Marie Curie, Paris, 281 pp.

Lee, J.-C. et Angelier, J., 1993. Localisation des déformations actives et traitement des données géodésiques : l'exemple de la faille de la Vallée Longitudinale, Taiwan, Bull. Soc. Géol. France, 164, 4, p. 533-540.

Lee, J.-C., Angelier, J. et Chu, H.-T., 1995. Back-thrusting and paleostress analysis in the straigraphic boundary: the Lishan fault, northern Taiwan, ACT international

conference and 3rd Sino-French symposium on active collision in Taiwan, program and extended abstracts, 22nd-23rd March, 1995, Geol. Soc. China, Taiwan, R.O.C., p. 185-192.

Lee, T.-Q., Angelier, J., Chu, H.-T. et Bergerat, F., 1991. Rotations in the northern eastern collision belt of Taiwan: preliminary results from paleomagnetism, Tectonophysics, 199, p. 109-120.

Lee, T.-Y. et Lawver, L. A., 1994. Cenozoic plate reconstruction of the South China Sea region, Tectonophysics, 235, p. 149-180.

Lee, T.-Y., Tang, C.-H., Ting, J.-S. et Hsu, Y.-Y., 1993a. Sequence stratigraphy of the Tainan basin, offshore southwestern Taiwan, Petrol. Geol. Taiwan, 28, p. 119-158.

Lee, T.-Y., Hsu, Y.-Y. et Tang, C.-H., 1995a. Structural geometry of the deformation front between 22°N and 23°N and migration of the Penghu canyon, offshore southwestern Taiwan arc-continent collision zone, ACT international conference and 3rd Sino-French symposium on active collision in Taiwan, program and extended abstracts, 22nd-23rd March, 1995, Geol. Soc. China, Taiwan, R.O.C., p. 219-227.

Letouzey, J. et Kimura, M., 1986. The Okinawa trough: genesis of a backarc basin developing along a continental margin, Tectonophysics, 125, p. 209-230.

Lin, M.-T. et Tsai, Y.-B., 1981. Seismotectonics in Taiwan-Luzon area, Bull. Inst. Earth Sciences, Academia Sinica, 1, p. 51-82.

Liu, C.-S., Liu, S.-Y., Kuo, B.-Y., Lundberg, N. and Reed, D.L., 1992. Characteristics of the gravity and magnetic anomalies off southern Taiwan, Acta Geologica Taiwanica, 33, p. 123-130.

Liu, C.-S., Lundberg, N., Reed, D. L. et Hung, Y.-L., 1993. Morphological and seismic characteristics of the Kaoping submarine canyon, Marine Geology, 111, p. 93-108.

Lu, C.-Y. et Hsü, K. J., 1992. Tectonic evolution of the Taiwan mountain belt, Petrol. Geol. Taiwan, 27, p. 15-35.

Lu, C.-Y. et Malavielle, J., 1994. Oblique convergence, indentation and rotation tectonics in the Taiwan Mountain Belt: Insight from experimental modelling, Earth Planet. Sci. Lett. 121, p. 477-494.

Lundberg, N., Reed, D. L., Liu, C.-S., Chen, M.-P. et Gerace, D. A., 1995. ACT international conference and 3rd Sino-French symposium on active collision in Taiwan, program and extended abstracts, 22nd-23rd March, 1995, Geol. Soc. China, Taiwan, R.O.C., p. 243-247.

Miki, M., 1995. Two-phase opening model for the Okinawa trough inferred from paleomagnetic study of the Ryukyu arc, J. Geophys. Res., 100, p. 8169-8184.

MRSO, 1982. Final report of SLAR survey of the Republic of China, Mining Research and Service Organization of Industrial Technology Research Institute, 84 pp.

232

Pelletier, B., 1985. De la fosse de Manille à la chaîne de Taiwan. thèse de Doctorat, Université de Bretagne Occidentale, Brest, 286 pp.

Rangin, C., 1989. The Sulu Sea, a backarc basin setting within a Neogene collision zone, Tectonophysics, 161, p. 119-141.

Reed, D. L., Lundberg, N., Liu, C.-S. et Kuo, B.-Y., 1992. Structural relations along the margins of the offshore Taiwan accretionary wedge: implication for accretion and crustal kinematics, Acta Geologica Taiwanica, 30, p. 105-122.

Sandwell, D.T. et Smith, W.H.F., 1994. New global marine gravity map/grid based on stacked ERS-1, Geosat and Topex altimetry, EOS, AGU, Spring meeting, 75, Abstract, p. 321.

Sandwell, D.T., Yale, M.M. et Smith, W.H.F., 1995. Gravity anomaly profiles from ERS-1, Topex and Geosat altimetry, EOS, AGU, Spring meeting, 76, Abstract, p. 89.

Sarewitz, D. R. et Karig, D. E., 1986. Geologic evolution of western Mindoro island and the Midoro suture zone, Philippines, J. Southeast Asian Earth Sci., 1, p. 117-141.

Seno, T., Stein, S. et Gripp, A.E., 1993. A model for the motion of the Philippine Sea plate with NUVEL-1 and Geological data, J. Geophys. Res., 98, p. 17941-17948.

Sibuet, J.-C., Letouzey, J., Barrier, F., Charvet, J., Foucher, J.-P., Hilde, T.W.C., Kimura, M., Chiao, L.-Y., Marsset, B., Muller, C. et Stephan, J.-F., 1987. Back arc extension in the Okinawa trough, J. Geophys. Res., 92, p.14041-14063.

Sibuet, J.-C., Hsu, S.-K., Shyu, C.-T. et Liu, C.-S., 1995. Structural and kinematic evolutions of the Okinawa trough backarc basin. *In* Taylor, B., Ed., Backarc basins: tectonics and magmatism, Plenum, New-York, p. 343-379.

Sun, S.-C. et Hsu, Y.-Y., 1991. Overview of the Cenozoic geology and tectonic development of offshore and onshore Taiwan, TAICRUST workshop proceedings, June 10-12, 1991, Taipei, Taiwan, R.O.C., p. 35-47.

Suppe, J., 1981. Mechanics of mountain-building and metamorphism in Taiwan, Mem. Geol. Soc. China, 4, p. 67-90.

Suppe, J., 1984. Kinematics of arc-continent collision, flipping of subduction, and back-arc spreading near Taiwan, Mem. Geol. Soc. China, 6, p. 21-34.

Tang, C.-H., 1977. Late Miocene erosional unconformity on the subsurface Peikang high beneath the Chiayi-Yulin coastal plain, Taiwan, Mem. Geol. Soc. China, 2, p. 155-168.

Teng, L. S., 1990. Geotectonic evolution of late Cenozoic arc-continent collision in Taiwan, Tectonophysics, 183, p. 57-76.

Teng, L. S., 1992. Geotectonic evolution of Tertiary continental margin basin of Taiwan, Petrol. Geol. Taiwan, 27, p. 1-19.

Tsai, Y.-B., 1978. Plate subduction and the Plio-Pleistocene orogeny in Taiwan, Petrol. Geol. Taiwan, 15, 1-10.

Tsai, Y.-B., 1986. Seismotectonics of Taiwan, Tectonophysics 125, p. 17-37.

Tsai, Y.-B., Feng, C. C., Chiu, J.-M. et Liaw, H.-B., 1975. Correlation between microearthquakes and geologic faults in the Hsintien-Ilan area, Petrol. Geol. Taiwan 12, p. 149-167.

Viallon, C., Huchon, P. et Barrier, E., 1986. Opening of the Okinawa basin and collision in Taiwan: a retreating trench model with lateral anchoring, Earth Planet. Sci. Lett., 80, p. 145-155.

Wageman, J.M., Hilde, T.W.C. et Emery, K.O., 1970. Structural framework of East China Sea and Yellow Sea, Am. Assoc. Pet. Geol. Bull., 54, p.1611-1643.

Williams, P. R., Johnston, C. R.., Almond, R. A. et Simamora, W. H., 1988. Late Cretaceous to Early Tertiary structural elements of West Kalimantan, Tectonophysics, 148, p. 279-297.

Wu, F.T., 1970. Focal mechanisms and tectonics in the vicinity of Taiwan, Bull. Seism. Soc. Amer., 60, p. 2045-2056.

Wu, F.T., 1978. Recent tectonics of Taiwan. In S. Uyeda, R.W. Murphy and K. Kobayashi (Eds.), Geodynamics of the Western Pacific, J. Phys. Earth, Suppl. Issue, p. 265-299.

Wu, F. T., Rau, R.-J. et Salzberg, D., 1995. Are we ready to critically evaluate hypotheses of Taiwan orogeny, ACT international conference and 3rd Sino-French symposium on active collision in Taiwan, program and extended abstracts, 22nd-23rd March, 1995, Geol. Soc. China, Taiwan, R.O.C., p. 293-300.

Yeh, Y.-H. et Yen, H.-Y., 1991. Gravity anomalies of Taiwan and their tectonic implications, TAICRUST workshop proceedings, June 10-12, 1991, Taipei, Taiwan, R.O.C., p. 175-184.

Yeh, Y.-H., Barrier, E., Lin, C.H. et Angelier, J., 1991. Stress tensor analysis in the Taiwan area from focal mechanism of earthquakes, Tectonophysics, 200, p.267-280.

Yen, T.-P., 1963. The metamorphic belts within the Tananao schist terrain of Taiwan, Proc. Geol. Soc. China, 6, p.72-74.

Yen, T.-P., 1975. Lithostratigraphy and geologic structure of Taiwan, Geol. Paleontol. S. E. Asia, 15, p. 303-323.

Yu, S.-B., Chen, H.-Y. et Kuo, L.-C., 1995. Velocity field of GPS stations in the Taiwan area, ACT international conference and 3rd Sino-French symposium on active collision in Taiwan, program and extended abstracts, 22nd-23rd March, 1995, Geol. Soc. China, Taiwan, R.O.C., p. 317-327.

Annexe : carte bathymétrique au large de Taiwan (1:1500000)